RADAR IMAGING

OF

SOLAR SYSTEM ICES

A DISSERTATION

SUBMITTED TO THE DEPARTMENT

OF ELECTRICAL ENGINEERING

AND THE COMMITTEE ON GRADUATE STUDIES

OF STANFORD UNIVERSITY

IN PARTIAL FULFILLMENT OF THE REQUIREMENTS

FOR THE DEGREE OF

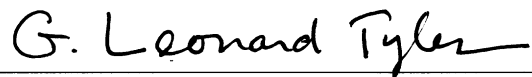DOCTOR OF PHILOSOPHY

Leif J. Harcke

May 2005

I certify that I have read this dissertation and that, in my opinion, it is fully adequate in scope and quality as a dissertation for the degree of Doctor of Philosophy.
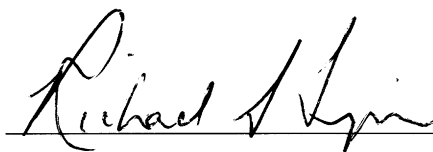
<div style="text-align: center;">
Prof. Howard A. Zebker   Principal Advisor
</div>

I certify that I have read this dissertation and that, in my opinion, it is fully adequate in scope and quality as a dissertation for the degree of Doctor of Philosophy.

<div style="text-align: center;">
Prof. G. Leonard Tyler
</div>

I certify that I have read this dissertation and that, in my opinion, it is fully adequate in scope and quality as a dissertation for the degree of Doctor of Philosophy.

<div style="text-align: center;">
Dr. Richard A. Simpson
</div>

Approved for the University Committee on Graduate Studies.

Abstract

We map the planet Mercury and Jupiter's moons Ganymede and Callisto using Earth-based radar telescopes and find that all bodies have regions exhibiting high, depolarized radar backscatter and polarization inversion ($\mu_c > 1$). Both characteristics suggest volume scattering from water ice or similar cold-trapped volatiles. Synthetic aperture radar mapping of Mercury's north and south polar regions at fine (6 km) resolution at 3.5 cm wavelength corroborates the results of previous 13 cm investigations of enhanced backscatter and polarization inversion ($0.9 \leq \mu_c \leq 1.3$) from areas on the floors of craters at high latitudes, where Mercury's near-zero obliquity results in permanent Sun shadows. Co-registration with Mariner 10 optical images demonstrates that this enhanced scattering cannot be caused by simple double-bounce geometries, since the bright, reflective regions do not appear on the radar-facing wall but, instead, in shadowed regions not directly aligned with the radar look direction. A simple scattering model accounts for exponential, wavelength-dependent attenuation through a protective regolith layer. Thermal models require the existence of this layer to protect ice deposits in craters at other than high polar latitudes. The additional attenuation (factor $1.64 \pm 15\%$) of the 3.5 cm wavelength data from these experiments over previous 13 cm radar observations supports multiple interpretations of layer thickness, ranging from 0 ± 11 to 35 ± 15 cm, depending on the assumed scattering law exponent n.

Our 3.5 cm wavelength bistatic aperture synthesis observations of the two outermost Galilean satellites of Jupiter, Ganymede and Callisto, resolve the previous north-south ambiguity, and confirm the disk-integrated enhanced backscatter and polarization inversion noted in prior investigations. The direct imaging technique more clearly shows that higher backscatter areas are associated with the terrain that has undergone recent resurfacing, such as the sulci and the impact crater basins. The leading hemispheres of both moons have

somewhat higher (20% $\pm 5\%$) depolarized echoes than their trailing hemispheres, suggesting additional wavelength-scale structure in the regolith. This may indicate gardening of material by micrometeoroid impacts.

Two improvements to existing delay-Doppler techniques enhance data reduction. First, correlating with subsets of the standard, repetitive pseudo-noise code alleviates Doppler dimension aliasing by satisfying the Nyquist criterion for sampling the output of the range compression stage. Application of the same algorithm to long-code data leads to a factor of five improvement in processing time for mildly overspread targets through the application of Fourier convolution. Second, a spectral weighting technique reduces clutter in long-code processing by equalizing clutter in the delay and Doppler dimensions.

Acknowledgements

Contents

List of Tables

List of Figures

List of Symbols

$*$	1D convolution operator
$**$	2D convolution operator
a	Planetary radius
a_{cr}	Crater radius
$a_i(t)$	Time-dependent signal amplitude
A	Area
$A(r)$	Radially-dependent annular area
$A(\xi)$	1D angle-dependent array power pattern
$A(\xi, \eta)$	2D angle-dependent array power pattern
A_{cr}	Crater area
$A_{\text{e}}(\xi)$	Antenna pattern of array element
A_{ill}	Radar-bright, illuminated area of crater floor
A_{r}	Receive antenna aperture
A_{eff}	Resolution element effective area
A_{res}	Area of a radar resolution element
A_{t}	Effective transmitting antenna area
b	PN baud length
B	Pulse bandwidth
B_{t}	Target bandwidth
$B(\xi)$	1D angle-dependent sky brightness distribution
$B(\xi, \eta)$	2D angle-dependent sky brightness distribution
c	Speed of light
c_n	BPSK chip symbol $\in \{-1, 1\}$

$C(\tau, v)$	Composite ambiguity function
d	Depth, or derivative operator (context dependent)
D	Diameter of antenna
∂	Partial derivative operator
$dA_\perp$	Differential area projected onto plane of sky
d_{eff}	Effective depth
Δd	Change in depth
$\vec{E}$	Position of Earth in planet-centered coordinates
E_{s}	Total energy of signal $s(t)$
$E_{\text{x}}(z,t)$	x component of electric field propagating in z direction
f_0	Carrier frequency
f_c	Cutoff frequency
f_{d}	Instantaneous Doppler frequency of a point on planet surface
f_m	Harmonic multiple m of pulse repetition frequency
f_{s}	Sampling frequency
f_P	Doppler coordinate of a point
$f(\bar{r})$	Composite model of radar backscatter
$\vec{F}$	Total normalized velocity
Δf	Planet bandwidth
G_{t}	Transmit antenna gain
$\vec{G}$	Geocentric position of planet under observation
$h_1(t), h_2(t)$	Time-dependent filter impulse responses
$h_{\tau, v}(t)$	Time-dependent delay-Doppler matched filter impulse response
$\vec{H}$	Geocentric vector velocity of planet under observation
I_0	Modified Bessel function
$I(x,y)$	Received power intensity
j	Integer valued quantity, or the imaginary constant $\sqrt{-1}$ (context dependent)
k	Integer valued quantity, or Boltzmann's constant (context dependent)
$\vec{k}$	Vector propagation constant
K	Integer valued quantity, or FFT length (context dependent)
l	Antenna array spacing

Δl	Incremental antenna array spacing
m	Integer valued quantity, or scattering law exponent (context dependent)
M	Integer valued quantity
n	Integer valued quantity, or scattering law exponent (context dependent)
N	Count of items in a discrete sequence (context dependent)
N'	Modified count of items in a discrete sequence
N_{clut}	Number of clutter elements
$\mathscr{O}_T(\tau, \nu)$	Matched filter response at time $t = T$
P_{t}	Transmit power
$P_n(t)$	Baseband random BPSK waveform
$\vec{P}$	Position of point on observed planet
$q(t)$	Delayed and Doppler-shifted signal
Q_{ext}	Extinction coefficient
$r(t)$	Time-dependent range, or received signal (context dependent)
$\bar{r}$	Normalized distance in planetary radii
$\vec{r}$	Position vector
r_{b}	Effective beam radius
r_k	Discrete autocorrelation function
r_x	Range from leading edge of planet to a point on surface
r_0	Initial range
$\dot{r}_0$	Initial velocity
R	Instantaneous range to target center of mass
$\vec{R}$	Position of target center of mass
$\dot{\vec{R}}$	Instantaneous velocity of target center of mass
ΔR	Range resolution
$\Delta R_{\mathrm{cross}}$	Cross-range resolution
s	Voltage sidelobe ratio
$s(t)$	Time-dependent transmitted signal
sinc	$\sin(\pi x)/(\pi x)$ function
S	Signal power
$S(\xi)$	1D angle-dependent "dirty" source image

$S(\xi, \eta)$	2D angle-dependent "dirty" source image
$S'(\xi, \eta)$	2D angle-dependent "cleaned" source image
t	Time
T	Pulse time extent, or causal system delay (context dependent)
T_M	Chebyshev polynomial coefficient
T_{sys}	System noise temperature
T_{t}	Target time extent or delay
u	1D spatial frequency coordinate
$u(t)$	Time-dependent baseband modulating signal
$\tilde{u}(t)$	Time-dependent baseband received signal
$\vec{u}_R$	Unit vector from radar to target
v	Instantaneous velocity, or 2D spatial frequency coordinate (context dependent)
$\vec{v}$	Instantaneous velocity of point on observed planet
$\vec{v}_E$	Instantaneous line of sight velocity
$v_i(t)$	Time-dependent complex voltage
$V_{\text{amb}}^{(c)}$	Volume under composite ambiguity function
$V(u)$	1D source visibility function
$V(u, v)$	2D source visibility function
w_n	Discrete windowing function weights
$w(r)$	Radially-dependent weighting function
$W(u)$	1D array spectral sensitivity function
$W_{\text{e}}(u)$	Fourier transform of antenna pattern of array element
$W(u, v)$	2D array spectral sensitivity function
$W(v)$	Frequency response of window function
$\bar{W}(\bar{v})$	Normalized frequency response of window function
x	Coordinate
x_n	Discrete sequence of PN data
$x(t)$	Time-dependent received signal
y	Coordinate
z	Coordinate
z_0	Chebyshev polynomial scale factor

α	Attenuation constant, or bandwidth ratio (context dependent)
α_λ	Wavelength-dependent attenuation constant
β	Scalar propagation constant
γ	Scale factor, or $\tan\delta_c$ (context dependent)
δ	BPSK chip length
$\delta(t)$	Unit impulse distribution
$\delta^2(\tau, f)$	2D impulse distribution
$\bar{\delta r}$	Synthesized image grid spacing in planetary radii
$\tan\delta_c$	Loss tangent
ε	Dielectric permittivity
ε'	Real part of dielectric permittivity
ε''	Imaginary part of dielectric permittivity
ε_r'	Real part of relative dielectric permittivity
ε_r''	Imaginary part of relative dielectric permittivity
ζ	Arbitrary scale factor
η	Angle on sky, or projected radar cross section (context dependent)
$\Delta\eta$	Differential radar cross section
θ	Angle (context dependent)
θ_i	Angle of incidence
$\theta_{i,\lambda}$	Angle of incidence for wavelength λ
θ_n	BPSK symbol phase $\in \{0, \pi\}$
θ_r	Angle of reflection
θ_t	Angle of transmission
λ	Wavelength
μ	Magnetic permeability
μ_c	Circular polarization ratio
μ_r	Relative magnetic permeability
ν	Instantaneous frequency
ν_0	Carrier frequency
$\bar{\nu}$	Normalized frequency
ξ	Angle on sky, or arbitrary scale factor (context dependent)

ξ_0	Initial angle on sky
ρ	Normal incidence specific cross section
σ	Radar cross section
$\bar{\sigma}$	Normalized planet radar cross section
$\hat{\sigma}$	Estimated, normalized planet radar cross section
$\hat{\sigma}(\tau, f)$	Estimated radar cross section
σ_d^2	Variance of layer thickness d
σ_C	Undesired clutter cross section of one resel
$\sigma_{C,\text{tot}}$	Undesired total clutter cross section
σ_{eff}	Effective conductivity of material
σ_S	Desired resolution element cross section
σ_{pc}	Perfect conductor RCS
σ_{OC}	Opposite sense circular polarization RCS
σ_{SC}	Same sense circular polarization RCS
σ_{res}	Radar cross section of a resolution element
σ_0	Specific radar cross section
$\sigma_{\varepsilon_r'}$	Variance of permittivity
σ_γ^2	Variance of loss tangent
σ_λ	Wavelength-dependent cross section
σ_ξ^2	Variance of the cross section ratio
τ	Instantaneous delay
τ'	Fractional baud delay
$\bar{\tau}$	Normalized delay
$\Delta\tau$	Planet delay depth
τ_P	Delay coordinate of a point
ϕ	Phase
$\phi(t)$	Time-dependent phase
χ	Ambiguity function
$\chi(\tau, \nu)$	Radar ambiguity function
$\chi_p(\tau, \nu)$	Fundamental chip radar ambiguity function
$\chi_s(\tau, \nu)$	Ambiguity function of signal $s(t)$

$\psi(t)$	Time-dependent phase-shifted signal
ω	Frequency, rad/s
$\vec{\omega}$	Vector angular velocity, rad/s
$\vec{\omega}_{\mathrm{s}}$	Angular velocity due to sidereal spin
$\vec{\omega}_{\mathrm{cr}}$	Angular velocity due to target cross-range velocity
$\vec{\omega}_{\mathrm{t}}$	Total angular velocity
$\Delta\omega$	Planet bandwidth, rad/s
Ω	Sidereal spin rate, rev/s
Ω_b	Angular synthesized beam size
$\bar{\Omega}_b$	Angular synthesized beam size normalized to units of planetary radii

List of Abbreviations and Acronyms

1D	One-dimensional
2D	Two-dimensional
A/D	Analog-to-Digital
AIPS	Astronomical Image Processing System
AU	Astronomical Unit
Bm	VLA synthesized beam
BPSK	Binary Phase Shift Keying
CW	Continuous Wave
dB	Decibels
Dec	Declination
DSS	Deep Space Station
FDTD	Finite-Difference, Time-Domain
FFT	Fast Fourier Transform
FIR	Finite Impulse Response
ISAR	Inverse Synthetic Aperture Radar
JPL	Jet Propulsion Laboratory
kW	Kilowatt
LCP	Left-hand circular polarization
LHEP	Left-hand elliptical polarization
LNA	Low-noise amplifier
MASER	Microwave Amplification by Stimulated Emission of Radiation
MHz	Megahertz
MIT	Massachusetts Institute of Technology

mJy	MilliJansky
MW	Megawatt
NAIC	National Astronomy and Ionosphere Center
NASA	National Aeronautics and Space Administration
NRAO	National Radio Astronomy Observatory
OC	Opposite sense circular polarization
PN	Pseudo Noise
RA	Right Ascension
RADAR	Radio Detection and Range
RCP	Right-hand circular polarization
RCS	Radar Cross Section
RF	Radio frequency
RHEP	Right-hand elliptical polarization
RSD	Radar Speckle Displacement
RSPIC	Residual south polar ice cap
SAR	Synthetic Aperture Radar
SC	Same sense circular polarization
SCR	Signal to Clutter Ratio
SNR	Signal to Noise Ratio
T/R	Transmit-Receive
UTC	Coordinated Universal Time
VLA	Very Large Array

Chapter 1

Introduction

Earth-based radar studies of the planets commenced at the end of World War II, enabled by the general availability of radar equipment that had been developed for the war effort. In January 1946, John DeWitt, Jr. led the first successful radar detection of the Moon using the Army Signal Corps facility at Fort Monmouth, New Jersey (DeWitt and Stodola, 1949). In February of that same year, Zoltan Bay, working at a United Incandescent Lamps and Electric Company facility in Budapest, Hungary, also detected lunar echoes (Bay, 1947). The ensuing fifty years of radar-astronomical research have been documented in detail in review articles by Pettengill (1978) and Ostro (1993), and the NASA History Series book by Butrica (1996). For the past two decades, most Earth-based radar studies have used either the Goldstone Solar System Radar near Barstow, California, or the Arecibo Observatory near Arecibo, Puerto Rico for both transmission and reception. For interferometric or bistatic geometry studies, radio telescopes of the National Radio Astronomy Observatories have been employed as receiving antennas, though these systems were designed primarily for passive observation and do not contain transmitters.

There are many applications of Earth-based radar astronomy to the study of solar system bodies, but two dominate the literature: i) measurement of astrometric and planetographic quantities, and ii) mapping of surface features. The former studies serve to update and maintain the orbital ephimerides of the planets, asteroids, and comets and support studies of the dynamical evolution of these bodies. The latter studies probe the properties of

surfaces and subsurfaces, leading to a better understanding of their geology and composition. Modern radar astronomy grew out of military technology which was developed for the detection and tracking of aircraft and missiles, and by design can measure accurately the range and velocity of distant objects. In fact, the etymology of the term radar is well known—it is an acronym for "RAdio Detection And Ranging." "Ranging" in this context denotes the measurement of the distance to, or range of, an object. In radar astronomy, measured astrometric quantities include distances to planets, orbit parameters, sidereal rotation rates, pole positions on the celestial sphere, and surface topography and scattering parameters.

In the 1950's, military technologists experimented with airborne radar systems to determine precisely the range and velocity of individual points on the ground below and to one side of the aircraft, and thus map the surface (Sherwin et al., 1962). This technique, known as side-looking or strip-map synthetic aperture radar (SAR), produces images at resolutions comparable to those of optical cameras. Radar imaging provides several advantages over optical methods. The long wavelength of the radar penetrates cloud layers which often obscure optical observations of targets. Moreover, since the radar provides its own illumination source, this type of imaging works equally well at daytime or nighttime.

The resolution of the instrument in the cross-track, or range, dimension is set by the bandwidth of the modulating waveform, while the resolution in the velocity or Doppler dimension is set by the bandwidth of echoes captured by the radar antenna and the coherent observing time. In radar astronomy, the motion of the Earth through the solar system and the rotation of the target body on its spin axis provide the necessary velocity. When the majority of the motion is provided by the rotation of the object under observation rather than platform motion, the mapping process is usually referred to as inverse synthetic aperture radar (ISAR). Price and Green (1960) proposed using unfocused ISAR to map planetary surfaces. In unfocused ISAR imaging, sometimes called delay-Doppler imaging, the radar cross-section of the target is computed for uniform spacings of resolution elements in both the delay and Doppler dimensions, producing a 2-D raster image of the rotating target.

Radar astronomy has evolved steadily over the past four decades. The small apertures, low transmitter powers, and high receiver noise temperatures characteristic of early planetary radars limited the utility of the technique from the mid-1940's through the late

1950's. During the 1960's, with the development of large-aperture antennas for both the military and civilian space programs, radar astronomy flourished. Significant results of the period included refinement of the astronomical unit (Victor and Stevens, 1961), determination of the retrograde rotation and spin rate of Venus (Goldstein, 1964), discovery of the 3:2 resonance between the spin rate of Mercury and its orbital period (Pettengill and Dyce, 1965), and a fourth confirmation of general relativity (Shapiro et al., 1968). As radar equipment developed during the Cold War became available to radar astronomers, spatially resolved maps of the Moon and Venus were formed using the MIT Haystack, JPL/Caltech Goldstone, and NAIC/Cornell Arecibo systems (Thompson and Dyce, 1966; Pettengill and Thompson, 1968; Goldstein, 1969; Jurgens, 1970). The lunar studies supported the Apollo manned missions to the Moon, while the imaging of Venus provided the first detections of significant features on a surface shrouded from optical observations by the planet's thick clouds. Continual upgrading of antenna reflecting surfaces, microwave transmitters, and low noise receivers during the 1970's put outer solar system objects such as the Galilean satellites of Jupiter (Goldstein and Morris, 1975; Campbell et al., 1977) and the rings of Saturn (Goldstein and Morris, 1973) within the reach of Earth-based instruments. In the 1980's, completion of the Very Large Array led to the adoption of aperture synthesis techniques developed for radio astronomy (Thompson et al., 1986) at the receiving site of bistatic Earth-based radar experiments. Significant results using synthesis imaging included detection of outer solar system objects such as Titan (Muhleman et al., 1990) and mapping of inner solar system planets such as Mars and Mercury (Muhleman et al., 1991; Butler et al., 1993). In the 1990's the increasing computing power available for post-processing of radar data led to the collection, archiving, and processing of immense data sets to achieve fine resolution imaging (Stacy, 1993; Harmon et al., 1994) and detailed topographic measurements using interferometric techniques (Margot, 1999). Our work builds on these by applying 21st century computational capability, waveform flexibility, and aperture synthesis to the study of solar system bodies.

1.1   Motivation

This dissertation addresses radar imaging of solar system objects that are thought to be composed of ice. The presence of water is a requisite to biological life as we know it, and the positive detection of water in liquid or solid form on other solar system bodies supports theories that life may exist or may have existed there, or that water may be available for future human explorers.

Though liquid water has not been detected directly on any extraterrestrial planetary body, ice exists in many places in the solar system. The three outer Galilean satellites of Jupiter, Europa, Ganymede, and Callisto, are known to have icy outer coverings since the Voyager interplanetary mission in the late 1970's. Recent observations of the Jovian system by the Galileo spacecraft support the theory that Jovian tidal forces acting on Europa dissipate sufficient energy in the interior to create an ocean several tens of kilometers deep between a surface ice crust shell and the solid bedrock beneath (Cassen et al., 1979; Carr et al., 1998). This hypothesis is consistent with magnetic field measurements from the Galileo magnetometer, which are best explained as the result of conducting layers at depth in the form of a salty ocean (Khurana et al., 1998). Closer to home, the laser altimeter on the Mars Global surveyor spacecraft confirmed that the north polar cap consists of up to 3 km of water ice (Zuber et al., 1998). More recently, the thermal emission imaging system on Mars Odyssey found direct evidence that the permanent south polar cap of Mars contains exposed water ice (Titus et al., 2003), while Mars Express found evidence for perennial ice at the south pole (Bibring et al., 2004).

It is interesting to note that Earth-based radar observations of both the Galilean satellites (Campbell et al., 1977) and Mars' residual south polar ice cap (RSPIC) (Muhleman et al., 1991) revealed the particular anomalous backscatter properties of these surfaces years before more definitive evidence about the presence of ice was obtained from spacecraft missions. The specific phenomena present are relatively high normalized backscatter, greater than ≈ 0.5 over a wide range of incidence angles, and "polarization inversion," which is the detection of greater power in the same circular polarization as transmitted, as compared with the opposite sense.

Radar reflections from rocky planetary regoliths, such as those of the Moon, Mercury,

Venus, and Mars, are characterized by specular or mirror-like reflections, which reverse the polarization of an incident circularly polarized plane wave. Thus, most reflected power appears with the sense of circular polarization opposite (OC) to that transmitted. Silicate regoliths have dielectric constants ≈ 3 and the reflection is dominated by glints from the region around the sub-radar point on the surface. The normalized radar cross section (RCS) is typically less than ≈ 0.2 in the polarized component, and is much less in the depolarized or same sense circular (SC) polarization as transmitted. The depolarized return is attributed to multiple specular scattering from surface features such as cracks, edges, and roughness on the scale of the wavelength of observation. The ratio of the depolarized to polarized reflected power, called the polarization ratio, is typically on the order of $\mu_c \approx 0.1$ for these surfaces.

On the other hand, the three icy Galilean satellites and the RSPIC of Mars have high total-planet-equivalent, normalized RCS approaching or exceeding ≈ 1, and polarization ratios $\mu_c > 1$. These large, contiguous icy surfaces exhibit volume scattering and are not as lossy to penetrating waves as are rocky planetary regoliths. These particular icy surfaces do not produce strong specular reflections in the exact backscatter direction, and return an enhanced depolarized echo, leading to polarization ratios ≈ 1 or greater for Earth-based, monostatic observations. Polarization inversion is indicative of multiple or volume scattering. A combination of: i) a search for high specific RCS for initial identification, followed by ii) estimation of the polarization ratio for confirmation, has been the primary method for finding regions of planetary surfaces that may contain water ice.

In the early 1990's, dual-polarization measurements of reflectivity from the planet Mercury (Harmon and Slade, 1992; Slade et al., 1992) showed both enhanced backscatter and polarization inversion from the floors of craters at the north and south pole. Results from thermal models led to suggestions that, since Mercury's obliquity is near zero, cold traps can form in the permanently shadowed floors of polar craters (Paige et al., 1992; Vasavada et al., 1999). Curiously, though the Moon is a close analogy to Mercury in many ways, Earth-based radar observations have not detected similar reflections from the permanently shadowed lunar poles (Stacy et al., 1997; Margot et al., 1999; Campbell et al., 2003a). A tentative ice detection by spacecraft-Earth bistatic radar (Nozette et al., 1996, 2001) has been challenged (Simpson and Tyler, 1999), but neutron spectrometer data are consistent

with the presence of water molecules (Feldman et al., 2001), though not necessarily in the form of large ice blocks required to produce volume scattering effects at radar wavelengths. Sources for water at Mercury include cometary bombardment and out-gassing from volcanism, though the prevalence of deposits in newer Class 3–4 impact craters and dearth in older Class 1–2 craters favors the exogenic source hypothesis.[1] One conclusion of the thermal modeling of cold traps on Mercury is that, for long term stability of ice deposits at latitudes less than 80 degrees, an insulating layer of dust or regolith material covering the deposit is necessary (Vasavada et al., 1999). Though volume scattering from icy bodies is fairly insensitive to wavelength throughout the centimeter-wavelength band (Ostro et al., 1992), an attenuating regolith layer could cause measurable wavelength dependent attenuation of the microwave radar signal (Butler, 1994; Harmon et al., 2001), depending on the material properties and the physical configuration of the blanketing layer and the ice.

In the first part of this study, we set out to form high-resolution maps of the polar regions of Mercury at 3.5 cm wavelength, which had not been accomplished previously due to a clutter problem which increases with decreasing wavelength. Detailed 15 km and 1.5 km resolution mapping at 13 cm wavelength has been previously reported by Harmon et al. (1994, 2001), while 3.5 cm mapping with the Goldstone/Very Large Array bistatic system by Butler et al. (1993) was limited to greater than 150 km resolution. At these wavelengths, the rotation of Mercury on its axis produces Doppler aliasing ambiguities in the resultant ISAR imaging maps. In order to mitigate such aliasing, we employ the pseudo-noise long-code SAR technique of Sulzer (1986), first implemented for planetary radar by Harmon and Slade (1992), to map the polar regions of Mercury at 6 km resolution using the Goldstone Solar System Radar. We examine the wavelength dependent nature of the backscatter, in order to examine the protective dust layer hypothesis. Subsequent analysis of these data show that the "unusual" radar echoes are located in areas of permanent shadow, and that a

---

[1]Mercury's craters were classified c_5–c_1, newest–oldest, by N.J. Trask and reported in McCauley et al. (1981) and the U.S.G.S. geologic maps of the polar regions by Grolier and Boyce (1984) and Strom et al. (1990). The classification scheme is: "Class 5—Craters characterized by sharp rims, crisp interior forms (for large craters), rays, and very few superposed craters. Class 4—Distinct but visibly modified rims and interior features; well-preserved radial faces around larger craters. Class 3—Relatively low, semirounded but continuous rims and subdued interior landforms. Class 2—Low rims and shallow interior relief. Interior forms scarce; secondary crater fields absent. Class 1—Low, partial rims. Some craters barely distinguishable from surrounding plains materials; interior features rare. Secondary crater fields absent."

blanketing regolith layer, if extant, ranges from 0 ± 11 to 35 ± 15 cm thick.

In the second part of this study, we employ the bistatic aperture synthesis technique of Muhleman et al. (1990, 1991) to map the surfaces of the Jovian satellites Ganymede and Callisto with the Goldstone/Very Large Array instrument without spatial ambiguity. Mapping of specific RCS variations on the surfaces of the icy Galilean satellites allows identification of terrains which cause the enhanced scatter. It is important to note that such an observation was first attempted in 1990 by Muhleman, Butler, and Slade, but without success due to atmospheric phase noise from the humid summer atmosphere over the Very Large Array. Previous mapping of Ganymede and Callisto by Ostro et al. (1992) used inversion of the Doppler spectrum (Hudson and Ostro, 1990), which is subject to a fold-over ambiguity of the northern and southern hemispheres. Standard delay-Doppler imaging also suffers from this fold-over ambiguity. Analysis of our unambiguous images shows that radar-bright features are associated with recently re-surfaced terrain in the sulci and impact craters.

1.2 Synopsis

This dissertation is structured as follows. Chapter 2 describes delay-Doppler or unfocused ISAR imaging as applied to planetary radar investigations. We first outline the achievable resolution and signal-to-noise ratio constraints; then we describe the translation of the processed data from radar coordinate systems to planetary coordinates. Next, we discuss the fold-over ambiguities inherent in conventional delay-Doppler methods of processing. We examine the long-code method for overcoming some of these ambiguities. Finally, we analyze clutter performance.

In Chapter 3 we present an overview of the standard aperture synthesis imaging technique as normally employed in radio-astronomical imaging, beginning with a derivation of the basic technique for a two element interferometer. We next discuss extending the one-dimensional array to two dimensions and examine the Fourier relationship between the imaging plane and the interferometer correlation measurements. We discuss briefly deconvolution of the array response or point spread function from the image output.

Chapter 4 contains a summary of models and measurements for interpreting dual-polarization backscatter from planetary surfaces. We describe the simple cosine law model for Minnaert scattering from a sphere as a useful model for interpreting typical visible-hemisphere backscatter from the icy Galilean satellites. We summarize previous scattering parameter measurements obtained by other experimenters for Europa, Ganymede, Callisto, and Mercury. We then develop an additional simple model for the wavelength dependence of scattering from a vacuum-regolith-ice interface, which we then apply in Chapter 5 to place boundaries on possible insulating dust layers blanketing anomalous scatterers on Mercury.

In Chapter 5 we describe our experiment and results for high-resolution imaging of Mercury's polar regions using the Goldstone Solar System Radar in monostatic mode and the techniques of Chapter 2. We present radar data co-registered with optical data from the Mariner 10 mission to highlight areas of enhanced backscatter with polarization inversion. We fit the dust-layer thickness model developed in Chapter 4 and derive an estimate of thickness for the blanketed crater model ranging from 0 ± 11 to 35 ± 15 cm, depending on the scattering law exponent n.

In Chapter 6 we describe the experiment and present results for low-resolution imaging of Ganymede and Callisto using the Goldstone and Very Large Array facilities in a bistatic configuration. We fit hemispherical backscatter models from Chapter 4 to the data. The radar data are co-registered with optical images from the Galileo mission to identify terrains exhibiting backscatter brighter than that of surrounding terrains.

Finally, in Chapter 7 we summarize our main conclusions.

In two appendices we give details of the radar coding and signal processing employed to image Mercury, and we present a combined radar/optical atlas of the Borealis and Australis quadrangles of the planet.

1.3   Contributions

The principal contributions of this work are:

- New 3.5 cm wavelength, dual-polarization specific RCS maps of the north and south polar regions of Mercury at 6 km resolution. We co-register these data with optical

images from the Mariner 10 mission. The co-registered observations corroborate earlier 13 cm observations (Harmon et al., 1994, 2001) which show the bright material exists in permanently shadowed areas of large craters.

- New 3.5 cm wavelength, dual-polarization RCS maps of the leading and trailing hemispheres of Ganymede and Callisto at 350 km resolution. These images are of comparable resolution to previous results but are free of north-south fold-over. Co-registration of the data with Galileo spacecraft optical imagery shows that bright albedo features are associated with recently re-surfaced terrain such as sulci and impact craters.

Chapter 2

Planetary Delay-Doppler Imaging

Delay-Doppler imaging of planets was first proposed by Price and Green (1960) for the purpose of creating maps of planetary surfaces by use of large ground-based radars. The technique resolves the planetary surface by transforming the radar echoes to surface locations from a grid of time-delay and Doppler frequency resolution elements. In traditional delay-Doppler imaging, standard pulse compression methods are used to achieve fine resolution in the range dimension. Fourier analysis of successive segments of data after the pulse compression stage yields resolution in the cross-range, or Doppler, dimension. In modern terminology, this type of imaging corresponds to "unfocused" synthetic aperture radar (SAR) processing. As the synthesized aperture is formed primarily by the rotation of the target object rather than the motion of the radar, in current times the technique is often referred to as inverse synthetic aperture radar (ISAR). We use this latter terminology here.

2.1 Standard technique

Schematic ISAR imaging geometry is shown in Figure 2.1. For a point at position $\vec{P}$ on the surface of a rigid, rotating object, the radar measures the range and line-of-sight velocity of the point. Define the unit vector pointing from the radar to the target center of mass to be

$$\vec{u}_R = \frac{\vec{R}}{|\vec{R}|}. \tag{2.1}$$

11
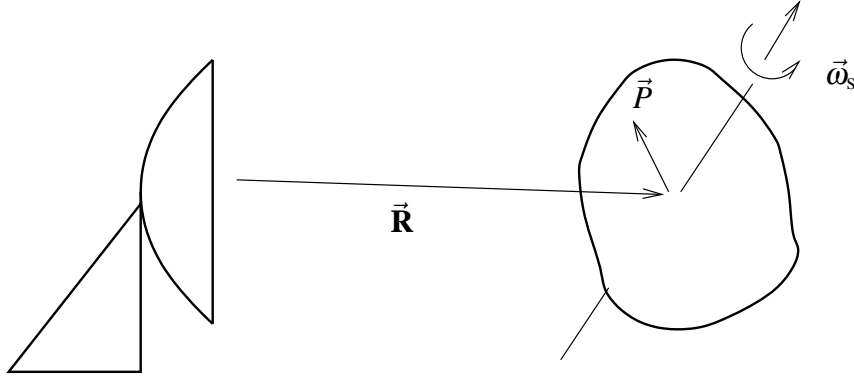
Figure 2.1 ISAR geometry for a spinning target. Surface locations are defined by vectors $\vec{P}$ from the center of mass of a rigid, rotating body. The center of mass of the body is at position $\vec{R}$ from the radar antenna. The body spins about an axis through the center of mass with angular velocity $\vec{\omega}_s$. This spin causes a position-dependent Doppler shift for the radar echo from point P.

For solar system geometries when the range to the target is much greater than the diameter of the target, or $|\vec{R}| \gg |\vec{P}|$, the scalar range r to the point is

$$r = |\vec{R}| + \vec{P} \cdot \vec{u}_R. \tag{2.2}$$

The instantaneous radial velocity of the point is equal to the vector cross product of the angular velocity of the body with the vector to the point, dotted into the line of sight to the radar

$$v = (\vec{\omega}_s \times \vec{P}) \cdot \vec{u}_R. \tag{2.3}$$

These two properties can be estimated by the radar which measures the instantaneous delay,

$$\tau = 2r/c \tag{2.4}$$

and the instantaneous Doppler shift,

$$f_d = -2f_0 v/c \tag{2.5}$$

of a transmitted and reflected waveform, where f_0 is the carrier frequency in Hertz.

In ISAR imaging, unless the radar and target are at rest, the relative motion between

the target's center of mass and the radar modifies the apparent rotation of the object. The instantaneous cross-range velocity of the target, as seen in the radar frame of reference, changes the spin axis of the object $\vec{\omega}_s$ to form an effective total angular spin vector $\vec{\omega}_t$. This composite rotation can be substituted into (2.3) to determine the apparent velocity of a point on the surface of the object.

Denoting the instantaneous velocity of the target's center of mass as $\dot{\vec{R}}$, the cross-range component of the velocity is

$$\vec{v}_{cr} = \dot{\vec{R}} - (\vec{u}_R \cdot \dot{\vec{R}})\vec{u}_R. \tag{2.6}$$

The total cross-range rotation $\vec{\omega}_{cr}$ is the sum of i) the the apparent rotation caused by the cross-range velocity, and ii) the target's true spin $\vec{\omega}_s$ crossed into the line of sight $\vec{u}_R$, or

$$\vec{\omega}_{cr} = \frac{\vec{v}_{cr}}{|\vec{R}|} + \vec{u}_R \times \vec{\omega}_s. \tag{2.7}$$

The total spin vector $\vec{\omega}_t$ is this cross-range rotation vector crossed into the line of sight $\vec{u}_R$

$$
\begin{aligned}
\vec{\omega}_t &= \vec{\omega}_{cr} \times \vec{u}_R \\
&= \frac{\vec{v}_{cr}}{|\vec{R}|} \times \vec{u}_R + (\vec{u}_R \times \vec{\omega}_s) \times \vec{u}_R \\
&= \frac{\vec{v}_{cr}}{|\vec{R}|} \times \vec{u}_R - \vec{u}_R \times (\vec{u}_R \times \vec{\omega}_s) \\
\vec{\omega}_t &= \frac{\vec{v}_{cr}}{|\vec{R}|} \times \vec{u}_R - (\vec{u}_R \cdot \vec{\omega}_s)\vec{u}_R + (\vec{u}_R \cdot \vec{u}_R)\vec{\omega}_s. \tag{2.8}
\end{aligned}
$$

A version of this expression was first derived by Goldstein (1964), for Venusian spin vector estimation. The middle term in (2.8) is not in his paper, but contributes significantly when the rotation axis of the planet and the line of sight to the radar are not perpendicular.

The output of the mapping radar is a two-dimensional grid of reflectivity measurements, with delay along one axis and Doppler shift along the second axis. The mapping of delay and Doppler coordinates to planetary latitude and longitude coordinates follows a simple procedure. The latitude and longitude are first translated to rectangular coordinates, $\vec{P}$. Delay is typically measured with respect to the planet's front edge or subradar point. For a

spherical target of radius a, this relative delay is then

$$\tau_P = \frac{2}{c}\left(a + \vec{P}\cdot\vec{u}_R\right). \qquad (2.9)$$

The Doppler coordinate is

$$f_P = -2\frac{f_0}{c}\left(\vec{\omega}_t \times \vec{P}\right)\cdot\vec{u}_R. \qquad (2.10)$$

2.1.1   Delay resolution

Waveform design plays an important role in determining the mapping resolution and cross-talk or clutter and, hence, the quality of radar images. Imaging radars usually employ transmitted signals consisting of a sequence of pulses of time duration T. The sensitivity of a radar instrument is directly proportional to the transmitted power (see Section 2.1.4). The available peak power from microwave radar telescopes is limited; therefore, pulse compression techniques are employed to achieve high effective pulse power. The attainable range resolution of a pulse compression system is given by

$$\Delta R \cong c/2B \qquad (2.11)$$

where B is the modulated pulse bandwidth. The achieved resolution is independent of the pulse length.

   The pulse compression waveform most often used in planetary radar ISAR imaging is the maximal length pseudo-noise (PN) sequence (Elspas, 1955), implemented as binary phase shift modulation of the carrier. Pseudo-noise sequences have well-known aperiodic and periodic correlation properties. Furthermore, they are readily generated by simple shift registers. The aperiodic correlation of a discrete PN sequence x_n of length N is defined as

$$r_k = \sum_{n=0}^{N-1} x_n x_{n+k}, \quad -(N-1) < k < N-1 \qquad (2.12)$$
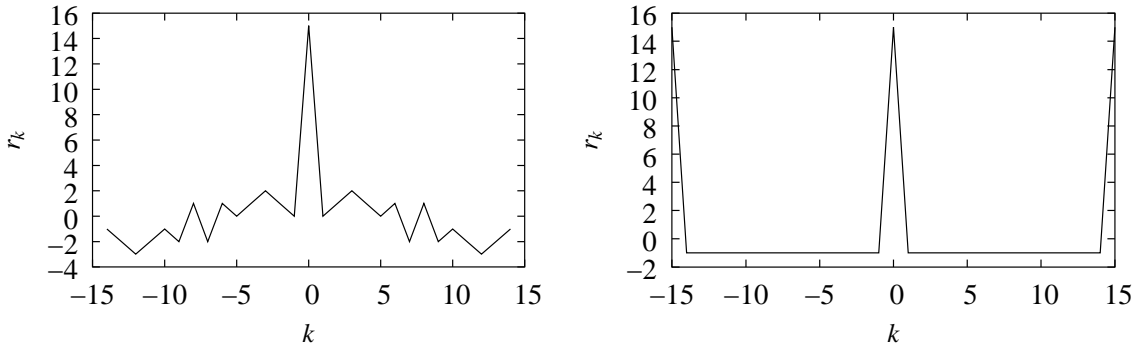
Figure 2.2 Aperiodic and periodic autocorrelation functions of a length 15 PN sequence. For a maximal length shift register sequence, the autocorrelation peak has a width of one baud.

while the periodic correlation is given by

$$r_k = \sum_{n=0}^{N-1} x_n x_{(n+k) \bmod N}, \quad \forall k. \tag{2.13}$$

Figure 2.2 displays aperiodic and periodic correlations of the standard maximal length shift register sequence.

The bandwidth of the PN signal, and hence the delay resolution, depends on the rate at which the bits in the PN sequence are clocked out of the shift register. The bit time is known as the baud, b, in seconds. The baud rate, or $1/b$, is the standard terminology used in communication theory to denote the rate at which symbols are transmitted over a communications channel. The bandwidth of the PN modulated signal is $B \cong 1/b$, which results in a range resolution of $\Delta R = cb/2$.

In planetary imaging, the true range to the planet is often known to a small fraction of the planet's radius—to better than 1–10 km—from an ephemeris. Aliasing of the true range to the leading edge of the planet, also called range ambiguity, can therefore be tolerated. The pulse repetition interval can be selected solely on the criterion that individual range gates on the planet should not alias the furthest delay bins containing the planet echo onto the delay bins containing echo from the sub-radar point or leading edge of the planet. This is accomplished by setting the pulse repetition interval equal to or longer than the delay

depth of the planet $\Delta\tau$ given by

$$\Delta\tau \geq 2a/c \tag{2.14}$$

where a is the planet radius in meters (see Figure 2.3). Dividing by the desired baud length b for a given range resolution and rounding up to the nearest quantity 2^{M-1} yields the size of the shift register M required to drive the modulator. The transmitted pulse sequence is a continuous stream, modulated binary phase-shift keyed (BPSK) waveform, with the PN sequence repeated at the pulse repetition interval set by $b \cdot 2^{M-1}$. Note that for this type of continuous wave (CW) waveform, the effective interpulse interval is equal to the length of the pulse sequence. This contrasts with the system design of pulse compression radars used in SAR mapping from aircraft or satellites, where the interpulse interval is typically several times longer than the pulse length. The round-trip light-time to the target is much shorter for ground-imaging radars than for planetary imaging. For the monostatic systems flown, the receiving periods must be interleaved with transmitted pulses.

The design of most monostatic radars does not provide for transmitting and receiving simultaneously, hence the radar is switched repeatedly between these two modes. In planetary imaging, the pulse stream is radiated continuously by the antenna until the time that the first portion of the echo is expected to return from the planet, at which point the system switches to receive mode and data are recorded for one round-trip light time. The matched filter impulse response of the range compression filter is the PN sequence. For standard, repetitive PN code delay-Doppler mapping, the periodic correlation function defined above adequately describes the output of the range compression stage after matched filtering. A total of 2^{M-1} unique delay bins are realized by the range compression process. On the surface of the planet, these delay bins correspond to a series of adjacent, concentric annuli expanding outward from the subradar point, as shown in Figure 2.3. The output of each of these range bins is complex sampled once per pulse, and subsequently match filtered in frequency in order to achieve resolution in the Doppler dimension.

Relative motion of the radar and planet within the solar system causes changes in the round-trip travel time, so that the stream of pulses received from the planet arrive at a variable rate. Modeling a unit amplitude transmitted signal $s(t)$ as,

$$s(t) = u(t)e^{j2\pi f_0 t} = e^{j\{2\pi f_0 t + \phi(t)\}} \tag{2.15}$$

ΔR_{cross}

Plane of
Sky View

Range ring

Doppler slice

$\Delta R = cb/2$

receding

A

approaching

Delay-Doppler
Space View

A

Delay
depth

Delay τ

Frequency f

Limb-to-limb bandwidth
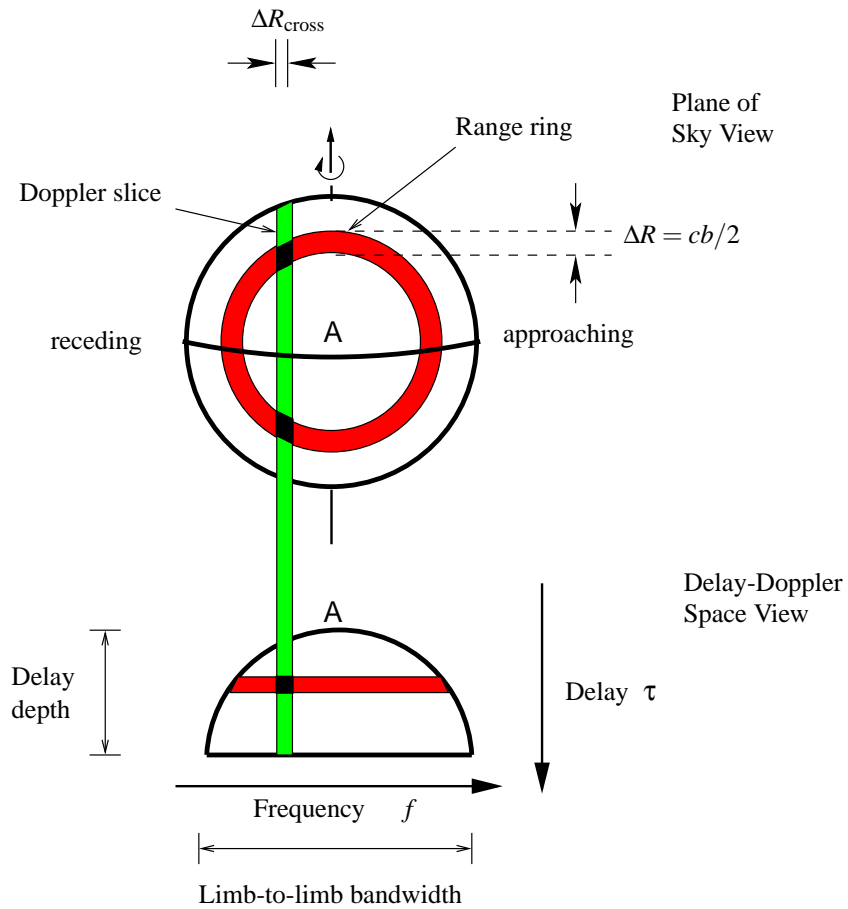
Figure 2.3 Illustration of Delay Doppler cells on planet (after Evans and Hagfors, 1968). The ground range-resolution is dependent on the angle of incidence θ_i on the approximately spherical planetary surface. The cross-range resolution ΔR_{cross} is defined in (2.20).

with carrier frequency f_0, phase modulation $u(t) = e^{j\phi(t)}$, range $r(t)$, and delay $2r(t)/c$, we have the received signal $x(t)$ from a point target as

$$
\begin{aligned}
x(t) &= s(t - 2r(t)/c) \\
&= e^{j\left\{2\pi f_0\left(t - \frac{2r(t)}{c}\right) + \phi\left(t - \frac{2r(t)}{c}\right)\right\}}
\end{aligned}
\tag{2.16}
$$

neglecting amplitude effects. By approximating the changing range to the target as $r(t) \approx r_0 + \dot{r}_0 t$, we have

$$
x(t) = e^{j\left\{2\pi f_0\left(1 - \frac{2\dot{r}_0}{c}\right)t - \frac{4\pi f_0 r_0}{c} + \phi\left[(1 - \frac{2\dot{r}_0}{c})t - \frac{2r_0}{c}\right]\right\}}.
\tag{2.17}
$$

After removing the effect of the carrier signal, we see that the received modulation starts with delay $2r_0/c$; but an additional time-varying delay term remains, so that the time history of the received phase modulation becomes

$$
\phi[(1 - 2\dot{r}_0/c)t].
\tag{2.18}
$$

This drift can be compensated at the transmitter exciter by appropriately changing the clock of the shift register, or similarly at the receiver by continuously varying the timebase of the A/D converter.

2.1.2   Doppler resolution

In order to realize resolution in the cross range or "Doppler" dimension, it is sufficient to Fourier analyze the output samples from each delay bin, and hence construct a two-dimensional output array of delay-Doppler resolution cells. The Fourier computations are most commonly implemented as a fast Fourier transform (FFT). The resolution of the FFT on the output of the range compression filter sampled every Nb seconds is $1/KNb$ Hz, where K is the FFT transform length. Thus, the Doppler resolution is set by the combination of the transform length and the the range compression filter length or, equivalently, the length of the combined matched filter, KNb.

The limb-to-limb planet bandwidth is the difference between the maximum and minimum Doppler shifts of the approaching and receding limbs of the planet. It can be calculated from

$$\Delta f = 8\pi\Omega f_0 a/c \qquad (2.19)$$

where Ω is the planetary rotation rate (rev/sec), f_0 is the radar carrier frequency, and a is the planet radius. The cross-range sample spacing can be obtained by dividing the planet diameter by the number of bins across the projected disk of the planet,

$$\Delta R_{\text{cross}} = \frac{2a}{KNb\Delta f} = \frac{c}{4\pi\Omega f_0 KNb}. \qquad (2.20)$$

Note that the cross-range resolution is defined in a plane tangent to the sub-radar point "A" (Figure 2.3) and perpendicular to the unit vector from the radar to the target $\vec{u}_R$. The cross-range resolution is also independent of the target radius a and the range to the target R. The Doppler frequency of each resolution cell is assumed constant in this analysis; processing by a bank of Doppler matched filters to form the cross range resolution generally is referred to as unfocused processing in the SAR literature. The bank of Doppler matched filters divides the echo spectrum of the planet into slices parallel to the total spin axis of the planet, as shown by the vertical band of width ΔR_{cross} in the upper half of Figure 2.3.

The relative motion of the radar and planet also affects the Doppler spectrum of the planet. From (2.17), the center frequency of the echo spectrum is Doppler shifted to

$$f_0 \left(1 - \frac{2\dot{r}_0}{c} \right). \qquad (2.21)$$

The shift may be removed either at the transmitter or at the receiver by varying the reference oscillator.

2.1.3 Resolution cell migration

In the discussions above, there is an implicit assumption that the planet does not rotate significantly on its axis during the period of coherent integration—over the period of time during which the motion-induced phase changes can be accurately modeled or applied. The

time delay and Doppler shift are taken to be essentially constant during the coherent integration period. In practice this assumption may be violated, in which case the movement of a point on the surface through the delay-Doppler grid must be accounted for to form a proper coherent matched filter. In the Doppler dimension, this migration is most significant for points near the Doppler equator, as these are the points of greatest instantaneous linear velocity in the plane of the sky. In the delay dimension, this migration is most significant near the radar terminator or limb, where the projection of the range bins onto the planet's surface results in the finest resolution cells.

The resolution cell size is a related consideration. Delay and Doppler migration become more problematic at higher resolutions, as longer coherent integration times are required to achieve fine resolution (2.20). In order to obtain high imaging resolutions, methods for following the exact phase history of a scattering center (Stacy, 1993) or for transforming the problem into a tomographic SAR geometry (Webb et al., 1998) can be employed.

In the observations of Mercury described in Chapter 5, we are primarily concerned with the polar regions of the planet. For the slow rotation of Mercury, the relatively coarse imaging resolutions considered in this study, and the limited area around the polar regions, delay-Doppler cell migration during primary, coherent imaging may be neglected. The effect of migration of surface points through delay-Doppler cells from one round-trip observation period to the next can be significant, however. As the planet rotates from one observing run to the next, migration of a particular resolution element on the surface through the delay Doppler array becomes an important factor. Migration of scatterers requires that incoherent averaging across multiple runs be implemented in a planetary coordinate system by first mapping delay-Doppler arrays from each run to a planetary grid (Evans and Hagfors, 1968; Harmon, 2002), if the intrinsic resolution of the radar data set is to be preserved.

2.1.4 Signal-to-noise ratio

Signal to noise ratio of a point target in one cell of an imaging radar can be obtained from the radar equation (Skolnik, 2002). A useful form of the monostatic radar equation is

$$\text{SNR} = P_t G_t \cdot \frac{1}{4\pi R^2} \cdot \sigma \cdot \frac{1}{4\pi R^2} \cdot A_r \cdot \frac{1}{kT_{\text{sys}}B} \qquad (2.22)$$

where P_t is the transmit power, G_t is the transmit antenna gain, R is the range to the target, σ is the target radar cross section (RCS), A_r is the receive antenna area, T_{sys} is the system temperature, $B = 1/KNb$ is the analysis bandwidth, or the inverse of the coherent integration time, and k is Boltzmann's constant.

In Chapter 5, we will be concerned with ISAR imaging of the polar regions of Mercury at high incidence angles θ_i to the surface normal. For ISAR imaging of an inclined surface element, the cross section $\sigma(\theta_i)$ may be expressed as

$$\sigma(\theta_i) = \sigma_0(\theta_i) A_{\text{res}} \tag{2.23}$$

where $\sigma_0(\theta_i)$ is the specific radar cross section of the reflecting surface (m^2 of RCS per m^2 of surface area), A_{res} is the area on the surface which projects into the resolution element, and θ_i is the angle of incidence on the mean spherical surface at the center of A_{res}. For delay-Doppler planetary mapping this becomes, upon expressing A_{res} in terms of the radar parameters,

$$\sigma = \sigma_0(\theta_i) \left(\frac{cb}{2} \right) \left(\frac{c}{4\pi\Omega f_0 KNb} \right) \csc \theta_i \tag{2.24}$$

where other constants were defined in the previous section. The analysis bandwidth is represented by the total coherent integration time $B = 1/KNb$ yielding the modified radar equation for a single resolution element as

$$\text{SNR} = P_t G_t \frac{1}{4\pi R^2} \sigma_0(\theta_i) \left(\frac{cb}{2} \right) \left(\frac{c}{4\pi\Omega f_0} \right) \csc \theta_i \frac{1}{4\pi R^2} A_r \frac{1}{kT_{\text{sys}}} \tag{2.25}$$

which we leave in semi-reduced form for clarity. As the coherent integration time KNb also sets the Doppler resolution of the imaging radar, it drops out of this equation. For a given radar system operating at frequency f_0, the SNR per resolution element is primarily set by the chosen baud length b.

As the total coherent integration time is generally much shorter than the typical round-trip light time observing run, multiple coherent images can be averaged incoherently to improve SNR and to decrease the "speckle" noise inherent in monochromatic imaging systems. The increase in SNR follows the well-known result that the improvement is proportional to the square root of the number of pulses averaged incoherently to form the final

image. In a typical observing run, there may be many coherent intervals which can be averaged incoherently. Several runs may also be averaged incoherently in order to improve image quality further.

2.2   Ambiguities

Interpretation of delay-Doppler imaging of solar system bodies suffers from several instrument and processing effects. These deficiencies are collectively labeled "ambiguities," but it is important to distinguish among the types of ambiguities. The two main types of degradation are the "north-south" fold-over ambiguity, and delay-Doppler aliasing which occurs when attempting simultaneously to extract the delay and Doppler information from a signal. Mitigation of these effects is a major issue in the observations described in this work.

2.2.1   North-south ambiguity

The north-south ambiguity is a consequence of the radar antenna's illuminating two hemispheres on the surface of the planet with identical trajectories through delay-Doppler space. For a radar lying in the plane of the target equator, the surface of a target planet is divided into delay-Doppler resolution elements, as shown in Figure 2.3. Every resolution element at a given value of time-delay and Doppler-shift in the northern hemisphere will have a conjugate cell with the same delay-Doppler position in the southern hemisphere. Since these two resolution cells map into the same delay-Doppler element, there is an ambiguity as to the associated location of the echo. An echo observed in an output delay-Doppler cell can be attributed to the corresponding point in either the northern or southern hemisphere or, more generally, to a combination of the two.

Several techniques exist for mitigating the effects of the north-south ambiguity. If the angular resolution of the antenna is sufficient, the telescope can be pointed so as to illuminate only one hemisphere. As the conjugate points in the opposite hemisphere appear in the sidelobe response of the telescope illumination pattern, they can often be discounted. The angular resolution of the single dish Goldstone and Arecibo radars is ≈ 0.1 deg for

the wavelengths used here, so this technique is limited to close targets with relatively large angular diameters, such as the Moon and Venus. Two or more antennas, each unable to resolve the ambiguity, may sometimes be arrayed into an interferometer to achieve the desired resolution (Rogers and Ingalls, 1970; Jurgens et al., 1980).

Another technique for resolving the two-hemisphere ambiguity stems from the low probability that the planet's spin axis is perpendicular to the line of sight of the radar telescope; in other words, the radar is not usually in the plane of the target's equator. As the planet rotates, a particular location on the surface of the planet migrates through a series of delay-Doppler resolution elements. As a result of polar tilt, the trajectory of a point in the northern hemisphere through the delay-Doppler array differs significantly from the trajectory taken by the conjugate point in the southern hemisphere (Green, 1962). If delay-Doppler arrays formed by coherent integration of the received data are first translated to planetary coordinates of one hemisphere and then incoherently averaged, the echo from points in the opposite hemisphere do not map consistently through the coordinate translation. Instead, with sufficient averaging, they appear as unresolved, additive clutter.

Hudson and Ostro (1990) developed a related imaging technique based on use of least squares inversion of a series of Doppler only projections, predicated on significant and variable polar tilt over the course of observations.

All of these techniques become more difficult as the areas of interest on the target approach the Doppler equator.

2.2.2 Overspread ambiguity

The second major ambiguity, which arises from delay and Doppler aliasing, is called the "overspread" planet ambiguity. This ambiguity is inherent in imaging large, rotating targets with standard pulse-compression delay-Doppler mapping. The planet's radius dictates the maximum pulse repetition rate as discussed in Section 2.1.1 above. If the pulse repetition rate required for Doppler sampling exceeds this criterion, then multiple pulses impinge on the planet at the same time and an ambiguity in range or Doppler or, more generally, both, results.

The output of the range compression filter for each range bin is sampled at the fundamental pulse period. To prevent range aliasing, we require that $Nb \geq 2a/c$ (2.14). The total echo received from the planet has a limb-to-limb bandwidth $\Delta f = 8\pi\Omega f_0 a/c$ (2.19). In order to avoid aliasing in the Doppler dimension of the output delay-Doppler array, we require that $1/Nb > \Delta f$. When the product of a planet's delay depth and its limb-to-limb bandwidth exceeds unity, it becomes impossible to avoid both range and Doppler aliasing. The planet is said to be overspread at the imaging frequency of interest. The overspread factor can be calculated from the product of (2.14) and (2.19)

$$\left(\frac{2a}{c}\right)\left(\frac{8\pi\Omega f_0 a}{c}\right). \tag{2.26}$$

2.2.3 Ambiguity function

Analysis of the resolution capabilities of a particular delay-Doppler waveform is aided by an understanding of the ambiguity function of the waveform. The ambiguity function shows the response of a matched-filter receiver to delayed and/or Doppler-shifted versions of the baseband modulation signal $u(t)$ where the transmitted signal is

$$s(t) = u(t)e^{j2\pi f_0 t}. \tag{2.27}$$

The ambiguity function $|\chi(\tau,f)|^2$ is defined as

$$|\chi(\tau,f)|^2 = \left|\int_{-\infty}^{\infty} u(t)u^*(t+\tau)e^{j2\pi f t}\, dt\right|^2. \tag{2.28}$$

The function is often plotted on either a magnitude scale $|\chi(\tau,f)|$ or a decibel scale $20\log_{10}|\chi(\tau,f)|$. The classic reference on the ambiguity function is Woodward (1953). There are two mathematically provable results from Woodward's analysis, i) that the volume under the ambiguity function, when normalized by the transmitted energy, is invariant, and ii) that the peak of the ambiguity function occurs at the point $\tau = 0, f = 0$. For a repetitive pulsed waveform with a fundamental pulse length T received by a sampled system, the central peak of the ambiguity function is periodic in both the delay dimension and the Doppler dimension. Typically, only the central instance of the function is plotted.

The imaging radar processor produces a delay-Doppler map of the target. The output map is the convolution of the true target distribution in delay-Doppler space with the ambiguity function of the transmitted waveform. Thus, the ambiguity function is the point-spread function[1] of the radar imaging process, and the estimated cross section $\hat{\sigma}(\tau, f)$ at the output of the processor is given by

$$\hat{\sigma}(\tau, f) = \int_{-\infty}^{\infty} \int_{-\infty}^{\infty} \sigma(\tau', f') \left| \chi(\tau - \tau', f - f') \right|^2 \, d\tau' df'. \tag{2.29}$$

Imaging without aliasing is possible if a waveform can be designed such that the periodic nature of its ambiguity function in the delay dimension is greater than the target delay extent T_t and the periodic nature of its Doppler dimension is greater than the target bandwidth B_t. The design and processing of such waveforms is discussed in Section 2.3.

2.3 Imaging overspread targets

Imaging an overspread target with the repetitive-pulse delay-Doppler methods of Section 2.1 causes aliasing in the delay dimension, the Doppler dimension, or both dimensions. One choice is to violate the bound on pulse repetition rate set by the planet delay depth and use shorter pulse lengths. This results in aliasing in the delay dimension in the output delay-Doppler array. An alternative choice is to choose the pulse repetition rate to satisfy the delay aliasing criterion, and instead violate the Nyquist criterion for sampling the bandwidth of the planet, resulting in aliasing in the Doppler dimension of the output delay-Doppler array. For some mapping geometries, slight aliasing in either the delay or Doppler dimension can be tolerated for a moderately overspread target. For highly overspread targets, though, compromise solutions must be employed.

One technique is to accept aliasing in the delay dimension and constrain the area of interest to the Doppler equator, where the projection of the range ring pattern will cause the leading edge to dominate the return (Zohar and Goldstein, 1974).

---

[1]The point-spread function is the impulse response of a 2-D imaging system. The ideal point-spread function is the 2-D delta function, $\delta^2(\tau, f)$, since convolution with $\delta^2(\tau, f)$ is the identity operation.

A second approach is to accept the aliasing if it is slight and does not affect the particular region of interest. Harmon et al. (2001) have employed this compromise to image Mercury's north pole at 13 cm wavelength utilizing the Arecibo telescope.

The overspread problem (2.26) can also be mitigated by lowering the carrier frequency of the radar system. As shown in (2.19), the extent of the target Doppler spreading Δf is directly proportional to the carrier frequency. There is not a wide selection of available wavelengths for planetary imaging, though. NASA funds two high-power microwave klystrons for planetary radar experiments, the 13 cm 1 MW transmitter at Arecibo, and the 3.5 cm 500 kW transmitter at Goldstone. A 70 cm instrument usually used for pulsed radar studies of the ionosphere is also available at Arecibo. Its low average power output, ≈ 10 db less than the 13 cm system, and the reduced gain of the Arecibo reflector at the long wavelength, are deterrents to most sensitive measurements or high-resolution mapping. Despite these shortcomings, the 70 cm system has been used recently to image Mercury (Black et al., 2002) and the Moon (Campbell et al., 2003a).

Each of these techniques is useful to some degree in imaging overspread objects in the solar system. There is yet another approach available for imaging these objects and maximizing the signal to clutter ratio, at the expense of more sophisticated signal processing. Application of this method, called "long-code" modulation, to the observation of solar system objects forms much of the work in this dissertation.

2.3.1   Long-code modulation

Long-code modulation is a technique which eliminates the delay aliasing inherent in standard delay-Doppler mapping. Each pulse is coded with a unique, random binary phase waveform. This coding produces low cross correlation between different pulses, in exchange for raising the background clutter level. Standard PN sequences achieve a $1/N^2$ range sidelobe level, where N is the length of the PN sequence. Random coding achieves only a $1/N$ range sidelobe level for an equivalent sequence length, but without range ambiguities.

Figure 2.4 shows the aperiodic cross correlation function of 100 bits of a random BPSK waveform with 1000 bits of data, which contains the 100 bit sequence embedded at an offset
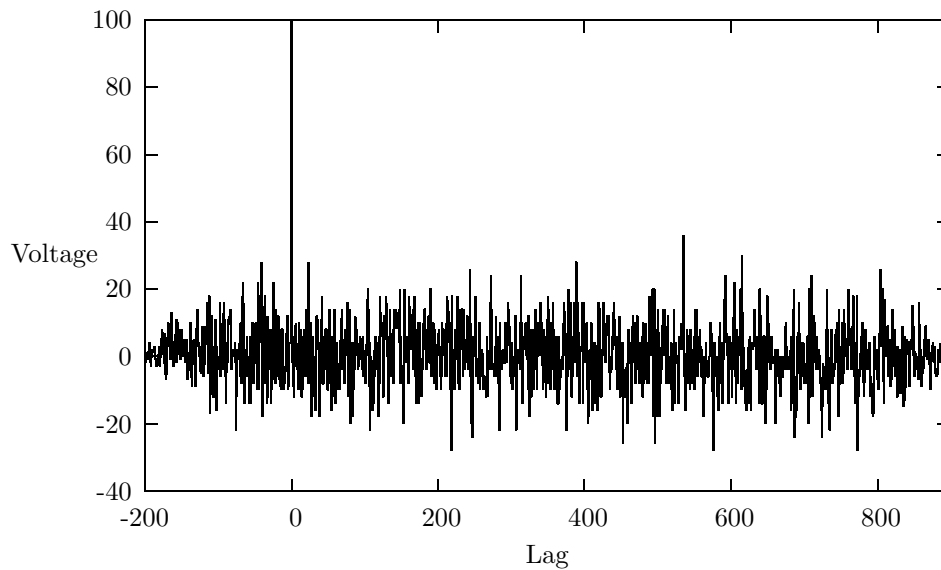
Figure 2.4 Cross correlation of a length 100 random binary sequence with a length 1000 binary sequence, which contains the length 100 sequence embedded at lag offset 0. The peak shows detection of the embedded sequence, but with correspondingly high sidelobes.

of 0. Note the single correlation peak, as well as the non-uniform and high delay sidelobes. This degradation is quantified in Section A.2.1.

The long-code method was pioneered for ionospheric observations by Sulzer (1986) at Arecibo, and adopted for planetary imaging by Harmon et al. (1992) after a suggestion by Hagfors and Kofman (1991). Hagfors and Kofman's proposal differed in one aspect from Harmon's implementation. They proposed using continuous analog noise as the waveform, rather than binary phase coded sequences. The use of random binary sequences to form the unique code for each pulse has become known as long-code in the radar astronomy community (Harmon, 2002).

A search of the historical literature shows that, though noise waveforms have been used only recently for astronomical imaging, the technique has been proposed and implemented in other arenas. A review of the field from the end of World War II through the mid-1950's is provided by Siebert (1956). Use of noise radar for ranging is reported by Horton (1959). The performance of pseudonoise BPSK signals in high Doppler environments was characterized by Lerner (1960). Work by Cooper and Purdy (1968) at Purdue University

on random noise radar measurements of natural processes led to experiments by Chadwick and Cooper (1972), primarily for measurement of ocean wave heights. A recent review of the field is given by Liu et al. (1999).

In the idealized long-code experiment, a truly random continuous BPSK waveform is transmitted at the target with a baud length chosen to produce the desired delay resolution. In practice, long shift register sequences are used as pseudo-random generators. The period of these shift register sequences is such that the period of repetition is on the order of hundreds of days, many times the length of the typical one to two hour duration of an observing run.

The transmitted sequence can be recorded for later cross correlation in one of two ways. Samples of every bit in the random waveform can be recorded during the transmitting portion of a cycle; or, more simply, the starting state of the shift register can be noted and the sequence regenerated from this starting state during the data processing stage.

The receiver for the long-code waveform consists of a simple matched filter. For each delay bin in the output delay Doppler array, the transmitted code is delayed according to the light time from the computed ephemeris, and then multiplied by the received data. This demodulates the echo in one delay bin, and is equivalent to the "despreading" process used in a spread-spectrum communications system. The demodulated samples from one delay bin form a sequence that can be Fourier analyzed to produce a Doppler spectrum for that delay bin. Longer Fourier transforms produce finer cross-range, or Doppler resolution. The echo power from other delay bins remains spread by the random sequence, and behaves as additive "white" noise clutter. A comparison can be made to multipath signals in radio telecommunications systems. Multipath signals, though initially modulated with the same spreading sequence as the desired, primary signal, arrive at different times. The time delay of the multipath signal does not match the time delay for the primary signal. Instead of demodulating properly, the multipath signals are again randomly modulated by the despreading process which is only matched to the primary signal. This results in an increase in the noise floor, but strong multipath interference experienced in non-spread-spectrum systems is mitigated. Returning to the radar imaging problem, the process of delay, multiply, and Fourier analyze is repeated for each delay bin on the planet, forming a complete delay-Doppler output array. The long-code technique for planetary imaging has
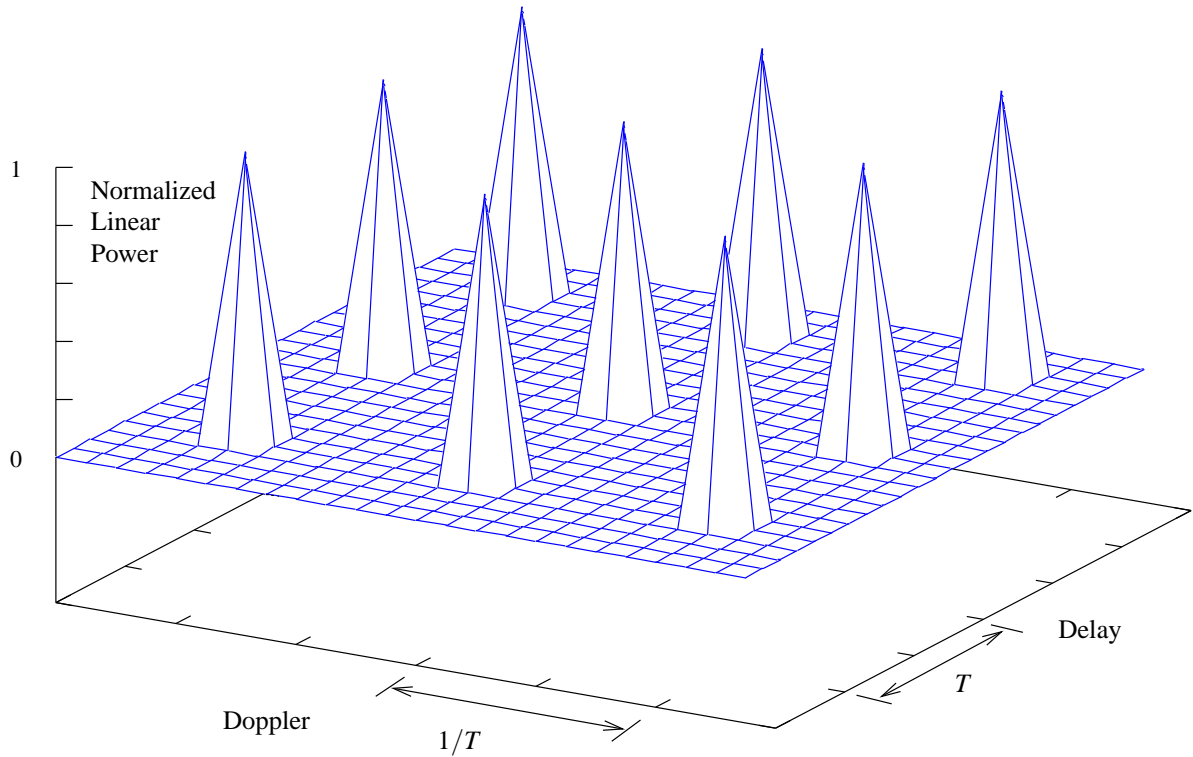
Figure 2.5 Continuous-time ambiguity function of the repetitive PN waveform of time extent T. The central peak of the ambiguity function is periodic with period T in the delay dimension, and period $1/T$ in the Doppler dimension. The waveform exhibits low range sidelobe level $\approx 1/N^2$ where N is the PN sequence length and $T = Nb$. The large periodic peaks in the delay dimension will result in range ambiguity if $T < 2a/c$.

been described extensively by Harmon (2002).

Figures 2.5 and 2.6 compare the continuous-time ambiguity functions for the repetitive PN code waveform and the random long-code waveform. Signal processing for the two waveforms is very similar. The waveforms are shown in Figure 2.7. In traditional repetitive code delay-Doppler imaging, the received signal is first range compressed to form a sequence of time histories for each range bin and then Fourier analyzed to produce cross-range or Doppler resolution, resulting in the ambiguity function shown in Figure 2.5. Processing of long-code data is identical, with the single exception that the range pulse compression waveform changes from pulse to pulse. The additional step required in the processing algorithm is to load new range compression filter coefficients for each pulse
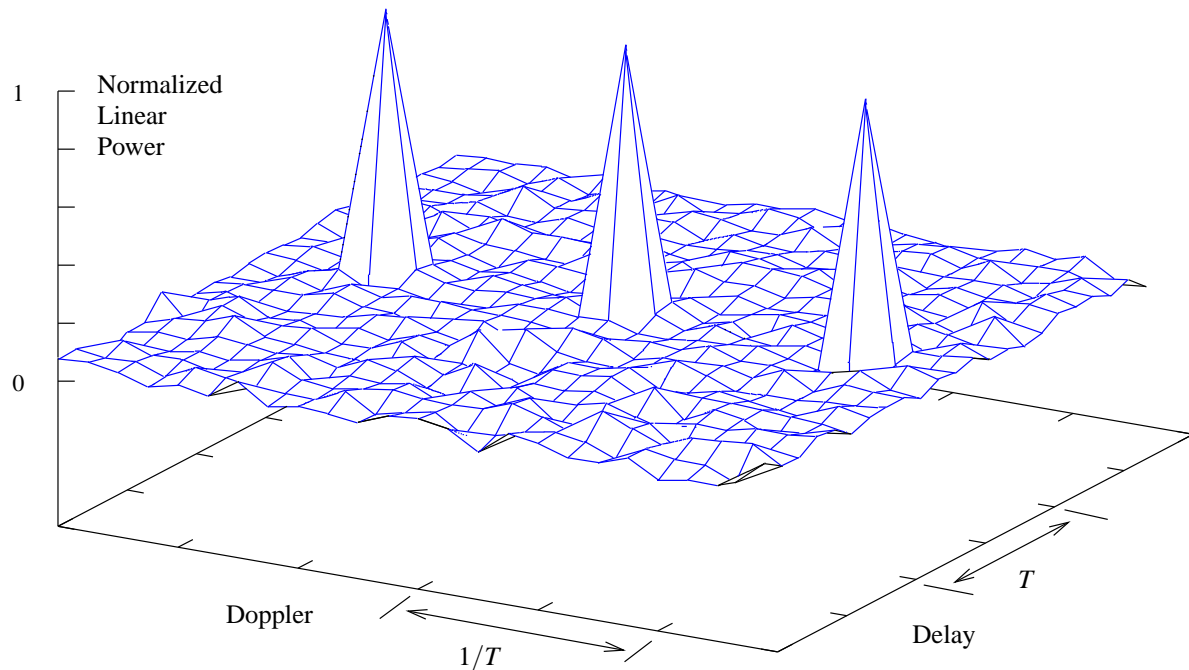
Figure 2.6 Continuous-time ambiguity function of an extended random PN waveform. The central peak of the ambiguity function is periodic with period $1/T$ in the Doppler dimension, but does not exhibit periodicity in the delay dimension. Use of this type of waveform avoids periodicity in the delay dimension, but has correspondingly higher sidelobe structure $\approx 1/N$ where N is the random sequence length, and $T = Nb$.
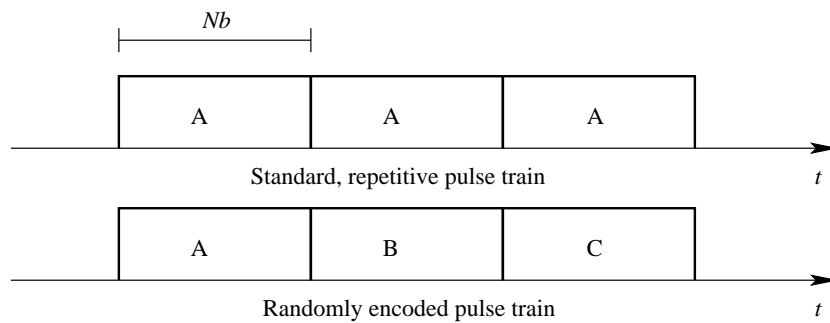
Figure 2.7 Repetitive and random coded pulse trains. In a repetitive pulse train, one length-N PN sequence, designated A, is used to encode each pulse in the waveform. In a randomly encoded pulse train, unique, non-repeating binary length-N sequences, denoted by A, B, C, are used to encode each pulse in the waveform. Signal processing for the repetitive waveform requires only one range compression filter matched to the sequence A. Signal processing of the random waveform requires many range compression filters, each matched to one particular coded sequence.
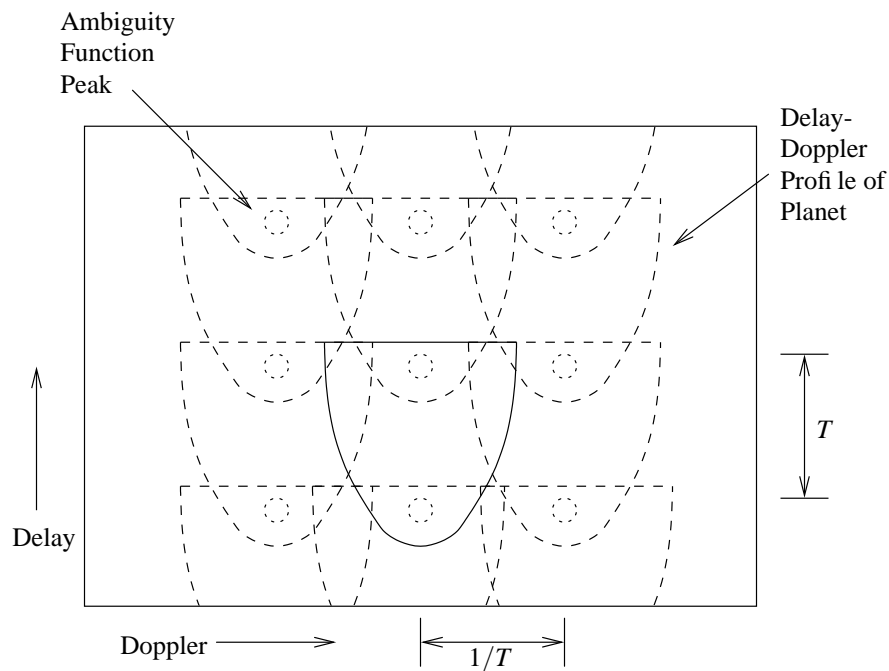
Figure 2.8 Repetitive PN waveform aliasing of an overspread target. The solid chevron represents one delay-Doppler response of a planetary target. Aliased versions extend to infinity in both delay and Doppler.

prior to applying pulse compression. The resulting ambiguity function is shown in Figure 2.6.

The standard, repetitive PN code waveform's ambiguity function is periodic in both the delay and Doppler dimensions. The random, long-code PN waveform exhibits no periodicity in the delay dimension, in exchange for higher sidelobes in both dimensions. Since the volume under the ambiguity function must remain constant (Woodward, 1951), the volume removed from the periodic delay peaks appears as an increase in sidelobe volume.

Figures 2.8 through 2.12 show the advantage of the random, long-code waveform for imaging overspread targets. When imaging an overspread target, the repetitive PN waveform suffers from aliasing (Figure 2.8). Extending the PN code length suppresses aliasing in the delay dimension but increases aliasing in the Doppler dimension (Figure 2.9).

Shortening the PN code length resolves aliasing in the Doppler dimension but increases aliasing in the delay dimension (Figure 2.10). When using the long-code PN waveform
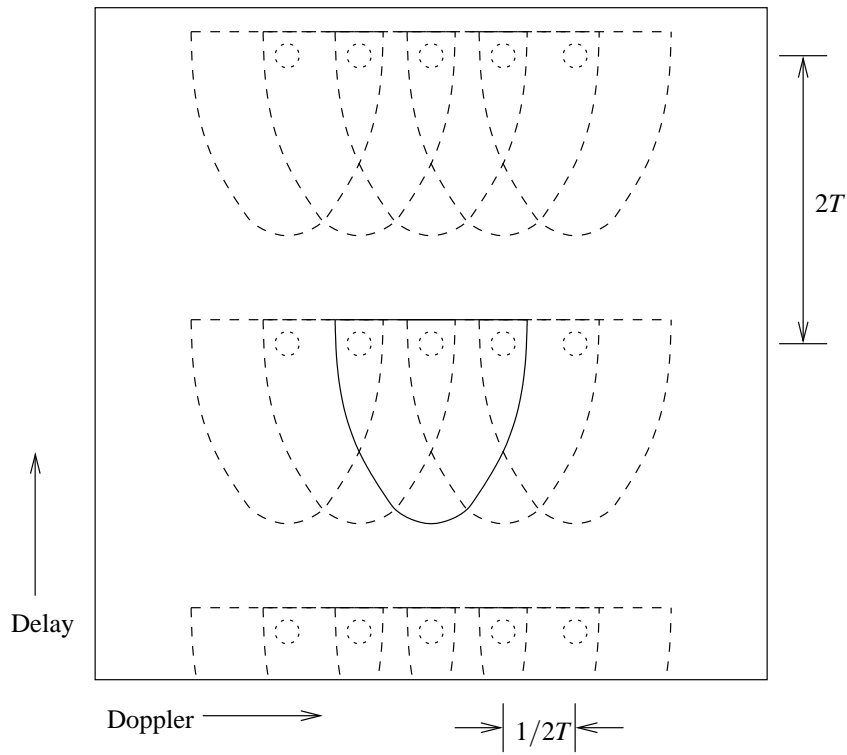
Figure 2.9 Mitigation of delay aliasing. Doubling the length of the repetitive PN code to $2T$ resolves delay aliasing, but increases Doppler aliasing (compare with Figure 2.8).
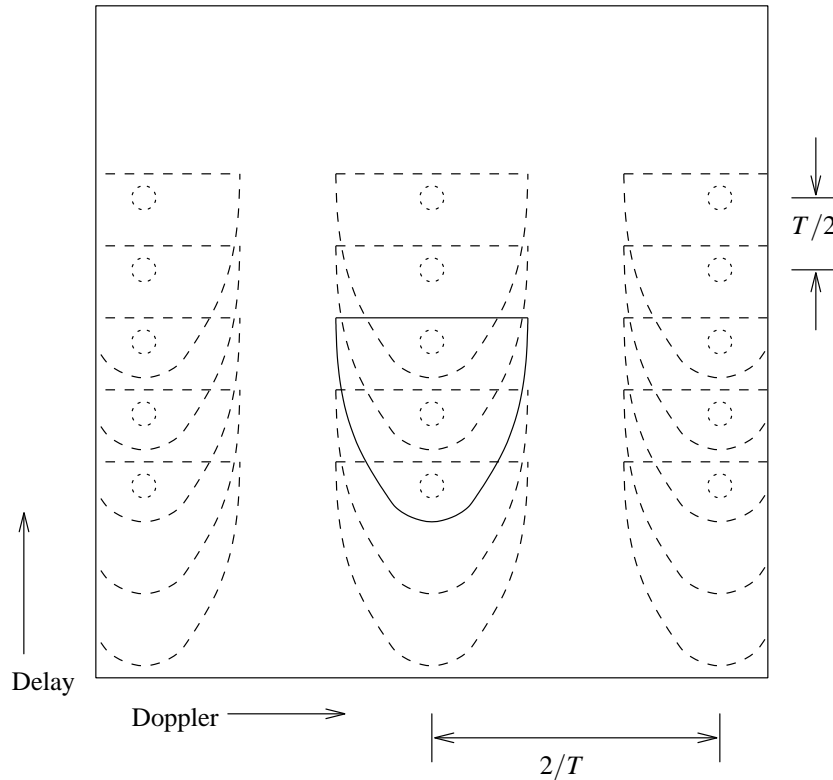
Figure 2.10 Mitigation of Doppler aliasing. Halving the length of the repetitive PN code to $T/2$ resolves Doppler aliasing, but increases delay aliasing (compare with Figure 2.8).

in combination with a sequence of processing filters matched to different segments of the long code, the delay processing length of the segments can be chosen to avoid aliasing in the Doppler dimension (Figures 2.11 and 2.12).

The trade-off in using the random, long-code waveform is that a higher overall sidelobe level results due to lack of orthogonality between the segments and remote portions of the code, which increases self-noise or clutter (Rihaczek, 1969).

2.3.2 Optimality of the long-code

Guey and Bell (1998) presented a method of delay-Doppler waveform design in which a composite ambiguity function is formed by the coherent sum of the ambiguity functions of individual pulse codes. The main theorem of the composite ambiguity function that they
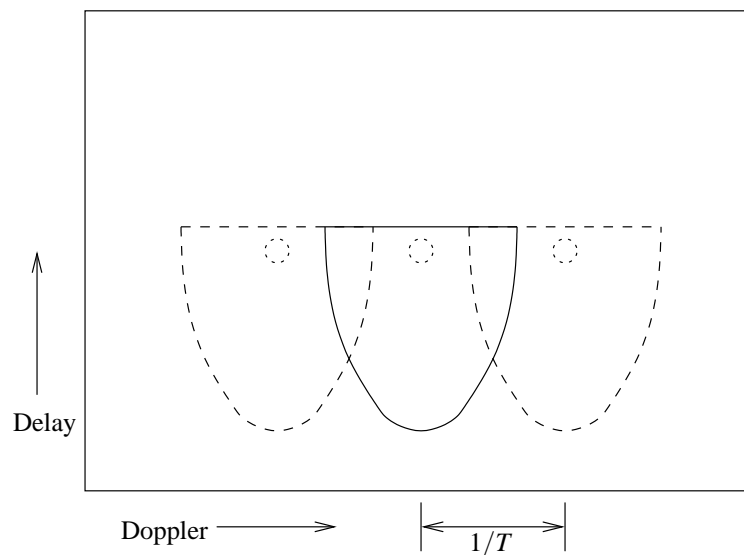
Figure 2.11 Random PN waveform aliasing of an overspread target. 2D-convolution of the ambiguity function with the target response results in Doppler aliasing (compare with Figure 2.8).

develop is that the merit of any particular set of waveforms, expressed as the volume under the composite ambiguity surface, represents a measure of the resolving ability of any particular set of pulse codes. This theorem states that the volume of the composite ambiguity function is minimized for the set of i orthogonal pulse codes $s_i(t)$. Collections of pulse codes satisfying the theorem fit one criterion of ideal delay-Doppler codes. Section A.3 shows that individual, baseband subsequences of pulses in the long-code waveform satisfy this theorem in a statistical sense. The composite long-code waveform does not satisfy a self-clutter canceling criterion, however, since the individual pulses that make up the long-code are transmitted sequentially in time on a carrier. This subject is explored more thoroughly in Section A.3.

2.3.3   Clutter performance

In traditional delay-Doppler or unfocused SAR imaging of underspread targets, the imaging algorithms are designed without regard to the contribution of clutter—the integrated sidelobes of the ambiguity function—to the estimation of reflectivity in any one resolution element. In the mapping of high time-bandwidth product or overspread targets, however,
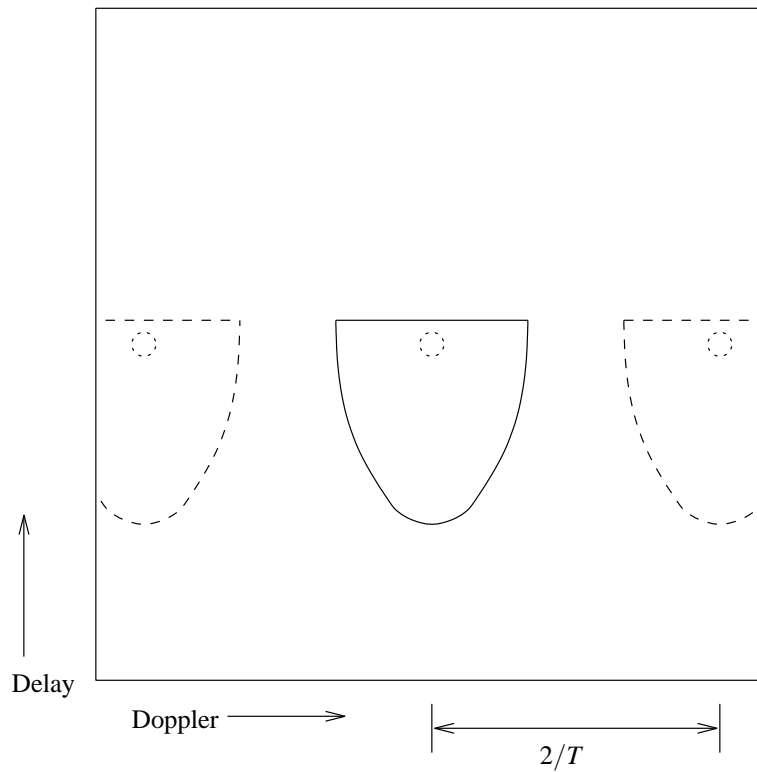
Figure 2.12 Mitigation of delay and Doppler aliasing when using a random PN waveform. Halving the length of the code to $T/2$ resolves Doppler aliasing (compare to Figure 2.8). With the random PN code there is no delay aliasing; but self-noise (clutter) is higher compared with the case of a repetitive code (Figure 2.6).

there are limits to using delay-Doppler imaging. Self-clutter can corrupt estimation of the RCS of a resolution element even in a high SNR environment. The description of the problem is involved, and rests on the volume invariance property of the ambiguity function first introduced by Woodward (1953). For a complete treatment, the reader is referred to Sections 5.3 and 9.4, and in particular pp. 137–138 and 347–348, of Rihaczek (1969). The issue at hand, in words, is: for a uniformly bright target resolved into a number of independent scattering delay-Doppler cells, when the sum of target energy appearing in the sidelobes of the ambiguity function (clutter) equals the energy in the main lobe, the signal to clutter ratio is unity, and estimation of the cross section of each independent resolution cell is deemed to have failed. A deeper understanding of the issue comes from analyzing the delay-Doppler extent of i) the target and ii) the high-resolution waveform's ambiguity function.

Figure 2.13 shows an idealized ambiguity function that could be used to image a target of cross section σ, extent B_t in Doppler, and extent T_t in delay. If the target cross section per unit of delay-Doppler space is approximately equal to its average value σ_{dD}, the expected cross section of a representative resolution element[2] σ_S is equal to the product of the average cross section, the area of the resolution element, and the height of the central peak of the ambiguity function (≈ 1), or

$$\sigma_S = \sigma_{dD} \left(\frac{1}{B}\frac{1}{T} \right) (1) = \frac{\sigma_{dD}}{BT}. \tag{2.30}$$

The expected cross section of the clutter return from resolution elements not under the primary peak of the ambiguity function is equal to the product of the average target cross section, the area of the resolution element, and the height of the pedestal of the ambiguity function ($\approx 1/BT$), or

$$\sigma_C = \sigma_{dD} \left(\frac{1}{B}\frac{1}{T} \right) (\frac{1}{BT}) = \frac{\sigma_{dD}}{(BT)^2}. \tag{2.31}$$

The total number of resolution elements contributing clutter to the estimation of the cross section of the desired resolution element is N_{clut}, and is approximately equal to the target

---

[2]The return from one resolution element is given by the discrete version of the continuous radar imaging equation (2.29).
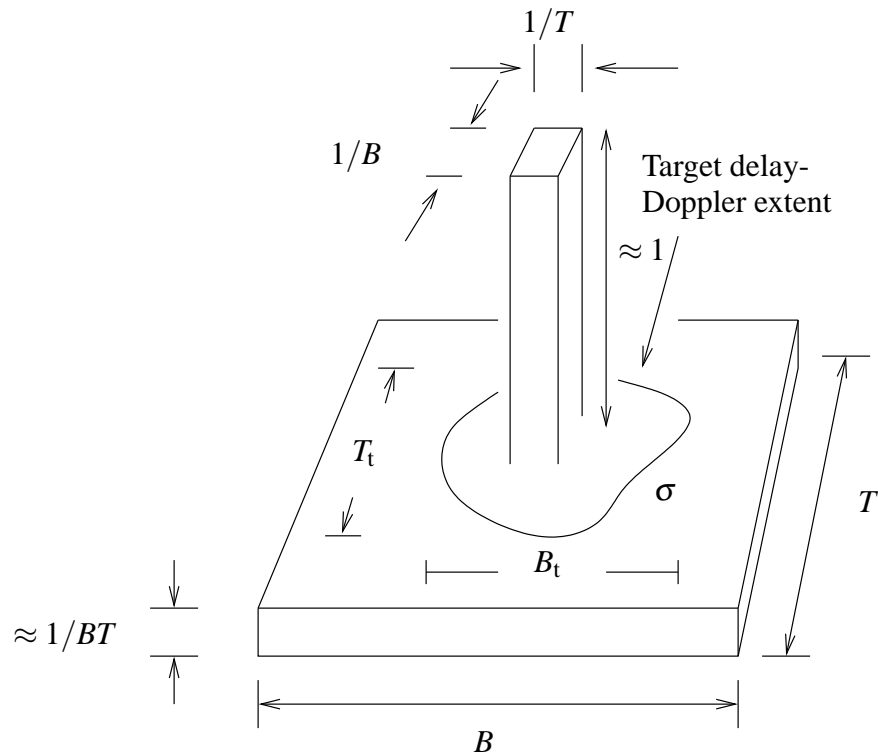
Figure 2.13 Idealized thumbtack ambiguity function of a high-resolution, large time-bandwidth product ($BT \gg 1$) radar pulse of bandwidth B and time duration T. The resolution is $1/T$ in the Doppler dimension and $1/B$ in the delay dimension. The target extent in delay-Doppler space is the shape on the pedestal denoted σ, for cross section; the target's delay depth is denoted by T_t and its Doppler bandwidth by B_t. Almost all of the energy, or volume in the ambiguity function is confined to the pedestal.

extent divided by the resolution element size, or

$$N_{\text{clut}} \approx \frac{B_t T_t}{1/BT} = B_t T_t BT. \tag{2.32}$$

The total clutter returned is equal to the product of the expected clutter per resolution element and the number of resolution elements returning clutter, or

$$
\begin{aligned}
\sigma_{\text{C,tot}} &= \sigma_C N_{\text{clut}} \\
&= \frac{\sigma_{\text{dD}}}{(BT)^2} (B_t T_t BT) \\
&= \sigma_{\text{dD}} \frac{B_t T_t}{BT}.
\end{aligned} \tag{2.33}
$$

The signal to clutter ratio (SCR) is the ratio of the expected cross section of the desired resolution element σ_S divided by the total cross section of the unwanted clutter $\sigma_{\text{C,tot}}$, or

$$
\begin{aligned}
SCR &\approx \frac{\sigma_S}{\sigma_{\text{C,tot}}} \\
&\approx \frac{\sigma_{\text{dD}}/BT}{\sigma_{\text{dD}} B_t T_t / BT} \\
&\approx \frac{1}{B_t T_t}.
\end{aligned} \tag{2.34}
$$

Following this argument, imaging of an overspread target appears hopeless, as once the time-bandwidth product of the target $B_t T_t$ reaches unity, the signal to clutter ratio becomes unity, and meaningful estimation of the reflectivity of any single resolution element is not possible, even by changing the transmitted waveform time duration T or bandwidth B (Rihaczek, 1969, p. 348).

In the above discussion, there is an assumption that the object to be imaged has approximately equal normalized cross section σ_{dD} for all delay-Doppler resolution elements. Real surfaces exhibit great variation in scattering cross section, however, and bright areas on any surface can return significant energy σ_S compared to the total clutter $\sigma_{\text{C,tot}}$. Estimation of the cross section of such bright areas is possible, if the scattering cross section within these certain individual resolution elements is high enough (Rihaczek, 1969, p. 138).

One technique to take advantage of heterogeneity in the distribution of cross section is

presented in Hagfors and Kofman (1991) and Harmon (2002). The idea is to over-resolve the imaging system in the delay and Doppler dimensions by decreasing the baud length and increasing the FFT size. Decreasing the baud length spreads the clutter out over a larger spectral bandwidth, at the expense of per-resolution element SNR, since the individual resolution elements are smaller. This higher-resolution, lower per-resolution element SNR image can then be smoothed and decimated to a lower resolution to increase per-resolution element SNR, regaining some of the SNR lost by over-resolving the target. There are limits to this process: first, Section 2.1.3 mentions an upper bound set by the migration of surface points through delay-Doppler resolution elements, and second, the incoherent integration process does not recover all of the per-resolution element SNR that a coherent integration at the proper baud rate would provide.

Hence a trade-off exists for balancing the advantage of over resolving to spread out the clutter return against the disadvantage of lower SNR that results from decreasing the resolution element size and then performing spatial averaging and decimation. In practice, this trade-off is rarely computed prior to observation, as it depends heavily on a priori information on the scattering cross section of the target. Details can be found in Section III.E and Appendix III of Harmon (2002).

2.4 Summary

Planetary surfaces can be mapped at high resolution using a delay-Doppler matched filter bank. Standard delay-Doppler techniques using repeated pulses coded with identical waveforms are not effective in imaging planets which have time-bandwidth products greater than one, due to the delay and/or Doppler folding. The long-code imaging technique successfully resolves aliasing at the cost of higher self-noise or clutter.

Chapter 3

Aperture Synthesis Imaging

The delay-Doppler technique can be quite powerful for synthesizing fine resolution images. The north-south ambiguity, however, can impair interpretation of a full-disk hemispherical RCS map. This is the situation for delay-Doppler images of the Galilean satellites of Jupiter, and for images of any other objects smaller than the projected single-dish antenna pattern. When the object of interest does not exhibit a large range of polar tilt angles when viewed from the Earth, it is difficult to map the equatorial regions due to the projection of the equatorial regions onto a reduced number of delay cells. One solution to this problem is to use the resolving power of a radio telescope interferometer array. By isolating the returns from the two hemispheres spatially, aperture synthesis mapping resolves the north-south ambiguity inherent in delay-Doppler mapping.

Aperture synthesis telescopes consist of a number of smaller antennas that, when used together, provide angular resolution equivalent to a single large aperture with a diameter equal to the maximum baseline between array elements. Since most telescope arrays useful for passive planetary astronomy observations do not contain transmitters, separate transmitting telescopes must be used to illuminate the target in a bistatic configuration. Such imaging for planetary radar was pioneered by Hagfors et al. (1968). Dramatic examples since have been reported by Muhleman et al. (1991) and Butler et al. (1993), who used the Goldstone radar as a CW illumination source and the Very Large Array (VLA) as the imaging telescope, returning the first unambiguous full-disk radar images of Mars and Mercury.

Resolution in these experiments is limited by the synthetic beam size at the receiving site, which depends on the wavelength of the observation and the spatial distribution of the array antennas. Operating at Goldstone's 3.5 cm wavelength and with 36 km maximum antenna separation, the VLA yields approximately 0.25 arcsec resolution.

3.1   One-dimensional interferometer

The basis of aperture synthesis can be understood by examining the behavior of a two element interferometer. With only two antennas and an adjustable baseline between them, it is possible to synthesize an aperture comparable in resolution to a single dish antenna with a diameter equal to the maximal extent of the adjustable baseline. This simple array can be used to map the brightness distribution of an astronomical source. Each spacing of the interferometer samples a different spatial frequency component of the source sky brightness distribution in the plane containing the interferometer baseline. Fourier synthesis processing of the array output produces an image (Bracewell, 1956) . A standard text for aperture synthesis techniques is Thompson et al. (1986). The methodology outlined in the following section is simplified greatly from that in Thompson.

3.1.1   Basic configuration

Consider the two element interferometer of spacing l pictured in Figure 3.1. For simplicity, assume that the element radiation pattern is omnidirectional. The measurement objective is the sky brightness distribution, or power pattern, of a radioastronomical source $B(\xi)$ where ξ is a small angle on the sky with respect to the normal to the baseline between the two antennas, exaggerated here in Figure 3.1 for clarity. The source is in the far-field of the array so that the wavefront arriving from the source is planar. Consider the source to be incoherent, so that any one point of the brightness distribution can be considered a point source that radiates independently of any other point on the source. The complex voltage received at each antenna from a point on the source is represented by the quantities $v_1(t)$ and $v_2(t)$ where

$$v_i(t) = a(t) \, e^{j(\omega t - \vec{k} \cdot \vec{r}_i)}, \tag{3.1}$$
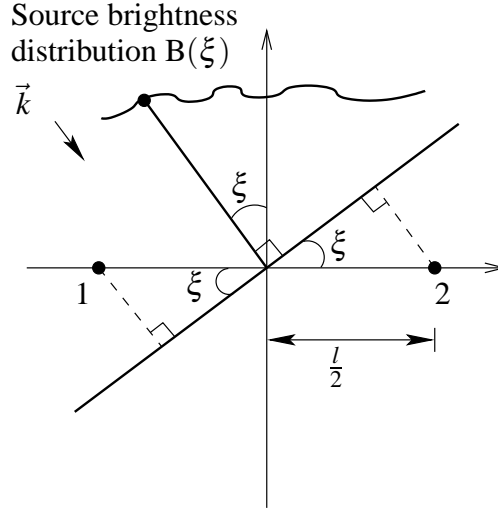
Figure 3.1 Geometry of a two element interferometer observing a point on an incoherently radiating source $B(\xi)$ at a small angle ξ from the normal to the interferometer baseline l. The angle ξ is exaggerated for clarity. Plane waves propagate from the point on the source toward the array with vector wavenumber $\vec{k}$, and arrive at the right-hand element 2 delayed by $\beta l \sin \xi$ relative to the left-hand element 1.

$\vec{r_i}$ is the position of antenna i relative to the origin of the coordinate system, $a(t)$ is the slowly varying source amplitude, and $\vec{k}$ is the vector wave number. The propagation constant is $\beta = |\vec{k}| = 2\pi/\lambda$.

Assuming $a(t) = 1$ for all t and dropping the common $e^{j\omega t}$ dependence, we can simplify the voltages to:

$$v_1 = e^{+j\beta \frac{l}{2} \sin \xi} \tag{3.2}$$

$$v_2 = e^{-j\beta \frac{l}{2} \sin \xi}. \tag{3.3}$$

The incoming wave from one point on the source distribution is either delayed or advanced from the phase center of the interferometer by the quantity $\beta \frac{l}{2} \sin \xi$. The interferometer may be used to form the cross correlation of the two complex voltages

$$v_1 v_2^* = \left(e^{+j\beta \frac{l}{2} \sin \xi} \right) \left(e^{-j\beta \frac{l}{2} \sin \xi} \right)^*$$

$$= e^{+j\beta l \sin \xi}. \tag{3.4}$$

Using the small angle approximation $\sin\xi = \xi$, we have

$$v_1 v_2^* = e^{j\frac{2\pi}{\lambda} l \sin\xi} = e^{j2\pi u_0 \xi}, \tag{3.5}$$

where $u_0 = l/\lambda$ is the interferometer spacing in wavelengths. The quantity $v_1 v_2^*$ is a measure of the response of the array to the point on the source at small angle ξ. This quantity is the complex power pattern response of the two-element array.

We can compute the Fourier transform of the complex array power pattern to obtain the spatial frequency content of the array pattern on the sky, $W(u)$,

$$\begin{aligned}
W(u) &= \int_{-\infty}^{\infty} e^{+j2\pi u_0 \xi} e^{-j2\pi u \xi} \, d\xi \tag{3.6} \\
&= \delta(u + u_0) \tag{3.7}
\end{aligned}$$

where $\delta(u)$ is the impulse distribution. $W(u)$ is also known as the spectral sensitivity function. So we see that the output of the complex correlator array samples one spatial frequency component, $u_0 = l/\lambda$, of the sky brightness distribution B. By changing the spacing of the array l, we can obtain other spatial frequency components of the brightness. The realization that a two element interferometer samples one spatial frequency of the sky brightness distribution is due to McCready et al. (1947).

Now consider the following Fourier transform pairs,

$$\begin{aligned}
B(\xi) &\rightleftharpoons V(u) \tag{3.8} \\
A(\xi) &\rightleftharpoons W(u) \tag{3.9} \\
S(\xi) &\rightleftharpoons V(u)W(u). \tag{3.10}
\end{aligned}$$

The Fourier transform of the sky brightness, $V(u)$, is commonly called the visibility function of the source. The array power pattern $A(\xi)$ is the transform of the sampling function of the aperture distribution $W(u)$. The sky brightness function $S(\xi)$ is discussed below.

It is important to note that the complex correlator array only samples one side of the spatial frequency axis, $u > 0$. As the power distribution $B(\xi)$ on the sky is real, we can use
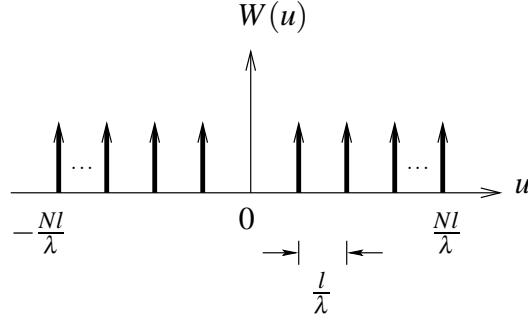
Figure 3.2 Spectral sensitivity function $W(u)$ for uniformly spaced samples of a two element interferometer. The arrow-tipped line at $u = 0$ is the ordinate of the plot, and not part of the sampling function. The "hole" in the spectral sensitivity function at $u = 0$ is a well-known property of correlating interferometers (Thompson et al., 1986) (see text).

the Fourier transform relations for real even and real odd functions (Bracewell, 2000)

$$\text{real, even} \quad \rightleftharpoons \quad \text{real, even} \tag{3.11}$$

$$\text{real, odd} \quad \rightleftharpoons \quad \text{imaginary, odd} \tag{3.12}$$

to compute the missing values on the negative frequency axis. The left hand side of the visibility axis $V(u), u < 0$ is simply the complex conjugate of the right hand side of the spatial frequency distribution.

Recording data at many different spatial separations of the array l allows for arbitrarily dense sampling of the visibility function $V(u)$. An estimate of the sky brightness function $S(\xi)$ may be obtained from the inverse Fourier transform of the sampled visibility function in (3.10) yielding the sky brightness distribution convolved with the array power pattern $S(\xi) = B(\xi) * A(\xi)$ (Bracewell and Roberts, 1954).

As an example of an array response pattern, let $l = n\Delta l, n = 1, \ldots, N$. where Δl is a fixed spacing and $l_{\max} = N\Delta l$. The spatial frequency sampling function, $W(u)$, of this array is shown in Figure 3.2. We have inserted the negative frequency components by taking the complex conjugates of the components for $u > 0$. The absence of a sample at $u = 0$, which corresponds to a constant background in the spatial image, is a well known property of correlator arrays (Thompson et al., 1986).

The sampling function obtained by varying the spacing of a two element interferometer
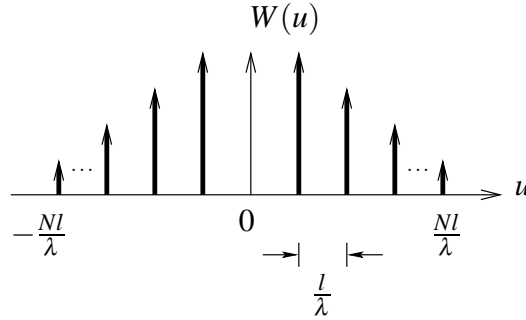
Figure 3.3 Spectral sensitivity function $W(u)$ for uniformly spaced linear correlating array. The linear array overweights the close spacings as compared to the far spacings (compare with Figure 3.2). The arrow-tipped line at $u = 0$ is the ordinate of the plot, and not part of the sampling function.

is not the sampling function which would result from a uniformly spaced linear array of N elements. A uniform array of element spacing l and N elements redundantly samples the spacing l since there are $N(N-1)/2$ antenna pairs with spacing l. The spectral sensitivity function of such a linear correlator array is shown in Figure 3.3.

The power pattern response of the array $A(\xi)$ is given by the inverse transform of the spectral sampling function $W(u)$. It is usually removed from the sky brightness image by non-linear deconvolution as explained in Section 3.4.

3.1.2   Correlation, addition, and spectral sensitivity

Most modern facilities operate as correlating interferometers, and are based on an extension of the basic ideas introduced above (Thompson et al., 1986). For a four-element linear array, a correlating interferometer produces the following power output at normal incidence ($\xi = 0$)

$$
\begin{aligned}
v_c v_c^* \;=\; & v_1 v_2^* + v_1 v_3^* + v_1 v_4^* + \\
& v_2 v_1^* + v_2 v_3^* + v_2 v_4^* + \\
& v_3 v_1^* + v_3 v_2^* + v_3 v_4^* + \\
& v_4 v_1^* + v_4 v_2^* + v_4 v_3^*.
\end{aligned}
\tag{3.13}
$$

An adding interferometer, on the other hand, produces

$$
\begin{aligned}
v_a v_a^* &= (v_1 + v_2 + v_3 + v_4)(v_1 + v_2 + v_3 + v_4)^* \\
&= v_1 v_1^* + v_1 v_2^* + v_1 v_3^* + v_1 v_4^* + \\
&\quad v_2 v_1^* + v_2 v_2^* + v_2 v_3^* + v_1 v_4^* + \\
&\quad v_3 v_1^* + v_3 v_2^* + v_3 v_3^* + v_3 v_4^* + \\
&\quad v_4 v_1^* + v_4 v_2^* + v_4 v_3^* + v_4 v_4^*.
\end{aligned}
\tag{3.14}
$$

The adding interferometer contains the summation of all components from all four antennas and obeys a Fourier transform relationship with the autocorrelation function of the aperture distribution first presented by Booker and Clemmow (1950). The correlating interferometer does not exhibit this property, as its output is missing the cross terms $v_i v_i^*$, $i = 1, \ldots, 4$, which are on the diagonal of (3.14). For this reason, standard antenna array theory cannot be used to compute the power pattern $A(\xi)$ of a correlating array, and the correlating array power pattern can have negative sidelobes.

Any interferometer of uniformly-sized individual apertures cannot position its elements closer than D meters, where D is the diameter of the individual apertures. The low-pass spatial frequency cutoff of the array is $u_{\text{low}} = D/\lambda$. As a result, the correlating array is less sensitive than a single, large aperture for determining the total flux density of a source at a known location in the sky. The low spatial frequency terms of the source distribution are unmeasured, and must be either interpolated from higher frequency data, or acquired from single-dish observations in order to fill in the missing data at the low end of the spatial frequency spectrum.

In Chapter 6, we report on the use of a correlating array, the VLA, to map Ganymede and Callisto. Though the VLA is the best instrument available for forming north-south unambiguous maps of Ganymede and Callisto, it is not the best instrument for measuring the total radar echo power from these bodies, since it is not sensitive to the entire spatial frequency distribution. Large, single-dish observations, such as those of Ostro et al. (1992), are more accurate.
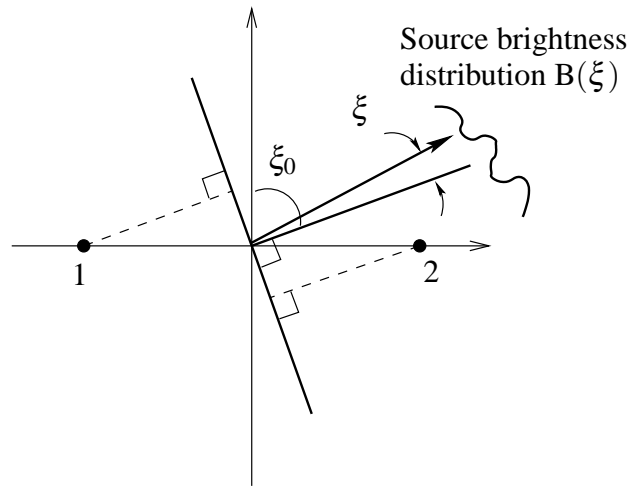
Figure 3.4 Projected baseline effect for an off-center source at angle ξ_0 from the normal to the array. Here the angle ξ_0 is not exaggerated; the interferometer is pointed off the normal to its physical baseline by a signifi cant angle. The source is imaged over a small angle ξ about this off-center angle ξ_0.

3.1.3 Projected baseline

Suppose we desire to image a source which is centered about some angle ξ_0 which is far off the centerline of the two element array, as suggested by Figure 3.4. For the point source located at ξ_0, the voltage $v_1(t)$ experiences a delay $\tau = \frac{l}{c}\sin\xi_0$ relative to the voltage $v_2(t)$. By introducing this instrumental delay τ into the v_2 channel, the virtual array baseline becomes that shown in Figure 3.5, equivalent to the case from Section 3.1.1 but with $u_0 = \frac{l}{\lambda}\cos\xi_0$. The measured spatial frequency of the brightness distribution is reduced by the projection of the baseline onto the line of sight to the source.

3.1.4 Tracking interferometer

For an Earth-based, two element, east-west aligned interferometer on the equator, the angle ξ_0 to the center of a sky-fixed source at zero declination will move as the Earth rotates on its axis. This rotation may be compensated by adjusting the instrumental delay τ to correct for the changing angle to the source center ξ_0. As the source moves across the sky, the projected baseline changes, providing sampling of different spatial coefficients of the
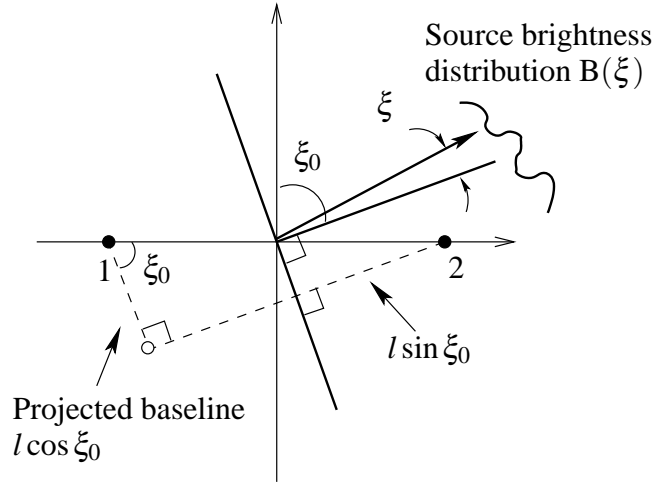
Figure 3.5 Virtual interferometer layout for an off-normal source. Delaying the voltage signal $v_2(t)$ by an amount $\tau = \frac{l}{c}\sin\xi_0$ causes the right-hand element 2 to be virtually displaced along the direction of propagation to effect an interferometer with the same layout as Figure 3.1, but with an effective element spacing of $l\cos\xi_0$.

source distribution without physically moving the antennas themselves.

If the antennas which are the individual elements of such a "tracking" array have finite beamwidth, they must actively follow the source as it moves across the sky. Each antenna measures the true sky brightness weighted by the antenna element pattern, $A_e(\xi)$. In this case, we have the Fourier transform pair

$$B(\xi)A_e(\xi) \rightleftharpoons V(u) * W_e(u) \tag{3.15}$$

where $W_e(u)$ is the Fourier transform of the element pattern. The array of elements measures a sky brightness distribution (3.10)

$$S(\xi) \rightleftharpoons [V(u) * W_e(u)]W(u) \tag{3.16}$$

where $W(u)$ is the array pattern from (3.10).
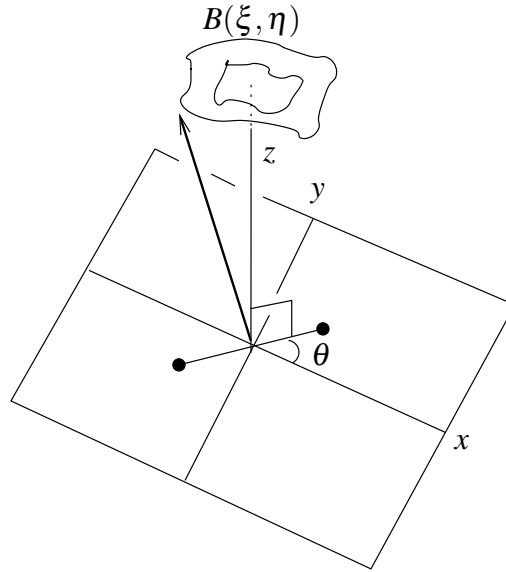
Figure 3.6 Two element interferometer in three dimensional space. Interferometer baseline sits at an angle θ with respect to the *x* axis.

3.2 Extension to two dimensions

We now consider a two-element array resting on a plane in a three-dimensional space. The baseline between the antennas is now rotated through an angle θ with respect to the *x* axis in the plane as shown in Figure 3.6. The sky brightness $B(\xi, \eta)$ is a function of two angles. In this situation, the complex visibility, $V(u,v)$, is given by the two dimensional Fourier transform of the sky brightness distribution (Bracewell, 1956, 1958)

$$V(u,v) = \int \int B(\xi, \eta) e^{-j2\pi(\xi u + \eta v)} \, d\xi d\eta. \tag{3.17}$$

The two-element interferometer set at spacing l and angle θ can now be viewed as sampling the two dimensional Fourier transform of the angular power pattern. The Fourier relationships are:

$$B(\xi, \eta) \; \rightleftharpoons \; V(u,v) \tag{3.18}$$

$$A(\xi, \eta) \; \rightleftharpoons \; W(u,v) \tag{3.19}$$

$$S(\xi, \eta) \quad \rightleftharpoons \quad V(u,v)W(u,v). \tag{3.20}$$

The two-dimensional Fourier transform of an object rotated through an angle θ also rotates through the same angle θ in the (u,v) plane (Bracewell, 2003). We can view the two element array in the two dimensional plane as sampling the visibility function at the spatial frequency pair

$$(u,v) = (\frac{l}{\lambda}\cos\theta, \frac{l}{\lambda}\sin\theta), \tag{3.21}$$

where l is the array spacing given previously.

For the case of a non-zenith pointing array, an expression for the projected baseline similar to that of Section 3.1.3 can be derived. An appropriate delay τ added to the signal from one element transforms the geometry of the problem to a projected baseline frame of reference. In this new reference frame, the results of this section may then be employed.

3.3 Mapping interferometer

As it can take several months using Earth-rotation to acquire enough samples of the complex visibility function $V(u,v)$ to form a two dimensional map of the source with a single two-element interferometer, modern radio synthesis telescopes use a two-dimensional array of antennas to speed data acquisition. Figure 3.7 shows the antenna configuration of the Very Large Array (VLA) near Socorro, New Mexico. High-gain antennas improve signal-to-noise ratio, and suppress undesirable signals from directions other than that of the target. Each element of the array must be steered in azimuth and elevation to stay centered on the source.

The (u,v) plane sampling function of the antenna at zenith is shown in Figure 3.8. This sampling pattern undergoes projection and rotation as the array tracks a source across the sky to yield the spectral sensitivity (u,v) plane coverage map of Figure 3.9. The Fourier transform of this spectral sensitivity function yields the array response on the sky, or the "dirty beam" as shown in Figure 3.10. The response of the array, $S(\xi, \eta)$, to a brightness distribution, $B(\xi, \eta)$, is the two dimensional convolution of the array with the pattern,
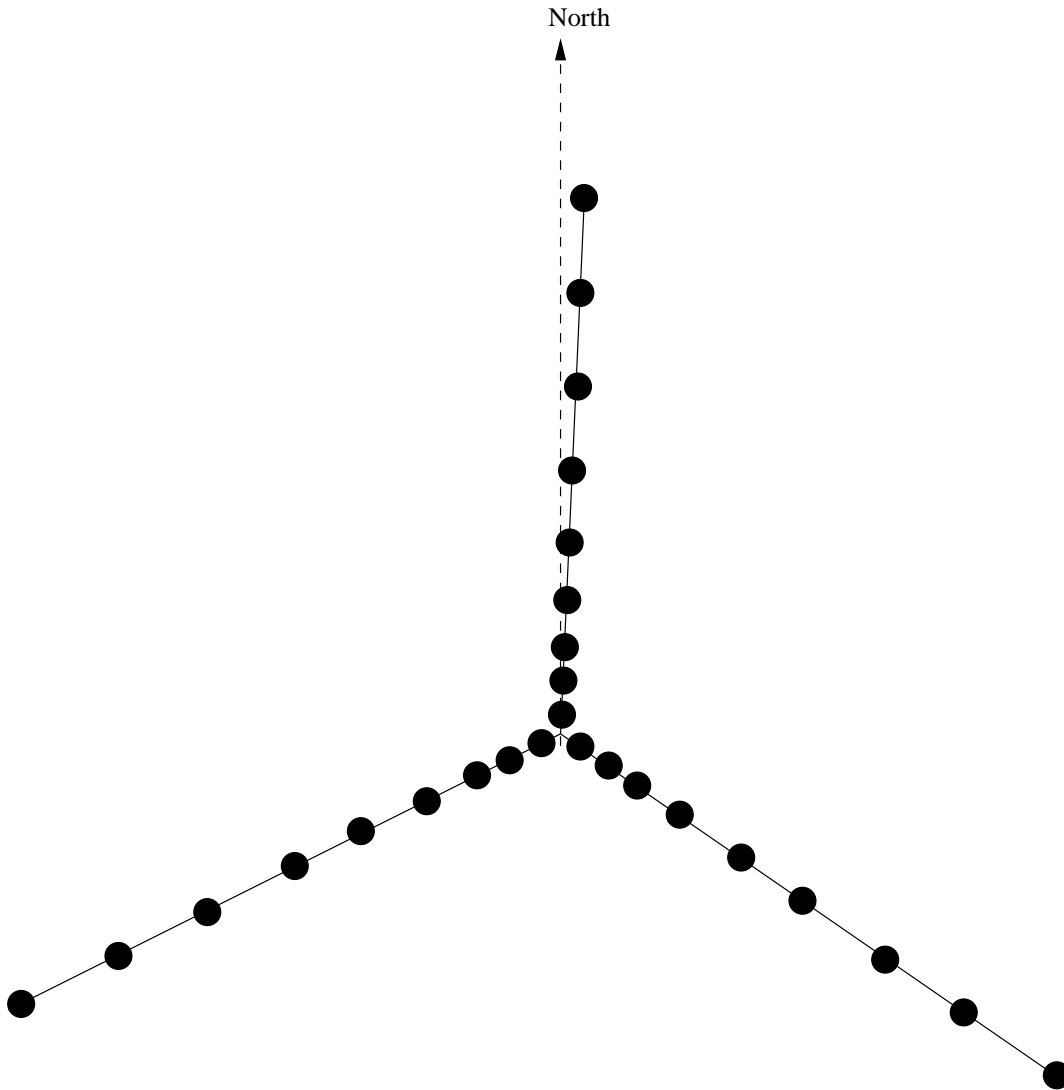
Figure 3.7 Very Large Array antenna configuration. The VLA has three principle arms, 21 km long, and separated by 120°, each containing nine 25 m diameter antenna elements (Thompson et al., 1986). The 5° offset clockwise rotation of the array improves the spectral sensitivity function for tracking sources near 0° declination. In the absence of this rotation, the spectral sensitivity function degenerates into horizontal lines (see Figure 3.9).
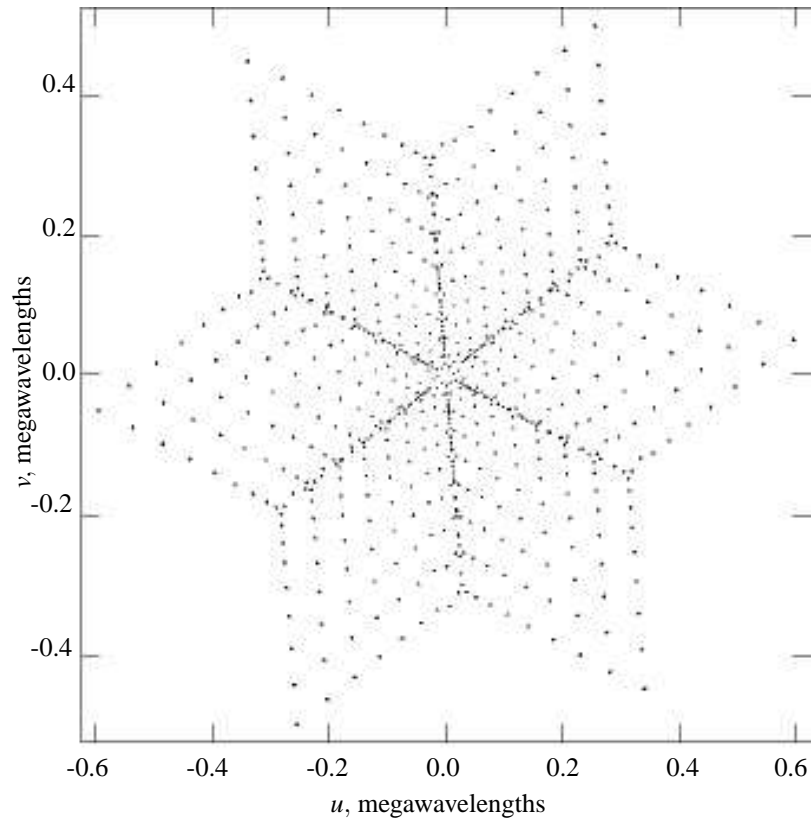
Figure 3.8 Spectral sensitivity function of the VLA in "A configuration" at 6 cm wavelength, observing a source at zenith (Bridle, 1996). This Fourier space image shows the (u, v) plane coverage of the array at a single instant in time. The units of u and v are dimensionless (3.21), and are commonly specified as megawavelengths, or 10^6 wavelengths. The 36 km maximum baseline of the VLA "A-configuration" provides a maximum spacing of $u \approx 36 \times 10^3$ m$/6 \times 10^{-2}$ m$/10^{-6} = 0.6$ megawavelengths.
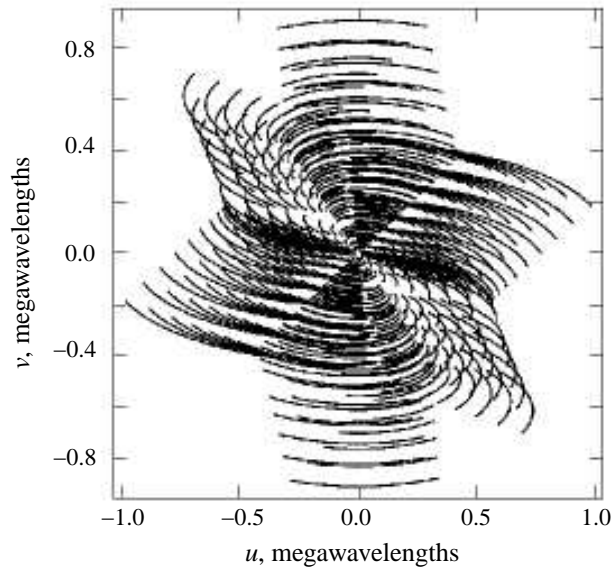
Figure 3.9 Spectral sensitivity function of the VLA resulting from several hours of tracking of a source at 3.5 cm wavelength on either side of transit. The pattern of Figure 3.8 undergoes projection and rotation as the array tracks the source across the sky, filling out the sampling of points in the Fourier space (u, v) plane. The 36 km maximum baseline of the VLA "A-configuration" provides a maximum spacing of $u \approx 36 \times 10^3$ m$/3.5 \times 10^{-2}$ m$/10^{-6} = 1.0$ megawavelengths.
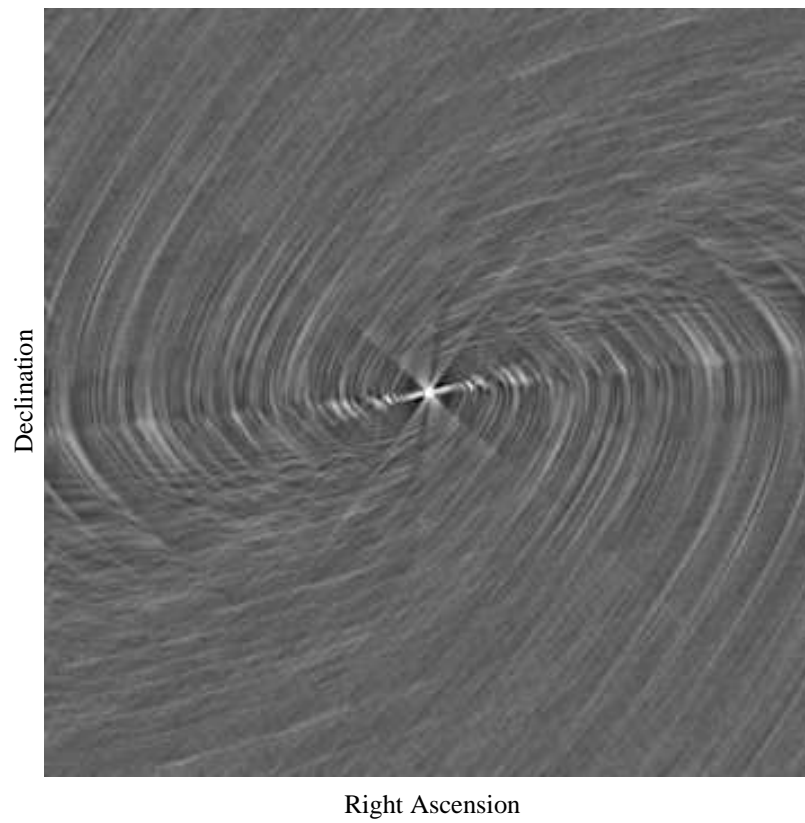
Figure 3.10 Plane-of-sky impulse response $A(\xi, \eta)$ or "dirty beam" pattern of the VLA as formed from the spectral sensitivity function in Figure 3.9. The output of the VLA is the convolution of this pattern with the true sky brightness pattern $B(\xi, \eta)$.

$A(\xi, \eta)$, or,

$$S(\xi, \eta) = B(\xi, \eta) * *A(\xi, \eta). \tag{3.22}$$

To recover $B(\xi, \eta)$, the effect of this convolution must be removed by approximate methods, since a unique inversion does not exist (Bracewell and Roberts, 1954).

3.4   Beam deconvolution

"Deconvolution" is the process used to estimate the true sky brightness distribution, $B(\xi, \eta)$, given the observed quantity, $S(\xi, \eta)$, above. As there is no exact solution to the deconvolution problem, approximate methods are employed. The most successful and widely employed algorithm discovered to date is the CLEAN algorithm originally conceived by Hogbom (1974), a non-linear, iterative approach.

The steps of CLEAN are as follows:

1. Find the brightest point (ξ_0, η_0) in the "dirty" image $S(\xi, \eta)$.

2. Shift the array power response $A(\xi, \eta)$ normalized to unity gain to the point (ξ_0, η_0) in the image. Multiply the array response by the value $S(\xi_0, \eta_0)$ and a "gain factor" γ. Subtract the resulting power response $\gamma S(\xi_0, \eta_0) A(\xi - \xi_0, \eta - \eta_0)$ from the dirty image $S(\xi, \eta)$.

3. Add the scalar quantity $\gamma S(\xi_0, \eta_0)$ to a "cleaned" image S' at point (ξ_0, η_0).

4. Repeat steps 1, 2, and 3 until a user-defined threshold is reached (see below).

After 30 years, the radio astronomy community has developed standard practices for employing the CLEAN algorithm. The CLEAN gain, γ, is typically chosen to be 0.1 based on experience. It can be shown that the deconvolution is unstable if $\gamma > 1$. CLEAN iterations are continued until the amount of power being removed at each iteration stage is on the order of the off-source, background noise power level. This level can be determined by computing the expected background noise level in the region of the sky being imaged either in advance or once the on-source flux in the "dirty" image is on the level of the off-source flux in the dirty image. Once this deconvolution process is complete, the "cleaned" image

is usually convolved with a truncated Gaussian, or "clean beam" to smooth the output image to the intrinsic resolution of the imaging array. The half-power point of the Gaussian beam used for reconstruction is the quoted resolution of the imaging system (see Chapter 6, Table 6.1).

Direct computation of the Hogbom CLEAN procedure is inefficient. For this reason, approximations to the procedure with greatly improved computation time have been developed since the original algorithm was published. Clark (1980) improved the efficiency of the Hogbom algorithm by computing many of the quantities using the sampled visibilities $V(u,v) \cdot W(u,v)$ in the Fourier domain, rather than carrying out all procedures in the image (ξ, η) domain.

Other researchers have extended the CLEAN algorithm for coherent radar imaging systems (Tsao and Steinberg, 1988; Bose et al., 2002). These extensions compensate for the high sidelobes of the ambiguity function used in many imaging radar systems. Harmon (2002) has used deconvolution to remove range sidelobes from the sub-radar specular point from delay-Doppler images.

3.5   Summary

This chapter reviews the basics of aperture synthesis imaging. The two element interferometer serves as an example from which two-dimensional mapping of sky brightness (power) of radio astronomical sources was developed. Modern mapping interferometers, such as the Very Large Array, operate on the basis of these same principles. The adding interferometer preserves the standard Fourier transform relationship between the aperture illumination function and the Fraunhofer far-field array pattern. The correlating interferometer does not preserve this relationship. The fact that a physical array has a minimum antenna spacing equal to the diameter of its individual elements causes either array to lack sensitivity at low spatial wavelengths. As a result of these two effects the correlating array is less sensitive for total flux measurements than an equivalent-aperture single-dish telescope, and can have negative sidelobes in its array response pattern. Correlating interferometers are good for achieving fine spatial resolution, but lack accuracy when measuring the absolute flux density, or radar cross section, of extended targets. Because the (u,v) plane coverage of an

aperture synthesis telescope is limited, the raw output image of the array is the convolution of the array power response with the true sky brightness distribution of the source. Iterative deconvolution methods, such as the CLEAN algorithm and its derivatives, must be employed to remove the effects of sparse sampling in the (u, v) plane and reconstruct the true brightness distribution.

Chapter 4

Radio-Wave Scattering

Radio wave scattering properties of solar system objects have been investigated continually for a half century (e.g., v. Evans and Hagfors (1968); Pettengill (1978); Ostro (1993); Butrica (1996)). Originally these studies, undertaken with small radiotelecopes at a number of institutions, were restricted to the Moon and inner planets due to power and sensitivity constraints. Starting in the early 1970's, new and more powerful microwave transmitters at the Arecibo and Goldstone observatories led to discoveries regarding the global scattering properties of moons and rings of the outer planets. The increase in instrument capability also led to fine resolution imaging of inner solar system bodies.

The first high-power microwave observations of the icy Galilean satellites Europa, Ganymede, and Callisto, were obtained at the Arecibo observatory in 1975–76, as reported by Campbell et al. (1977, 1978). The high geometric albedo of these objects at optical wavelengths had been noted previously. Radar observations found high values of radar cross section and, surprisingly, the phenomenon of circular polarization inversion, which is the detection of greater power in the same circular polarization as transmitted, as compared with the opposite sense.[1] Detection of polarization inversion led the radar astronomers to conclude that a multiple scattering effect, such as volume scattering, was likely responsible for these anomalous measurements as compared to typical inner solar system terrestrial planets (Campbell et al., 1978) where backscatter is dominated by Fresnel reflection at the

---

[1]This effect cannot be detected by optical astronomers relying on natural sources of illumination, which are unpolarized.

visible surface. Subsequent flybys by the twin Voyager spacecraft confirmed predictions of an icy composition for the surfaces of these moons (Stone and Lane, 1979). Extensive, additional radar studies by Ostro et al. (1992) further refined the measurements of the global scattering properties of these objects at the 13 cm and 3.5 cm wavelengths.

A variety of specific physical models was put forth to explain the observed backscattering phenomena. Gurrola (1995) summarizes many of these models, including surface craters in ice (Ostro and Pettengill, 1978), the presence of random cracks (Goldstein and Green, 1980; Ostro, 1982), the structure of refractive lenses (Hagfors et al., 1985), the radar "glory" effect (Eshleman, 1986), and "coherent" backscatter phenomena (Hapke, 1990). Subsequent evaluation of these models has been carried out by Peters (1992), Gurrola (1995), and Black (1997).

In the late 1980's and early 1990's, the addition of 3.5 cm receivers to the Very Large Array synthesis mapping telescope, and an increase in computational power available for post-acquisition data processing, permitted high-resolution bistatic observations of Mars and Mercury. Muhleman et al. (1991), using the combined Goldstone/VLA instrument, reported the combination of high-albedo and an inverted circular polarization ratio in scattering from the south polar cap of Mars, similar to that observed from the Galilean satellites. Slade et al. (1992) and Harmon and Slade (1992) made use of the Goldstone/VLA and the Arecibo radars, respectively, observing these same anomalous reflection properties in signals from the polar regions of Mercury. The similarities in scattering to the Galilean satellite results led to the conclusion that the anomalously high radar cross sections and polarization inversion are due to the presence of cold-trapped volatiles—such as ice—on these much warmer worlds.

This peculiar backscattering also has been found at several locations on Earth. Rignot et al. (1993) and Haldemann and Muhleman (1999) employed Earth-orbiting satellite radars to observe the glacial ice of Greenland and glacial deposits in the Kunlun Shan and central Andes, respectively. In these cases, the "unusual" backscatter properties—the combination of high RCS and the reversal of the incident sense of circular polarization—are attributed to single scattering from explicit structures embedded in the ice (Rignot et al., 1993) , or multiple scattering within the ice by inhomogeneities (Haldemann and Muhleman, 1999).

4.1 Models for planets and geophysical surfaces

As introduced in Chapter 2, radar cross section (RCS) is a scalar quantity linearly related to the amount of power scattered by an object in the far field of the radar. Radar cross section, σ, is derived from the radar equation (2.22) written in the form

$$P_r = P_t G_t \frac{1}{4\pi R^2} \sigma \frac{1}{4\pi R^2} A_r + k T_{sys} B, \tag{4.1}$$

in which total received power P_r is expressed as a function of the transmitted power P_t, the transmitting antenna gain G_t, the range to the target R, the receiving antenna area A_r, the receiving system temperature T_{sys}, the effective signal bandwidth B, and Boltzmann's constant k.[2] Given a radar measurement of received power, and knowing the system parameters, the radar cross section of the target is calculated from

$$\sigma = \frac{16\pi^2 R^4}{P_t G_t A_r}(P_r - k T_{sys} B). \tag{4.2}$$

The field of electromagnetic scattering theory is concerned with developing models relating the observed backscatter σ to the physical properties and configuration of the target material. For most radar remote sensing experiments, the target is in the far-field of the radar, and the emitted wave propagates through free-space for some distance before impinging on the target. The scattering mechanisms can be broadly classified into two categories: surface scattering from waves reflected at the free-space/target interface, and volume scattering from waves which penetrate into the target, undergo multiple scattering from inhomogeneities within the target, and are returned to the observer through the target/free-space boundary.

The scattering behavior from rough targets such as planetary bodies includes several components. These are commonly denoted i) specular or mirror-like, from single-bounce geometries, and ii) diffuse, from multiple scattering off surface features or sub-surface structures. The power returned from specular scattering is concentrated around an angle of reflection equal to the angle of incidence $\theta_r = \theta_i$. The power returned from diffuse

---

[2]For high-resolution, long-code imaging as employed in Chapter 5, in addition to the thermal noise contribution, $k T_{sys} B$, a non-thermal "clutter" noise component must also be considered. See Section 5.3, page 88.

scattering is distributed over a wider range of reflected angles θ_r. Scattering models for natural surfaces therefore employ several parameters which model both the specular and diffuse scattering components of the radar cross section.

4.1.1 Sphere

The predicted radar cross section of many basic geometrical shapes can be calculated from electromagnetic theory (Ruck et al., 1970). For example, the RCS of a perfectly conducting sphere of radius a that is large compared to the radar wavelength is its projected area:

$$\sigma = \pi a^2. \tag{4.3}$$

The normalized RCS $\bar{\sigma}$ may be defined as the measured cross section divided by a reference cross section.[3] For a general sphere, the cross section is commonly normalized by the projected area

$$\bar{\sigma} = \frac{\sigma}{\pi a^2}. \tag{4.4}$$

The exact RCS solution was first derived rigorously by Mie (1908). A plot showing the dependence of backscattered $\bar{\sigma}$ on frequency is shown in Figure 4.1.[4]

For a perfectly conducting sphere much larger than the wavelength of observation, $\bar{\sigma} \approx$ 1. For large dielectric spheres, the normalized RCS is typically less than one, since much of the incident power passes into the material and is either absorbed or leaves the sphere at an angle different from the exact backscatter direction. Counter to this intuition, the icy Galilean moons of Jupiter have been found to have $\bar{\sigma} > 1$. This effect has been attributed to volume scattering from inhomogeneities within the icy regolith covering these bodies, which preferentially focus energy in the backscatter direction (see Section 4.1.3).

---

[3]Other investigators denote this quantity as $\hat{\sigma}$ and term it the 'total planet albedo" or just 'albedo" of a target. See Eq. (5) of Ostro (1993). We depart from the use of the caret as it is commonly used to indicate an estimator in the electrical engineering literature.

[4]We thank D. Dougherty of the Naval Surface Warfare Center, Dahlgren Division (NSWC DD) for making the Mie scattering code `sphere_rcs` available.
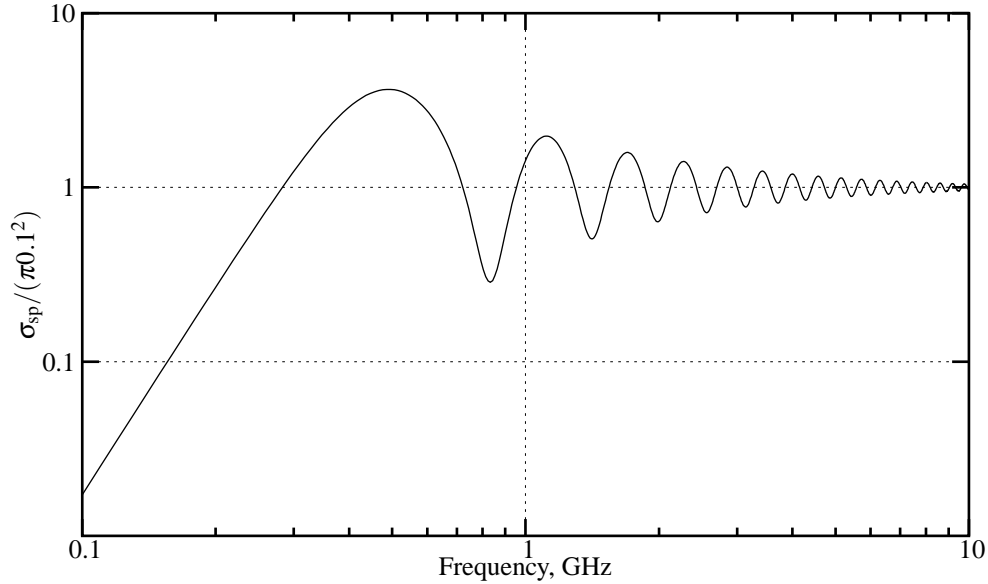
Figure 4.1 Mie backscatter from a perfectly conducting sphere. The normalized RCS, $\bar{\sigma} = \sigma/\pi a^2$, is plotted for $a = 10$ cm as a function of frequency from 100 MHz to 10 GHz.

4.1.2 Extended surface

In Chapter 5, we will be concerned with high-resolution imaging of the polar regions of Mercury, to detect patches of radar-bright material which have similar scattering character-istics to the icy regoliths of the three outer Galilean satellites. The imaging radar divides the region of interest into individual resolution elements, and it is desirable to compute the RCS of each element. The RCS per unit area σ_0 and the angle of incidence θ_i which the radar wave makes with respect to the mean local surface are important parameters in models of surface scattering.

For extended surface areas resolved by an imaging radar, it is often convenient to dis-cuss an area-normalized, or "specific," RCS of the surface rather than the cross section itself, as this separates the electrical properties of the surface from resolution "achieved" or "obtained" by the radar instrument. If an imaging radar has an projected resolution el-ement area of A_{res} on the ground, the specific RCS $\sigma_0(\theta_i)$ of the surface can be defined as the measured cross section in a resolution element σ_{res} divided by the projected surface
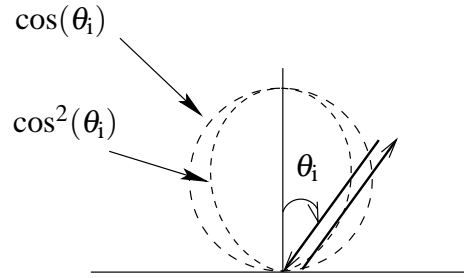
Figure 4.2 Minnaert scattering from a surface. In the Minnaert model, backscattered power is proportional to $\cos^n \theta_i$, where θ_i is the incidence angle.

area

$$\sigma_0(\theta_i) = \frac{\sigma_{res}(\theta_i)}{A_{res}} \tag{4.5}$$

where θ_i is the angle of incidence.

For diffusely scattering surfaces, there are many applicable surface and volume scattering models (Rees, 2001). The Minnaert scattering model has been found to fit the observed diffuse backscatter from solar system bodies in a variety of situations (Ostro, 1993). The Minnaert model states that the backscattered power is proportional to the cosine of the angle of incidence, θ_i, of the wave raised to the power n (Figure 4.2). If we define the normal-incidence specific cross section as $\sigma_0(0) = \rho$, then the specific radar cross section as a function of incidence angle is

$$\sigma_0(\theta_i) = \frac{d\sigma}{dS} = \rho \cos^n \theta_i. \tag{4.6}$$

It is important to note that the exponent n need not be an integer; for example, $n = 1.5$ is a common value for icy targets.

4.1.3   Diffusely scattering sphere

The total radar cross section of a large diffuse sphere can be computed by integrating the specific cross section over the visible surface. Using the Minnaert scattering model (4.6),

we find

$$
\begin{aligned}
\sigma &= \int_S d\sigma \\
&= \int_S \sigma_0(\theta_i)\, dS \\
&= \int_S \rho \cos^n \theta_i\, dS \\
&= \frac{2\rho}{n+1} \pi a^2,
\end{aligned}
\tag{4.7}
$$

where S is the surface of the visible hemisphere. With this, the normalized RCS becomes

$$
\bar{\sigma} = \frac{\sigma}{\pi a^2} = \frac{2\rho}{n+1}.
\tag{4.8}
$$

In Chapter 6, we compare our two-dimensional maps of surfaces with the total cross sections and cosine law models described in (4.6–4.8).

4.2 Dual-polarization measurements

For many radar investigations of planets and other objects in our solar system, it is possible to transmit one polarization and receive an orthonormal pair, such as two linear polarizations at right angles to one another, or oppositely rotating circular polarizations. For the high-power microwave radars at Goldstone and Arecibo, only right-hand circular polarization (RCP) is transmitted, but both RCP and left circular polarization (LCP) can be received. The RCP echo is referred to as the same-sense circular (SC) or "depolarized" echo, while the LCP echo is referred to as the opposite-sense circular (OC) or "polarized" echo. The term "polarized" is derived from the expected polarization return from a perfectly smooth, conducting metal plate viewed at normal incidence. In this case, the expected echo is LCP, which is also the OC polarization. The term "depolarized" refers to the sense of polarization not expected from specular reflection from a perfectly conducting sphere.

The more general case—reflection at an oblique angle from a dielectric interface—is shown in Figure 4.3. When the angle of incidence is less than the Brewster angle for
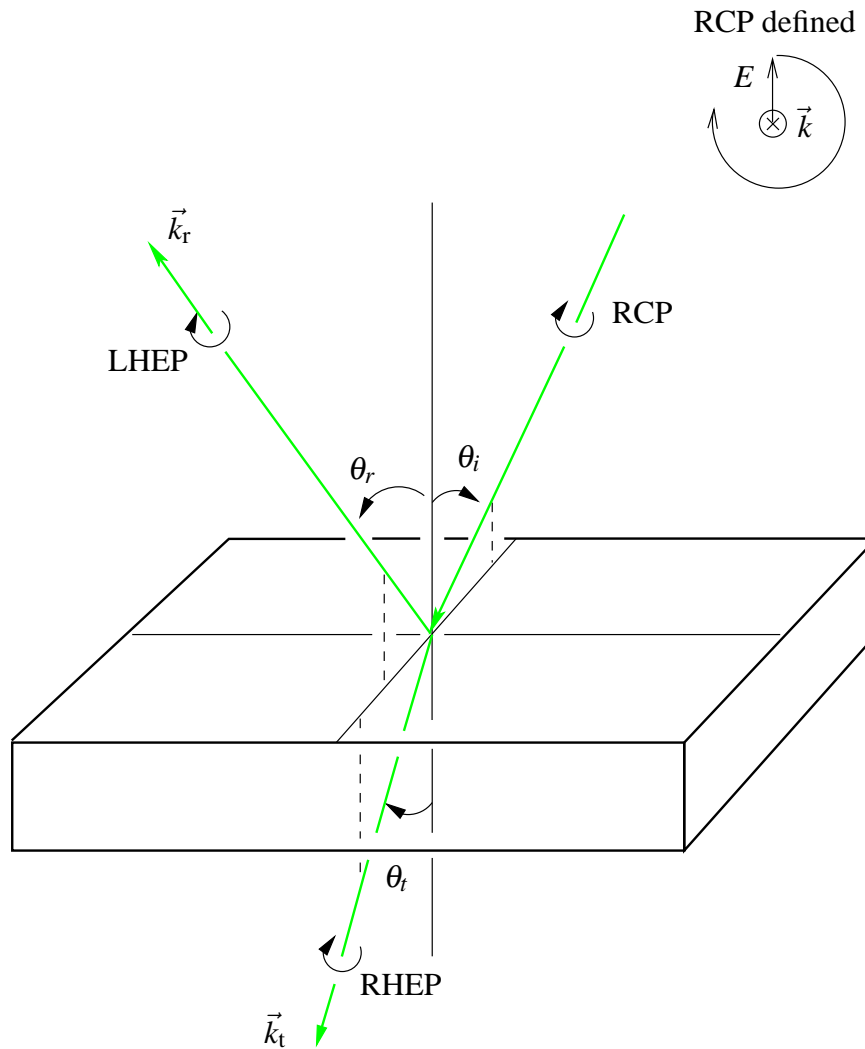
Figure 4.3 Polarization change upon reflection from a dielectric (after Inan and Inan, 2000). Right-hand circular polarization (RHCP) is defined in the inset, which shows the electric field E at a given point in space tracing a clockwise circular locus when looking in the direction of travel $\vec{k}$. When θ_i is less than the Brewster angle, the incident right-hand circular polarization is reflected in the specular direction as left-hand elliptical polarization (LHEP). The sense of rotation of the electric field is shown to reverse direction for the reflected wave. Right-hand elliptical polarization (RHEP) is transmitted into the material. When the incidence angle θ_i is greater than the Brewster angle θ_B, the sense of polarization of the reflected wave will be reversed from that shown here.

the material, incident circular polarization will be reflected in the opposite-sense elliptical polarization as that transmitted. The singly-reflected wave does not return to the radar unless the angle of incidence is 0, and thus a second, favorable reflection from another structure (not shown) is required to return energy in the exact backscatter direction. If this second reflection is again at an angle of incidence less than the Brewster angle for the material, the returned wave will be in the same-sense elliptical polarization as that transmitted. Multiple scattering from surface structures is one component of the diffuse reflection from a target object.

The wave which penetrates into the dielectric material in Figure 4.3 retains the same-sense elliptical polarization as that transmitted, independent of the angle of incidence. This wave may also undergo multiple scattering from structures or inhomogeneities within the dielectric, and return through the air/dielectric boundary in the exact backscatter direction. Volume scattering from multiple reflections within the target object is a second component of the diffuse reflection.

For dual-polarization measurements, we need to distinguish between two distinct cross sections: the RCS with same circular polarization (σ_{SC}) and the RCS with opposite circular polarization opposite to that transmitted (σ_{OC}). The ratio μ_c of these two distinct cross sections is known as the circular polarization ratio

$$\mu_c = \frac{\sigma_{SC}}{\sigma_{OC}}. \tag{4.9}$$

Though our study is concerned only with observations made with circular polarization, similar definitions exist for linear polarization, σ_{SL}, σ_{OL}, and μ_L (Ostro, 1993). For a large sphere such as a terrestrial planet, we expect specular reflection from the subradar point to dominate the return. This results in $\sigma_{OC} \gg \sigma_{SC}$ and $\mu_c \ll 1$. Some power is returned in the SC polarization due to multiple scattering events from the rough surfaces of these objects or from single scattering by discrete objects such as non-spherical rocks. Total planet RCS measurements of terrestrial planets exhibit low radar cross sections and polarization ratios consistent with this expectation. Results are quite different for icy moons of the outer solar system, however. For icy planets, it is not uncommon to measure $\bar{\sigma}_{OC} \approx \bar{\sigma}_{SC} \approx 1$ and $\mu_c > 1$, presumably as a result of multiple or volume scattering. Table 4.1 shows the

Body	$\bar{\sigma}_{OC}$	$\bar{\sigma}_{SC}$	μ_c
Moon	0.07	0.01	0.1
Mercury	0.06	0.01	0.1
Venus	0.11	0.01	0.1
Mars	0.08	0.02	0.3
Titan	0.15	0.08	0.5
Io	0.20	0.10	0.5
Europa	1.00	1.50	1.5
Ganymede	0.60	0.84	1.4
Callisto	0.30	0.36	1.2
Mercury's polar craters	0.71	0.89	1.3
Mars' RSPIC	0.31	0.72	> 2.0

Table 4.1 Polarization ratios typical of planetary bodies after Ostro (1993) except Mars polar cap datum from Butler (1994), Mercury crater data from Harmon et al. (2001), and Titan datum from Campbell et al. (2003b).

average normalized radar cross sections and polarization ratios for several objects in the solar system.

Ostro et al. (1992) report an extensive campaign to investigate the scattering properties of the icy Galilean satellites. The dual-polarization measurement results are reproduced in Table 4.2. The new column for ρ has been generated from the table values for n, $\bar{\sigma}$, and

$$\rho = \frac{n+1}{2}\bar{\sigma}, \tag{4.10}$$

from (4.8).

4.3   A model for icy crater floors

For deposits of ice that may lie on the floors of craters, we can apply the extended surface model developed in Section 4.1.2 (Figure 4.2) as have Harmon et al. (1994) and Harmon et al. (2001).

The specific RCS of the crater floor as a function of θ_i is

$$\sigma_0(\theta_i) = \rho \cos^n \theta_i. \tag{4.11}$$

Body	λ, cm	Pol.	$\bar{\sigma}$	n	ρ
Europa	13	OC	1.03	1.8	1.44
	13	SC	1.58	1.8	2.21
	3.5	OC	0.91	1.7	1.23
	3.5	SC	1.40	1.7	1.89
Ganymede	13	OC	0.57	1.5	0.71
	13	SC	0.82	1.5	1.03
	3.5	OC	0.65	1.3	0.75
	3.5	SC	0.90	1.3	1.04
Callisto	13	OC	0.32	1.5	0.40
	13	SC	0.37	1.5	0.46
	3.5	OC	0.32	1.4	0.38
	3.5	SC	0.40	1.4	0.48

Table 4.2 13 cm and 3.5 cm global radar backscatter results for the icy Galilean satellites. Values for $\bar{\sigma}$ and n are from Ostro et al. (1992). Values for ρ are computed from (4.10). Total error in $\bar{\sigma}$ is estimated to be $\pm 20 - 50\%$.

For a crater of radius a_{cr}, area $A_{cr} = \pi a_{cr}^2$, and uniform scattering across the floor, this model represents the RCS as

$$\sigma_{cr} = A_{cr} \rho \cos^n \theta_i. \tag{4.12}$$

To confirm the phenomena of "high" specific cross section and polarization inversion, Harmon et al. (1994) solve for the equivalent total-planet normalized RCS, $\bar{\sigma}$, of Mercury's polar craters (Table 4.3) and compare this with the icy Galilean satellites normalized RCS $\bar{\sigma}$, given in Ostro et al. (1992) (Table 4.2). Performing such a comparison involves the use of a model for the angle-dependent scattering behavior of the specific RCS, $\sigma_0(\theta_i)$. The model is used to convert the measured specific RCS at a given θ_i to normalized total planet RCS $\bar{\sigma}$ as follows.

From (4.11) the reflectivity at normal incidence is

$$\rho = \frac{\sigma_0(\theta_i)}{\cos^n \theta_i}. \tag{4.13}$$

The specific RCS at the angle of observation is determined from the measured RCS by

$$\sigma_0(\theta_i) = \frac{\sigma(\theta_i)}{A_{ill}}, \tag{4.14}$$

where A_{ill} is the area of the crater floor illuminated by the radar and exhibiting bright backscatter, which may be less than the total floor area. The equivalent full-disk RCS is obtained by substitution of (4.13) and (4.14) into (4.8),

$$\bar{\sigma} = \frac{2\rho}{n+1} = \frac{2\sigma(\theta_i)}{(n+1)A_{ill}\cos^n\theta_i}. \tag{4.15}$$

The solution for equivalent total planet normalized RCS thus depends on an assumed value for the scattering law exponent n (Harmon et al., 2001). When applying (4.15) to crater floors, experimenters must choose a diffuse scattering law exponent n based upon observations of other icy surfaces. For example, a choice of $n = 1.5$ yields model-derived ρ and $\bar{\sigma}$ for several of Mercury's polar craters as shown in Table 4.3.

From viewing Harmon et al.'s results (Table 4.3), it is apparent that all of the craters containing radar bright material exhibit high normalized RCS $\bar{\sigma} \approx 1$ and polarization inversion $\mu_c > 1$. This is consistent with the hypothesis that the material in these craters exhibits scattering behavior nearly identical to that of the icy Galilean satellites (Table 4.2), and therefore the investigators concluded that ice exists in shadowed cold traps on Mercury's polar crater floors.

4.3.1   Vacuum-to-dielectric boundaries

Thermal stability of putative ice in large diameter craters at the poles of Mercury or in craters generally at low latitudes appears to require an insulating layer of dust or regolith to thermally insulate and protect the ice from sublimating due to the effects of re-radiation of absorbed solar energy from the crater walls (Butler et al., 1993; Vasavada et al., 1999). Figure 4.4 illustrates the geometry of the situation. Below ≈ 110 K, it takes about one billion years for 1 m of ice exposed to space to sublimate. At ≈ 130 K, the time scale is about one million years. Temperatures lower than 110 K are predicted for large craters within a few degrees of the pole. Temperatures in excess of 145 K are predicted for some craters

Coordinates	Crater ID	θ_i (deg.)	σ_{SC} (km^2)	$\bar{\sigma}_{SC}$	μ_c	A_{ill} (km^2)	ρ
128W, 88.3N	D	78.0	57	0.79	1.31	6.09e2	0.99
165W, 89.5N	E	78.5	35	0.96	1.21	3.28e2	1.20
205W, 88.8N	H	77.8	63	0.66	1.19	7.86e2	0.83
281W, 88.0N	J	79.3	152	0.90	1.23	1.69e3	1.13
297W, 85.0N	K	81.1	188	0.99	1.28	2.50e3	1.24
150W, 88.3S	X	83.7	450	0.53	1.12	1.89e4	0.66
86W, 80.7S	V	83.1	28	0.41	1.43	1.32e3	0.51

Table 4.3 Scattering properties of Mercury's polar craters at 13 cm from Harmon et al. (1994) and Harmon et al. (2001). Only one Harmon-labeled crater has a U.S.G.S. assigned name—Crater X near the south pole corresponds to Chao Meng-Fu. The error on μ_c is less than 5%, while the error on absolute cross sections $\sigma_{OC,SC}$ is 15–20%. The normal incidence reflectivity ρ and effective illuminated area A_{ill} follow from other data given in Harmon et al. (2001). For the north polar craters, σ_{SC} is as listed in Harmon et al. (2001). For the south polar craters, σ_{SC} is calculated based upon the values for $\bar{\sigma}$ reported in Harmon et al. (1994), adjusted for a calibration error of $3/2$ (Harmon, 1997), and scaled by physical diameters reported in Vasavada et al. (1999). The angle of incidence for the south craters was taken from the average subradar point for the March 1992 observations and the crater physical locations listed in Vasavada et al. (1999). Harmon et al. (1994, 2001) assume a scattering law exponent $n = 1.5$ based upon the icy Galilean satellite results of Ostro et al. (1992). An error of ±0.2 in the assumed value of n will change the normalized cross section $\bar{\sigma}$ by 25%. See the discussion in Harmon et al. (1994, 2001).
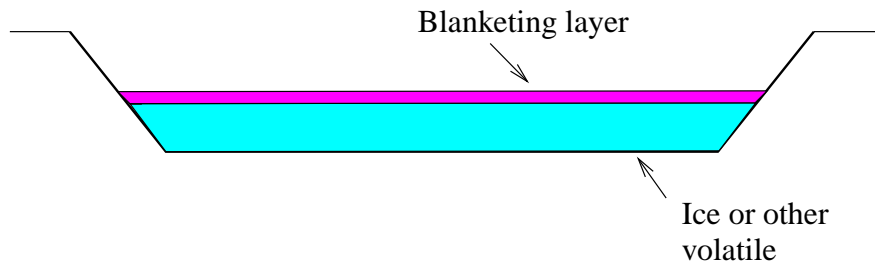
Figure 4.4 Thermally insulating regolith layer protecting ice deposit in near polar crater.

near 80 deg. latitude which exhibit enhanced reflection and polarization inversion in radar images. Vasavada et al. (1999) show that a layer 10–50 cm in thickness can provide the thermal stability needed to maintain ice deposits in these locations. If such a layer does exist, it cannot be too thick, however. Otherwise the phenomena of enhanced backscatter would not be observed, as a result of attenuation in the material at radar wavelengths. Experimental confirmation of the theoretically-derived bound on the thickness of this putative layer is of interest.

Using the electromagnetic properties of dielectric materials, it is possible to derive a model for wavelength-dependent attenuation through the dust. Although the radar reflection from known solar system ices is wavelength independent to within experimental error across the microwave band (Ostro et al., 1992)[5], an insulating layer of lossy regolith covering such ice could introduce frequency dependent attenuation of the radar signal since the attenuation constant α is inversely proportional to wavelength (see Section 4.3.2). Since the total cross section of the deposits in the polar craters can be measured as a function of wavelength, fitting an attenuation model to these measurements can place a bound on the thickness of such a regolith layer.

4.3.2   Absorbing regolith

We estimate the thickness of a dielectric layer by first considering an electromagnetic plane wave propagating in $\pm\hat{z}$ direction, which can be written[6]

$$E_x(z,t) = C_1 e^{-\alpha z}\cos(\omega t - \beta z) + C_2 e^{+\alpha z}\cos(\omega t + \beta z) \tag{4.16}$$

where the attenuation constant α is

$$\alpha = \omega\sqrt{\frac{\mu\varepsilon}{2}}\left[\sqrt{1+\tan^2\delta_c} - 1\right]^{\frac{1}{2}} \tag{4.17}$$

---

[5]Contrary to microwave observations demonstrating little variation in RCS between 13 and 3.5 cm wavelength, Black et al. (2001) have noted a decreased RCS for the icy Galilean satellites at 70 cm wavelength (the UHF radio band).

[6]See any standard reference on electromagnetic waves, e.g. Inan and Inan (2000).

and the propagation constant β is

$$\beta = \omega \sqrt{\frac{\mu \varepsilon}{2}} \left[\sqrt{1 + \tan^2 \delta_c} + 1 \right]^{\frac{1}{2}}. \tag{4.18}$$

In these equations, μ and ε are the permeability and permittivity of the medium, and ω is the radio carrier frequency in rad/sec.

The loss tangent $\tan \delta_c$ is defined by

$$\tan \delta_c = \frac{\sigma_{\text{eff}}}{\omega \varepsilon'} = \frac{\varepsilon''}{\varepsilon'} \tag{4.19}$$

where σ_{eff} is the effective conductivity of the material, and ε' and ε'' are the real and imaginary parts of the complex permittivity ε. In microwave remote sensing of rock and soil, the loss tangent $\tan \delta_c$ and the relative permittivity ε'_{r} do not have strong wavelength dependence (Campbell and Ulrichs, 1969). This leads to an attenuation constant which is inversely proportional to wavelength λ

$$\alpha_\lambda = \frac{2\pi}{\lambda} \sqrt{\frac{\mu_{\text{r}} \varepsilon'_{\text{r}}}{2}} \left[\sqrt{1 + \tan^2 \delta_c} - 1 \right]^{\frac{1}{2}}. \tag{4.20}$$

The geometry of the problem is shown in Figure 4.5. If, as above, we make the assumption that the net loss in passing through a regolith layer is exponentially related to the effective path length d_{eff} traveled, then the wavelength dependent cross section σ_λ is proportional to

$$\sigma_\lambda \propto \cos^n(\theta_{\text{i},\lambda}) e^{-4\alpha_\lambda d_{\text{eff}}}. \tag{4.21}$$

The factor of 4 in the attenuation exponent arises because power is proportional to the square of the electric field and the effective path length d_{eff} is traversed twice.

Measurements of Mercury's polar crater cross sections were obtained at 13 cm and 3.5 cm wavelength at separate inferior conjunctions on different years, when the sub-Earth latitudes were 11.2 and 7.7 degrees, respectively. The angle of incidence of a radar wave at the polar region is thus dependent on the date of observation. For this reason, we adopt a somewhat non-standard convention of associating a wavelength with a particular angle of incidence $\theta_{\text{i},\lambda}$. This indicates that for our observations, the angle of incidence at the two
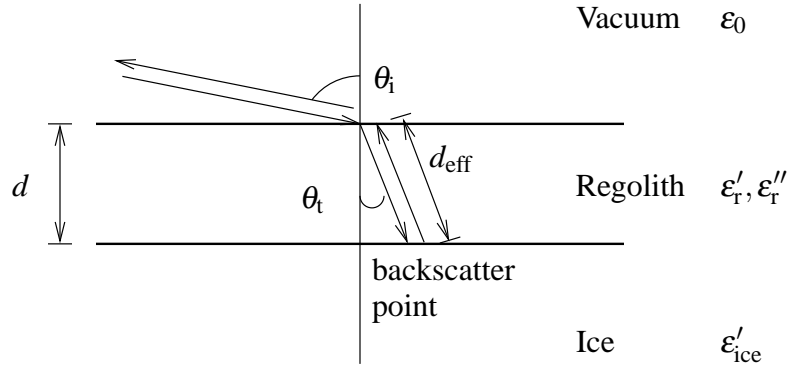
Figure 4.5 Apropos Snell's law for angle of incidence θ_i and angle of transmission θ_t at an vacuum/dielectric interface. Dominant backscatter is assumed to occur through the dust-ice interface from the ice below. The effective path length d_{eff} that the wave traverses through the material is greater than the physical depth of the material d.

wavelengths of interest is different.

In (4.21), the term $\cos^n(\theta_{i,\lambda})$ accounts for a diffuse scattering component from either the surface of the blanketing material, or from the volume scattering material below the material. In general, $\theta_{i,\lambda}$ can take on any value between 0 and 90 deg. In our analysis for crater floors—and lacking other specific information—we assume that any vacuum/ice interface is parallel to a spherical model of Mercury and, therefore, $\theta_{i,\lambda}$ is known from the ephemeris for the date of observation at a radiotelescope using an observation wavelength $\lambda \in \{3.5, 13 \text{ cm}\}$. We do not assume any particular value of scattering law exponent, n. Previous observations of solar system ices show that n typically varies between $\approx$1–2 (Ostro et al., 1992), so we constrain our analysis to the interval $0 < n < 2.5$.

The thickness of the layer d is related to the effective path length d_{eff} by Snell's Law (Figure 4.5), so

$$\theta_t = \sin^{-1}\left(\frac{1}{\sqrt{\varepsilon_r'}} \sin \theta_i\right) \tag{4.22}$$

and

$$d = d_{\mathrm{eff}} \cos \theta_t. \tag{4.23}$$

Here we have made an approximation that the transmitted angle into the material is insensitive to the wavelength of observation. We justify this approximation as follows. For our

Mercury polar observations, $\varepsilon'_r \approx 2.7$ is essentially constant at the two wavelengths of interest (Mitchell and de Pater, 1994). For this value of ε'_r and the angles of incidence involved, which are $\theta_{i,\lambda} \approx 80 \pm 3°$, Snell's law yields $\theta_{t,3.5} \approx \theta_{t,13} \approx 36.8 \pm 0.4$ deg.

Knowing the cross section of a deposit at the two wavelengths, $\lambda = 13$ cm and 3.5 cm, the cross section ratio is given by the ratio of the wavelength-dependent portions of the cross sections (4.21)

$$\frac{\sigma_{13}}{\sigma_{3.5}} \approx \left[\frac{\cos(\theta_{i,13})}{\cos(\theta_{i,3.5})}\right]^n \frac{e^{-4\alpha_{13}d_{\mathrm{eff}}}}{e^{-4\alpha_{3.5}d_{\mathrm{eff}}}}. \tag{4.24}$$

Solving (4.24) for insulating layer thickness, we find

$$d \approx d_{\mathrm{eff}} \cos\theta_t = \ln\left\{\frac{\sigma_{13}}{\sigma_{3.5}}\left[\frac{\cos(\theta_{i,3.5})}{\cos(\theta_{i,13})}\right]^n\right\} \frac{\cos\theta_t}{4(\alpha_{3.5} - \alpha_{13})}. \tag{4.25}$$

4.3.3 Sensitivity to error

Solution for the thickness of a lossy dielectric layer requires an estimate of the electrical properties of the layer in addition to knowledge of the imaging geometry. In order to assess the accuracy of our thickness estimates, it is necessary to understand the dependence of these estimates on errors in our model inputs. The error sensitivity of the simple model in Section 4.3 can be examined on the basis of the partial derivatives of the layer thickness estimate d with respect to the input parameters.

The cross section ratio $\sigma_{13}/\sigma_{3.5}$, being the ratio of two quantities each distributed as a Gaussian random variable, is a Cauchy random variable which has an unbounded second moment. Define ξ to be the weighted cross section ratio

$$\xi = \frac{\sigma_{13}}{\sigma_{3.5}}\left[\frac{\cos(\theta_{i,3.5})}{\cos(\theta_{i,13})}\right]^n \tag{4.26}$$

where the weighting term depends on solar system geometry and the scattering law exponent n. The partial derivative of the layer thickness estimate d with respect to ξ is

$$\frac{\partial d}{\partial \xi} = \frac{\cos\theta_t}{4\xi(\alpha_{3.5} - \alpha_{13})}, \tag{4.27}$$

showing that the error in the thickness is inversely proportional to the measured ratio.

For loss tangent ($\tan \delta_c$) sensitivity, we approximate the attenuation constant from (4.20) by first approximating the term

$$\left[\sqrt{1 + \tan^2 \delta_c} - 1 \right]^{\frac{1}{2}} \approx \left[1 + \frac{1}{2} \tan^2 \delta_c - 1 \right]^{\frac{1}{2}} \tag{4.28}$$

$$\approx \frac{1}{\sqrt{2}} \tan \delta_c.$$

Then, setting

$$\gamma = \tan \delta_c, \tag{4.29}$$

we compute the partial derivative and find

$$\frac{\partial d}{\partial \gamma} \approx -\ln(\xi) \frac{c}{2\gamma^2} \frac{\cos \theta_t}{\sqrt{\mu_r \varepsilon_r'}(\omega_{3.5} - \omega_{13})}, \tag{4.30}$$

indicating that the error in the thickness estimate is inversely proportional to the square of $\tan \delta_c$.

Dependence of the the thickness estimate on the real part of the relative permittivity ε_r' is more complex due to its appearance in Snell's law as well as the attenuation constant α. In order to simplify the $\cos \theta_t$ term, we observe that for the polar regions of Mercury, $\theta_i \approx 80 \pm 3°$, so we may take $\sin \theta_i \approx 1$. We linearize the dependence of $\cos \theta_t$ on the relative permittivity ε_r' as

$$\cos \theta_t = \cos \left[\sin^{-1} \left(\frac{1}{\sqrt{\varepsilon_r'}} \sin \theta_i \right) \right]$$

$$\approx \cos \left[\sin^{-1} \left(\frac{1}{\sqrt{\varepsilon_r'}} \right) \right]$$

$$\approx 1 - \frac{1}{2} \left(\frac{1}{\sqrt{\varepsilon_r'}} \right)^2$$

$$\approx 1 - \frac{1}{2\varepsilon_r'}. \tag{4.31}$$

Setting other terms in (4.25) which are constant with respect to ε'_r equal to the constant ζ

$$\zeta = \frac{1}{c}\sqrt{\frac{\mu_r}{2}}\left[\sqrt{1+\tan^2\delta_c}-1\right]^{\frac{1}{2}} \tag{4.32}$$

we can rewrite (4.25) as

$$d \approx \ln(\xi)\frac{1}{4\zeta\sqrt{\varepsilon'_r}(\omega_{3.5}-\omega_{13})}\left(1-\frac{1}{2\varepsilon'_r}\right). \tag{4.33}$$

The partial derivative of d with respect to ε'_r gives

$$\frac{\partial d}{\partial \varepsilon'_r} \approx \ln(\xi)\left[\frac{1}{4\zeta(\omega_{3.5}-\omega_{13})}\right]\frac{1}{2\varepsilon'^{3/2}_r}\left(\frac{3}{2}-\frac{1}{\varepsilon'_r}\right). \tag{4.34}$$

These partial derivatives are used in Chapter 5 to examine the sensitivity of the attenuating regolith layer thickness to the model input parameters.

4.4 Summary

In this chapter we examine some of the properties of diffusely scattering media. We derive simple power scattering models for large spheres. The standard $\cos^n(\theta_i)$ law is sufficient for modeling the total planet cross section. We apply this model to remove a hemispherical backscatter term in observations of the Galilean satellites in Chapter 6. Since off-pole craters depend on an attenuating blanket of regolith to prevent sublimation, we postulate a second model for the frequency dependent attenuation of a regolith layer covering bright backscattering material, and derive its thickness. We fit this model to observations of the radar bright deposits of Mercury's polar craters in Chapter 5.

Chapter 5

Mercury's Polar Regions

Mercury, the innermost planet in the solar system, challenges traditional optical astronomers because of its proximity to the Sun. It can be seen from Earth only in the twilight of dawn or evening, when located at or near its maximum eastward or westward elongation; glow from sunlight scattered by Earth's atmosphere lowers the effective sensitivity of optical telescopes significantly. Space-based telescopes, although above the atmosphere, are limited by thermal and scattered light constraints of the instruments themselves; Hubble, for example, cannot point within $50°$ of the Sun. For these reasons, knowledge about Mercury is limited even though it is relatively close to the Earth. For example, for over 70 years Mercury was thought to have a sidereal rate of rotation locked to its orbit period of 88 days so that the same side always faced the sun, as our Moon faces Earth (Schiaparelli, 1889). This fundamental fact about Mercury went unchallenged until the correct rotation was obtained by Pettengill and Dyce (1965) using the Arecibo radar.

Radar detection of Mercury was first claimed by Kotelnikov et al. (1962) in the U.S.S.R. and by Carpenter and Goldstein (1963), who used the 26 m Goldstone instrument. It was not until the Arecibo observations of Pettengill and Dyce (1965) that reproducible results were obtained, however. The Arecibo observations produced the startling discovery that Mercury is not locked in synchronous rotation with its orbit period, but that it is in fact in a 2/3 resonance, with a sidereal period of rotation of approximately 58.65 days.

In early 1991, using the Goldstone/VLA synthesis mapping instrument at 3.5 cm wavelength, Slade et al. (1992) detected localized regions of polarization inversion (Chapter 4),

and high values of specific cross section σ_0 in radar images of the northern polar region. Previously, such polarization inversion had been seen only in radar observations of Europa, Ganymede, and Callisto—the icy moons of Jupiter–and Mars' residual south polar ice cap (RSPIC). This result was immediately confirmed in delay-Doppler images from the Arecibo 13 cm system by Harmon and Slade (1992). As the polar regions of a planet are fortuitously located at the point of maximum resolution of the standard delay-Doppler technique (Chapter 2), additional observations from the Arecibo monostatic system and reanalysis of existing data produced excellent images at 15 km resolution, four times finer than previous imaging (Harmon et al., 1994). By comparing the radar results with Mariner 9 optical images, Paige et al. (1992) and Butler et al. (1993) concluded that the anomalous scattering could be explained by presence of water ice deposits trapped in permanently shadowed craters. Vasavada et al. (1999) have since expanded on the thermal modeling, including scattered light and "dark" sky radiation.

The best conditions for imaging Mercury's polar regions include: i) the planet at northern declinations to allow maximum observing time for telescopes in Earth's northern hemisphere, ii) inferior conjunction for minimum range, and iii) high northern or southern sub-Earth latitude for best visibility of the pole (Figure 5.1). These conditions permit viewing the floors of craters at high latitudes as well as minimizing north-south ambiguities from the opposite pole (Section 2.2.1). In 1998 and 1999, such favorable geometry allowed Harmon et al. (2001) to acquire high resolution (1.5 km) images of the north pole using a new Arecibo 13 cm system, which had been upgraded compared to its early 1990's capabilities. The narrow zenith angle window of the Arecibo observatory prevented observations of the southern hemisphere during the 1998 and 1999 inferior conjunctions.

The Goldstone radar, being fully articulated, does not have the zenith angle limitations of Arecibo, so that data can be acquired with Goldstone at times when Arecibo is unable to view Mercury. Hence, we decided to implement an experimental campaign to image the northern and southern polar regions with Goldstone during the 1999-2001 period.
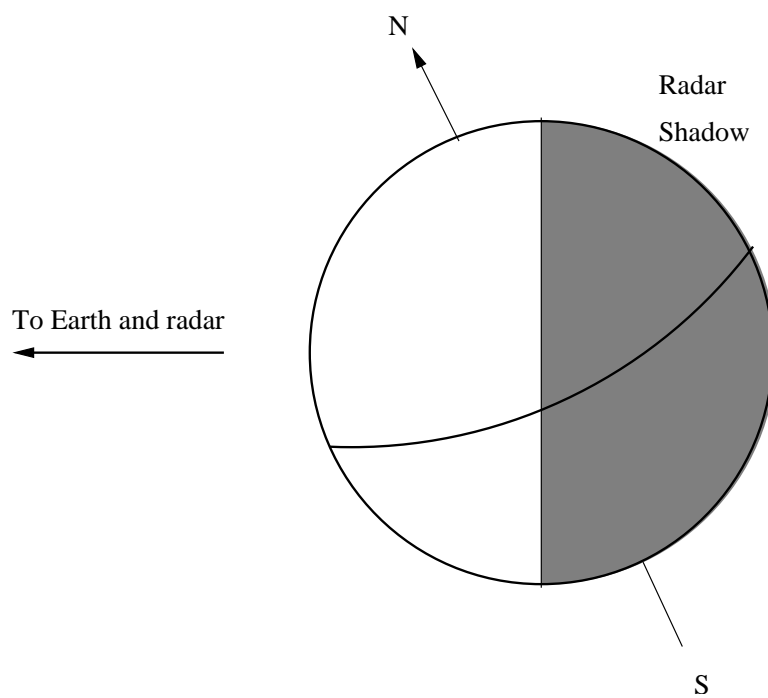
Figure 5.1 Polar tilt aids imaging of one polar region over another. Here the radar illuminates the north polar region, while the south polar region lies in radar shadow.

Opposition			Observations	
Date (2001)	Range (AU)	Sub-Earth Latitude	Dates (2001)	Number of Sessions
Feb. 13	0.65	$-10.6°$	Feb. 9–20	4
Jun. 16	0.55	$+7.68°$	Jun. 13–Jul. 1	3

Table 5.1 Mercury 2001 inferior conjunctions. Observations of Mercury reported here were obtained during two inferior conjunctions in 2001. A 3 dB difference in range loss led to weaker observations of the south polar region in February than were obtainable from the north polar regions in June. This difference was partially mitigated by incoherently averaging twice as many observations of the south pole.

5.1   Observations

Since Mercury is overspread by a factor of 8:1 at 3.5 cm, methods such as use of the long-code waveforms, developed in Chapter 2, must be employed to escape the problems of overspreading. We chose a PN code with baud $b = 40$ μsec in order to achieve 6 km resolution in the polar regions, a factor of 2 better than previously obtained in the south (Harmon et al., 2001). The only available matched filter was for 20 μsec baud, which required us to sample at 50 kHz, twice the required $1/b$ rate.

Preliminary attempts at imaging of Mercury's north pole during July 1999 verified proper system operation, and confirmed enhanced backscatter from several of the large north polar craters (Slade et al., 2000). During the 2001 inferior conjunctions (Table 5.1) our experiments yielded good data from both the northern and southern polar regions. The observing procedure on each day was as follows.

The Goldstone DSS-14 antenna was used both for transmitting and receiving. The transmitter exciter frequency was Doppler-compensated to remove the effects of radar/Mercury motion so that the center frequency of the received echo appeared at a fixed frequency of 8560 MHz. DSS-14 transmitted right-hand circular polarization. The transmitted PN sequence was recorded, together with timing data, in the record headers to facilitate synchronization and cross correlation with the received data. One round-trip light time after the beginning of the transmission sequence the antenna was switched to receive and the echo was recorded in both right- and left-hand circular polarizations. During the experiment, the

uplink carrier frequency was monitored by connecting the output of the programmable local oscillator to a counter. The uplink timebase drift was observed in a similar manner. The counter frequencies were compared to the expected Doppler frequencies calculated from the ephemeris to verify proper Doppler compensation.

The coherent processing interval required to achieve cross-range resolution equal to the range resolution is typically on the order of a few seconds (Table 5.2). One complete round trip transmit/receive cycle lasted 20 to 25 minutes, depending on the range to Mercury. Multiple coherent processing intervals collected during one round-trip cycle can be incoherently averaged in delay-Doppler coordinates to improve SNR. A single round-trip transmit/receive cycle does not have sufficient SNR to perform high-resolution imaging, however. To further improve SNR, we recorded data from multiple cycles, so that additional incoherent averaging across round-trip cycles could be employed later. Since a typical observing session was six to eight hours per day, we acquired between four and thirteen round-trip cycles of data on each date of observation as detailed in Tables 5.3–5.4.

We performed consistency checks of system operation each day to ensure accurate calibration of the recorded data. The end-to-end data system was verified at the start of each day by recording the leakage signal of the transmitter into the receiving chain. A quick computer analysis of these data verified the correctness of software range compression. A slight frequency offset was added to the exciter during this testing to insure that the I/Q channels were identified properly. We also checked the validity of the data by processing a portion of each round-trip cycle on the Sun workstation network at Goldstone after each observing run. Detailed post processing and analysis were implemented later at Stanford University.

5.2   Equipment configuration

Figure 5.2 shows the experiment configuration at Goldstone. The station master frequency reference, shown in the center of the diagram, also serves as the timing standard for both

the transmitting and receiving systems. The lower portion of Figure 5.2 shows the transmitting system consisting of the PN coder,[1] timebase shifter, exciter, and klystron amplifier. The VAX-based timebase shifter receives the station reference and an ephemeris as inputs, and generates a Doppler-compensated clock signal for the PN generator. The PN generator synchronizes to this clock signal, and drives the exciter. The output of the PN generator is also passed to the A/D converters and recorded on disk storage for later cross-correlation with the received data. The output of the exciter modulates a Doppler-compensated carrier supplied by a programmable oscillator. The modulated signal passes through an IF stage (not shown) to the klystron amplifier. The output of the klystron passes through a microwave transmit/receive switch to the antenna.

The upper portion of Figure 5.2 shows the receiving system consisting of a maser LNA, downconverter, filters, and A/D sampling system. Both circular polarizations of the received signal pass through the microwave transmit/receive switch to the dual-channel ruby maser. The output of the maser is downconverted to IF and filtered (not shown), and then quadrature mixed to baseband and filtered again by a 20 μsec rectangular pulse matched filter. The A/D converters run at 2 samples/baud, and store 8 bit samples of the in-phase and quadrature components for both polarizations, for a total of four channels. Data are written to disk storage for later processing.

5.3   Data processing and mapping

The data processing system implementation is shown in Figure 5.3. We used the same long-code data processing technique outlined by Harmon (2002). Recorded data include the transmitted PN sequence and the received echo for each round trip cycle. In order to form delay-Doppler images, the transmitted sequence is delayed appropriately and multiplied by the received data to form a time series for each delay bin. This removes the high-bandwidth range code from the signal in each delay bin, and is equivalent to the despreading process in a direct-sequence, spread-spectrum communications system. The resultant time series for each bin contains the narrowband echo of the planet at a much higher sampling rate than is

---

[1]We thank John Harmon of NAIC for making a spare Arecibo long-code generator available for these experiments.

Parameter	Value
Receive cycle time	≈ 12 min.
Carrier frequency, f_c	8560 MHz
Mercury delay depth, $\Delta\tau$	16.3 msec
Mercury bandwidth, Δf	≈ 370 Hz
Complex sample rate, f_s	50 kHz
Bits per sample	8
PN baud (delay resolution element), b	40 μsec
Range resolution, ΔR	6 km
Range compression length, N	64 bauds
Doppler compression (FFT) length, K	1024 samples
Doppler resolution element width	0.38 Hz
Cross-range resolution, ΔR_{cross}	≈ 5 km
Coherent integration time, KNb	2.62 sec
System temperature, T_{sys}	17 K
Processed resolution	624 delay $\times$ 1024 Doppler resolution elements

Table 5.2 Data acquisition and processing parameters.

necessary to represent the planet echo. To reduce the data input to the Doppler compression process, the time series for each bin are averaged and downsampled by a factor $N = 64$ bauds. The resulting signal is Fourier transformed by a length $K = 1024$ FFT to obtain cross-range resolution for each delay bin. The achieved cross-range resolution was 5.6 km for the north pole and 4.8 km for the south pole. Data processing parameters appear in Table 5.2. As mentioned previously, the coherent processing interval is several seconds, while the recorded data from one transmit/receive cycle span several minutes. The delay-Doppler arrays from each transmit/receive cycle time are incoherently averaged to form an output array for each receive cycle. Since the data are recorded and processed later in non-real time, while the delay and Doppler matched filters or compression filters are of finite length, the processing can proceed in a parallel manner. We implemented the matched filter processing on a cluster of workstations.

We made one augmentation to the algorithms in Harmon (2002) for our data set. Since the 20 μsec analog baud filter in the receive chain before the digital sampler was a factor of two shorter than the 40 μsec baud used in the experiment, final baud filtering and

Dual−channel RCP and LCP Receiver Chain
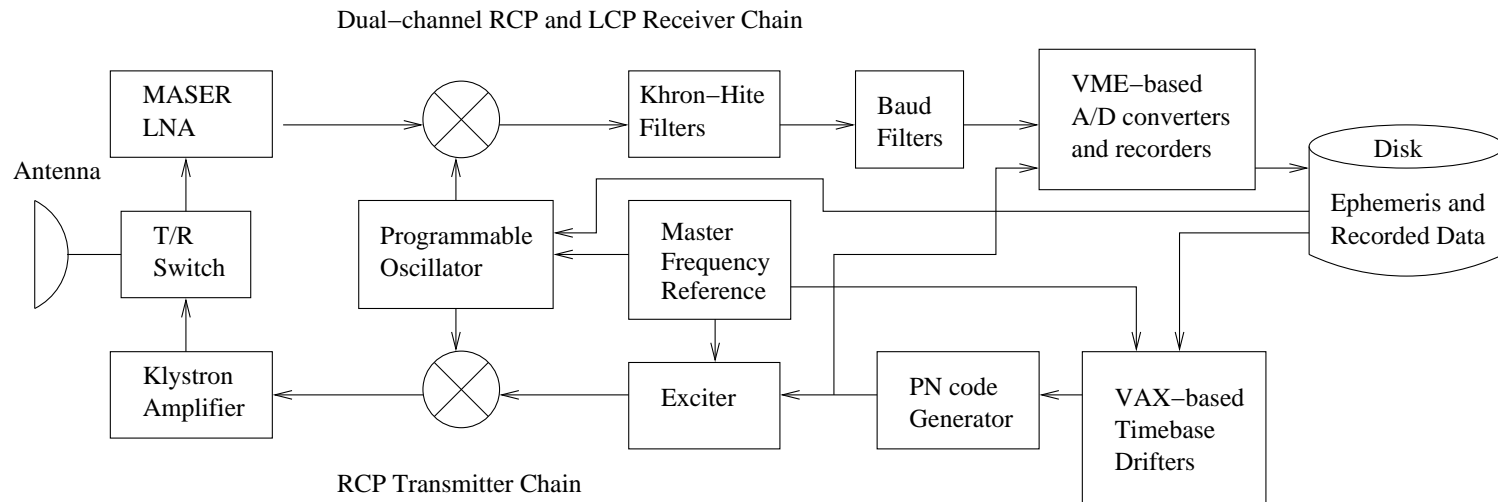
Figure 5.2 Block diagram of Goldstone DSS-14 experiment configuration. The dual-channel receiving LNA and data processing chain is capable of recording RCP and LCP simultaneously. The T/R switch is implemented using RF optics and switches between two feed horns, one attached to the transmitter and the other attached to the LNA. Details of the IF distribution network are not shown.
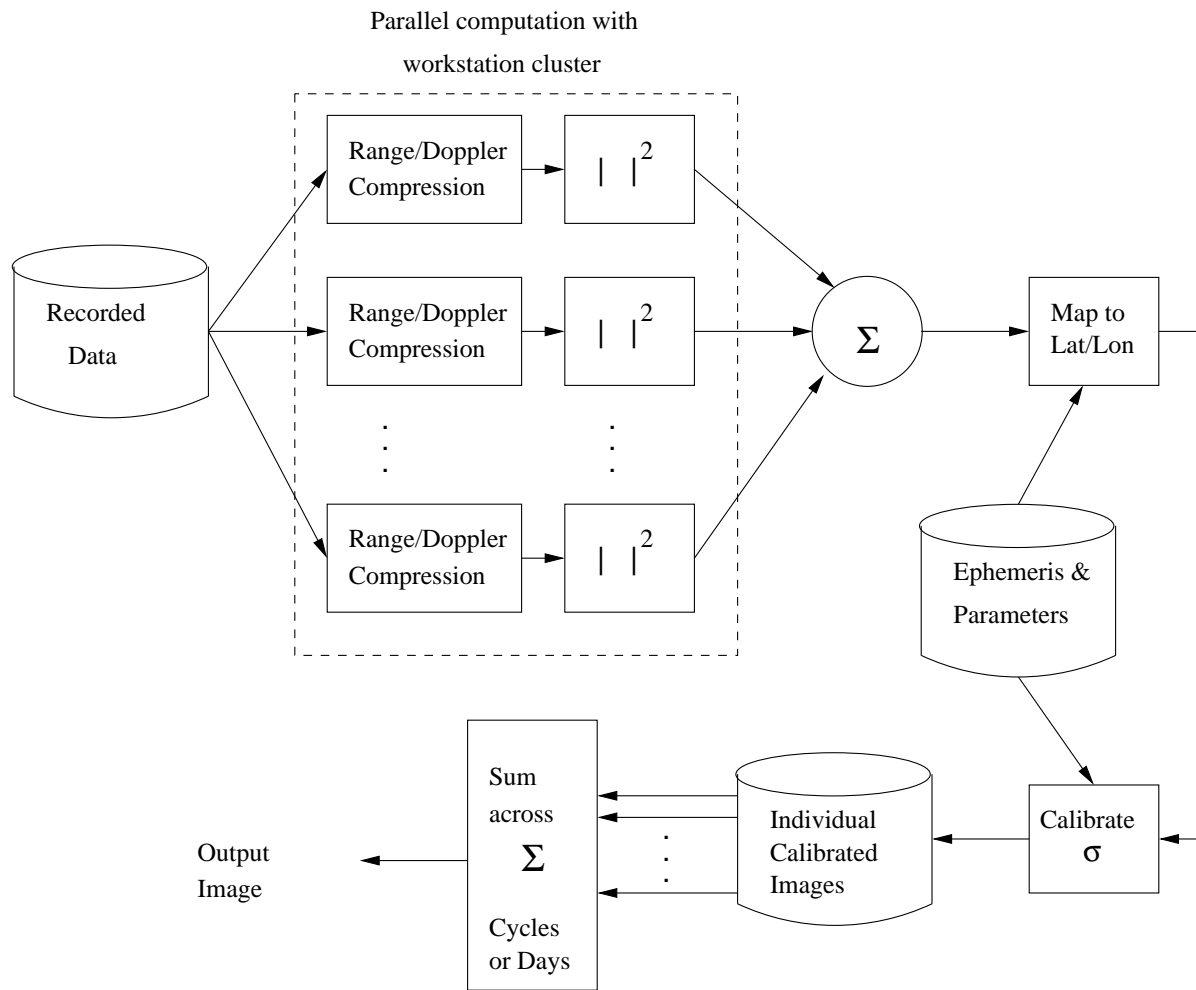
Figure 5.3 Parallel delay-Doppler processor for Mercury experiment.

downsampling—effectively a length-two boxcar filter—was applied in the digital processing software to complete the baud matched filtering process.

At completion of the processing of one receive cycle, the final delay-Doppler array represents 624 delay (25 msec) by 1024 frequency (390 Hz) resolution elements of data. Mercury's echo begins approximately 50 delay resolution elements from the start of the array, and is centered at zero frequency.

Data from each transmit/receive cycle were calibrated according to the procedure in Harmon (2002). The total noise plus clutter power was estimated by taking the average value of ≈ 125 delay resolution elements outside the delay extent of the planet's echo. This mean noise plus clutter power was subtracted from each pixel in the array. A template of the delay-Doppler profile of the planet was then used to mask all pixels on the planet. These identified on-planet pixels were integrated to form a total cross section estimate in uncalibrated units of power. In each delay bin i, the total planet clutter from other bins $j \neq i$ is spread over the entire Doppler spectrum by the PN code, so the clutter in each bin is estimated as the sum of the on-planet power divided by KN. This clutter power estimate, again in uncalibrated units, was subtracted from the mean noise plus clutter to obtain the noise-only power. This value was equated to the expected noise power $kT_{sys}f_s/KN$ to transform the arbitrary units to watts. The system temperature T_{sys} was recorded during each round-trip cycle, and provides the baseline value for calibration of the data. The radar equation was then solved for total planet normalized cross section $\bar{\sigma}$ using the calibrated P_r in watts.

Sixty-four independent round-trip cycles were collected and calibrated according to the above procedure (Tables 5.3–5.4). For each cycle, the normalized total planet cross section was computed for both the OC and SC polarizations. This was accomplished by summing the echo power from every delay-Doppler cell containing echo power from the planet to find an estimate of the total echo power received. Our disk-integrated results of $\bar{\sigma}_{OC} = 0.062 \pm 0.009$ and $\bar{\sigma}_{SC} = 0.012 \pm 0.002$ agree with previous 3.5 cm total cross section measurements at (274W, 6N) by Clark et al. (1986) and 3.8 cm cross section estimates averaging 6% at numerous sub-Earth longitudes by Evans (1969) and Ingalls and Rainville (1972).

Table 5.3 Mercury north pole observations. These 21 observations are combined incoherently to form the composite image of Figure 5.4.

Date 2001	Time UTC	Lon. deg. W	Lat. deg. N	P_t kW	T_{sys} K	Ant. Elev. deg.	$\bar{\sigma}_{OC}$	$\bar{\sigma}_{SC}$
Jun 13	20:55:58	82.6	7.3	428.7	16.9	71.3	0.043	0.008
Jun 13	21:14:26	82.6	7.3	431.6	16.6	68.7	0.038	0.007
Jun 13	21:32:52	82.7	7.3	428.5	16.7	65.6	0.035	0.006
Jun 13	22:09:47	82.9	7.3	434.9	17.0	58.9	0.028	0.005
Jun 29	20:32:15	186.4	8.2	427.2	16.9	54.1	0.068	0.014
Jun 29	21:03:13	186.5	8.2	427.2	16.9	54.1	0.068	0.013
Jun 29	21:47:48	186.7	8.2	423.6	17.1	45.3	0.065	0.012
Jun 29	22:10:00	186.8	8.2	432.8	17.0	40.9	0.061	0.012
Jun 29	22:32:11	186.9	8.2	433.5	17.5	36.4	0.062	0.012
Jun 29	22:54:24	187.0	8.2	432.1	18.2	31.8	0.059	0.011
Jun 29	23:16:36	187.1	8.2	431.4	18.9	27.3	0.052	0.009
Jul 01	14:03:07	196.7	8.1	429.2	21.1	28.8	0.082	0.014
Jul 01	15:08:48	196.9	8.1	426.5	19.2	42.2	0.073	0.013
Jul 01	15:31:56	197.0	8.1	432.6	18.5	46.8	0.066	0.012
Jul 01	15:55:04	197.1	8.1	432.3	17.7	51.4	0.061	0.011
Jul 01	16:18:12	197.2	8.1	429.5	17.4	55.9	0.058	0.010
Jul 01	16:41:20	197.3	8.1	427.1	16.7	60.2	0.055	0.011
Jul 01	17:04:29	197.4	8.0	432.3	16.4	64.3	0.054	0.010
Jul 01	17:27:37	197.5	8.0	431.5	14.7	68.0	0.050	0.010
Jul 01	17:50:45	197.6	8.0	430.4	14.7	70.9	0.049	0.011
Jul 01	18:13:56	197.7	8.0	426.8	14.9	72.9	0.051	0.010

Table 5.4 Mercury south pole observations. These 43 observations are combined incoherently to form the composite image of Figure 5.5.

Date 2001	Time UTC	Lon. deg. W	Lat. deg. N	P_t kW	T_{sys} K	Ant. Elev. deg.	$\bar{\sigma}_{OC}$	$\bar{\sigma}_{SC}$
Feb 09	16:56:48	158.8	-10.2	455.7	19.6	24.1	0.060	0.013
Feb 09	17:19:31	158.9	-10.2	455.4	19.4	27.9	0.067	0.014
Feb 09	17:42:15	159.0	-10.2	452.6	18.6	31.5	0.067	0.014
Feb 09	18:04:40	159.1	-10.2	451.1	18.7	34.8	0.069	0.013
Feb 09	18:32:49	159.2	-10.2	453.1	18.0	38.4	0.066	0.013
Feb 09	19:15:10	159.4	-10.2	448.7	17.3	42.7	0.064	0.014
Feb 09	19:37:44	159.6	-10.2	452.1	17.0	44.2	0.064	0.013
Feb 09	20:00:20	159.7	-10.2	454.2	16.6	45.1	0.062	0.013
Feb 09	20:22:56	159.8	-10.2	452.1	16.6	45.5	0.062	0.013
Feb 09	20:49:56	159.9	-10.2	456.2	16.7	45.0	0.059	0.013
Feb 09	21:12:30	160.0	-10.2	452.1	16.8	43.9	0.060	0.013
Feb 09	21:35:06	160.1	-10.2	449.7	16.6	42.3	0.061	0.013
Feb 09	21:57:42	160.3	-10.2	450.3	16.6	40.1	0.061	0.013
Feb 10	16:49:05	165.9	-10.4	452.5	23.0	23.9	0.059	0.012
Feb 10	17:11:15	166.0	-10.4	455.2	25.4	27.7	0.068	0.014
Feb 10	17:33:25	166.1	-10.4	451.8	20.6	31.2	0.062	0.013
Feb 10	17:55:35	166.2	-10.4	451.0	25.3	34.4	0.073	0.014
Feb 10	18:20:58	166.3	-10.4	442.2	27.9	37.8	0.072	0.014
Feb 10	18:43:09	166.4	-10.4	440.2	34.9	40.3	0.058	0.012
Feb 10	19:09:06	166.6	-10.4	446.6	42.7	42.6	0.053	0.011
Feb 10	19:31:16	166.7	-10.4	446.9	41.6	44.1	0.059	0.012
Feb 10	20:18:21	166.9	-10.4	441.9	28.8	45.3	0.061	0.012
Feb 10	20:40:35	167.0	-10.4	438.9	23.4	44.9	0.060	0.012
Feb 10	21:30:24	167.3	-10.4	446.4	18.6	41.8	0.063	0.013
Feb 10	21:52:35	167.4	-10.4	447.6	18.7	39.6	0.064	0.013
Feb 10	22:14:45	167.5	-10.4	449.2	18.9	37.0	0.062	0.012

Date 2001	Time UTC	Lon. deg. W	Lat. deg. N	P_t kW	T_{sys} K	Ant. Elev. deg.	$\bar{\sigma}_{OC}$	$\bar{\sigma}_{SC}$
Feb 17	16:56:06	216.7	-10.5	439.8	21.3	32.1	0.075	0.014
Feb 17	17:17:49	216.8	-10.5	433.1	19.9	34.9	0.070	0.014
Feb 17	17:39:34	216.9	-10.5	437.0	19.1	37.4	0.068	0.015
Feb 17	18:17:08	217.1	-10.5	445.8	19.0	40.7	0.064	0.013
Feb 17	18:38:51	217.2	-10.5	442.5	17.6	41.9	0.063	0.013
Feb 17	19:00:31	217.3	-10.5	443.2	18.4	42.7	0.066	0.013
Feb 17	19:22:14	217.4	-10.5	445.3	19.6	42.8	0.070	0.013
Feb 17	19:43:55	217.5	-10.5	444.9	19.5	42.4	0.069	0.013
Feb 20	15:42:06	237.1	-10.1	457.5	22.0	23.1	0.071	0.014
Feb 20	16:26:51	237.4	-10.1	453.0	20.6	29.9	0.073	0.015
Feb 20	16:49:18	237.5	-10.1	452.4	19.3	32.9	0.071	0.015
Feb 20	17:19:07	237.6	-10.1	451.5	15.8	36.4	0.057	0.015
Feb 20	17:41:29	237.7	-10.0	449.7	18.3	38.4	0.068	0.015
Feb 20	18:03:52	237.8	-10.0	450.2	17.8	40.1	0.067	0.015
Feb 20	18:26:16	237.9	-10.0	448.2	17.4	41.1	0.065	0.015
Feb 20	18:54:39	238.0	-10.0	451.8	17.1	41.7	0.064	0.014
Feb 20	19:17:01	238.1	-10.0	427.4	16.8	41.5	0.059	0.014

We mapped the reduced data to planetary coordinates in a polar orthographic grid using the transformations from planetary to delay-Doppler coordinates outlined in Section 2.1. This grid was 2001 by 2001 pixels in size and extended to 68 deg. latitude, with a resolution of 0.91 km at the pole. The projection was formed by looping over all pixels in the orthographic grid. For each pixel in the orthographic grid, we first calculated its planetary coordinates, and then projected this value to the corresponding delay-Doppler point (τ_P, f_P). We then bilinearly interpolated the value of this delay-Doppler point from the 624 by 1024 resolution element output array of the data processor. The gridded data were then averaged over all superposed round-trip observations.

A total of 21 cycles were averaged to form the north-polar map shown in Figure 5.4, while 43 cycles were averaged to form the south-polar map of Figure 5.5. These 6 km resolution maps are the finest resolution 3.5 cm wavelength maps of the polar regions to date. Additionally, the south-polar map exceeds the resolution of existing 13 cm maps by a factor of 2. The five large northern polar craters noted in Harmon et al. (1994) are clearly visible in Figure 5.4. The large diameter impact crater Chao Meng-Fu is visible near the south pole in Figure 5.5, along with many brighter spots in smaller craters out to $75°$ S latitude.

5.4   Analysis

The high-resolution imaging data presented here exhibit enhanced backscatter and polarization inversion from the same large features reported by Harmon et al. (1994, 2001), who associated these features with the floors of craters. Figure 5.6 depicts the polar illumination geometry, showing how ice-like deposits might be shielded from direct sunlight for very long periods of time. Craters on Mercury have depth-to-diameter ratios of 1:5 for craters less than 10 km in diameter, decreasing to 1:25 for craters greater than 100 km in diameter (Pike, 1988). Though the exact obliquity of Mercury is unknown, it is nearly zero; previous radar measurements have shown it to be $0.5 \pm 0.4°$ (De Vries and Harmon, 1994;
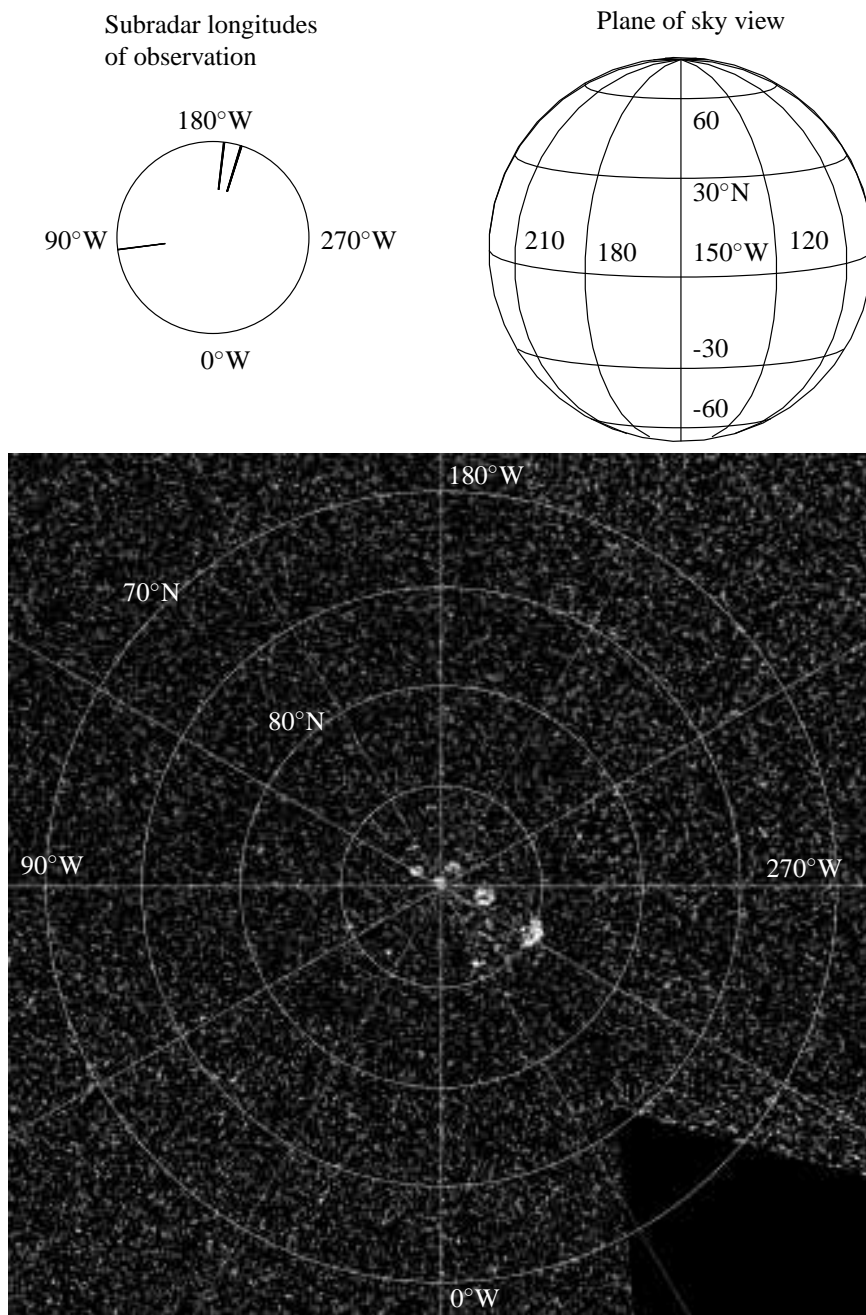
Figure 5.4 Mercury's north polar SC image. Latitude grid lines are separated by 5°. Lighter areas correspond to higher albedos. The five large, bright objects within ≈ 5° of the pole are the craters identified by Harmon et al. (1994). The 21 data sets listed in Table 5.3 were combined incoherently to generate this image. The image comprises data taken from three sub-Earth longitudes as shown in the key diagram in the upper left.
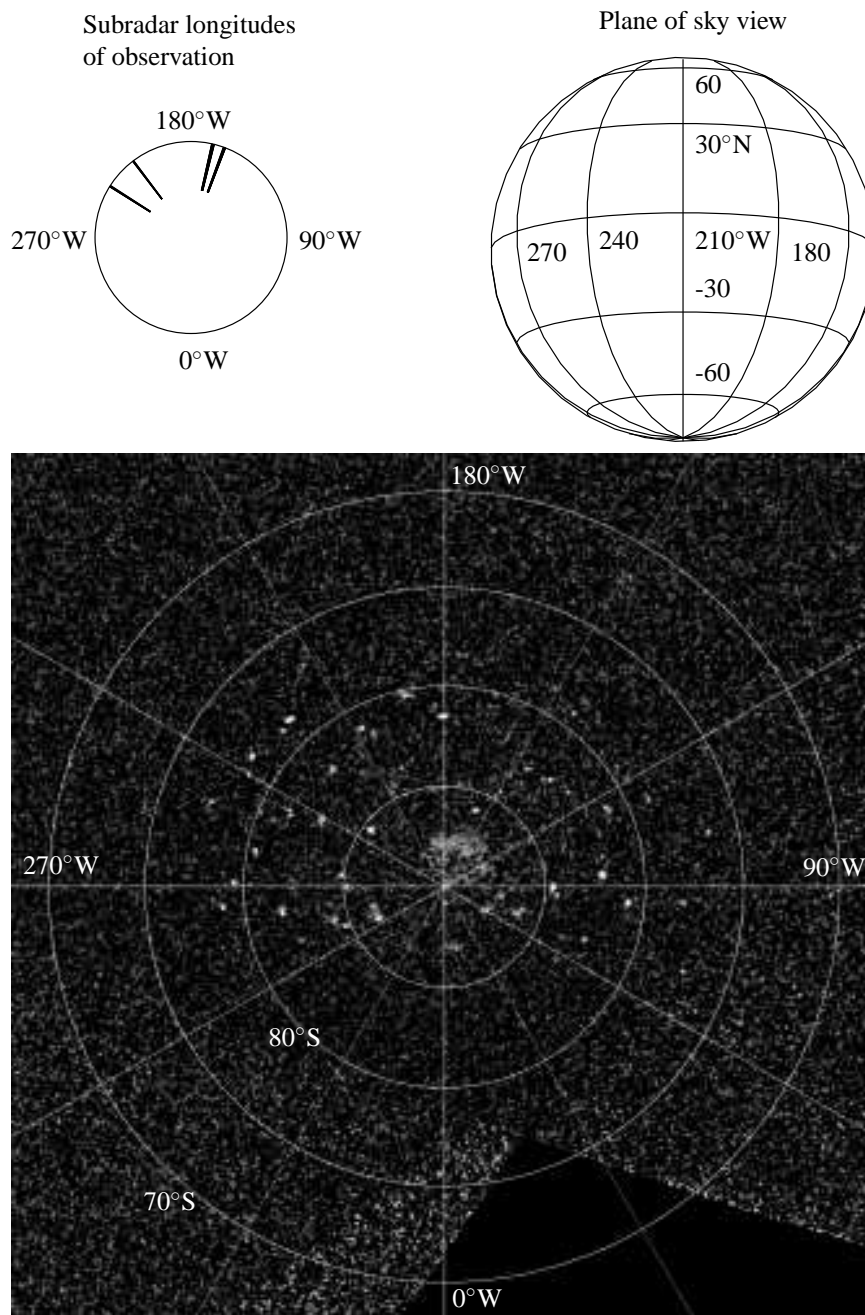
Figure 5.5 Mercury's south polar SC image. Latitude grid lines are separated by 5°. Lighter areas correspond to higher albedos. The diffuse patch centered on 88.5S, 148.6W is associated with the Chao Meng-Fu crater identified in previous 13 cm maps by Harmon et al. (1994). The 43 data sets listed in Table 5.4 were combined incoherently to generate this image. The image comprises data taken from several sub-Earth longitudes as shown in the key diagram in the upper left.
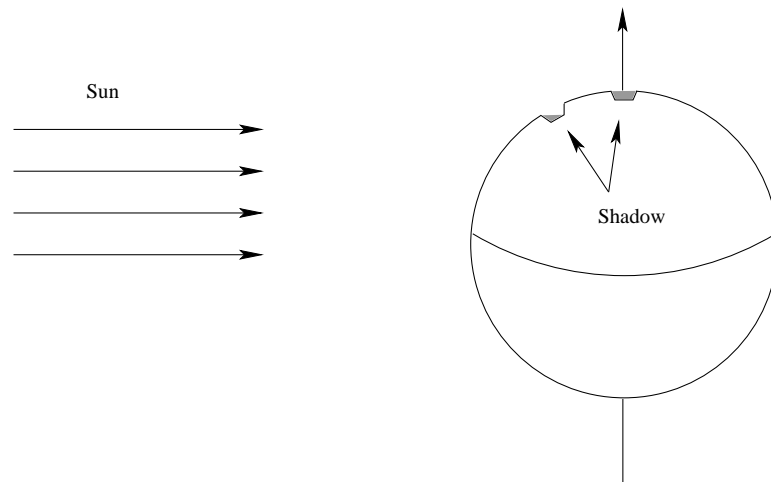
Figure 5.6 Crater illumination geometry. Since Mercury's obliquity is near zero, Mercury has no seasons. Craters exactly at the pole, and with sufficiently high floor-to-rim height to avoid penumbral effects, will have their entire floors in permanent shadow; similar craters at lower latitudes will have only the equator-ward portions of their floors in permanent shadow (Vasavada et al., 1999).

Seidelmann et al., 2002).[2] Permanently shadowed crater floors can exist near the pole if crater rim-to-floor height, wall slope, and penumbral effects permit such shadowing. At somewhat lower latitudes, only the equatorward wall of the crater floor will be in shadow all the time. As noted by Harmon et al. (2001), the floor of the large crater K (85N, 297W) has radar bright material primarily along the arc of its southern rim, as is clear in the detailed view of Figure 5.7. Other craters located at more southerly latitudes also exhibit this behavior—for example, the crater Despréz (80.9N 104.1W), which can be seen in the atlas in Appendix B. The bright radar features, in fact, overlay shadows in existing optical images of Mercury (see Figure 5.9).

Table 5.5 provides a comparison of the polarization ratio of the five major north-polar craters with values from Harmon et al. (2001). High polarization ratio is observed for all five northern craters. Comparison of our 3.5 cm results with Arecibo 13 cm results from the south pole (Table 5.6) shows similar polarization inversion. Feature X has been

---

[2]Recent observations by Margot et al. (2003) demonstrate the potential for Earth-based radar speckle displacement (RSD) interferometry to refine the pole location by two orders of magnitude over current understanding, when the viewing geometry is favorable. All sets of RSD observations required for precise pole placement have not been obtained at this time.
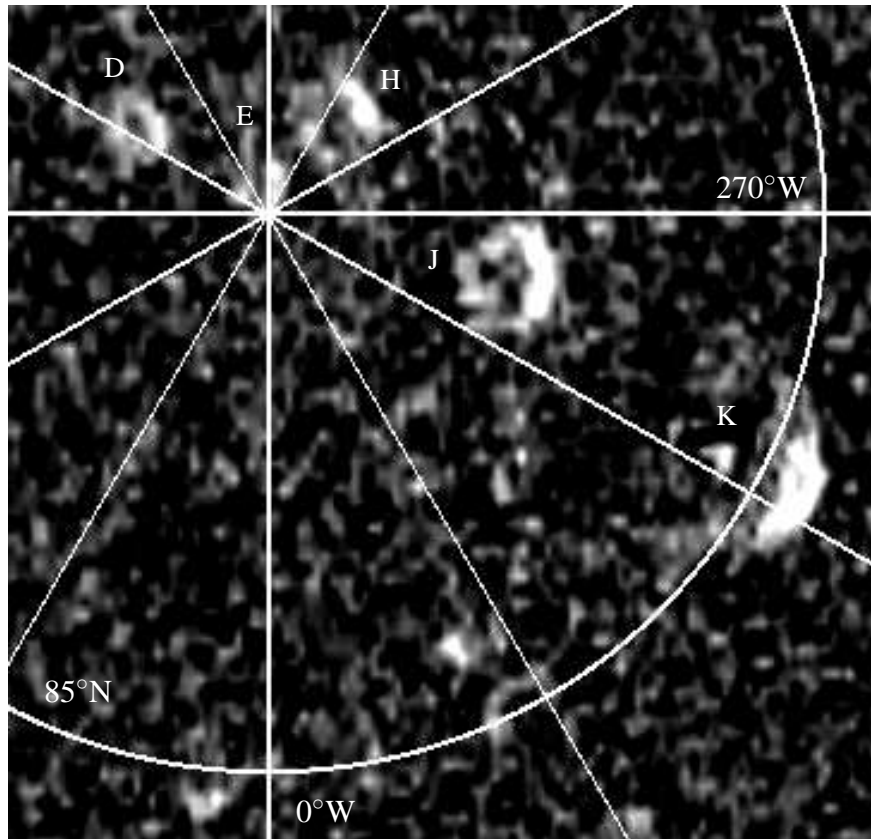
Figure 5.7 Detailed view of northern craters. Significant features are denoted D, E, H, J, and K, following Harmon et al. (1994). Imaging geometry is shown in Figure 5.4.

Feature	Harmon et al. (2001) 13 cm	This Work 3.5 cm	Resolution elements 3.5 cm
D	1.31 $\pm$ 0.07	1.06 $\pm$ 0.02	18
E	1.21 $\pm$ 0.06	1.03 $\pm$ 0.03	10
H	1.19 $\pm$ 0.06	0.95 $\pm$ 0.02	24
J	1.23 $\pm$ 0.06	1.25 $\pm$ 0.02	50
K	1.28 $\pm$ 0.06	1.32 $\pm$ 0.02	75

Table 5.5 13 and 3.5 cm polarization ratios $\mu_c = \sigma_{SC}/\sigma_{OC}$ of major northern features. Cross sections are given in Table 5.8. Error in 13 cm polarization ratios is as quoted in Harmon et al. (2001). Error in 3.5 cm polarization ratios is computed numerically as the ratio of two Gaussian distributions, one for σ_{OC} and one for σ_{SC}. To compute the distribution for the OC and SC cross sections, the standard deviation of a single resolution element is multiplied by the square root of the number of resolution elements in a feature.

Feature	Harmon et al. (1994) 13 cm	This Work 3.5 cm	Resolution elements 3.5 cm
V	1.43±1.16	1.20 ± 0.03	660
X	1.12±0.09	1.17 ± 0.01	46

Table 5.6 13 and 3.5 cm polarization ratios $\mu_c = \sigma_{SC}/\sigma_{OC}$ of major southern features. Error in 13 cm polarization ratios is as stated in Harmon et al. (1994). Error in 3.5 cm polarization ratios is determined as described in Table 5.5.

identified previously as corresponding to Chao Meng-Fu, a newer, c_4-class crater[3] (Harmon and Slade, 1992; Harmon et al., 1994).

Not all features identified in the north polar high-SNR Arecibo images of Harmon et al. (2001) appear in our 3.5 cm Goldstone images. As the Goldstone data are of lower SNR, it is not possible to identify the "diffuse patch" of radar bright material surrounding the major impact craters identified in recent 13 cm Arecibo images (Harmon et al., 2001). We do not believe this is a wavelength effect, as Harmon et al. (1994) did not observe this patch of material with the pre-upgrade Arecibo system at 13 cm wavelength and 15 km resolution.

Our 3.5 cm observations have revealed 35 new south pole features, previously unlabeled by Harmon et al. (1994). These features are listed in Table 5.7 and correspond primarily with c_3 craters. U.S.G.S. named craters associated with new features include: Belinskij (s5), Scopas (s28), Li Ch'ing Chao (s34), and a secondary crater in Bernini (s30). In a band along the 90–270°W meridian and bounded by lines tangent to the 85°S parallel, Harmon et al. (1994) identify 7 significant features, four of which have letter designations. We find over 20 significant features in this same region. Also, outside this band along the 180°W longitude line, we find an additional 10 bright features. There is a difference in the radar illumination geometry for the south pole between the Arecibo 1991–1992 data and the 2001 Goldstone data set. The illumination in the Arecibo images was generally from

---

[3]Mercury's craters were classified c_5–c_1, newest–oldest, by N.J. Trask and reported in McCauley et al. (1981) and the U.S.G.S. geologic maps of the polar regions by Grolier and Boyce (1984) and Strom et al. (1990). The classification scheme is: "Class 5—Craters characterized by sharp rims, crisp interior forms (for large craters), rays, and very few superposed craters. Class 4—Distinct but visibly modified rims and interior features; well-preserved radial faces around larger craters. Class 3—Relatively low, semi-rounded but continuous rims and subdued interior landforms. Class 2—Low rims and shallow interior relief. Interior forms scarce; secondary crater fields absent. Class 1—Low, partial rims. Some craters barely distinguishable from surrounding plains materials; interior features rare. Secondary crater fields absent."
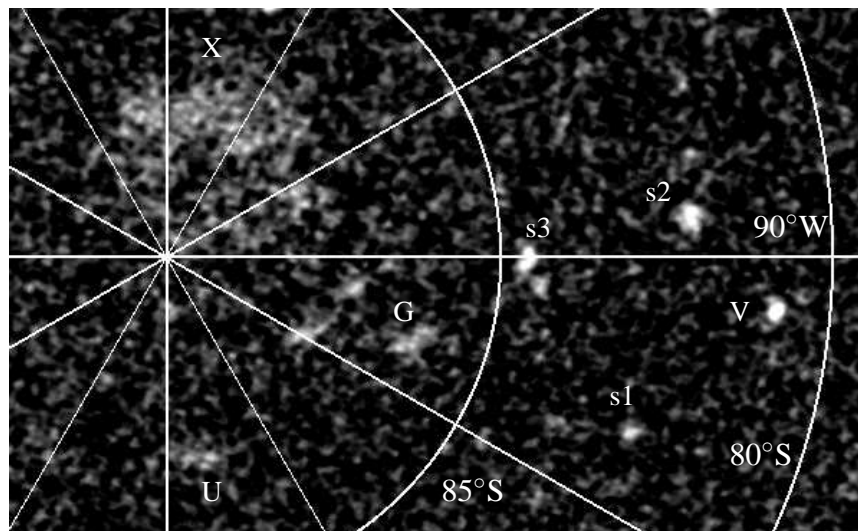
Figure 5.8 Detail view of southern craters. Significant features are denoted G, U, V, and X, following Harmon et al. (1994). Feature X corresponds to the impact crater Chao Meng-Fu. Imaging geometry is shown in Figure 5.5. Several other features denoted s1, s2, and s3, are apparent in the figure, but these lack either U.S.G.S. or Harmon et al. (1994) nomenclature. We provide a listing of these new, previously unlabeled features in Table 5.7.

near the plane of the central meridian, or the bottom of the image. In the Goldstone images the illumination is primarily from the 180 degrees west longitude, or the top of the image (Figure 5.5). In the Goldstone data, the preponderance of small, bright craters exhibiting polarization inversion is seen in the upper half of the image. This could be caused by the illumination geometry of the 3.5 cm experiment, which favors crater floors in the upper half of the image. Harmon et al. (1994) do not show bright features in the lower half of their south polar image, however, even though the Arecibo geometry favored this region.

The image of the south polar region, Figure 5.5, and the listing of associated features, Table 5.7, poses one issue for the ice hypothesis. Fourteen small, bright deposits appear in craters at latitudes north of the $80°$S parallel where thermal modeling indicates that trapped volatiles are unlikely (Paige et al., 1992; Vasavada et al., 1999) unless blanketed by a layer of thermally insulating dust. As discussed in Section 5.5, the blanket hypothesis can be consistent with our observations.

Table 5.7 Table of newly observed south polar features. Longitudes and latitudes are coordinates of the center of the radar-bright feature, and do not necessarily correspond to the center of an associated crater.

Feature Name	Lon. deg.	Lat. deg.	μ_c	σ_{SC} km^2	Resolution elements
s1	69W	82.5S	3.53	10.6	10
s2	94W	82.1S	1.35	24.3	15
s3	90W	84.6S	2.19	19.5	13
s4	115W	81.1S	1.03	17.5	16
s5	102W	76.5S	1.14	7.3	4
s6	295W	86.4S	1.70	18.7	10
s7	292W	84.8S	1.20	13.0	12
s8	285W	86.4S	1.36	11.6	9
s9	287W	84.4S	1.70	16.7	14
s10	279W	81.8S	1.08	19.1	14
s11	270W	85.1S	2.77	8.3	8
s12	263W	84.9S	1.04	12.7	7
s13	275W	78.9S	1.67	11.1	7
s14	269W	79.5S	4.14	9.9	6
s15	259W	80.4S	1.25	11.7	8
s16	233W	85.4S	1.18	23.3	17
s17	242W	83.1S	1.47	19.8	16
s18	244W	81.5S	0.72	13.5	13
s19	224W	82.0S	1.34	18.6	19
s20	250W	77.6S	0.96	7.9	6
s21	240W	78.8S	1.70	6.9	6
s22	236W	78.5S	1.59	17.2	9
s23	226W	78.9S	1.43	9.2	7
s24	223W	78.7S	1.57	26.5	16
s25	205W	81.6S	1.56	11.7	12

Feature Name	Lon. deg.	Lat. deg.	μ_c	σ_{SC} km^2	Resolution elements
s26	208W	81.1S	1.07	14.0	11
s27	191W	80.3S	1.19	22.5	20
s28	180W	81.5S	1.16	23.4	13
s29	158W	85.9S	1.61	15.7	8
s30	143W	79.2S	1.40	7.6	6
s31	151W	78.7S	1.34	5.4	5
s32	95W	77.3S	1.21	4.1	4
s33	86W	78.1S	2.76	9.4	7
s34	70W	77.4S	1.48	7.2	7
s35	113W	78.9S	1.50	8.8	7

In Figure 5.9, we co-registered the radar images with visible-light images from the Mariner 10 mission. These optical images have been gridded to a new cartographic control network and adjusted for gain variations between still-camera frames (Robinson et al., 1999). It can be seen that for off-pole craters, the areas of enhanced radar backscatter are confined to the equator-ward, shadowed regions of the crater floors, which is consistent with the accumulation of ice in areas that are in perpetual shadow. This has been remarked upon previously by Harmon et al. (1994, 2001). Vasavada et al. (1999) predicted that potential cold traps must be at these precise locations for long term stability of ice deposits in off-pole craters.

Scattering effects other than ice deposits have been advanced (Stacy et al., 1997) to explain enhanced backscatter and polarization inversion from craters at the lunar poles, and an argument could be made that such effects explain the reflections seen at the poles of Mercury. Thus, it is important to note that our location of the radar bright material discounts a glinting phenomenon observed for lunar polar craters by Stacy et al. (1997), who attributed enhanced backscatter and polarization inversion to geometrical effects, basically double-bounces, from crater walls farthest from the radar line of sight. Our observations show that the enhanced reflections occur from equator-ward regions of craters, even when the equator-ward wall is the near wall for the radar viewing geometry.
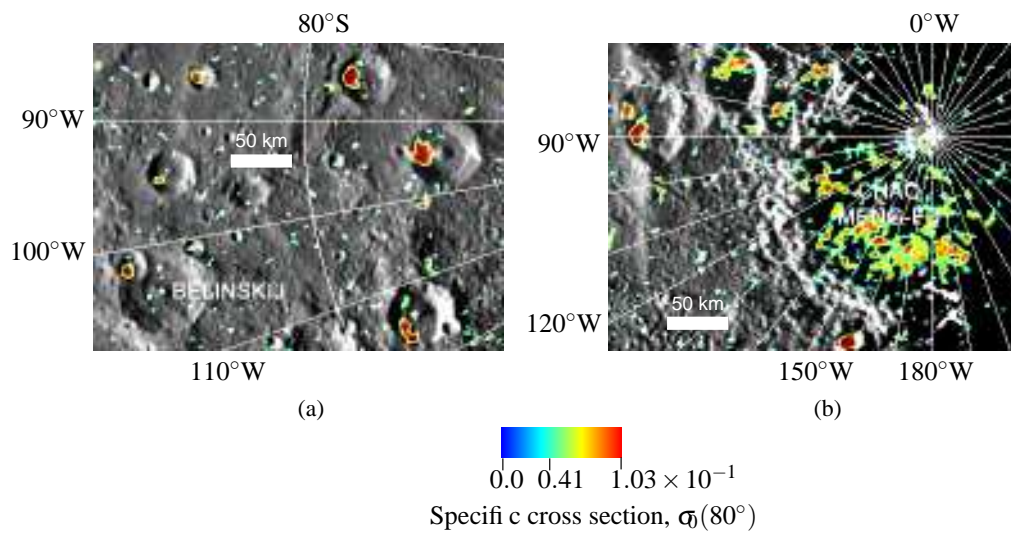
Figure 5.9 Co-registration of the 3.5 cm radar images with optical imagery from Robinson et al. (1999). Resolution is approximately 0.8 km for the grayscale optical data and 6 km for the colored radar data. Scenes are from the south polar region (a) near the 70 km impact basin Belinskij and (b) the 155 km impact crater Chao Meng-Fu. Full stereographic projections of both northern and southern polar regions out to 70° latitude are displayed in Appendix B. The specific cross section σ_0 is computed as the RCS per radar resolution element (6 km by 4.8 km), projected at an average angle of incidence of $\approx 80°$ for the south polar observations, or $\sigma_0(80°) = \sigma/(6 \cdot 4.8/\sin 80°)$.

5.5   Applying the dust layer model

Delivery mechanisms for polar ice at Mercury favor episodic bombardment, rather than gradual accumulation (see the discussion in Vasavada et al. 1999). Morgan and Shemansky (1991) argue that micrometeoroid impact vaporization and interstellar hydrogen Lyman alpha radiation could erode gradually accumulating deposits as quickly as they settle into cold traps. The existence and detectability of the radar-bright polar deposits favor episodic delivery over gradual accumulation, and indicate that ice should exist in the form of relatively large, pure volumes, similar to the ice on the surface of the Galilean satellites. If the episodically deposited ice were covered by episodically deposited blankets of dust, the ice could be protected from further sublimation and erosion while still behaving like an anomalous radar scatterer. The blanket could not be too thick, however; otherwise attenuation of the radar signal below the threshold of detectability would result.

The fundamental input to the regolith blanket model described by (4.25) is the total radar cross section of a crater measured at two frequencies. We perform the analysis for SC cross sections only, since the SC component of the echo must undergo multiple scattering, while the OC component may contain single-bounce returns from favorably-oriented facets. Since 13 cm absolute cross section measurements have been published only for five north polar craters (Harmon et al., 2001), we restrict our modeling to these largest north polar craters. Table 5.8 lists the measured depolarized cross sections at the two wavelengths. The unweighted, average cross section ratio is

$$\frac{\sigma_{13}}{\sigma_{3.5}} = 1.64 \pm 0.25. \tag{5.1}$$

The observed RCS ratio is several standard deviations greater than the expected value of 1 if the scattering were wavelength independent and there were no geometrical effects, i.e. if the scattering law exponent $n = 0$ in (4.25). The departure from 1 can be attributed to either geometrical scattering effects through the $cos^n(\theta_{i,\lambda})$ scattering law, or to wavelength-dependent effects through the $e^{-4\alpha_\lambda d}$ extinction law, or a combination of these two effects. The 3.5 cm and 13 cm observations were obtained at sub-Earth latitudes averaging 7 and 11 degrees, respectively, or equivalently, average polar incidence angles of 81 and 78 degrees.

| Feature | Harmon et al. (2001) | | This Work | | Ratio |
	σ_{13}	$\theta_{i,13}$	$\sigma_{3.5}$	$\theta_{i,3.5}$	$\sigma_{13}/\sigma_{3.5}$
D	57±11.4 km^2	78.0°	31.4±4.7 km^2	81.1°	1.82±0.28
E	35±7.0	78.5	23.0±3.5	81.4	1.52±0.23
H	63±12.6	77.8	36.3±5.4	80.7	1.74±0.27
J	152±30.4	79.3	87.1±13.1	81.8	1.75±0.27
K	188±37.6	81.1	134±20.1	83.1	1.40±0.21
Avg.					1.64±0.25

Table 5.8 Comparison of 13 and 3.5 cm depolarized cross sections σ_{SC} of major northern craters. Angles of incidence $\theta_{i,13}$ for single-date 13 cm observations, and average angles of incidence $\theta_{i,3.5}$ for multi-date 3.5 cm observations are listed. The differences in i) solar system geometry and ii) characteristics of the two different radiotelescopes introduce systematic errors which are not represented in the standard deviation of the measurement quoted with each value. Error for 13 cm cross sections is as reported in Harmon et al. (2001). Error for 3.5 cm cross sections is estimated as the standard deviation of a sum of independent Gaussian distributions with a second moment equal to the variance of an individual resolution element. The number of Gaussian distributions summed is set equal to the number of independent resolution elements making up one deposit. Error in cross-section ratio is derived from computing—via Monte Carlo method—the standard deviation of the ratio of two Gaussian distributions with first and second moments equal to those of the 13 cm and 3.5 cm cross sections. The reported average in the bottom line of the table is an unweighted mean.
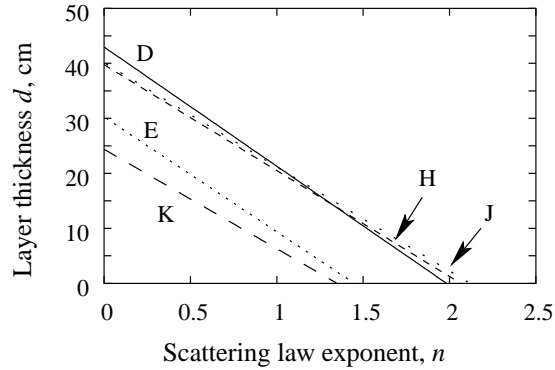
Figure 5.10 Regolith thickness d vs. scattering law index. For each north polar crater D, E, H, J, and K, we let n in the specific RCS scattering law vary from 0 to 2.5, and estimate the layer thickness supported by the residual attenuation not predicted by the scattering law. For a choice of $n > 2$, a non-physical solution of $d < 0$ results. The error bound on the estimate of d ranges from 15 cm at $n = 0$ to 11 cm at $n = 1.5$ (see text).

An additional important input to the model is the complex dielectric constant of Mercury's regolith, for which we take an average value of $\varepsilon'_r = 2.7$ with a loss tangent $\tan\delta_c = 0.0026 \pm 25\%$, on the basis of passive microwave radiometry as reported in Mitchell and de Pater (1994), and with relative permeability $\mu_r = 1$. Using these values, and at a grazing incidence angles from Table 5.8, the average dust layer thickness is calculated via (4.25).

Figure 5.10 shows the estimated layer thickness as a function of assumed scattering law exponent n. If the scattering law exponent is $n = 0$, then the scattering is independent of angle-of-incidence, and a layer of $\approx 35 \pm 15$ cm is implied by the observations. If the RCS σ_λ follows a $\cos(\theta_{i,\lambda})$ rule from projected area effects only, then $n = 1$, and the estimated layer thickness is $\approx 15 \pm 13$ cm. For $n = 1.5$ as reported for the Galilean satellites by Ostro et al. (1992), the estimated layer thickness is $\approx 0 \pm 11$ cm. Thus, inferences of the layer thickness depend critically on the form of the scattering function. Yet, reasonable bounds ranging from 0 to 35 cm result from several different values for the exponent. We discount values of $n > 2$, as these lead to a negative layer thickness estimate $d < 0$ which is non-physical.

Error sources are evaluated as follows according to the expressions derived in Section 4.3.3. Assuming that the inputs to the model (4.25) are independent, we can compute

the variance of the modeled layer thickness d, or σ_d^2 from

$$\sigma_d^2 = \left(\frac{\partial d}{\partial \xi}\right)^2 \sigma_\xi^2 + \left(\frac{\partial d}{\partial \gamma}\right)^2 \sigma_\gamma^2 + \left(\frac{\partial d}{\partial \varepsilon_r'}\right)^2 \sigma_{\varepsilon_r'}^2, \tag{5.2}$$

and the standard deviation as $\sigma_d = \sqrt{\sigma_d^2}$. In the following, we assume that the scattering law exponent $n = 0$ forms the upper bound on the layer estimate, and revisit the case $n \neq 0$ at the end of the section.

Sensitivity to absolute cross section. In (5.1), we measure $\xi = \sigma_{13}/\sigma_{3.5}$ with an error of 15%, yielding

$$\left(\frac{\partial d}{\partial \xi}\right) \sigma_\xi = \left(\frac{\partial d}{\partial \xi}\right) 0.15\xi = \pm 11 \text{ cm}. \tag{5.3}$$

Sensitivity to loss tangent. The loss tangent $\gamma = \tan \delta_c$ has an error of 25% (Mitchell and de Pater, 1994), yielding

$$\left(\frac{\partial d}{\partial \gamma}\right) \sigma_\gamma = \left(\frac{\partial d}{\partial \gamma}\right) 0.25\gamma = \pm 9.0 \text{ cm}. \tag{5.4}$$

Sensitivity to dielectric constant. Finally, ε_r' has an error of 20% based upon differences between the radar and passive thermal emission estimates of this quantity (Mitchell and de Pater, 1994), giving

$$\left(\frac{\partial d}{\partial \varepsilon_r'}\right) \sigma_{\varepsilon_r'} = \left(\frac{\partial d}{\partial \varepsilon_r'}\right) 0.20\varepsilon_r' = \pm 5.1 \text{ cm}. \tag{5.5}$$

It follows from the above that the total cross section and loss tangent are the largest potential error inputs to the model. The total error is given by substitution of these individual errors into (5.2), giving a standard deviation of $\sigma_d = 15$ cm.

Note that if the scattering law exponent is non-zero, then a significant fraction of the difference between the 13 and 3.5 cm cross sections can be explained by the geometrical term

$$\frac{\cos(\theta_{i,3.5})}{\cos(\theta_{i,13})}. \tag{5.6}$$

in (4.25). From viewing the abscissa of Figure 5.10, a value of n ranging from 1.5 to 2.0,

depending on the particular crater deposit, can fit all of the observed difference in cross section, yielding a thickness estimate of $d = 0$. For $n = 1.5$, substituting into (5.2–5.5) yields an error standard deviation of $\sigma_d = 11$ cm.

5.6 Summary

We employ the high-resolution long-code imaging technique to study putative ice deposits in the polar regions of Mercury. North polar deposit cross-section measurements at 3.5 cm, when compared to the 13 cm measurements of Harmon et al. (2001), are inconclusive in supporting a proposed insulating blanket of regolith that allows deposits of ice or other cold-trapped volatiles to be preserved in the shadowed areas of lower latitude polar craters. Multiple interpretations of layer thickness, ranging from 0 ± 11 to 35 ± 15 cm are possible, depending on an assumed scattering law exponent n. Our observations of the south polar region are the highest resolution images to date. Co-registration of these images with optical data from Mariner 10 shows that the locations of the radar bright deposits are exactly where predicted by thermal modeling, and cannot be due to radar glints from geometrical effects as noted in Stacy et al. (1997), since the radar-bright areas do not necessarily lie along the crater far-wall normal to the radar line of sight. Other scattering mechanisms could possibly be responsible for the enhanced backscatter and polarization inversion seen from these deposits, however, the strong backscatter is associated only with the shadowed areas of crater floors, and an alternative model which favors shadowed areas over sunlit areas is not extant.

Chapter 6

Galilean Satellites of Jupiter

The four largest satellites of Jupiter have fascinated astronomers since the beginning of the telescopic age. They are named to honor their discoverer, Galileo Galilei, who first saw them on January 7, 1610. Telescopic observations early in the twentieth century revealed the relatively high optical albedos of the three outer Galilean satellites, as compared to terrestrial planetary bodies such as the Earth's moon or Mars. These observations also showed that the moons' sidereal rates of rotation were synchronous with their orbits. Tidal forces had dissipated the moons' rotational energy to the point that the same side always faced Jupiter, just as the same hemisphere of our moon always faces Earth.

The limited sensitivity of early radar instruments and the great distance to the Jovian system (4–6 AU) put the Galilean satellites out of range of Earth-based radar observations until the mid-1970's. The first reported radar detection of a Galilean satellite was by Goldstein and Morris (1975) with the Goldstone radar. Also in the 1974–75 time frame, a resurfacing of the Arecibo telescope allowed a change to 13 cm from 70 cm wavelength. This upgrade included the installation of a new 500 kW 13 cm transmitter. A subsequent favorable northerly declination of the Jovian system permitted Campbell et al. (1977) to follow with a very successful observing run. The upgraded Arecibo instrument provided five times higher signal-to-noise ratio than the Goldstone system. The Campbell et al. (1977) observations exhibited the phenomenon of polarization inversion, in which the SC echo is stronger than the OC echo, for all three outer moons. These are now known to be icy in composition (Stone and Lane, 1979).

One difficulty in observing the Galilean satellites with the Arecibo radar is that the Jovian system is not always at a sufficiently northerly declination to appear in the telescope's viewing window. The Arecibo antenna has a $\pm 20°$ zenith angle pointing constraint. For the $18°$N latitude of Puerto Rico, this translates into an observing window of $2°$S–$38°$N declination. Consequently the Jovian system is observable from Arecibo for only about half of the time during a cycle of approximately 11 years. For this reason, Campbell et al.'s observations were not repeated until the late 1980's, when Ostro et al. (1992) undertook a five-year campaign using both the Arecibo 13 cm system and the Goldstone 3.5 cm system. In addition to detailed observations of the total RCS at a large number of sub-Earth longitudes, these later observations yielded the first radar images of the three outer moons via the method of Hudson and Ostro (1990). The technique, which involves a least-squares fit of a spherical harmonic series representing the albedo, requires observations covering a large range in satellite sub-Earth latitude and longitude in order to provide unambiguous results. Unfortunately, when viewing the Galilean satellites, the geometry is such that the sub-Earth latitude is never greater than a few degrees. Using the Doppler spectra method, Ostro et al. (1992) produced low-resolution, full-disk images that were subject to the north-south ambiguity.[1]

As discussed in Chapter 2, aperture synthesis imaging does not suffer from the north-south ambiguity. During the late 1980's to early 1990's, Butler and Muhleman attempted to observe Ganymede and Callisto using the Goldstone/VLA bistatic radar system. Jovian opposition occurred during the summer months of those years. This effort did not yield useful results, however, as the imaging ability of the system was compromised by phase noise from water vapor in the summer atmosphere above the VLA.[2] Although the Goldstone/VLA system does not have the zenith articulation constraint of Arecibo, for good (u, v) plane coverage of the spectral sensitivity function it is best to observe with the VLA when the object of interest is at northern declinations. In addition, in order to achieve the greatest angular resolution possible, the array must be extended to its maximum size, known as the "A-configuration," with a 36 km maximum baseline between antennas. As the configuration of the array is switched among four baseline spacings on a quarterly basis,

---

[1]For a description of the north-south hemispherical ambiguity, see Section 2.2.1.

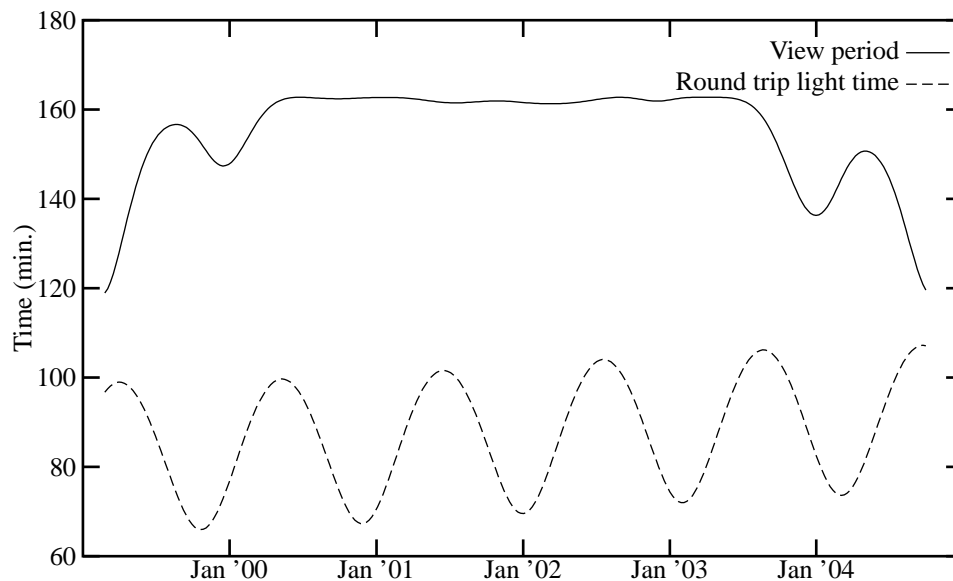[2]B. Butler, private communication, February 2001.

Figure 6.1 Arecibo viewing of Jupiter. A period providing several hours of viewing per day of the Jovian system occurs every eleven years. Radar studies of the Jovian system are usually performed during this period to permit observations at both 13 and 3.5 cm wavelengths. To minimize path loss, radar observations are conducted at minimum range, or minimum round-trip light time.

it is not always possible to have the array in the A-configuration during Jovian opposition. Use of the A-configuration results in approximately 350 km resolution at Jupiter's minimum range of $\approx$ 4 AU.

6.1   2000-2002 Goldstone/VLA Experiment

During the 1999–2003 period, the Jovian system again returned to northern declinations and had favorable viewing (Figure 6.1). Jovian opposition occurred in the northern latitude winter months of November through January. In addition, the VLA was in the A-configuration during these months. This fortuitous alignment of the cycles of the Jovian declination, range, Earth's northern hemisphere winter, and the VLA schedule prompted a second Goldstone/VLA bistatic radar observation campaign.

Noise contributed by Jupiter's radiation is always a concern when observing the Jovian system at radio wavelengths because Jupiter is a strong emitter of both synchrotron

and thermal radiation in the microwave band. Since the Galilean satellites are only a few hundred arcseconds from Jupiter when viewed from Earth, Jupiter always is either at the edge of a mainlobe or in a sidelobe of a radiotelescope when studying these objects. Large apertures, such as the Arecibo and Goldstone monostatic systems, have fairly narrow beamwidths—on the order of ≈ 120 arcsec at the 13 and 3.5 cm radar wavelengths. Jupiter does not usually appear in the main beam of these antennas when observing the three outer, icy Galilean satellites. On the other hand, although the VLA at 3.5 cm has a fairly tight synthesized beam of approximately 0.25–0.30 arcseconds, individual elements of the array have fairly wide beam patterns, on the order of 340 arcsec, or approximately the radius of Ganymede's orbit. Except at maximum separation, Jupiter appears either in sidelobes or the main lobe of the individual interferometer elements, decreasing the sensitivity of the array by pushing the desired signal into the quantization noise of the VLA's 3-bit A/D converter, and making arrayed observations in the narrowband spectral-line mode infeasible. Therefore, experiments must be timed for maximum elongation of the Galilean satellites as viewed from the Earth (Figure 6.2). Europa and Io are never sufficiently far from Jupiter to avoid significant noise from the planet, and we did not attempt to image these two moons.

We acquired data from both the leading and trailing hemispheres of Ganymede and the leading hemisphere of Callisto during the December 2000 opposition. We intended to image the trailing hemisphere of Callisto during the same period, but an error in the Goldstone transmitter Doppler tracking prevented successful data acquisition. We repeated the Callisto experiment during the January 2002 opposition. The VLA was not in the A-configuration until February 2002, by which time the range to Callisto was greater than during our year 2000 observations. Although the range was greater than desired, the signal-to-noise ratio was sufficient for imaging. Our successful observations are listed in Table 6.1. Callisto is easily visible in the power spectrum plot from February 2002 (Figure 6.3).
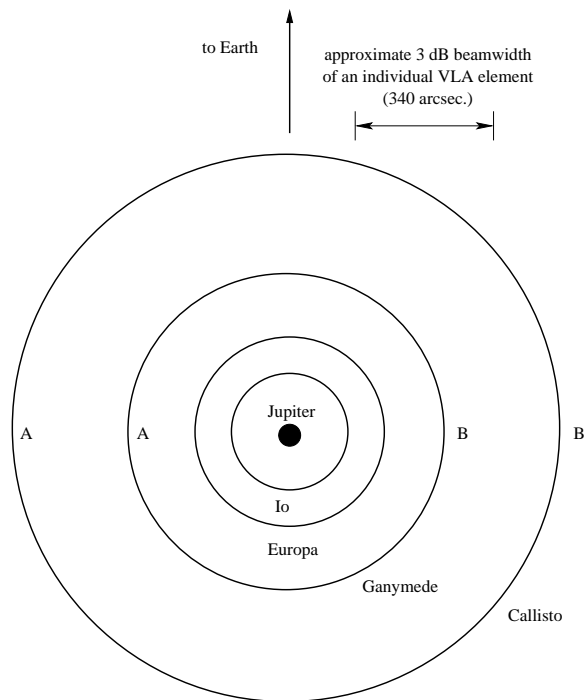
Figure 6.2 Galilean satellite orbits. Ground-based observations with the VLA were scheduled when the moons were at maximum westward or eastward elongation as denoted by points A and B in the diagram, respectively. This minimizes the noise contribution from Jupiter's blackbody radiation. The angular separations attained by Ganymede and Callisto on the dates of observation are listed in Table 6.1.

Parameter	Observation dates			
	2000 Dec. 1	2000 Dec. 5	2000 Dec. 3	2002 Feb. 4
Moon	Ganymede	Ganymede	Callisto	Callisto
Range, AU	4.05	4.06	4.06	4.38
Sub-Earth lat., deg.	3.1	3.1	2.9	1.7
Sub-Earth lon., deg. W.	81	282	77	277
Hemisphere	Leading	Trailing	Leading	Trailing
Angular sep., arcsec.	348	362	624	584
Carrier freq., MHz	8560	8560	8560	8560
TX power, kW	460	460	460	460
TX waveform	CW	CW	CW	CW
Target bandwidth, Hz	3000	3000	1200	1200
RX channel width, Hz	3052	3052	1526	1526
# Channels	64	64	128	128
Collected data, hrs.	8	8	5	8
Beam diam., arcsec.	0.26	0.29	0.28	0.27
Map size, pixels	512×512	512×512	512×512	512×512
Map spacing, arcsec.	0.05	0.05	0.05	0.05

Table 6.1 Goldstone/VLA 3.5 cm bistatic observations. The angular separation is the angle, in arcseconds, between the moon and Jupiter as viewed from Earth. Both moons are tide-locked with Jupiter, such that the 0 deg. meridian always faces the planet. Beam diameter given in the last column of the table is that following imaging with CLEAN.
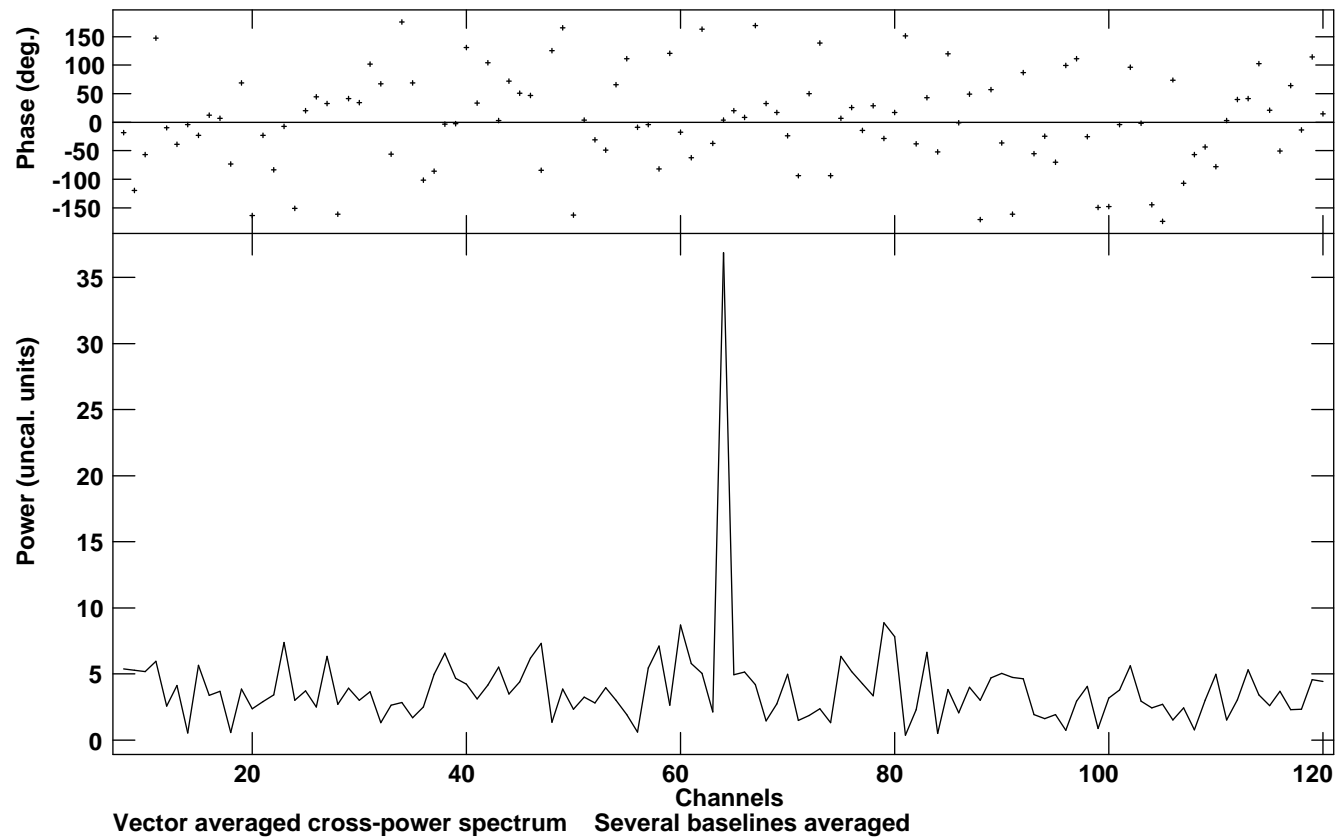
Figure 6.3 Callisto cross power spectrum from Goldstone/VLA, 2002 Feb. 4. The abscissa is the frequency channel number in VLA spectral line observing mode. The line width is set to 1526 Hz, slightly larger than the ≈ 1200 Hz bandwidth of Callisto's echo. The power shown is that in a single resolution element at the subradar point. The echo appears in the single, central line of the spectrum. The power level in the non-central bins comprises the moon's blackbody radiation, and receiver noise.

The experiments listed in Table 6.1 proceeded as follows. The Goldstone transmitting and VLA receiving observatories were scheduled to have the same view window of the satellite. Goldstone transmitted a CW tone; its frequency was adjusted to compensate for Doppler effects at the sub-radar point on the moon, so that the VLA received a constant nominal frequency of 8,560 MHz. At the start of the track, the VLA initially observed well-characterized natural radio sources for amplitude and phase calibration purposes. When the echos from the satellite began to arrive, the VLA antennas switched to tracking the moon. Approximately every 10 minutes throughout the track, the VLA would shift temporarily off the target moon, track a radio point source for a minute or two, and then resume tracking the moon. In this way, the phase response of the VLA was measured continuously throughout the observation period, so that in post-processing, gain and phase adjustments could be applied to the "complex visibility" data (see Section 3.1.1) to correct for array irregularities.

The VLA system is designed primarily to observe galactic and extragalactic sources rather than solar system objects, therefore some changes to the standard observing procedure were required. These modifications were developed first by Butler and Muhleman for their previously mentioned experiments. Planets are not stationary against the celestial sphere as are the deep space sources normally studied with the VLA, so a refinement to the system tracking was necessary; this was achieved through adaptation of the standard VLA tracking system to make use of a JPL planetary ephemeris. Since the array usually images broadband sources, it is necessary to employ the VLA's spectral line observing mode. In this mode, the VLA uses real-time hardware to divide the received data into narrow spectral channels. The bin width of the spectral channel was set so that the Doppler bandwidth of the Jovian moon under observation just fits into the central spectral bin, maximizing the SNR in that bin. For our observations, we used a bandwidth of either 3052 or 1526 Hz per channel, to match the expected 3000 or 1200 Hz echo bandwidths of Ganymede and Callisto.

We processed the data at the VLA Array Operations Center in Socorro, making use of the Astronomical Image Processing System (AIPS) software developed by NRAO staff. An example of a plane-of-sky image of Callisto is shown in Figure 6.4. The radioastronomical unit of flux density used in this figure is the Jansky, or 10^{-26} W/m^2/Hz. To generate these images, first the complex visibility or spatial frequency domain data were loaded from tape
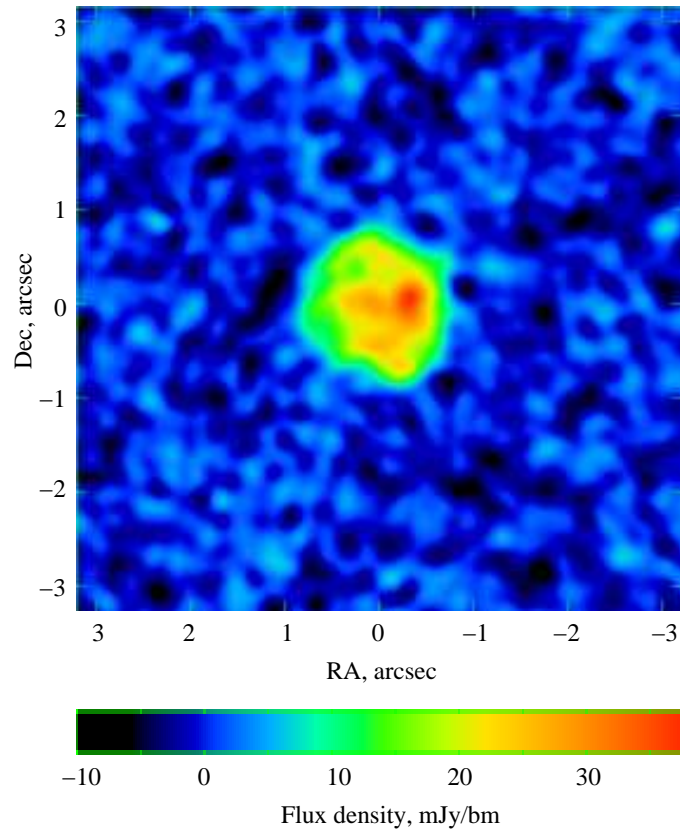
Figure 6.4 Goldstone/VLA 3.5 cm plane-of-sky image of Callisto on 2000 Dec 3. The synthesized beam resolution is 0.28 arcsec. This total observed power image shows the positive detection of Callisto against the cold sky. The image is formed from the echo power in the central channel of the VLA spectral line mode. One radar-bright feature, Valhalla, appears as a bright red area on the right-hand side of the moon. The peak flux density received from this feature, 37.5 milliJansky per beam, is $\approx$ 15 times greater than the standard deviation of the image background, 2.4 mJy/bm.

and visually flagged for bad points. Array amplitude and phase response correction tables were computed using the data from the calibration radio sources. A polarization calibration using the calibration sources was performed and stored in a table. These correction tables were then applied to the planet visibilities to calibrate the data. The baseline thermal noise of the planet was computed using the off-planet spectral channels, and this estimate of the planet thermal radiation was subtracted from the spectral channel containing the radar echo. The subtraction took place in the complex visibility or (u, v) plane prior to final imaging (Clark, 1980). In this way, the final plane-of-sky brightness map of the moon is not biased by the moon's own blackbody radiation. We imaged the moon by transforming the calibrated, complex visibilities from the spatial frequency domain into the time domain. The CLEAN algorithm was used as a feedback loop around this imaging process to remove the array response. We specified a circular "clean box" or restricted cleaning region (see Section 3.4) which was approximately one resolution element larger than the target disk and guided the CLEANing. The cleaned visibilities, representing the estimate of the true source visibilities, were then transformed from the spatial frequency domain to the image domain onto a 512 by 512 pixel grid at 0.05 arcsec spacing using an ideal Gaussian beam weighting equal to the achieved array resolution.

6.2 Radar cross-section model

Diffuse backscatter from an icy Galilean satellite is well-represented on a disk-integrated basis by a simple $\cos^n \theta_i$ law where θ_i is the angle of incidence (Campbell et al., 1978). The application of this law to the computation of the total normalized RCS $\bar{\sigma}$ of a diffuse reflecting sphere is discussed in Section 4.1.3.

When comparing VLA observations to monostatic radar results, it is important to note the distinction between the backscatter per unit surface area and the backscatter per unit projected area. Define η as radar backscatter cross section per unit projected area on the plane of sky $dA_\perp$, then

$$\eta = \frac{d\sigma}{dA_\perp}. \tag{6.1}$$

The Goldstone/VLA instrument directly images η, which we relate to σ_0 by

$$dA_\perp = \cos(\theta_i)\, dS, \tag{6.2}$$

where dS is the unit of actual (not projected) surface area. The radar backscatter per unit projected area is then

$$\eta(\theta_i) = \frac{\sigma_0(\theta_i)}{\cos(\theta_i)} = \rho \cos^m(\theta_i), \tag{6.3}$$

where $m = n - 1$. In the analysis which follows, we use η and m whereas Ostro et al. (1992) and others use σ_0 and n.

6.3   Observations and model fits

For the VLA, the power intensity $I(x,y)$ received in Jansky per beam (Jy/bm) is written (Butler, 1994)

$$I(x,y) = 10^{26}\, \frac{P_t A_t \Omega_b}{4\pi\lambda^2 R^2 B} \eta(x,y), \tag{6.4}$$

where P_t is the transmitter power, A_t is the effective transmitting antenna area, λ is the wavelength, R is the range to the satellite, B is the receiver channel bandwidth, η is the projected specific cross section, and

$$\Omega_b = \pi \frac{r_b^2}{R^2} \tag{6.5}$$

is the solid angle of the beam for an effective beam radius r_b. Using (6.4), the sky maps of the moons are converted from Jy/bm to projected cross section η. Figures 6.5 and 6.6 show the depolarized η_{SC} and polarized η_{OC} cross sections, and the circular polarization ratio μ_c in plane-of-sky coordinates.

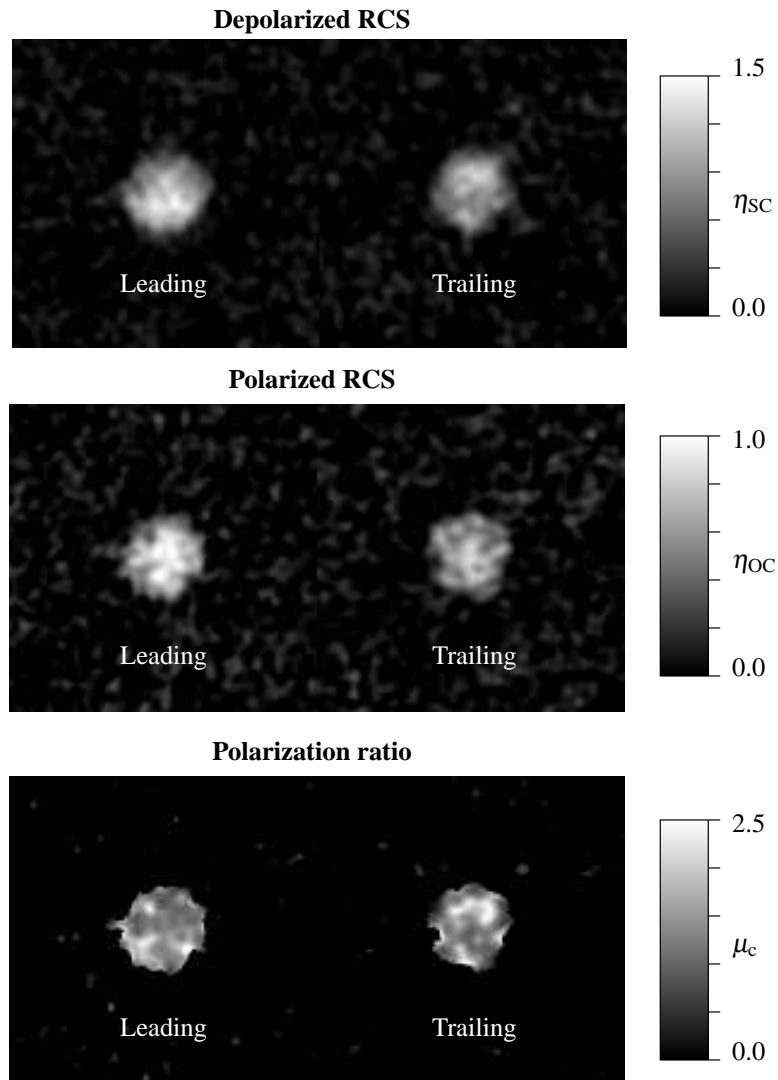**Figure 6.5** Ganymede dual-polarization images. Plane-of-sky images for the leading ($\approx 90°$W) and trailing ($\approx 270°$W) hemispheres are shown. The images are rotated from RA/Dec coordinates so that i) the projection of the moon's rotation axis onto the plane-of-sky is aligned vertically on the page, and ii) the North pole of the moon is 'up.' The ratio μ_c is computed only for those resolution elements where the weaker OC echo exceeds the off-planet background noise by two standard deviations. This leads to a "scalloping" effect around the edge of the radar-illuminated disk, as the SNR is lowest at the radar terminator.
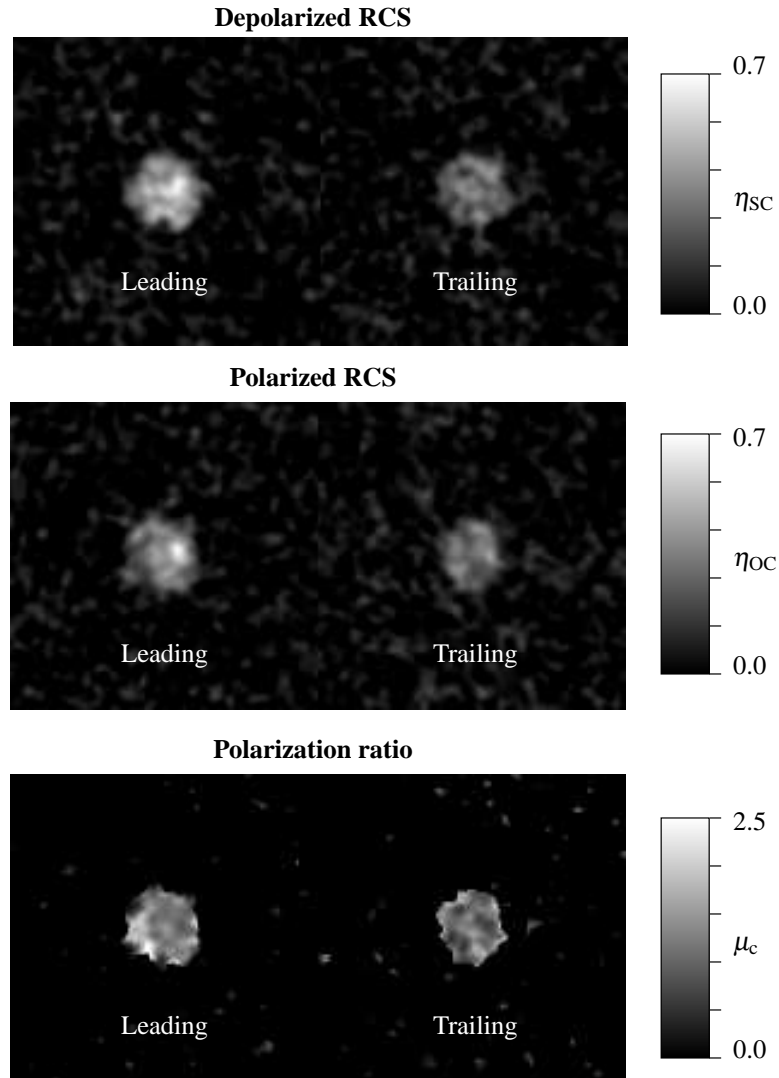
Figure 6.6 Callisto dual-polarization images. Plane-of-sky images for the leading ($\approx 90°$W) and trailing ($\approx 270°$W) hemispheres are shown. The images are rotated from RA/Dec coordinates so that i) the projection of the moon's rotation axis onto the plane-of-sky is aligned vertically on the page, and ii) the North pole of the moon is "up." The ratio μ_c is computed only for those resolution elements where the weaker OC echo exceeds the off-planet background noise by two standard deviations. This leads to a "scalloping" effect around the edge of the radar-illuminated disk, as the SNR is lowest at the radar terminator.

Mapping from right ascension and declination coordinates to standard planetary carto-
graphic coordinates allows direct comparison of the radar data with optical albedo maps
obtained with the Galileo and Voyager spacecraft. The satellite's polar angle with respect
to north on the plane-of-sky and the sub-Earth latitude of the center of the disk were ob-
tained from the JPL planetary ephemeris DE-405 (Standish, 1998) and used to compute the
coordinate transformation. In order to compare the radar and optical albedo images, we
overlay a grayscale high-resolution optical image with the lower resolution radar data on a
color scale. The resulting images for Ganymede and Callisto are shown in the upper panels
of Figures 6.7 and 6.8.

The normalized backscatter image is dominated by the effective hemispherical scatter-
ing law model. Removal of this background model can make deviations due to surface
heterogeneities more apparent. We employ a procedure developed by Butler (1994) to fit
and subtract the hemispherical backscatter model, finally achieving the residual backscatter
maps shown in the lower panels of Figures 6.7 and 6.8. In the process, we obtain estimates
of the normal incidence reflectivity ρ and the scattering law exponent m components of the
hemispherical scattering model (6.3).

The procedure for model fitting is as follows. Consider that the processed and CLEANed
images, Figure 6.4, are a convolution of an ideal Gaussian beam response, or "CLEAN
beam," with the actual source distribution. In order to extract the scattering law exponent
m, we first form the radial average of the plane-of-sky map, Figure 6.4. The VLA image is
centered on the source by the observing ephemeris. The radial integration of the plane-of-
sky map is therefore centered on the target. We then modify (6.3) to include the convolution
of the "CLEAN beam" with (6.3), thus obtaining the more complex model,

$$f(\bar{r}) = \bar{\Omega}_b \int_0^1 \rho \cos^m[\sin^{-1}(\bar{r}')] e^{-(\bar{r}^2 + \bar{r}'^2)/\bar{\Omega}_b} I_0\left(\frac{2\bar{r}\bar{r}'}{\bar{\Omega}_b}\right) \bar{r}' d\bar{r}', \qquad (6.6)$$

from Appendix A of Butler (1994). Here $\bar{r} = \sin(\theta_i)$ is the normalized radius at incidence
angle θ_i, $\bar{\Omega}_b$ is the actual Gaussian beam area in units of normalized radius, and I_0 is
the modified Bessel function. Since radial averaging of the source distribution over the
observed disk produces a decreasing variance in our estimate of ρ with increasing radius,
we used weighted non-linear least squares to fit the complex radial profile model $f(\bar{r})$ of

(6.6) to the observations, thereby extracting ρ and m. As mentioned in Appendix A of Butler (1994), the variance of the noise is inversely proportional to an annulus of area

$$
\begin{aligned}
A(\bar{r}) &= \pi(\bar{r} + \delta^2 r) - \pi \bar{r}^2 \\
&= \pi[2\bar{r}\delta\bar{r} + \delta^2]r
\end{aligned}
\tag{6.7}
$$

where $\delta\bar{r}$ is the image plane grid spacing in planetary radii. Taking the weight to be $w(\bar{r}) = 1/A(\bar{r})$, we obtain the results shown in Figure 6.9. These one dimensional models show the radial average projected cross section.

Once the parametric estimation is complete, we can check the accuracy of the model. This is accomplished by substituting our estimates for ρ and m into equation (4.8) to give a model estimate of the total normalized RCS $\hat{\sigma}$. This number, $\hat{\sigma}$, can be compared with the true normalized RCS, $\bar{\sigma}$. We compute $\bar{\sigma}$ directly by integrating all received flux in the plane-of-sky image and applying (6.4) :

$$
\bar{\sigma} = \int_x \int_y \eta(x,y)\, dydx = 10^{-26} \frac{4\pi\lambda^2 R^2 B}{P_t A_t \Omega_b} \int_x \int_y I(x,y)\, dydx.
\tag{6.8}
$$

The comparison of values is given in Table 6.2. Since the limb-to-limb bandwidth of the target can approach the bandwidth of the central channel of the VLA spectral line mode, some energy spills into adjacent channels because the total RCS is biased by the spectral weighting function. This effect of the frequency response of the VLA is outlined in Appendix B of Butler (1994). To compensate, a correction factor is applied to the measured total RCS $\bar{\sigma}$. This correction consists of dividing $\bar{\sigma}$ by a factor γ, where

$$
\begin{aligned}
\gamma = \ & \frac{m+2}{2\pi} \int_{x=-1}^{1} \int_{y=-\sqrt{1-x^2}}^{\sqrt{1-x^2}} \left(1 - x^2 - y^2\right)^{m/2} \\
& [\operatorname{sinc}(\alpha x) + \frac{1}{2}\operatorname{sinc}(\alpha x - 1) + \frac{1}{2}\operatorname{sinc}(\alpha x + 1)]\, dydx,
\end{aligned}
\tag{6.9}
$$

and α is the ratio of the planet limb-to-limb bandwidth to the VLA spectral line mode channel bandwidth. This equation for γ accounts for power which falls into the side lobes of the Hann window function used for imaging in spectral line mode.

To highlight the areas of the planet surface which differ from the hemispherical model,
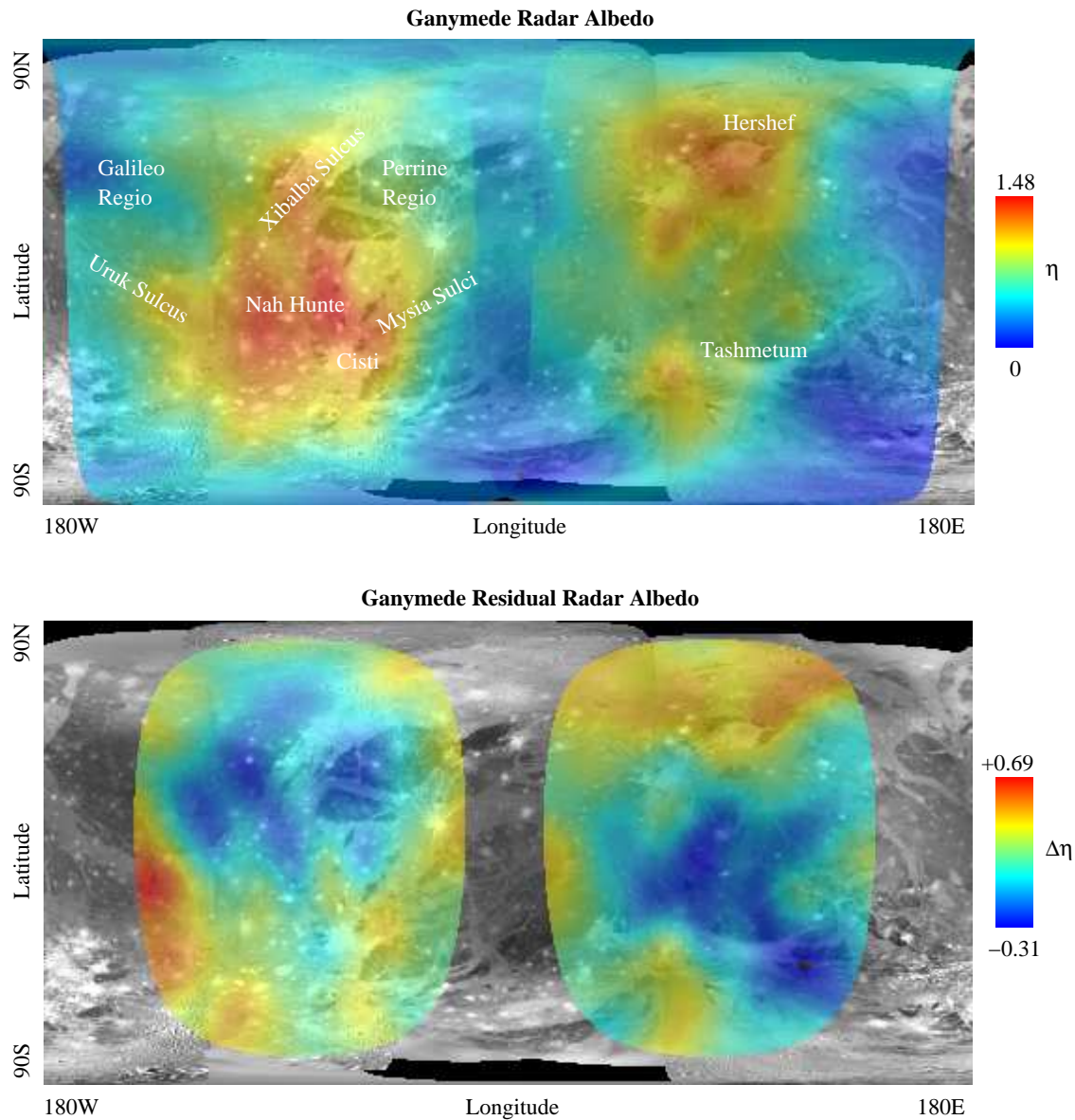
Figure 6.7 Ganymede radar and optical albedo maps. The observations show that higher radar albedo is associated with the terrains of Xibalba Sulcus and Uruk Sulcus ringing Galileo Regio on the leading (left) hemisphere, and the impact crater Hershef on the trailing (right) hemisphere. The lower image shows the data with the hemispherical backscatter law (6.6) removed. The subtraction of the backscatter law is truncated outside a radial boundary where the standard deviation of the image exceeds the value of the backscatter. See the feature coordinates listed in Table 6.3 and the discussion in Section 6.4.
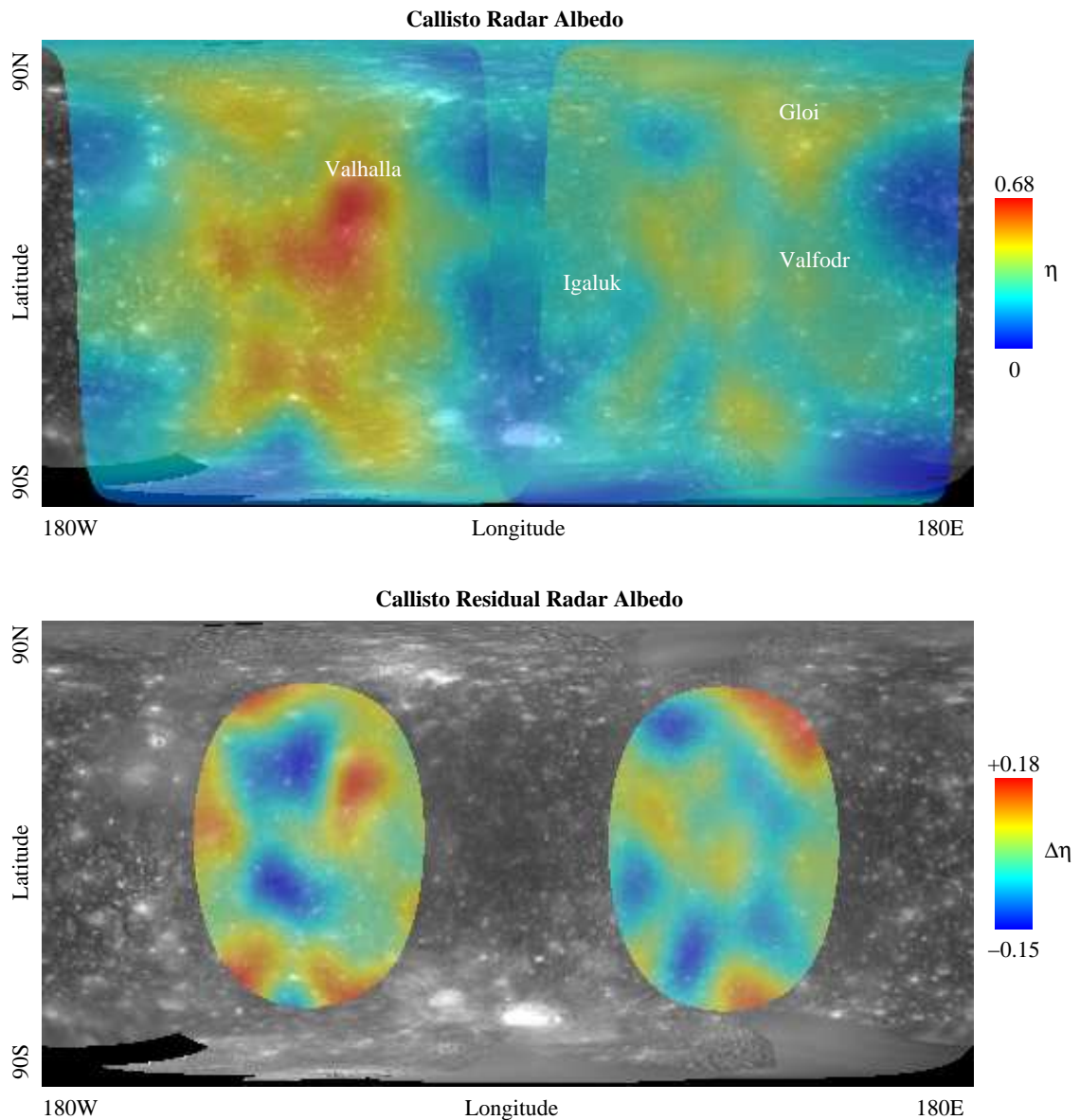
Figure 6.8 Callisto radar and optical albedo maps. The observations show that there is signifi cant brightening associated with the large 600 km diameter Valhalla impact crater on the leading (left) hemisphere, while on the trailing (right) hemisphere, the brightest radar feature is the impact crater Gloi. The lower image shows the data with the hemispherical backscatter law (6.6) removed. The subtraction of the backscatter law is truncated outside a radial boundary where the standard devia-tion of the image exceeds the value of the backscatter. See the feature coordinates listed in Table 6.3 and the discussion in Section 6.4.
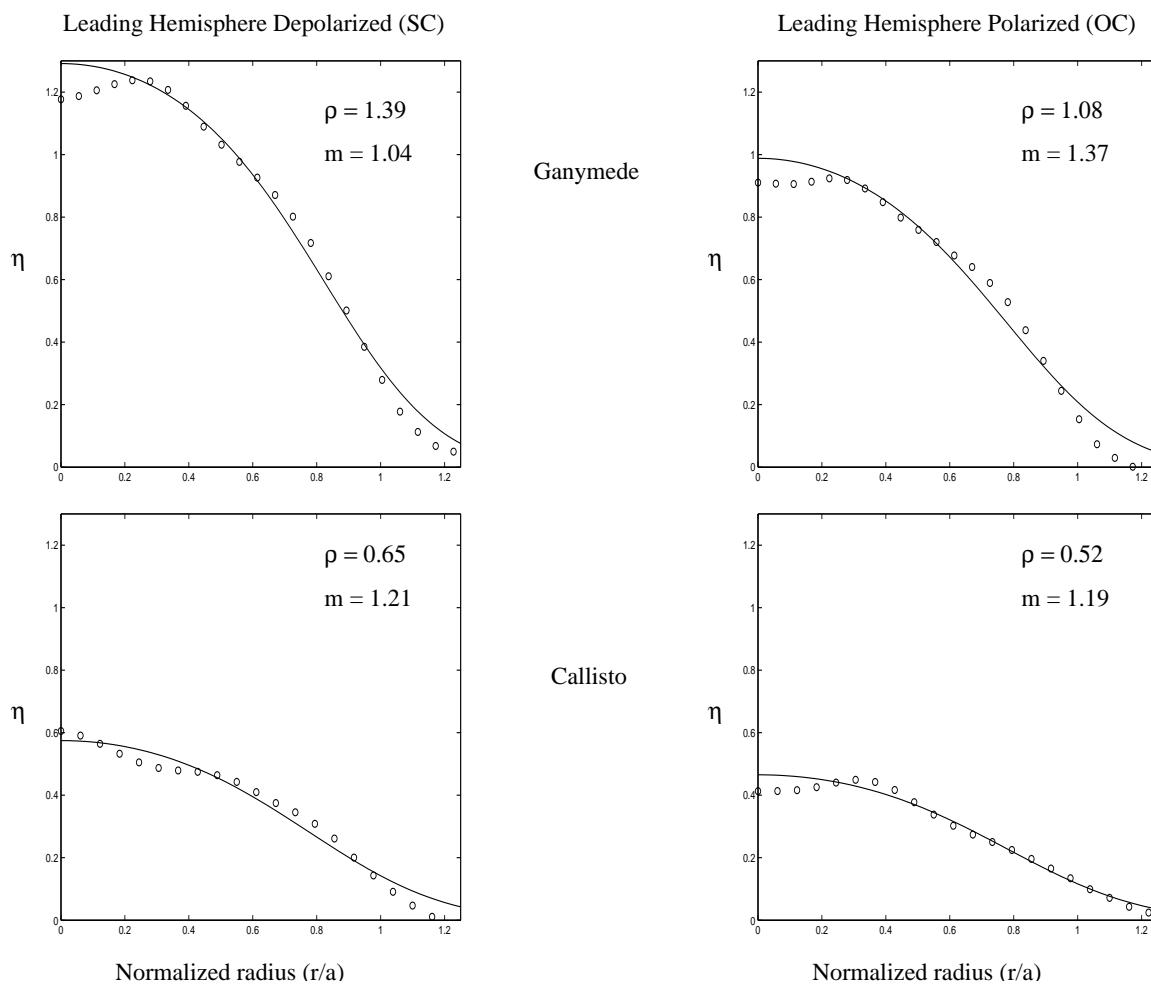
Figure 6.9 $\rho \cos^m(\theta_i)$ model fi ts. These plots compare the least-squares backscatter model in (6.6) as solid lines with the radially integrated plane-of-sky brightness for the leading hemispheres of Ganymede and Callisto, here plotted with open circles. The estimated model parameters obtained as the output of the fi tting process—normal incidence refl ectivity ρ and scattering law exponent m—are those listed in each frame. Also see Table 6.2.

SC Hemispherical Backscatter Parameters

Moon	Hemi-sphere	ρ	m	Model $\hat{\sigma}_{SC}$	Measurement $\bar{\sigma}_{SC}$
Ganymede	Leading	1.39 ± 0.04	1.04 ± 0.10	0.91 ± 0.04	0.97 ± 0.02
	Trailing	1.13 ± 0.07	1.00 ± 0.21	0.75 ± 0.07	0.78 ± 0.03
Callisto	Leading	0.65 ± 0.04	1.21 ± 0.24	0.40 ± 0.04	0.40 ± 0.02
	Trailing	0.32 ± 0.02	0.28 ± 0.17	0.32 ± 0.04	0.31 ± 0.02

OC Hemispherical Backscatter Parameters

Moon	Hemi-sphere	ρ	m	Model $\hat{\sigma}_{OC}$	Measurement $\bar{\sigma}_{OC}$
Ganymede	Leading	1.08 ± 0.05	1.37 ± 0.19	0.64 ± 0.05	0.67 ± 0.02
	Trailing	0.85 ± 0.03	1.21 ± 0.16	0.53 ± 0.03	0.56 ± 0.03
Callisto	Leading	0.52 ± 0.02	1.19 ± 0.12	0.33 ± 0.02	0.34 ± 0.02
	Trailing	0.35 ± 0.03	0.49 ± 0.23	0.28 ± 0.03	0.28 ± 0.02

Table 6.2 Ganymede and Callisto model fits. We use non-linear least squares to fit the model (6.3) to the radially averaged data. Errors quoted for normal incidence albedo ρ and scattering law exponent $m = n - 1$ are formal errors for the least-squares process (Ryan, 1997). Modeled $\hat{\sigma}$ comes from substitution of the estimated parameters into (4.8), and the error is estimated from Monte Carlo simulation. Measured $\bar{\sigma}$ is the disk-integrated flux in the image plane; error is estimated from the off-planet noise background. In Section 6.4 of the text, these data are compared to Table 4.2, which summarizes results from Ostro et al. (1992).

the model (6.6) is subtracted from the data to generate a residual backscatter image, shown in the lower panels of Figures 6.7 and 6.8. This subtraction step is unstable near the limb of the planet for two reasons. First, the signal-to-noise ratio is low near the limb. Second, as mentioned in Butler (1994), the plane-of-sky image is the convolution of the cleaned map with the Gaussian "CLEAN beam," and therefore contains edge effects near the limb. For this reason, the subtraction is truncated outside a radial boundary where the standard deviation of the image exceeds the value of the backscatter. This results in a smaller truncation radius for Callisto, because Callisto has a lower radar albedo and was observed from a less favorable distance.

6.4   Discussion

The absolute accuracy of the Goldstone/VLA total-power measurement is determined by the variance of parameters in the radar equation. The dominant uncertainties in these parameters are the $\approx 5\%$ fluctuation of the received power measurement, the transmitted power accuracy at $\approx 10\%$ over the time-span of the 8 hour track, and the transmitting antenna pointing accuracy of up to 0.5 dB. These error sources combine to provide an absolute calibration standard deviation of $\approx 20\%$ for the Goldstone/VLA instrument measurement of normalized RCS, $\bar{\sigma}$.

Although these experiments are designed to map spatial variations in albedo, and not measure total reflectivity, our values for disk-integrated scattering parameters are within experimental error of prior observations. Our values for scattering parameters summarized in Table 6.2 differ somewhat from those measured by Ostro et al. (1992), as summarized in Table 4.2.

We expect to obtain somewhat different model parameters for several reasons. First, the nature of the measurements is quite different. Ostro et al. (1992) recorded Doppler spectra using a single, 70 m dish, while we synthesized an aperture using an array of 25 m dishes. As mentioned in Chapter 3, there is a "hole" in the spectral sensitivity function of a correlating array near zero spatial frequency, so the array is not as sensitive to total flux as a single dish antenna. Second, we fitted the radial limb-darkening model directly to a plane-of-sky brightness image, while Ostro et al. (1992) fitted a model to Doppler spectra

which are lineal projections of the model. Both inversion methods are non-linear due to the use of a $\cos^n(\theta)$ scattering law, and are not necessarily guaranteed to converge to a unique solution. Third, the measurements are separated by more than a decade in time. Specifically, we report systematically higher normal incidence reflectivity, ρ, and scattering law exponent, m, and lower normalized RCS, $\bar{\sigma}$. On average, our normal incidence albedos are $\approx 45\%$ higher for Ganymede, and $\approx 30\%$ higher for Callisto. The scattering law exponents, $m = n - 1$, are $\approx 60\%$ and 30% higher, respectively. The higher scattering law exponent of this study indicates that limb darkening is stronger in our data than in the data of Ostro et al. (1992). We measure the total normalized RCS $\bar{\sigma}$ to be 17% lower for Ganymede, and 22% lower for Callisto. The RCS estimates are within the absolute calibration accuracy of 20-50% reported by Ostro et al. (1992).

We find the leading hemispheres of each moon to have a slightly higher average albedo than the trailing hemisphere by $20\% \pm 5\%$. Such asymmetry has been noted in optical observations for many years (Morrison and Morrison, 1977), and has been attributed to sputtering by energetic particles from the Jovian magnetosphere (Clark et al., 1980). Sputtering causes erosion or composition changes of the ice surface, affecting optical wavelength observations. Though such sputtering is not expected to cause changes of the surface on the centimeter scale of the radar wavelength, one possible explanation for the noted heterogeneity at 3.5 cm wavelength is gardening by micrometeoroids (Pang et al., 1979), which could cause a slight roughening (surface and volume) of the leading hemisphere relative to the leeward hemisphere.

Terrain on Ganymede can be divided roughly into two classes. These are: i) older, heavily cratered terrain with low optical albedo (regionis), and ii) newer, furrowed, resurfaced terrain with high optical albedo (sulci); for example, see Pappalardo et al. (1998). The observations (Figure 6.7) show that higher radar albedo is associated with the terrains of Xibalba Sulcus and Uruk Sulcus ringing Galileo Regio on the leading (left) hemisphere, and the impact crater Hershef on the trailing (right) hemisphere. While detailed studies of these returns remain to be completed, these radar observations appear to show differences in either the composition or the surface roughness of different regions of the moons. The sulci are thought to have been resurfaced more recently than the more heavily cratered dark terrain making up the regionis, and appear brighter in the radar images. One possible

Moon	Feature	Lat. (deg.)	Lon. (deg.)
Ganymede	Bubastis Sulci	72.3S	282.9W
	Cisti	31.7S	64.2W
	Galileo Regio	47.0N	129.6W
	Nah-Hunte	17.8S	85.2W
	Hershef	47.3N	269.5W
	Mysia Sulci	7.0S	7.9W
	Perrine Regio	33.2N	32.5W
	Uruk Sulcus	0.8N	160.3W
	Xibalba Sulcus	43.8N	71.1W
Callisto	Gloi	49.0N	245.0W
	Igaluk	5.6N	316.0W
	Valfödr	1.3S	247.0W
	Valhalla	14.7N	56.0W

Table 6.3 Listing of Ganymede and Callisto terrain features. The locations of major craters, plains (regionis) and furrows (sulci) are given as listed in the U.S. Geological Survey astrogeology catalog.

mechanism for this enhancement in the sulci is the infusion of newer, relatively pure water ice exhibiting less attenuation to the radar signal, and formation of associated wavelength-scale heterogeneities in the newly effused material. In Figure 6.7 in particular, Xibalba Sulcus is apparent as a region of an enhanced RCS relative to Galileo and Perrine Regionis on either side. On the leading hemisphere, the brightest RCS regions are associated with the terrain between the Cisti and Nah-Hunte craters, the terrain on the northeastern side of Cisti where the Mysia Sulci begin, and Xibalba Sulcus. On the trailing hemisphere, the brightest features are associated with the Bubastis Sulci in the south, and the impact crater basin Hershef in the north. The coordinates of prominent, named features are listed in Table 6.3.

Some points can be made about our observations of Callisto. The disk-integrated cross sections show that Ganymede is 2.1 ± 0.3 times as reflective as Callisto. Additionally, radar features on Callisto do not stand out as well above the disk-integrated average as do those in the Ganymede radar images. Optical observations of Callisto from Voyager and Galileo show a lack of sulci-type resurfacing. As a result, the surface of Callisto is thought to consist of older and less-pure ice, which is thought to be less bright than that of

Ganymede. For the spatially resolved data in Figure 6.8, there is a statistically significant brightening associated with the large 600 km diameter Valhalla impact crater on the leading hemisphere. On the trailing hemisphere, the brightest radar feature is the impact crater Gloi, followed by unnamed terrain between Igaluk and Valfödr, though the significance of the brightness of this latter region is discounted due to poor signal to noise conditions. The brightness is on the order of the standard deviation of the noise background.

6.5 Summary

A confluence of solar system geometry and telescope scheduling permitted Goldstone/VLA aperture synthesis mapping of Ganymede and Callisto in late 2000 and early 2002. Aperture synthesis can produce high quality images free of the unavoidable fold-over ambiguities of single-dish radar imaging of planets. Fitting disk-integrated diffuse scattering laws to the Ganymede and Callisto observations confirms the high backscatter cross section and circular polarization inversion that has been noted in previous Doppler spectra observations. Our spatially resolved radar images show higher albedos associated with recently resurfaced terrain on Ganymede and Callisto, either through tectonic motion as in the sulci, or through cratering.

Chapter 7

Conclusions

In this work we focused on 3.5 cm wavelength radar imaging of i) Mercury's north and south polar regions at 6 km resolution and ii) the disks of Jupiter's Galilean satellites Ganymede and Callisto at 350 km resolution. We applied two previously developed techniques, random long-code delay-Doppler synthetic aperture imaging and aperture synthesis imaging, to acquire and process new data from these solar system objects.

Our results include the following.

- New 3.5 cm wavelength, dual-polarization specific RCS maps of the north and south polar regions of Mercury at 6 km resolution. We co-registered these data with optical images from the Mariner 10 mission. The co-registered observations corroborate earlier 13 cm observations (Harmon et al., 1994, 2001) which showed the bright material exists in permanently shadowed areas of large craters.

- New 3.5 cm wavelength, dual-polarization RCS maps of the leading and trailing hemispheres of Ganymede and Callisto at 350 km resolution. These images are of comparable resolution to previous results but are free of north-south fold-over. Co-registration of the data with Galileo spacecraft optical imagery shows that bright albedo features are associated with recently re-surfaced terrain such as sulci and impact craters.

131

The new Mercury images, co-registered with Mariner 10 optical imagery, show that the radar-bright and unusually polarized echoes indeed arise from within portions of Class 3–4 craters that are in permanent shade, as modeled by Paige et al. (1992); Vasavada et al. (1999) and posited by Harmon and Slade (1992); Slade et al. (1992); Butler et al. (1993); Harmon et al. (1994); and Harmon et al. (2001). This type of backscatter is also associated with volume scattering from ice deposits from the three outer Galilean satellites of Jupiter and the polar caps of Mars. The previous conclusion, that these spots represent scattering by cold-trapped volatiles in the floors of the craters, such as water ice, is supported by thermal modeling requiring an insulating layer of regolith or dust to cover deposits in off-pole craters to allow long-term stability. For materials with nominal electrical properties, such a layer would cause wavelength dependent attenuation of a passing electromagnetic wave. A model that combines angle-of-incidence dependent backscatter, with attenuation through the layer shows that the decrease in total cross section seen at the 3.5 cm wavelength, relative to 13 cm measurements reported by other investigators, can yield estimates of layer thickness from 0 ± 11 to 35 ± 15 cm, depending on the scattering law exponent n. Other scattering models could explain the polarization behavior—wavelength dependent backscatter from an angled rough surface, for example. Since strong backscatter is observed only in shadowed crater floors, however, and not from crater walls in exact backscatter geometry, the "glinting" phenomenon noted for lunar echoes by Stacy et al. (1997) is discounted.

Our Ganymede and Callisto images improve upon previous findings of Ostro et al. (1992) by removing the north-south ambiguity while achieving similar resolution. Co-registration of the radar albedo images with global mosaics of visual images from the Voyager and Galileo missions shows that high backscatter areas are associated with terrain that has been resurfaced in the recent past, such as the sulci features and the Herschef and Valhalla impact basins. The imaging technique allows estimation of the exponent in the standard diffuse $\cos^n \theta$ scattering law for each hemisphere. Least-squares fits to this model show that although disk-integrated scattering parameters are somewhat different from values that other investigators derive, our total cross section estimates are consistent, within experimental error, with previous observations. The absolute reflectivity of the trailing

hemispheres of both moons is shown here to be somewhat lower than the leading hemisphere.

In reducing the data, we have made some improvements to existing processing techniques. These include Dolph-Chebyshev windowing of the long-code imaging data to equalize the sidelobes of the radar ambiguity function in the delay and Doppler dimensions. Also, we show that long-code data can be processed using standard FFT correlation techniques, and that repetitive code data can be processed to avoid Doppler folding ambiguities. Since the ISAR imaging process is inherently in the class of "embarrassingly parallel" signal processing problems, our implementation of a processor is suitable for large, parallel computer clusters.

Several extensions of this work are possible, including both experimental and theoretical studies. In the experimental area, the recent upgrade to the Arecibo Observatory to support 3.5 cm receive capability has opened the opportunity for Goldstone-Arecibo bistatic observations of the polar regions of Mercury. The additional receiving area that the Arecibo Observatory provides permits 1.5–3 km resolution imaging, which can further constrain the exact locations and scattering characteristics of the radar bright material. A preliminary investigation (Slade et al., 2004) has demonstrated the feasibility of the experiment, but the low declination of Mercury kept the planet confined to the edge of the Arecibo beam. Better viewing geometries in 2005 and 2006 will yield additional opportunities for 3.5 cm investigations of Mercury's polar craters. Arecibo also has increased gain at 13 cm wavelength from improved surface panel alignment as part of the 3.5 cm upgrade, and should be able to support 30–50 km resolution images of the Galilean satellites which would further resolve the regions exhibiting enhanced backscatter. There is much work remaining in the theoretical area in terms of modeling the observed backscatter effects. Many of the existing models for surface and volume scattering are decades old, and newer volume scattering models have been explored only tentatively (Peters, 1992; Gurrola, 1995; Black, 1997). The increase in available computing power, and migration to 64-bit address space, should enable finite-difference, time-domain (FDTD) simulations of scattering from complicated regolith structures.

Appendix A

Radar Coding and Processing

In this Appendix, we explore alternative signal processing methods to standard long-code processing (Harmon, 2002). For slightly overspread targets, a processing method we call the "subset code" technique can be used either i) to process standard, repetitive code data sets to alleviate Doppler aliasing, or ii) to speed up the processing of long-code data sets.

We also provide a technical explanation of an observation made in Section 2.3.2, namely that the individual sub-codes of the long-code method can be considered essentially random since the generator can be started in any state. As a result, these sub-codes satisfy orthogonality in a statistical sense. The composite waveform is not an optimal delay-Doppler imaging waveform, however, since the individual pulses are transmitted sequentially in time.

A.1   Subset codes

An adaption of the long-code technique which does not require the use of extremely long repeating sequences, is to use shorter PN sequences, and to divide each sequence into subsections. This subset code technique, as does use of the long-code, relies on the property that one piece of a PN sequence does not correlate well with another piece. The disadvantage of this technique is that since only a few unique pulse encoding waveforms are used, unwanted sidelobes are not randomized. For example, in Figure 2.7, instead of using an infinite number of random sequences to encode the pulses in the pulse train, A, B, C, …,

we instead use just two unique sequences, and encode the pulse train as A, B, A, B, …. The sidelobes are no longer random, and can be prominent. Deconvolution methods must be employed to remove the sidelobe contributions to the image.

The idea of subset codes is not unique to planetary radar imaging. Independently coded pulses are quite common in other pulse compression contexts, where multiple pulses must impinge on a target simultaneously in order to achieve sufficient sampling for the Doppler bandwidth of the expected return. Coding each pulse with the same sequence results in unwanted correlation between the pulse echo responses, so varying the applied code from pulse to pulse is a straightforward solution. For example, Sivaswamy (1982) developed "subcomplementary sequences," Gerlach and Kretschmer (1992) explored "zero cross-correlation waveforms," while more recently Guey and Bell (1998) formulated what they call "diversity [sic] waveform sets." In the application arena, Lehtinen and Haggstrom (1987) develop repeated sets of codes for imaging of the ionosphere, which is an overspread medium at the wavelengths of incoherent scatter radar facilities.

A.1.1   Subset code processing

To demonstrate subset code processing, we present 13 cm imaging of Mercury at 20 μsec baud, or 3 km range resolution.[1] The delay depth of Mercury is $\approx$ 16 msec, corresponding to 813 range bins. Thus, imaging of the visible hemisphere requires use of a length 1023 maximal length shift register sequence for standard delay-Doppler imaging. At the 13 cm wavelength, Mercury is overspread by a factor of approximately two, resulting in a factor of two overlap in the Doppler dimension of the output delay-Doppler array. Figure A.1 shows the result of using standard delay-Doppler processing. Aliasing in the Doppler dimension is apparent in the outer edges of the image as a "folding" about the Doppler bins equal to the inverse of the pulse rate, $1/2T$.

One way to view this standard pulse code signal processing technique is as a length Nb range compression filter, followed by a downsampler of length N bauds and a FFT matched filter bank, as shown in Figure A.2. Aliasing in the Doppler dimension happens because the Nyquist criterion for sampling the output of the range compression filter is

---

[1]We are grateful to John Harmon of the Arecibo Observatory for providing one round-trip cycle of data from a 1998 observation campaign for this analysis.
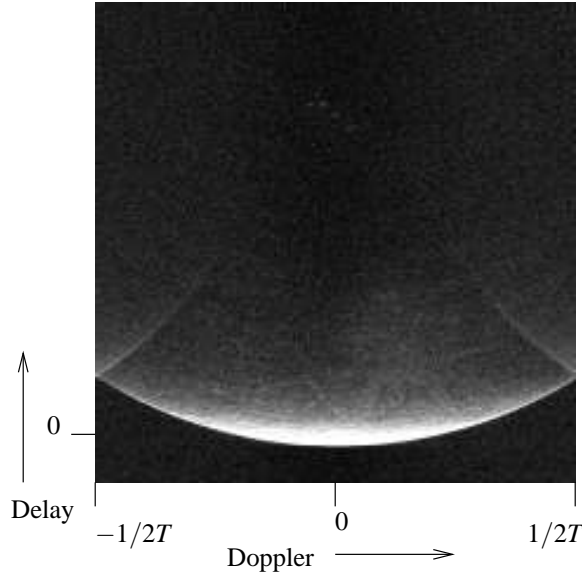
Figure A.1 Standard delay-Doppler processing applied to Mercury, showing aliasing in Doppler dimension. The overspread factor at 13 cm is approximately a factor of two. The corresponding aliasing folds the outer left and right halves of the echo, corresponding to the higher, aliased frequencies, in on the central, lower frequency echo.
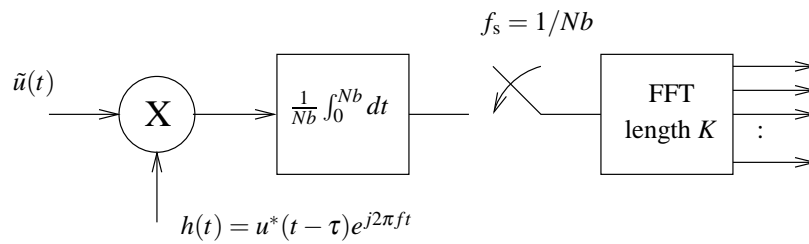

Figure A.2 Standard delay-Doppler decoding implemented as a correlation receiver. The receiver consists of a range compression filter, comprising the multiplier and integrator, followed by a sub-sampler and FFT. The baseband received signal experienced both delay and Doppler shift. The range compression filter $h(t)$ takes the form of the complex conjugate of the delayed signal. The FFT constitutes a Doppler matched filter bank.
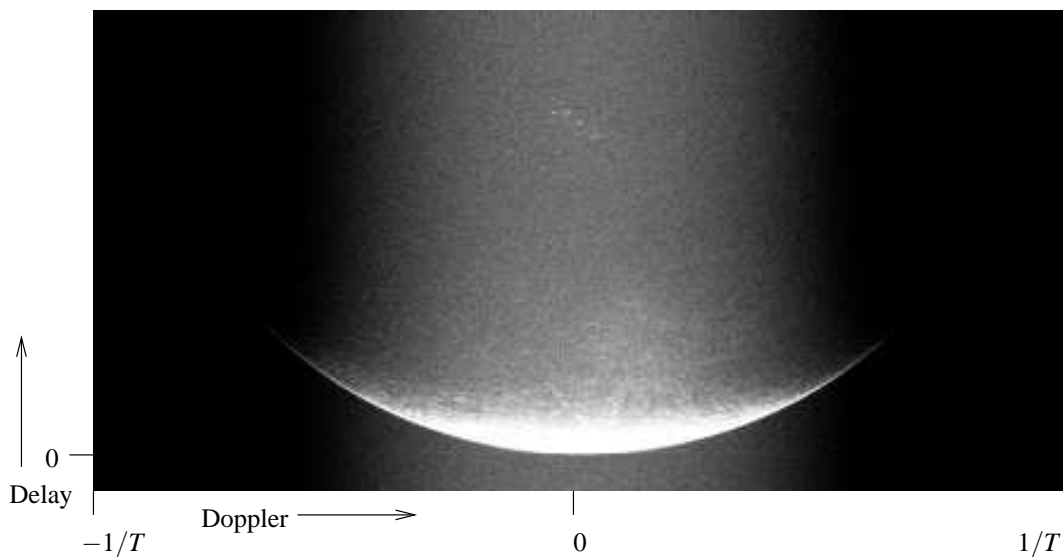
Figure A.3 Mercury imaged with standard, repetitive PN code, but processed by oversampling the output of the range compression fi lter. The dark areas on the left and right sides of the image are caused by correlation introduced into the output samples by the range compression fi lter (see text).

violated; Mercury is overspread by a factor of two. Doppler aliasing can be avoided by sampling the output of the range compression filter at twice the default rate. For example, decimating by $N/2$ bauds rather than N bauds, or equivalently sampling at $2/Nb$. By sampling at an interval which is shorter than the length of the range compression filter, however, correlation is introduced into the output samples, and the samples are no longer independent. This introduced correlation manifests itself as a shaping of the response in the Doppler dimension of the output delay-Doppler array, as shown in Figure A.3. One way of thinking about this cosine rolloff is as the spectral response of a two tap boxcar filter applied to the output samples of the subset code process described below. Though folding is eliminated in this case, the information at higher Doppler frequencies is lost.

For subset code processing, the PN sequence is divided into two halves, one of length 512 and one of length 511. The delay autocorrelation and cross correlation functions of these sequences are shown in Figure A.4. As can be seen, the functions do not display the ideal constant N/1 ratio of peak to sidelobe intensities. There is a strong correlation peak at the proper delay for each subset code, however, so together these codes perform as
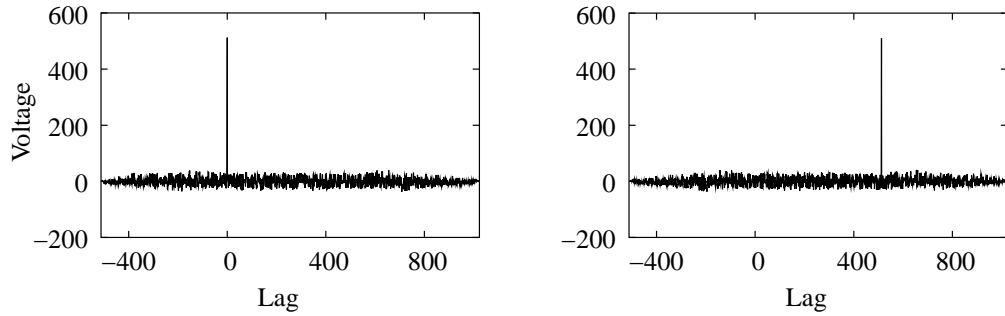
Figure A.4 Length 512 and 511 subsets of a 1023 PN sequence, cross correlated with the length 1023 sequence. The correlation peaks occur at lags 0 and 512. The correlation value at other lags is sufficiently low to permit imaging using the two subsets of the standard 1023 length PN sequence as independent, non-ideal pulse compression waveforms. The range sidelobes are $\approx 1/511$ in power, while for a length 511 PN sequence they would be $\approx 1/511^2$.

suboptimal range compression pulse codes with low cross correlation. The timing diagram for the two filter impulse responses is shown in Figure A.5. The correlation filter structure for subset code processing is shown in Figure A.6. The output of the two filters consists of a stream of range-compressed samples sampled at twice the rate of standard code processing.

After Doppler processing, the output image is as shown in Figure A.7. Subset code processing suppresses the aliasing in the Doppler dimension as seen in the standard code processing of Figure A.1. It also avoids the spectral nulls present in the oversampled data set of Figure A.3. Subset code processing of standard repetitive code data sets display significant leakage from the leading edge of the planet in all delay gates at multples of the pulse repetition frequency $f_m = m/T$ for integer m. As the leakage is inherent to the use of a repetitive waveform with base period T, the only solution to date for suppressing the leakage is deconvolution of the imaging impulse response function from the final delay-Doppler array. Harmon (2002) has used deconvolution with standard delay-Doppler coding to remove delay clutter from the strong specular echo of the leading edge. Deconvolution could be applied analogously to subset code-processed images.

For the central region of the output delay-Doppler array in the SC polarization, it is possible to use the subset code processed data without any deconvolution, as the effect of the subradar point leakage is minimal. Figure A.8 shows this for length-1 subset code pro-
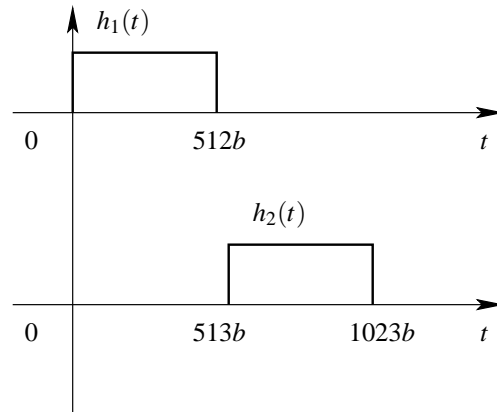
Figure A.5 Subset code filter impulse responses. The impulse response of the first filter, $h_1(t)$, leads the impulse response of the second filter, $h_2(t)$ by 512 bauds.
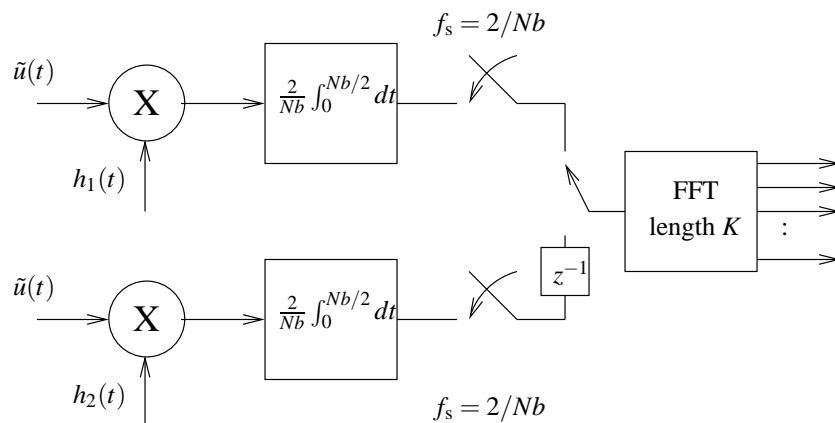

Figure A.6 Subset code delay-Doppler decoding implemented as two range compression filters with impulse responses $h_1(t)$ and $h_2(t)$ running in parallel. The subsampled output of the range compression filters alternately provide input samples to a FFT, which serves as the Doppler matched filter bank.
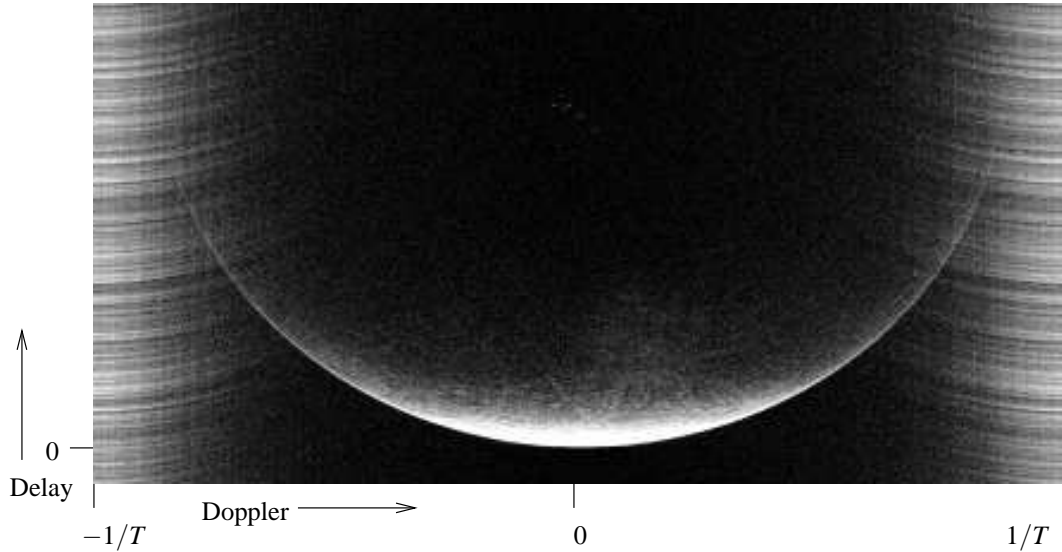
Figure A.7 Mercury imaged with a standard, repetitive PN code, but processed by the subset code method. Doppler aliasing is mitigated, but clutter from the leading edge of the planet at zero delay and Doppler appears at multiples of the pulse repetition frequency $f_m = \pm m/T = \pm m/Nb$.

cessing of a length 1023 PN sequence repetitive code data set. Length-1 subset code processing is equivalent to applying the long-code processing technique to standard repetitive code data sets with an FFT long enough to provide the necessary cross-range resolution. Rather than separating the delay and Doppler matched filters into two processes, a range compression filter and an FFT, one long multiply followed by an FFT can be applied to the data. In Figure A.8, an FFT of length $N \times 1024 = 1023 \times 1024 = 1047552$ was applied after multiplying the received data by a suitably lagged version of the transmitted sequence. In the OC image, the periodic clutter appears at frequency multiples m/T where $T = Nb$. In the SC image, the clutter is still present, but it is not that visible since the SC data lacks the large, specular echo from the subradar point.

Would an alternate choice of waveform result in reduction of the periodic clutter at points m/T? This approach was discussed in Harcke et al. (2000). For Mercury, a choice of PN code length $2^{20} - 1$ for the same baud b used in the above experiments would allow sufficient cross-range resolution by a length-1048575 FFT, and without periodic clutter since the PN code would not exhibit periodicity over the coherent integration period.
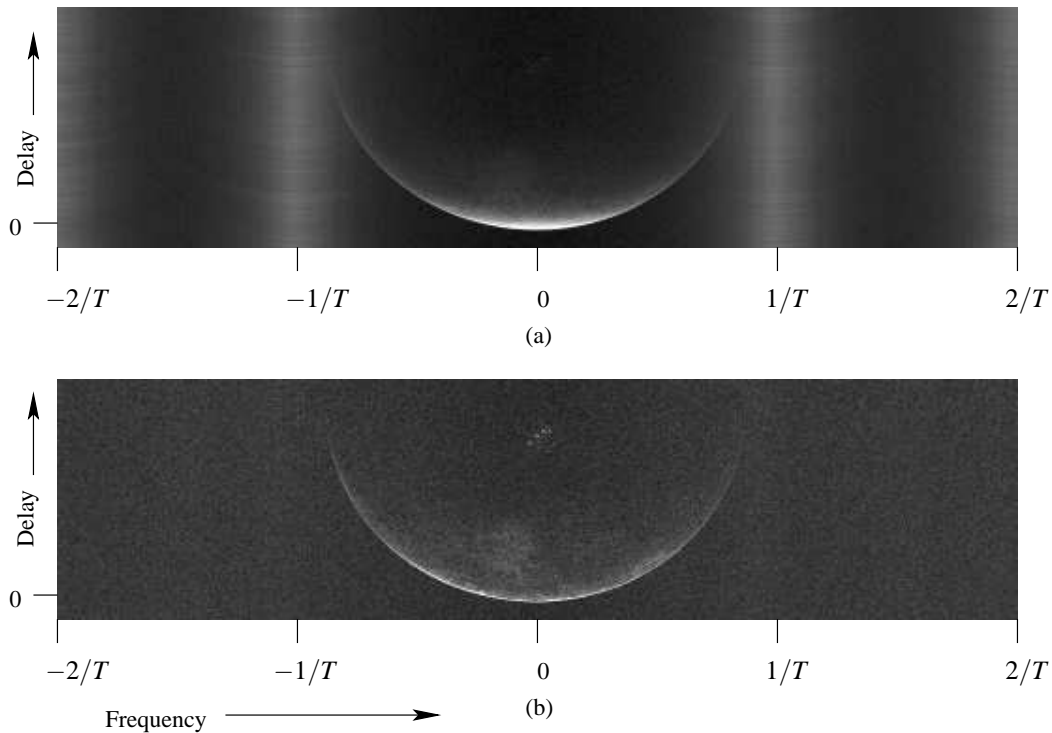
Figure A.8 Mercury imaged with a standard, length $N = 1023$ repetitive PN code, but processed by length-1 subsets. The data set is the same as that from Figure A.1. This is equivalent to applying the long-code processing methodology to a repetitive code data set. The OC echo shown in (a) displays mitigated Doppler aliasing, but clutter from the leading edge of the planet appears at multiples of the pulse repetition frequency $\pm m/T$ for integer m and $T = Nb$. The SC echo shown in (b) does not exhibit strong clutter, since the specular echo from the leading edge does not dominate the return. The FFT length is $1023 \times 1024 = 1047552$, but only the central 4092 points are shown. All 1023 possible delays are computed and shown.
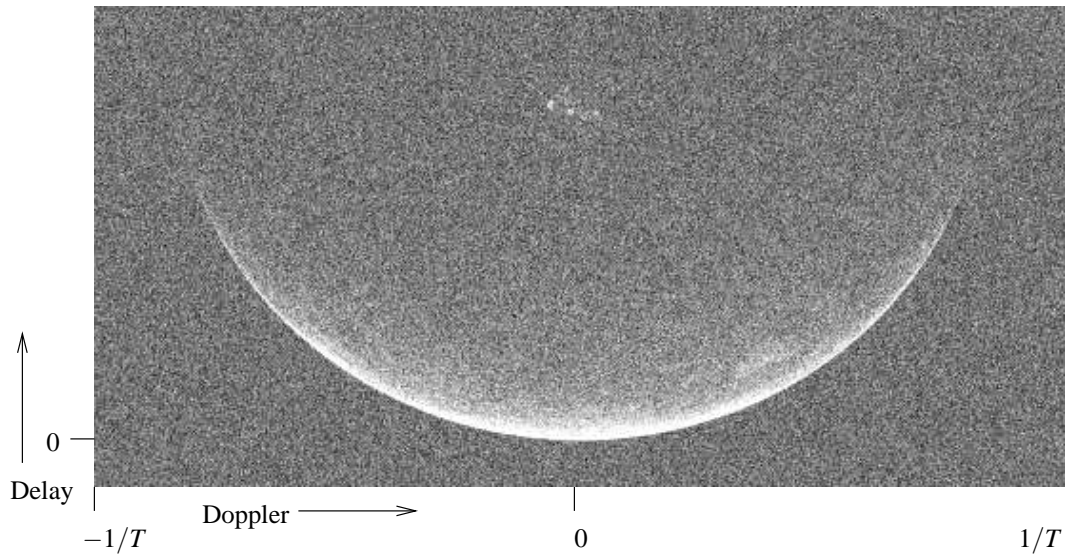
Figure A.9 Mercury imaged by long-code method. Doppler aliasing is mitigated, and the clutter sidelobes are randomized, and appear as additive noise rather than in any one particular area. The additive noise in this image is not solely due to the use of the long-code method. A radar system with ≈ 8 dB lower SNR was used to generate this data set as compared to the system which generated Figure A.7, as both short- and long-code data sets from the same radar system were not available.

Two conclusions regarding waveform design and processing can be made from the above examples: i) re-processing of existing, repetitive code data sets with different signal processing algorithms can yield usable images without the effects of Doppler folding but with periodic clutter, and ii) use of a longer than normal PN sequence, on the order of the coherent integration time necessary for the required cross-range resolution, can yield images without Doppler folding or periodic clutter.

A.1.2 Comparison of long-code and subset code

The advantage of the long-code method over the subset code method is evident when viewing the extent of the leading edge leakage into the high Doppler bins in the output delay-Doppler array. Such leakage is not present in a long-code image shown in Figure A.9. By effectively changing the range compression filters for each realization of the coherent integration, the long-code method randomizes the undesirable sidelobe response of any one

realization of the delay-Doppler ambiguity function and averages this sidelobe response across multiple incoherent-averaging periods. The disadvantage of the long-code technique is the appearance of the undesired leakage as an overall increase in the noise floor of the imaging process, which can mask weaker features. The randomized leakage of the long-code method cannot be estimated and removed by deconvolution in the image domain, as the exact sidelobe structure of the imaging point spread function changes on a pulse-to-pulse basis.

Since the subset code processor can be implemented as a convolution with two fixed FIR filters, one of length 512 and one of length 511, the processing can proceed nearly as efficiently as with standard code processing.

A.1.3 Subset-code processing of long-code data

Long-code imaging can be viewed as a subset code problem, in which a savings of three to five in processing time can be realized if significant downsampling of the data is carried out between the range and Doppler matched filtering stages. The smoothing and decimation process implemented in standard long-code processing of each delay bin (Harmon, 2002), which is implemented as a time-domain convolution in standard processors, is mathematically equivalent to convolution with a length N filter to form the output of all delay bins. Transforming time-domain convolution to the frequency-domain yields the speed improvement noted above for slightly overspread targets such as Mercury. For massively overspread targets such as Mars, there is no downsampling of the output of the convolution process, and therefore no corresponding savings in processing time. For highly overspread targets, the coherent integration time required to form the images is very short, and therefore the equivalent range compression filter is only 1 or 2 bauds long. Transforming this short convolution to the frequency domain does not save but, in fact, adds to the processing time.

The improvement to total processing time for standard long-code imaging is not as dramatic as the reduction in processing time for the equivalent length subset code processing. The reason for this discrepancy is that the values of the taps in the range compression filter

in subset code processing do not change over the course of the observation, so transformation of the filter taps to the frequency domain requires only one FFT for each filter at the outset of processing. For fast long-code processing, the values of the taps of the range compression filter change over the course of the observation, so the frequency domain representation of the filters must be computed for each coherent integration interval, which results in many additional FFTs over the course of an observing run.

A.2   Windowing to suppress long-code sidelobes

The ambiguity function is a powerful tool for examining the effectiveness of the radar imaging process. As has been noted earlier, high sidelobes in the ambiguity function lead to artifacts in the output delay-Doppler array, degrading the final image. By studying the ambiguity function of the long-code imaging process, we can identify deficiencies and develop filters to alleviate the artifacts created by the deficiencies.[2]

A.2.1   Long-code ambiguity function

Since the coded sequence changes for each pulse in the train, analysis of the long-code ambiguity function is best carried out using a random signal analysis approach. As many coherent integration intervals are averaged incoherently to form the final output delay-Doppler array, we use a statistical description of the average ambiguity function of a coherent integration interval.

The statistical ambiguity function of the random BPSK waveform was first described by Lin (1985) at the Naval Research Laboratory. If the period of the PN sequence generator used for the long-code is many times the total observation interval, then the subsets of the output of the PN generator can be taken as uncorrelated. We summarize the method of Lin (1985) in this derivation.[3]

---

[2]We thank Bryan Butler of the National Radio Astronomy Observatories for prompting this exploration by asking the question, "Why don't you window your transforms in long-code processing?"

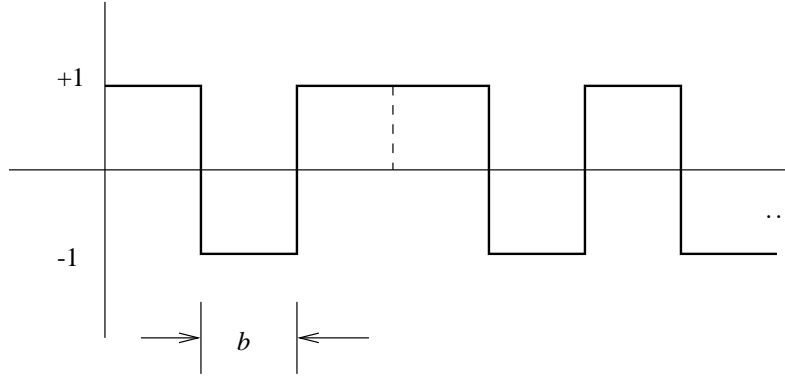[3]An alternate formulation for the ambiguity function of a random PN waveform has been given by Harmon (2002).

Figure A.10 Random BPSK waveform. The baud or "chip" length b sets the range resolution of the waveform. The voltage state -1 or 1 can occur with equal probability.

Define the random binary phase-shift keyed signal as

$$\psi(t) = \sum_{n=1}^{N} P_n(t)e^{j(2\pi f_0 t + \theta_n)}, \ \ 0 \le t \le Nb \tag{A.1}$$

where

$$P_n(t) = \begin{cases} 1 & (n-1)b \le t \le nb \\ 0 & \text{else} \end{cases}, \tag{A.2}$$

$\theta_n \in \{0, \pi\}$ with equal probability, f_0 is the carrier frequency, and N is the number of bauds of length b in the section of waveform as shown in Figure A.10 (Cook and Bernfeld, 1967). Let $c_n = e^{j\theta_n} \in \{-1, 1\}$. From the definition of the ambiguity function χ,

$$\begin{aligned} \chi(kb + \tau', f_d) &= \chi_p(\tau', f_d) \sum_{n=1}^{N} c_n c_{n+k} e^{-j2\pi f_d (n-1)b} \\ &\quad + \chi_p(b - \tau', f_d) \sum_{n=1}^{N} c_n c_{n+k+1} e^{-j2\pi f_d nb}, \\ &\hspace{4cm} 0 < \tau < \infty, \ -\infty < f_d < \infty \end{aligned}$$

where

$$\chi_p(\tau', f_d) = \int_0^{b-\tau'} e^{-j2\pi f_d t} \, dt, \ 0 < \tau' < b. \tag{A.3}$$
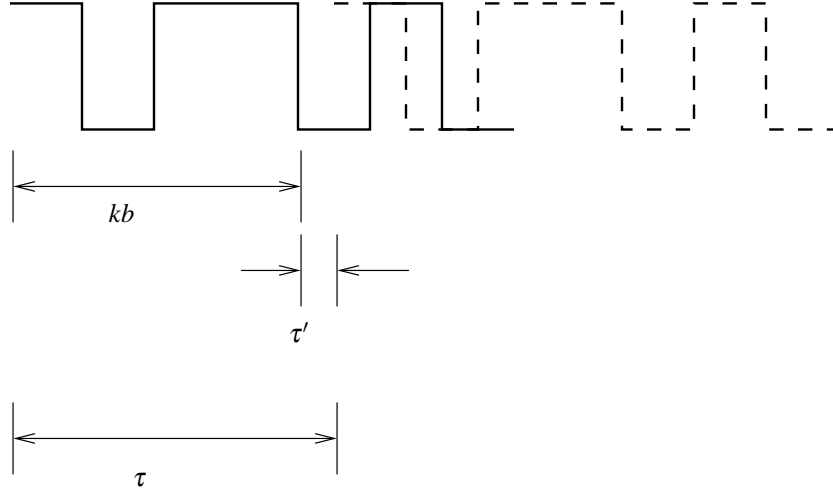
Figure A.11 Lagged waveform. To compute the ambiguity function at zero Doppler, the random PN waveform is delayed by an integer number of bauds k and by a fractional baud τ' (see text).

We define the quantities τ' and k by

$$\tau = kb + \tau', \quad \begin{cases} 0 < \tau' < b \\ k = 0, 1, \dots \end{cases} \tag{A.4}$$

where k represents an integer number of bauds of lag, and τ' represents the fractional baud lag. As k can be any non-negative integer, the definition of the ambiguity function has been changed to allow cross correlation of Nb seconds of the random BPSK sequence with any other length Nb section of the sequence. Temporarily setting $f_d = \tau' = 0$, we see

$$\chi(kb, 0) = b \sum_{n=1}^{N} c_n c_{n+k}. \tag{A.5}$$

This is the autocorrelation function for a random binary sequence.

The ambiguity function for zero Doppler and integer offsets is

$$|\chi(kb, 0)|^2 = b^2 E \left[\sum_{n=1}^{N} \sum_{m=1}^{N} c_n c_m c_{n+k}^* c_{m+k}^* \right]. \tag{A.6}$$

To evaluate the expectation in (A.6), recall that $c_i \in \{-1, 1\}$ with equal probability, and note that the expected value of a product of unity powers of c_i is

$$E[c_i] = E[c_i c_j] = \ldots = 0, \tag{A.7}$$

and the expected value of a product of squares c_i^2 is

$$E[c_i^2] = E[c_i^2 c_j^2] = \ldots = 1. \tag{A.8}$$

The ambiguity function for zero Doppler and integer offsets (A.6) thus becomes

$$|\chi(kb, 0)|^2 = \begin{cases} b^2 N^2, & k = 0 \\ b^2 N, & k = 1, 2, \ldots \end{cases}, \tag{A.9}$$

with a range sidelobe ratio of

$$\frac{|\chi(kb, 0)|^2_{k \neq 0}}{|\chi(0, 0)|^2} = \frac{b^2 N}{b^2 N^2} = \frac{1}{N}. \tag{A.10}$$

For non-zero Doppler ($f_d \neq 0$) and fractional offsets ($\tau' \neq 0$) it can be shown (Lin, 1985) that the ambiguity function is

$$|\chi(\tau, f_d)|^2 = \begin{cases} \mathrm{sinc}^2[f_d(b - \tau')] \, N^2(b - \tau')^2 \left[\frac{\mathrm{sinc}^2(f_d N b)}{\mathrm{sinc}^2(f_d b)} \right] \\ + \, \mathrm{sinc}^2(f_d \tau') N \tau'^2 & k = 0 \\ \\ \mathrm{sinc}^2[f_d(b - \tau')] \, N(b - \tau')^2 \\ + \, \mathrm{sinc}^2(f_d \tau') \, N \tau'^2 & k = 1, 2, \ldots \end{cases} .$$

Normalizing by substituting $\bar{\tau} = \tau'/b$, $\bar{f}_d = f_d N b$ gives

$$\left| \bar{\chi}(\bar{\tau}, \bar{f}_d) \right|^2 = \left| \chi(\bar{\tau}, \bar{f}_d) \right|^2 / N^2 b^2. \tag{A.11}$$

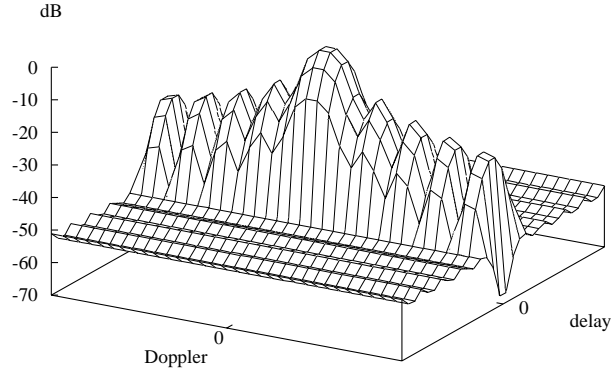This ambiguity function is shown in Figure A.12.

Figure A.12 Statistical ambiguity function of the long-code method. For the typical long-code waveform employed for 3.5 cm wavelength imaging of Mercury, the ambiguity surface exhibits low delay sidelobes, but high Doppler sidelobes. At 40 μsec baud, the matched filter length is $N = 2^{16}$, leading to $10\log_{10}(2^{16}) = 48$ dB delay sidelobes.

Viewing the resolution elements around the peak in the ambiguity diagram, it is apparent that though the ambiguity diagram has good sidelobe suppression (-50 dB) along the delay axis, there are significant sidelobes (-12 dB) along the Doppler axis. These high Doppler sidelobes result from lack of weighting in the Fourier analysis which forms the bank of Doppler matched filters. This window response is commonly called the rectangular or Dirichlet window in the signal processing literature. We can view $\chi(\tau, f_{\mathrm{d}})$ as the multiplication of the ambiguity function of a width b pulse with the discrete time Fourier transform of the Dirichlet kernel

$$\chi(\tau, f_{\mathrm{d}}) = \chi_p(\tau', f_{\mathrm{d}}) \sum_{n=1}^{N} w_n c_n c_{n+k} e^{-j2\pi f_{\mathrm{d}}(n-1)b} \ldots \tag{A.12}$$

where $w_n = 1$, $n = 1, \ldots, N$ are the Dirichlet window weights with discrete time Fourier transform

$$w_n \xrightarrow{|\mathscr{F}|^2} |W(f_{\mathrm{d}})|^2 = N^2 \frac{\mathrm{sinc}^2(f_{\mathrm{d}}Nb)}{\mathrm{sinc}^2(f_{\mathrm{d}}b)}. \tag{A.13}$$
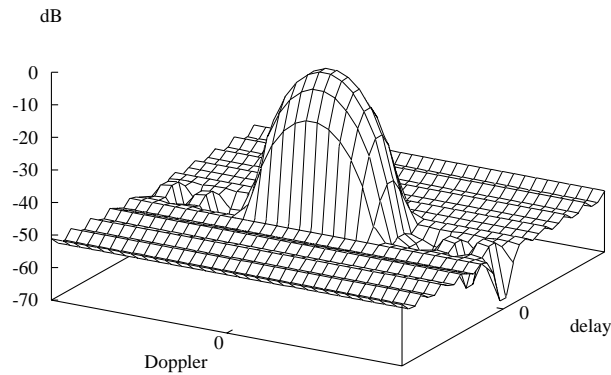
Figure A.13 Hamming weighted ambiguity function for Mercury imaging at 3.5 cm wavelength. The Hamming sidelobe ratio of ≈ 43 dB closely matches the delay sidelobe level for Mercury imaging of 48 dB, resulting in a near-ideal thumbtack-like ambiguity surface. Some broadening of the main lobe occurs as a result of windowing.

As the sidelobes contribute to blurring in the final image, we can form a more accurate image by modifying the imaging function to eliminate the sidelobes. This is achieved by changing the windowing function at the input to the Doppler matched filtering process.

A.2.2   Hamming and Dolph windows

There are many standard windows available for improving the sidelobe response, such as the Hamming window. Applying the Hamming window results in the Doppler sidelobe suppression shown in Figure A.13. The Hamming window exhibits a fixed amount of sidelobe suppression equal to ≈ 43 dB near the main lobe. For the case of Mercury imaging at 3.5 cm as shown in Figure A.13, the Hamming window coincidently results in a level of sidelobe attenuation in the Doppler dimension equal to that produced by the coherent integration time sets for the delay dimension.
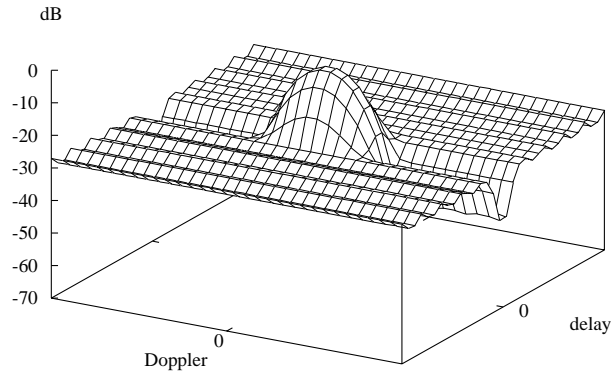
Figure A.14 Hamming weighted ambiguity function for 3.5 cm Mars imaging. At 40 μsec baud, the matched filter length is $N = 2^9$, resulting in $10\log_{10}(1/2^9) = -27$ dB delay sidelobes. A mismatch between delay and Doppler sidelobe suppression produces a non-ideal ambiguity surface. The delay sidelobes are ≈ 15 dB higher than the Hamming-weighed Doppler sidelobes.

The needed amount of Doppler sidelobe suppression is not fixed, however. One characteristic of the long-code ambiguity function not previously mentioned specifically, but apparent when viewing the result in (A.9), is that the sidelobe level of the ambiguity function in the delay dimension is $1/N$. As discussed in Section 2.1.2, the total coherent integration time for one particular chosen delay resolution or radar baud will change as a function of planet rotation angular velocity.

The shorter coherent integration time in the case of Mars imaging at 3.5 cm results in ≈ 30 dB delay sidelobes as shown in Figure A.14. The sidelobe attenuation provided by the Hamming window is too great in this case, as Figure 2.13 shows that an idealized thumbtack ambiguity function has flat skirts (Rihaczek, 1969).

We introduce here a design method for long-code imaging, adapting the amount of Doppler sidelobe suppression so that the sidelobe level in the delay and Doppler dimensions can be equalized, while keeping the Doppler resolution consistent with the range resolution.

The Dolph window is rare among data windows in that it has an adjustable design parameter, which makes it possible to trade main lobe width for lower sidelobes, without
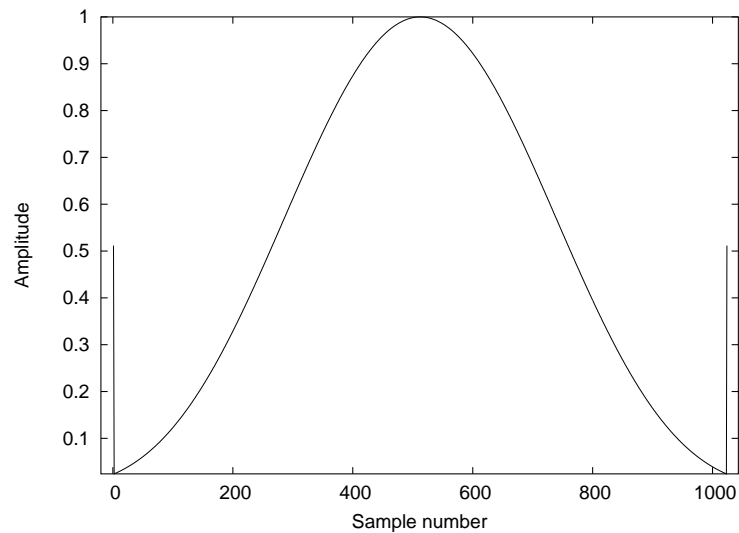
Figure A.15 Length 1023 Dolph-Chebyshev window. The distinguishing characteristic of the Dolph window is the impulse at each end of the weighting function. This impulse is responsible for the equiripple property of the sidelobe response.

changing the length of the window. Dolph (1946) developed the window as a weighting function for broadside linear arrays of antenna elements. The window is computed from a series of Chebyshev polynomials, and is sometimes called the Dolph-Chebyshev window as a result. An example Dolph weighting function is shown in Figure A.15. Note the impulses at either end of the weighting function. Dolph sought a uniform sidelobe response across the sidelobe region, and the Chebyshev polynomial construction allows this.[4] The Dolph window did not find much use in its original application because the impulse at opposite ends of the weighting function is difficult to achieve in linear antenna arrays. As long as it does not cause numerical instability in the integration of the final result, the impulse is readily applied in digital signal processing. For the FFT transforms used in current long-code imaging, numerical stability is not an issue for digital floating point arithmetic.

---

[4]The equal ripple property is also desirable in FIR filter design, and Chebyshev polynomials were found ideal for the task by Parks and McClellan (1972). The correspondence between windowing functions and filter design is well known—see for example Oppenheim and Schafer (1989)—and will not be discussed further.

The Dolph-Chebyshev window sidelobe level is specified readily. The window's normalized frequency response is

$$\left|\bar{W}(\bar{f}_{\mathrm{d}})\right|^2 = \frac{\left|T_{N-1}\left(z_0\cos(\pi\bar{f}_{\mathrm{d}}/N)\right)\right|^2}{\left|T_{N-1}(z_0)\right|^2}, \tag{A.14}$$

where the Chebyshev polynomial $T_M(z)$ is defined as

$$T_M(z) = \begin{cases} \cos[M\cos^{-1}(z)], & |z| \le 1 \\ \cosh[M\cosh^{-1}(z)], & |z| > 1 \end{cases}, \tag{A.15}$$

where for a desired sidelobe level of $-20\log_{10}(s)$ dB the scaling constant z_0 is

$$z_0 = \cosh\left[\frac{1}{(N-1)}\cosh^{-1}(s)\right]. \tag{A.16}$$

In order to apply the Dolph window to long-code processing, it is necessary to derive a relationship between sidelobe attenuation in the delay and Doppler dimensions. Equalizing the delay and Doppler sidelobes causes the ambiguity function to approach the ideal thumbtack-like point spread function as shown in Figure A.16. The sidelobes in this figure should be compared to those in Figure A.14, where Hamming weighting produces over 15 dB of unwanted sidelobe attenuation.

A.2.3   Consideration of cross-range resolution

Use of windowing broadens the central lobe of the ambiguity function in the f_{d} dimension. This necessitates correlating for a longer time Nb to equalize range and cross range resolutions. Longer correlation times result in a lower sidelobe level in the delay dimension, which decreases as

$$10\log_{10}(1/N). \tag{A.17}$$

Simultaneously optimizing the range and cross range sidelobes requires solution of the transcendental equation

$$\sqrt{N} = T_{N-1}\left[\frac{\cos(\pi/2N)}{\cos(\pi f_c/f_{\mathrm{s}})}\right], \tag{A.18}$$
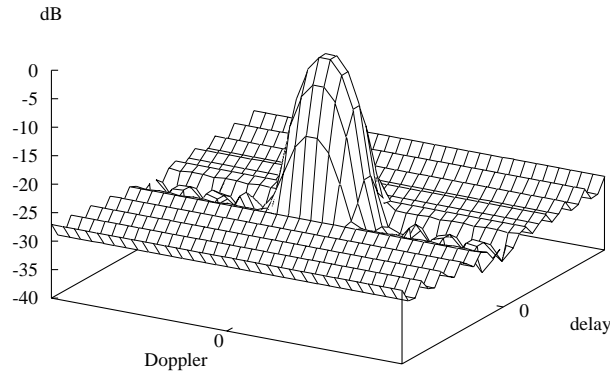
Figure A.16 Dolph weighted ambiguity function for Mars imaging. By correctly choosing the Dolph window coefficients to match the ≈ 27 dB attenuation in the delay dimension, the sidelobe suppression in the Doppler and delay dimensions is equalized.

where the cutoff frequency is $f_c = \omega_s f_0 b / 2$.

The solution point N' for a particular imaging problem is easily obtained numerically. That a solution to the expression (A.18) exists as can be seen from Figure A.17, a plot of both sides of the equation. As the Chebyshev polynomial increases exponentially, a solution point indicated by the intersection of the two curves exists for all non-trivial window lengths. Applying the design equation to the Mars imaging problem results in the equalization of delay and Doppler sidelobes of the long-code imaging process as shown in Figure A.16. The criterion for equal resolution in the delay and Doppler dimensions can be incorporated into the equation by including the effect of the broadening of the main lobe into the equation for delay sidelobe level.

Applying the proper window to the data before Doppler matched filtering results in an enhancement to the apparent quality of the radar imaging system as the contributions from sidelobes of the imaging function are equalized in both the delay and Doppler dimensions. The resulting ambiguity function more closely approximates the ideal thumbtack point spread function. There are two caveats to this enhancement. First, the broadening of the main lobe of the Dirichlet window requires increasing the coherent integration time to
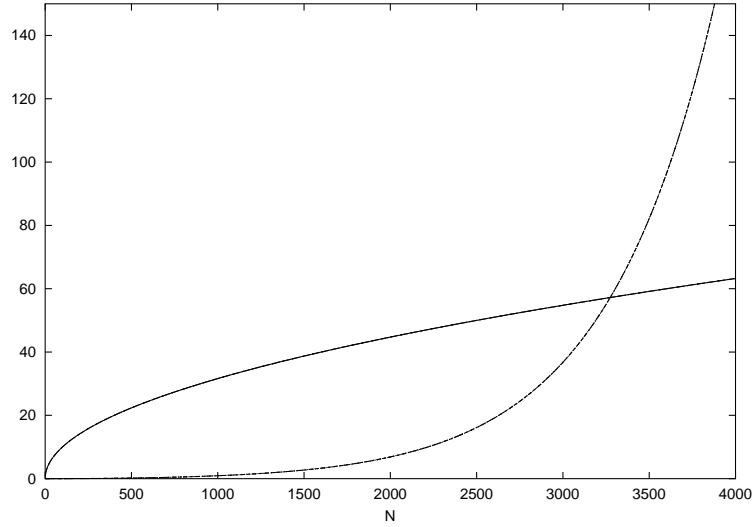
Figure A.17 Plot of both sides of (A.18) for Mars imaging at $f_0 = 8560$ MHz (3.5 cm) and baud $b = 40$ μsec. The intersection point of the curves gives the window length $N' \approx 3300$ which equalizes the delay and Doppler sidelobe levels of the long-code radar ambiguity function.

achieve equal resolution in the delay and Doppler dimensions, and this increase can cause blurring due to migration through delay-Doppler resolution elements. The limit for unfocused processing must be adhered to, or an alternate focusing method (Stacy, 1993) must be employed. Second, weighting of the received pulse causes a loss in peak SNR due to the filter mismatch (Urkowitz et al., 1973). For a window of length N, the loss factor γ is defined by

$$\gamma = \frac{N \sum_{n=1}^{N} w_n^2}{\left(\sum_{n=1}^{N} w_n \right)^2}, \tag{A.19}$$

and the Dolph-Chebyshev weights w_n for N even are

$$w_n = \frac{2}{N} \left\{ s + 2 \sum_{k=1}^{N/2-1} T_{N-1} \left[z_0 \cos \left(\frac{\pi k}{N} \right) \right] \cos \left[\frac{2\pi k}{N} \left(n - \frac{N+1}{2} \right) \right] \right\}. \tag{A.20}$$

$$n = 1, \ldots, N \tag{A.21}$$

Parameters z_0 and s are as defined previously. This decrease can be alleviated using periodogram methods (Welch, 1967), but the typical 50 percent overlap of such methods can

result in a doubling of the processing time.

A.3   Orthogonality of sub codes of the long-code waveform

As mentioned in in Section 2.3.2, the individual sub-codes of the long-code method can be considered essentially random since the generator can be started in any state. Here we use statistical signal analysis to show that the baseband, unmodulated sub codes of the long-code method are orthogonal, and hence exhibit one property of optimal delay-Doppler codes Guey and Bell (1998). We emphasize that satisfying this condition does not mean that the long-code method—which uses time-division multiplexing of the pulses on a RF carrier—is optimal in practice.

Let $s(t)$ be the complex baseband transmitted signal defined on the interval $0 \leq t \leq T$. A single point scatterer is located at delay τ_0 and Doppler v_0. The corresponding baseband received signal from a point scatterer after demodulation is

$$r(t) = s(t - \tau_0)e^{j2\pi v_0 \tau}e^{j\phi}, \tag{A.22}$$

where the term $e^{j\phi} = e^{j2\pi f_0 \tau_0}$ accounts for accumulated carrier phase at frequency f_0, and τ is the matched filter delay. Assume the signal is passed through a matched filter for a signal $q(t)$, where

$$q(t) = s(t - \tau)e^{j2\pi v \tau} \tag{A.23}$$

is the signal from a point scatterer assumed to be at point (τ, v). The differences

$$(\tau - \tau_0, v - v_0) \tag{A.24}$$

then represent the difference between the assumed location of the point scatterer and the actual location at (τ_0, v_0). The matched filter for the initial point is

$$\begin{aligned} h_{\tau,v}(t) &= q^*(T - t) \\ &= s^*(T - t - \tau)e^{-j2\pi v(T - t)}, \end{aligned} \tag{A.25}$$

where the asterisk represents complex conjugation, and the filter has been delayed by a time T to make the solution causal.

The maximum output of the filter occurs at $t = T$. To demonstrate this, we can compute the convolution of $q(t)$ and $h_{\tau,\nu}(t)$ evaluated at $t = T$

$$q(t) * h_{\tau,\nu}(t) = \int_{-\infty}^{\infty} s(\gamma - \tau) e^{j2\pi\nu\gamma} s^*[T - (t - \gamma) - \tau] e^{-j2\pi\nu[T-(t-\gamma)]} \, d\gamma, \qquad (A.26)$$

where $*$ in binary operator context denotes the convolution operation and γ represents the time shift inherent in the convolution. Evaluating the convolution at $t = T$ gives

$$q(t) * h_{\tau,\nu}(t) = \int_{-\infty}^{\infty} s(\gamma - \tau) s^*(\gamma - \tau) \, d\gamma = E_{\text{s}}, \qquad (A.27)$$

where E_{s} is the signal energy, the maximum output of the matched filter.

The response of the matched filter to the incident wave from the point scatterer at (τ_0, ν_0) evaluated at time $t = T$ is denoted by $\mathcal{O}_T(\tau, \nu)$. The response is computed as

$$\begin{aligned} \mathcal{O}_T(\tau, \nu) &= r(t) * h_{\tau,\nu}(t)|_{t=T} \\ &= \int_{-\infty}^{\infty} s(\gamma - \tau_0) e^{j2\pi\tau_0\gamma} e^{j\phi} s^*[T - (t - \gamma) - \tau] e^{-j2\pi\nu[T-(t-\gamma)]} \, d\gamma \Big|_{t=T} \\ &= e^{j\phi} \int_{-\infty}^{\infty} s(\gamma - \tau_0) s^*(\gamma - \tau) e^{j2\pi(\nu_0-\nu)\gamma} \, d\gamma. \qquad (A.28) \end{aligned}$$

Making a change of dummy integration variable $\xi = \gamma - \tau_0$

$$\begin{aligned} \mathcal{O}_T(\tau, \nu) &= e^{j\phi} \int_{-\infty}^{\infty} s(\xi) s^*[\xi - (\tau - \tau_0)] e^{j2\pi(\nu_0-\nu)(\xi+\tau_0)} \, d\xi \\ &= e^{j\phi} e^{j2\pi(\nu_0-\nu)\tau_0} \int_{-\infty}^{\infty} s(\xi) s^*[\xi - (\tau - \tau_0)] e^{j2\pi(\nu_0-\nu)\xi} \, d\xi \\ &= e^{j\phi} e^{j2\pi(\nu_0-\nu)\tau_0} \int_{-\infty}^{\infty} \chi_s(\tau - \tau_0, \nu - \nu_0) \qquad (A.29) \end{aligned}$$

where the ambiguity function of the signal $s(t)$, denoted by $\chi_s(\tau, \nu)$ is

$$\chi_s(\tau, \nu) = \int_{-\infty}^{\infty} s(t) s^*(t - \tau) e^{j2\pi\nu t} \, dt. \qquad (A.30)$$

With this notation, Guey and Bell (1998) continue to show that for a set of N signals $s_i(t), i = 0, \ldots, N-1$ transmitted on independent channels, the response of the array of matched filters $\mathscr{O}_T^i(\tau, v)$ to a single point scatterer at (τ_0, v_0) is

$$
\begin{aligned}
\mathscr{O}_T^0(\tau, v) &= e^{j\phi} e^{j2\pi(v-v_0)\tau_0} \chi_{s_0}(\tau - \tau_0, v - v_0) \\
&= \tilde{\chi}_{s_0}(\tau - \tau_0, v - v_0) \\
\mathscr{O}_T^1(\tau, v) &= e^{j\phi} e^{j2\pi(v-v_0)\tau_0} \chi_{s_1}(\tau - \tau_0, v - v_0) \\
&= \tilde{\chi}_{s_1}(\tau - \tau_0, v - v_0) \\
&\;\;\vdots \\
\mathscr{O}_T^{N-1}(\tau, v) &= e^{j\phi} e^{j2\pi(v-v_0)\tau_0} \chi_{s_{N-1}}(\tau - \tau_0, v - v_0) \\
&= \tilde{\chi}_{s_{N-1}}(\tau - \tau_0, v - v_0).
\end{aligned}
\tag{A.31}
$$

These response signals can be combined coherently to form

$$
\mathscr{O}_T^C(\tau, v) = e^{j\phi} e^{j2\pi(v-v_0)\tau_0} \sum_{i=0}^{N-1} \chi_{s_i}(\tau - \tau_0, v - v_0)
\tag{A.32}
$$

which has the form of a point target at (τ_0, v_0) imaged by a new point spread function

$$
C(\tau, v) = \sum_{i=0}^{N-1} \chi_{s_i}(\tau, v)
\tag{A.33}
$$

and is called the "composite ambiguity function."

Using this foundation, Guey and Bell (1998) define the following terms and prove the following two-part theorem:

Definition: For a set of N signals $s_0(t), s_1(t), \ldots, s_{N-1}(t)$ each with total energy

$$
E_s = \sum_{i=0}^{N-1} \int_{-\infty}^{\infty} |s_i(t)|^2 \, dt,
\tag{A.34}
$$

define the volume $V_{\text{amb}}^{(c)}$ under their associated composite ambiguity function $C(\tau, \nu)$ as

$$V_{\text{amb}}^{(c)} = \int_{-\infty}^{\infty} \int_{-\infty}^{\infty} \left| \sum_{i=0}^{N-1} \chi_{s_i}(\tau, \nu) \right|^2 d\tau d\nu. \tag{A.35}$$

Theorem:

1. The volume $V_{\text{amb}}^{(c)}$ under the composite ambiguity function satisfies

$$\frac{E_s^2}{N} \leq V_{\text{amb}}^{(c)} = \sum_{n=0}^{N-1} \sum_{m=0}^{N-1} \left| \int_{-\infty}^{\infty} s_n(t) s_m^*(t) \, dt \right|^2 \leq E_s^2. \tag{A.36}$$

2. Furthermore, the minimum volume is achieved when $\{s_0(t), s_1(t), \ldots, s_{N-1}(t)\}$ is a set of equal-energy orthogonal signals. $\diamond$

This theorem shows that by proper choice of an optimal signal set $\{s_i(t)\}$, the volume under the composite ambiguity function can be reduced, resulting in an overall imaging point spread function with better resolution characteristics than a single repeated waveform.

We now show that randomly chosen, binary phase-shift-keyed waveforms satisfy the conditions of this theorem. From the definition of the long-code signal in Section A.2.1 we can see that any two length M sections of the truly random code will satisfy the orthogonality requirement of part 2 of the theorem. Neglecting fractional offsets, the expected value of the inner product of the two sections $s_1(t), s_2(t)$ of long-code will be

$$E \int_{-\infty}^{\infty} s_1(t) s_2^*(t) \, dt = E \sum_{i=0}^{M-1} (\delta c_{1,n})(\delta c_{2,n}) \tag{A.37}$$

where δ is the pulse baud or chip length, $c_{1,n}, c_{2,n} \in \{-1, 1\}$ with probability $\frac{1}{2}$ are the chip values, and E is the expectation operator. Since $E(c_{1,n} c_{2,n}) = 0$ for random chips, we have

$$E \sum_{i=0}^{M-1} (\delta c_{1,n})(\delta c_{2,n}) = \delta^2 \sum_{n=0}^{M-1} E(c_{1,n} c_{2,n}) = 0 \tag{A.38}$$

The energy of the selected subset signal is

$$E_{\mathrm{s}} = E \int_{-\infty}^{\infty} s_i(t) s_i^*(t) \, dt = \delta^2 \sum_{i=0}^{M-1} E(c_i^2) = \delta^2 M \tag{A.39}$$

which is independent of the particular instance of the random binary waveform. Since subsets of the random binary waveform satisfy (1) and (2) of the theorem, it would appear that they form an optimal set of diversity waveforms for enhanced resolution imaging.

There is one difficulty in satisfying the constraint under which the theorem was proved. Guey and Bell (1998) assume that the signals are sent at the same time and at the same carrier frequency by non-interfering channels. In practice, it is desirable to send all pulses on the same channel via time-division multiplexing, as suggested by Sivaswamy (1982). But Zeoli (1982) points out, as do Guey and Bell (1998), that even if motion of the target through range-Doppler cells is insignificant over the time interval NT needed to transmit N pulses, a transmit time dependent total carrier phase term $e^{j2\pi v_0 iT}$ is present in the received signal for each pulse, so that the output of the matched filters becomes

$$
\begin{aligned}
\mathcal{O}_T^0(\tau, v) &= \tilde{\chi}_{s_0}(\tau - \tau_0, v - v_0) \\
\mathcal{O}_T^1(\tau, v) &= e^{-j2\pi v_0 T} \tilde{\chi}_{s_1}(\tau - \tau_0, v - v_0) \\
&\vdots \\
\mathcal{O}_T^{N-1}(\tau, v) &= e^{-j2\pi v_0 (N-1)T} \tilde{\chi}_{s_1}(\tau - \tau_0, v - v_0).
\end{aligned}
\tag{A.40}
$$

These terms may be combined by estimating the unknown Doppler $\hat{v}_0$ and multiplying each received signal $s_i(t)$ by the correction term $e^{-j2\pi \hat{v}_0 iT}$ before coherent combining. The problem with this method is that if there is a second point target in the target space at location (τ_1, v_1), then there will be a mismatch between this target's velocity v_1 and the estimated velocity for the first point target $\hat{v}_0$. The response of the coherent sum to this additional target will be

$$\mathcal{O}_T^C(\tau, v) = \sum_{i=0}^{N-1} e^{j2\pi(v_1 - v_0)iT} \chi_{s_i}(\tau - \tau_1, v - v_1) \tag{A.41}$$

This is called "defocusing" by Guey and Bell (1998) or "self noise" by Harmon (2002).

Guey and Bell (1998) suggest that an iterative technique may be attempted to correct for this issue, and note that when the field of the radar is filled with many strongly scattering point sources, unbiased estimation becomes problematic.

A.4   Summary

Long-code imaging can be cast into a more general form called subset codes, which improves the processing efficiency. The subset code technique may also be used to process conventional repetitive code data sets to remove the effects of Doppler aliasing, albeit again at the cost of higher clutter. The higher clutter of long-code processing can be partially offset by the choice of a Dolph window that equalizes the sidelobe ratio in the delay and Doppler dimensions. The long-code waveform ultimately fails to meet the optimal waveform criteria, even though the individual, baseband sub-pulses satisfy the orthogonality condition of the theorem of Guey and Bell (1998). We desire to image a natural surface which effectively consists of many point sources, one in each resolution cell of the imaging radar's field of view. All resolution elements contribute a "defocus" or "self-noise" term when using a time-division-multiplexed, modulated waveform. Guey and Bell (1998) remains an interesting information-theoretic result, but implementing the concept for radar imaging of natural surfaces remains an unsolved problem.

Appendix B

Mercury Polar Region Maps

This appendix collects the 6 km resolution radar maps of Mercury from Chapter 5 and presents them co-registered with optical data from the Mariner 10 mission prepared by Robinson et al. (1999).[1] Each polar stereographic projection is broken up into six panels and presented in order according to the key in Figure B.1 on page 164.
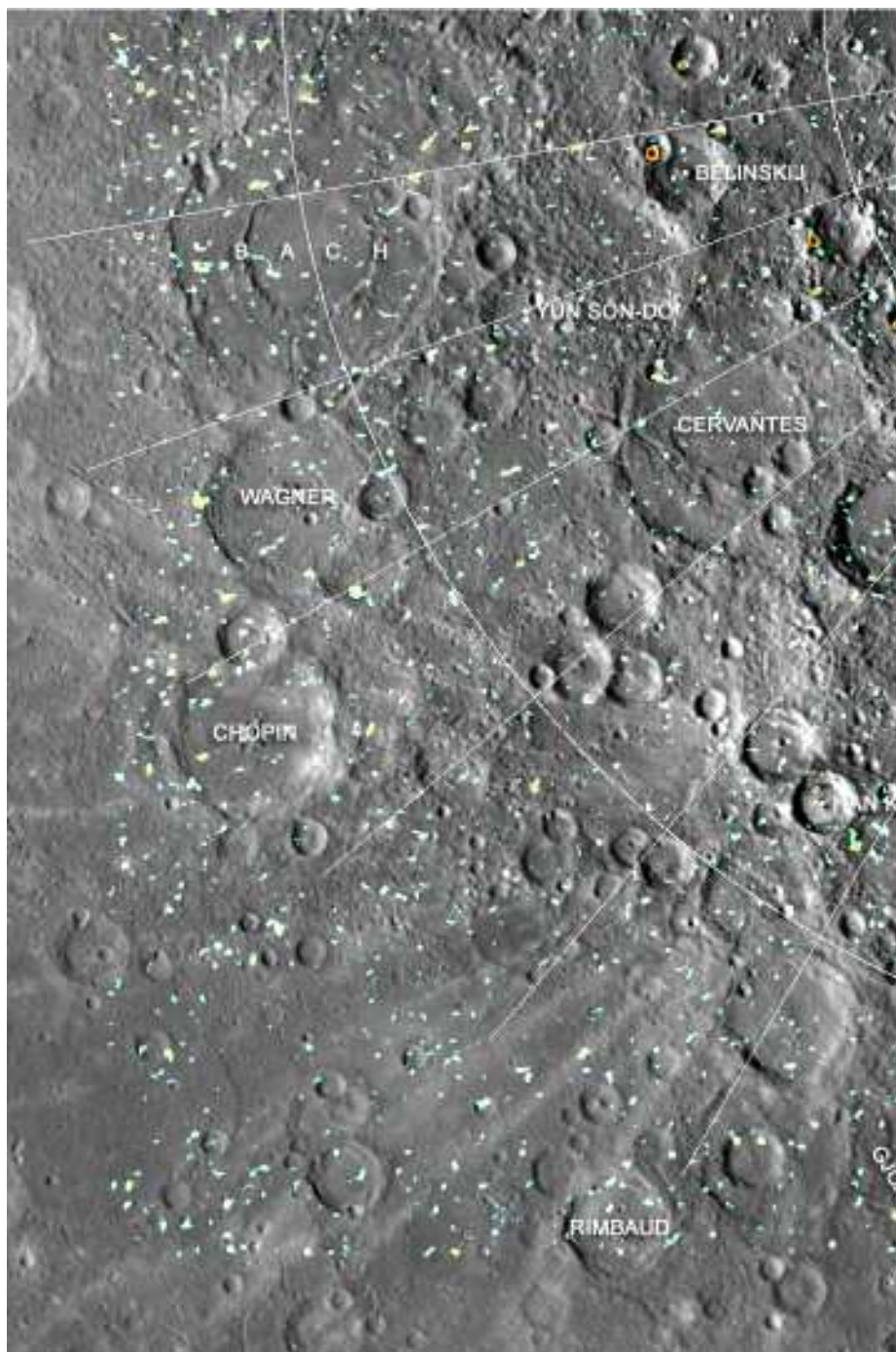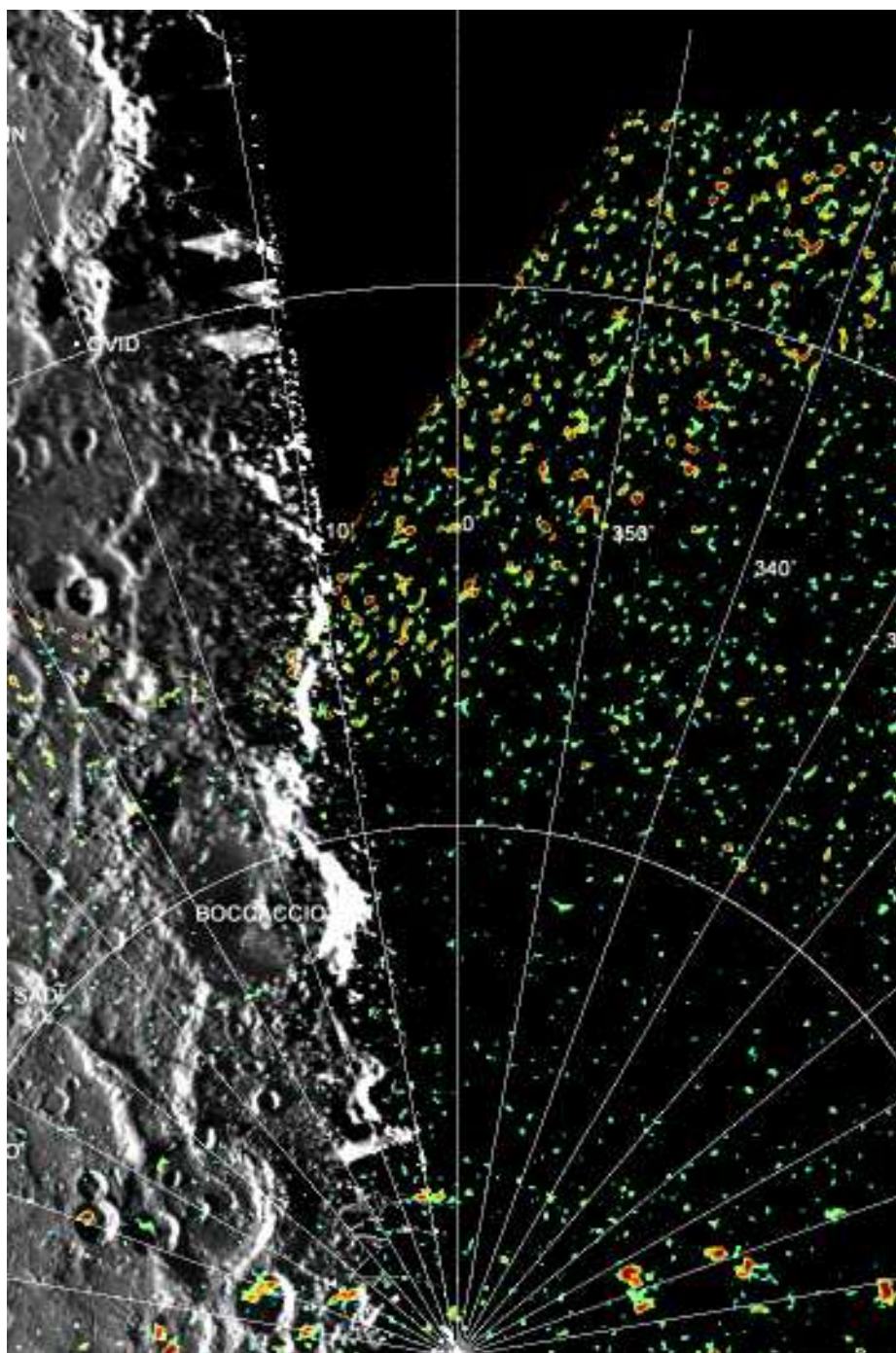
---

[1]Electronic versions are available on-line from `http://cps.earth.northwestern.edu/merc.html`

1	3	5
2	4	6

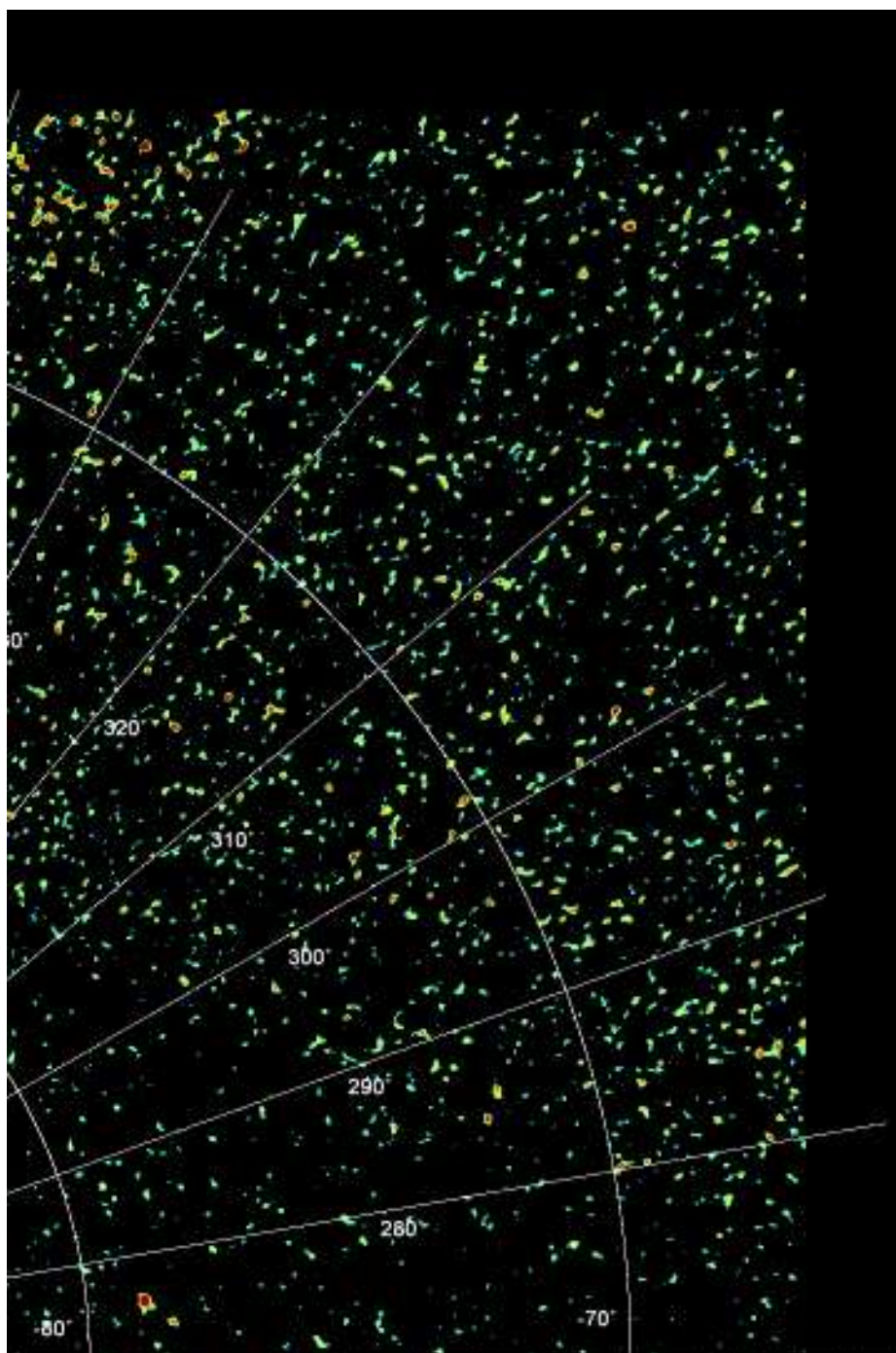**Figure B.1** Key for alignment of Mercury image plates.
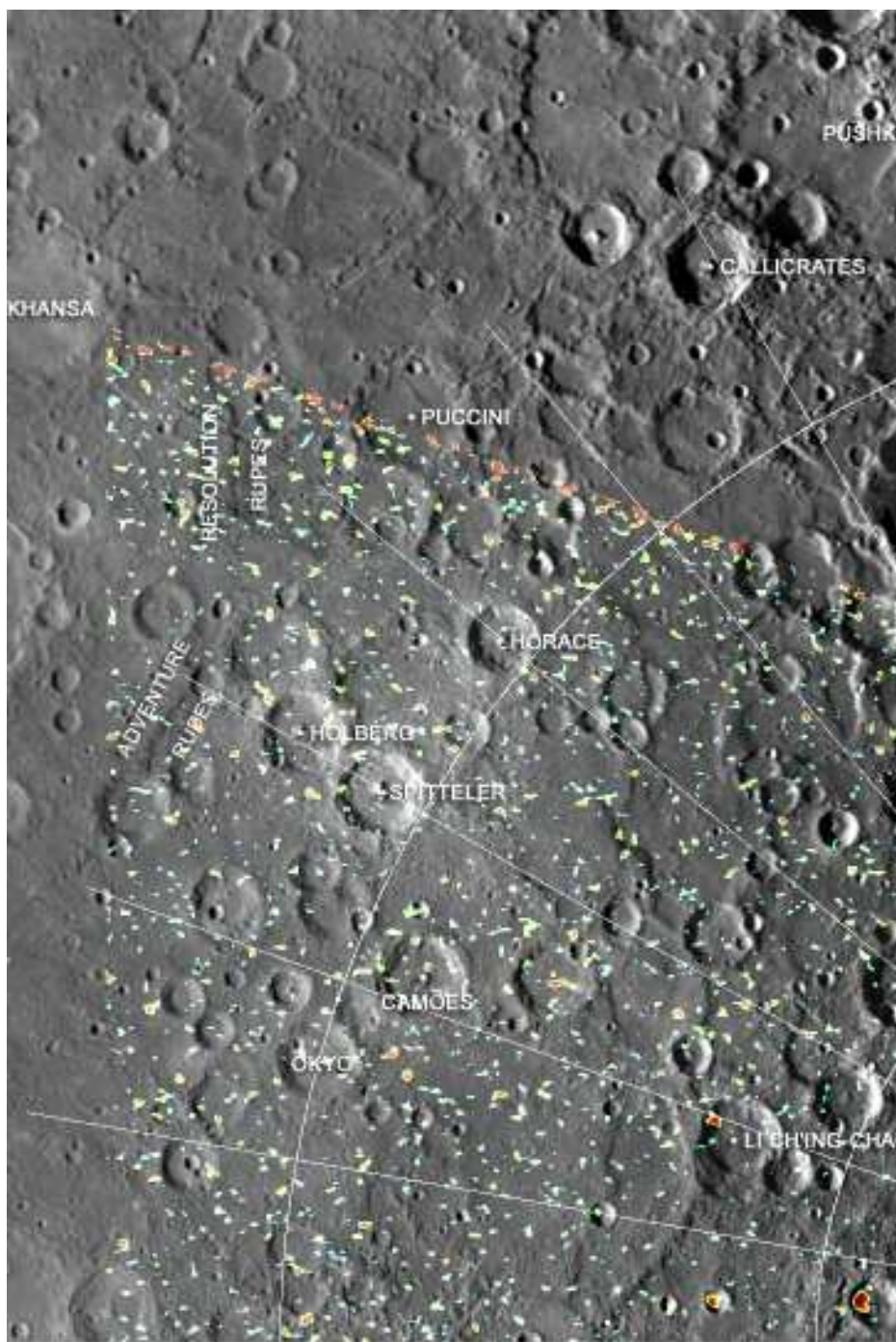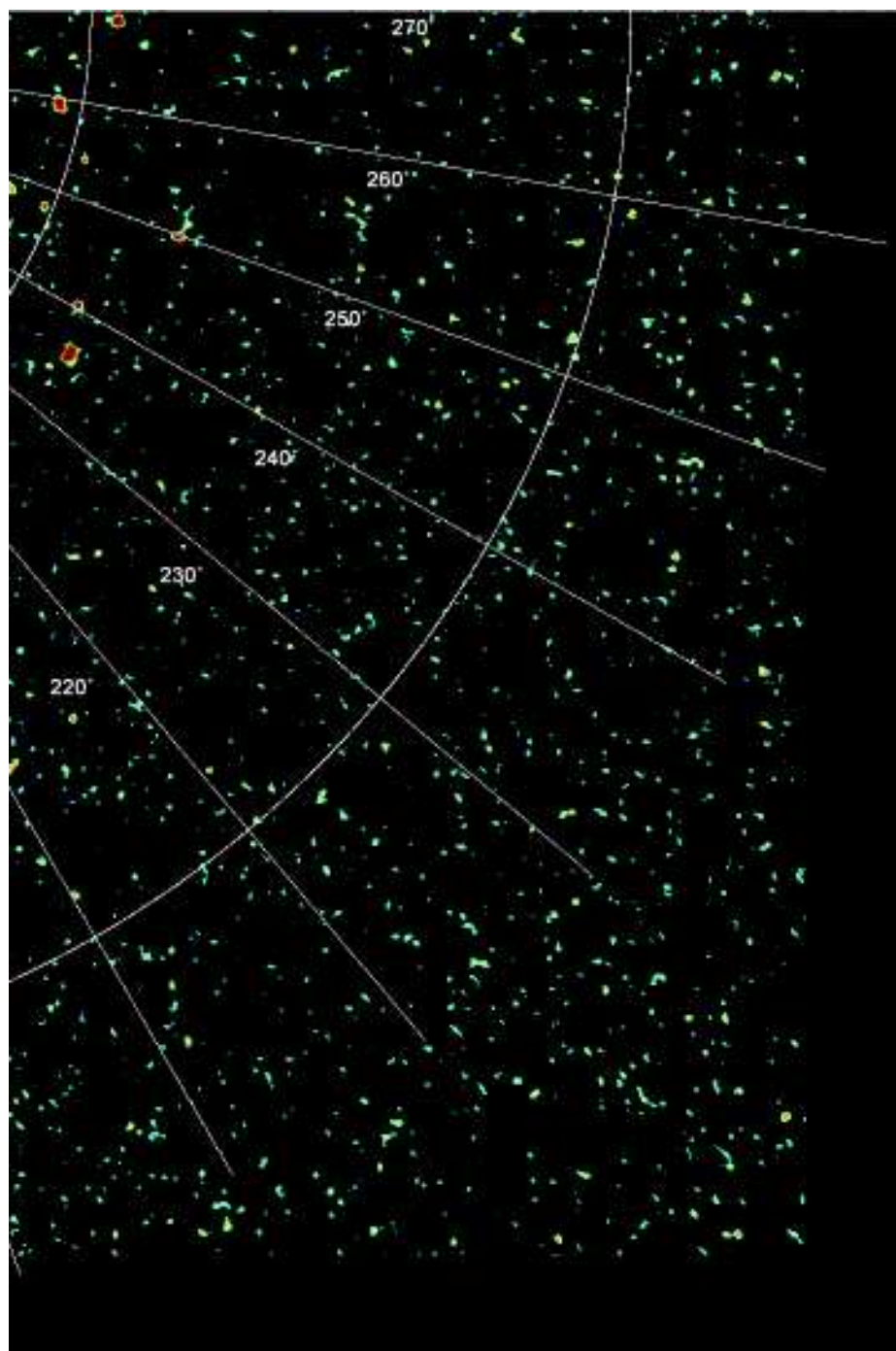
South Pole Plate 1
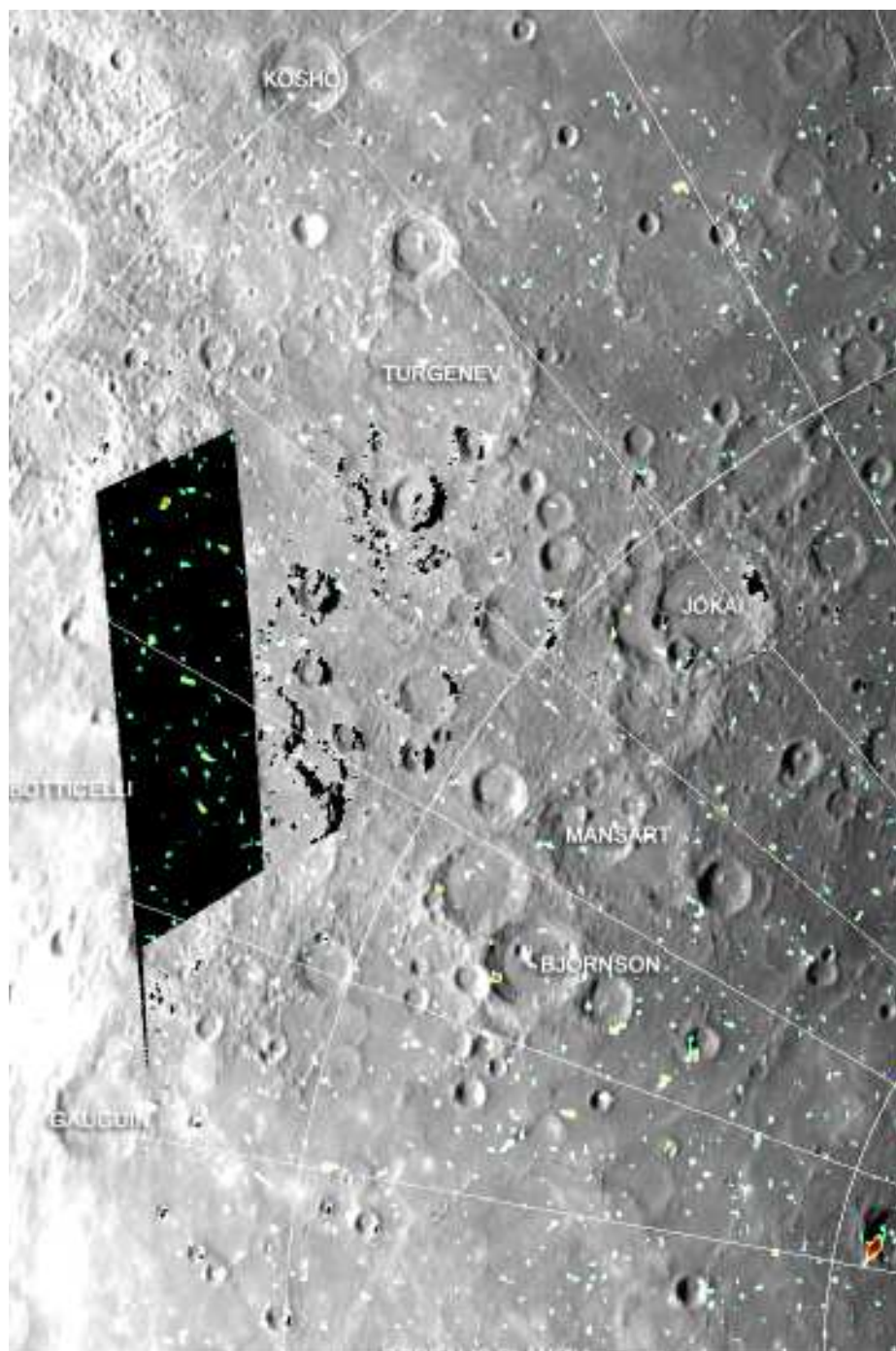
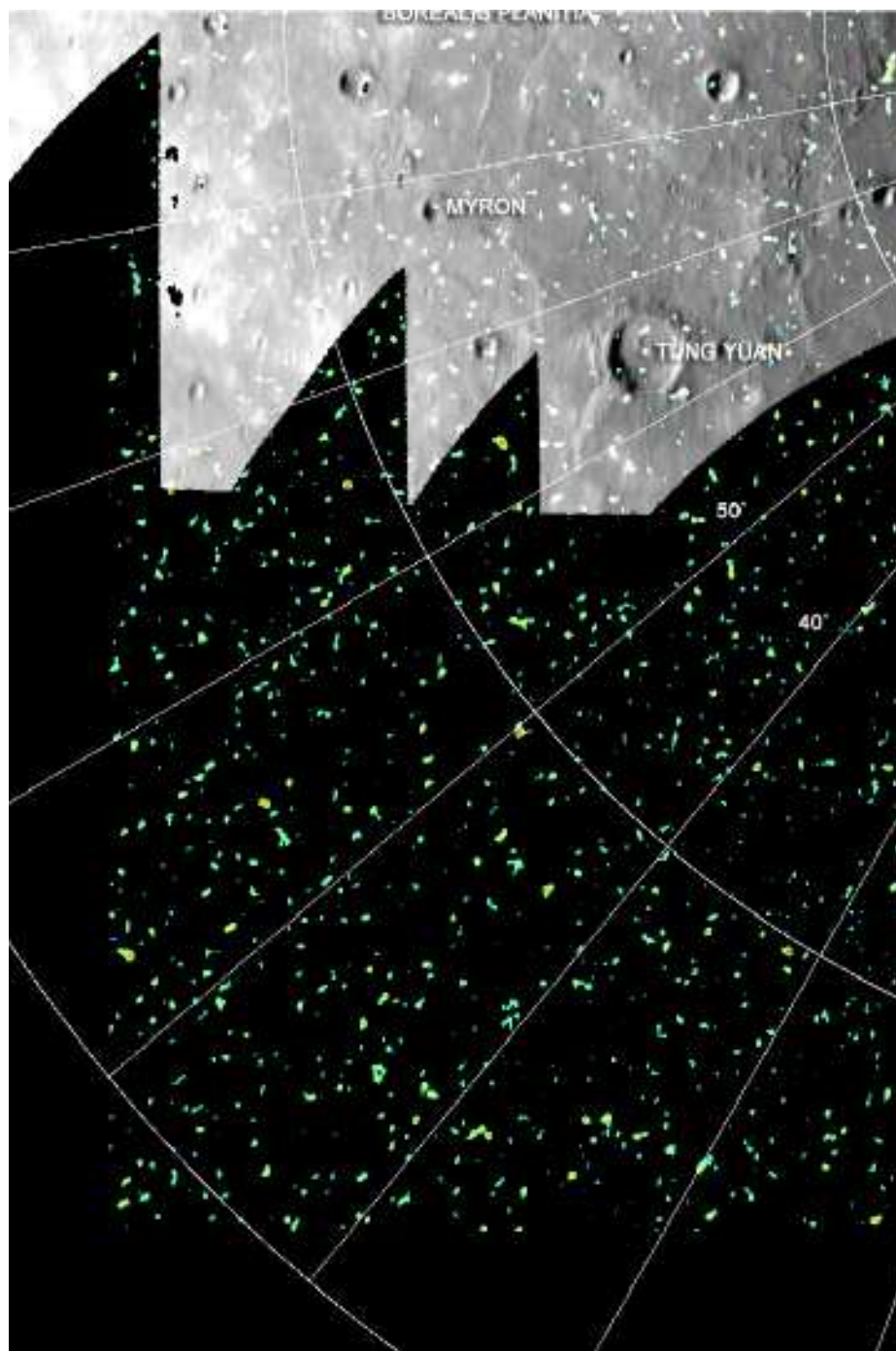South Pole Plate 2

South Pole Plate 3
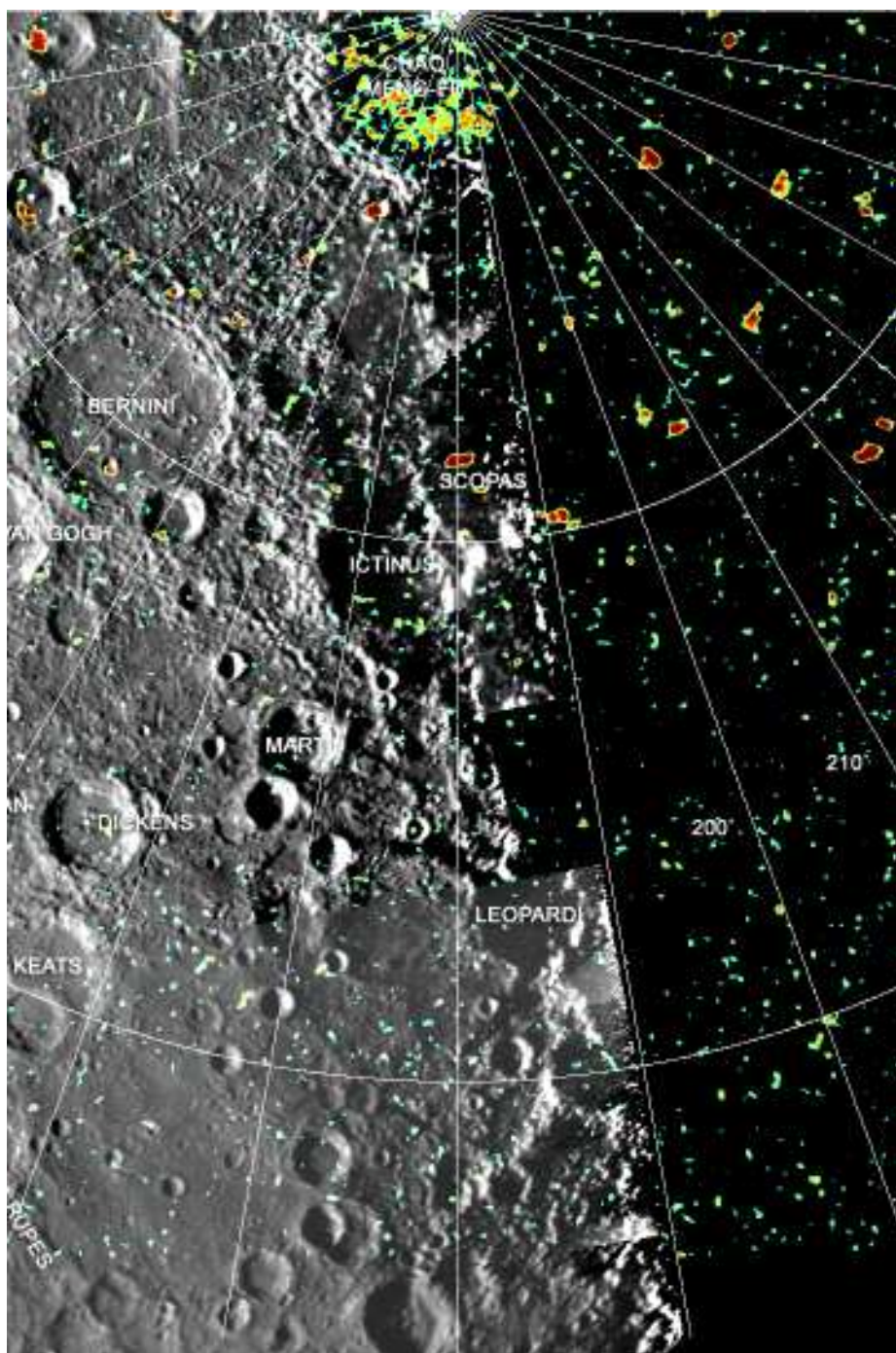
South Pole Plate 4
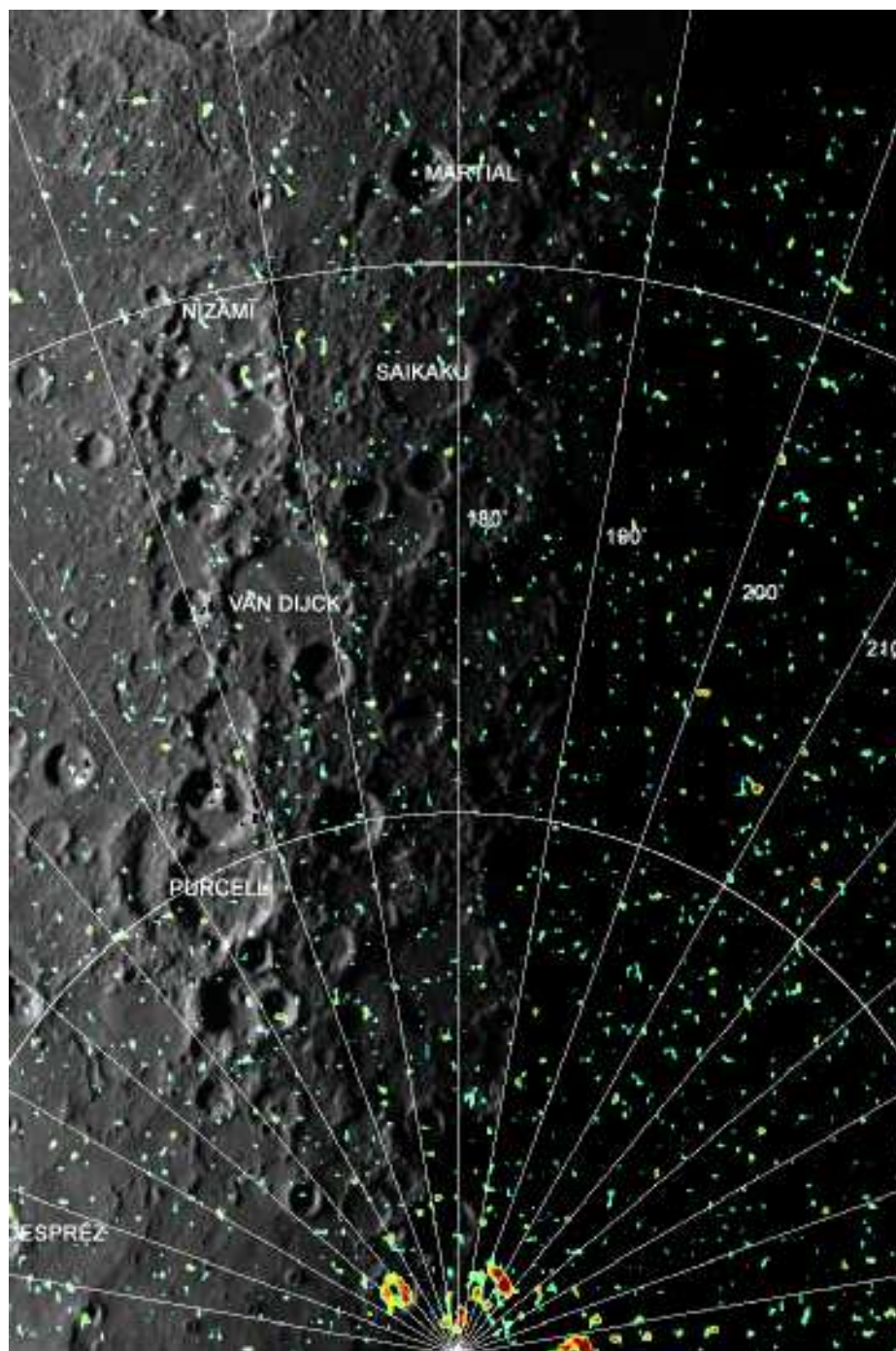
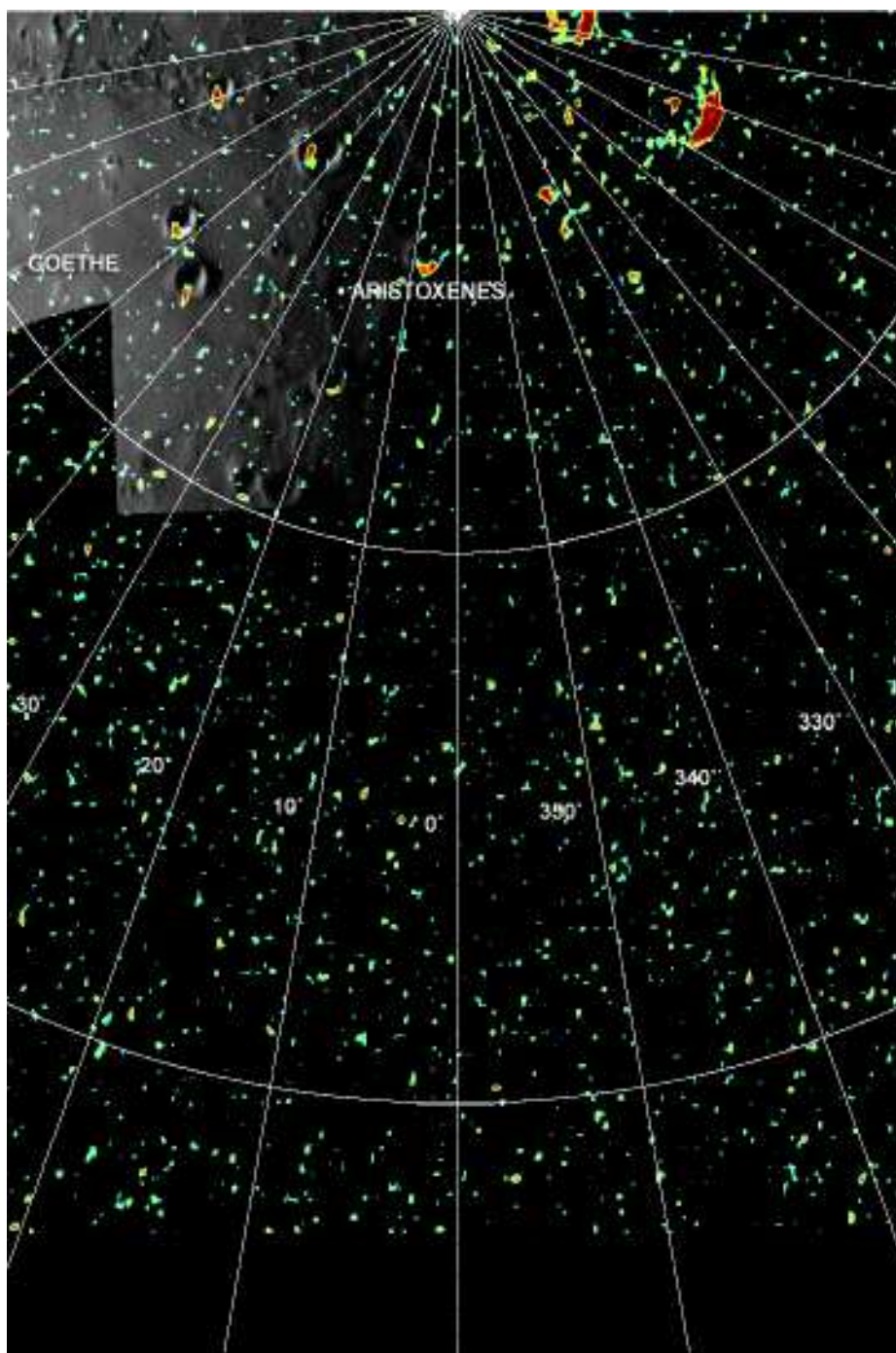South Pole Plate 5

South Pole Plate 6
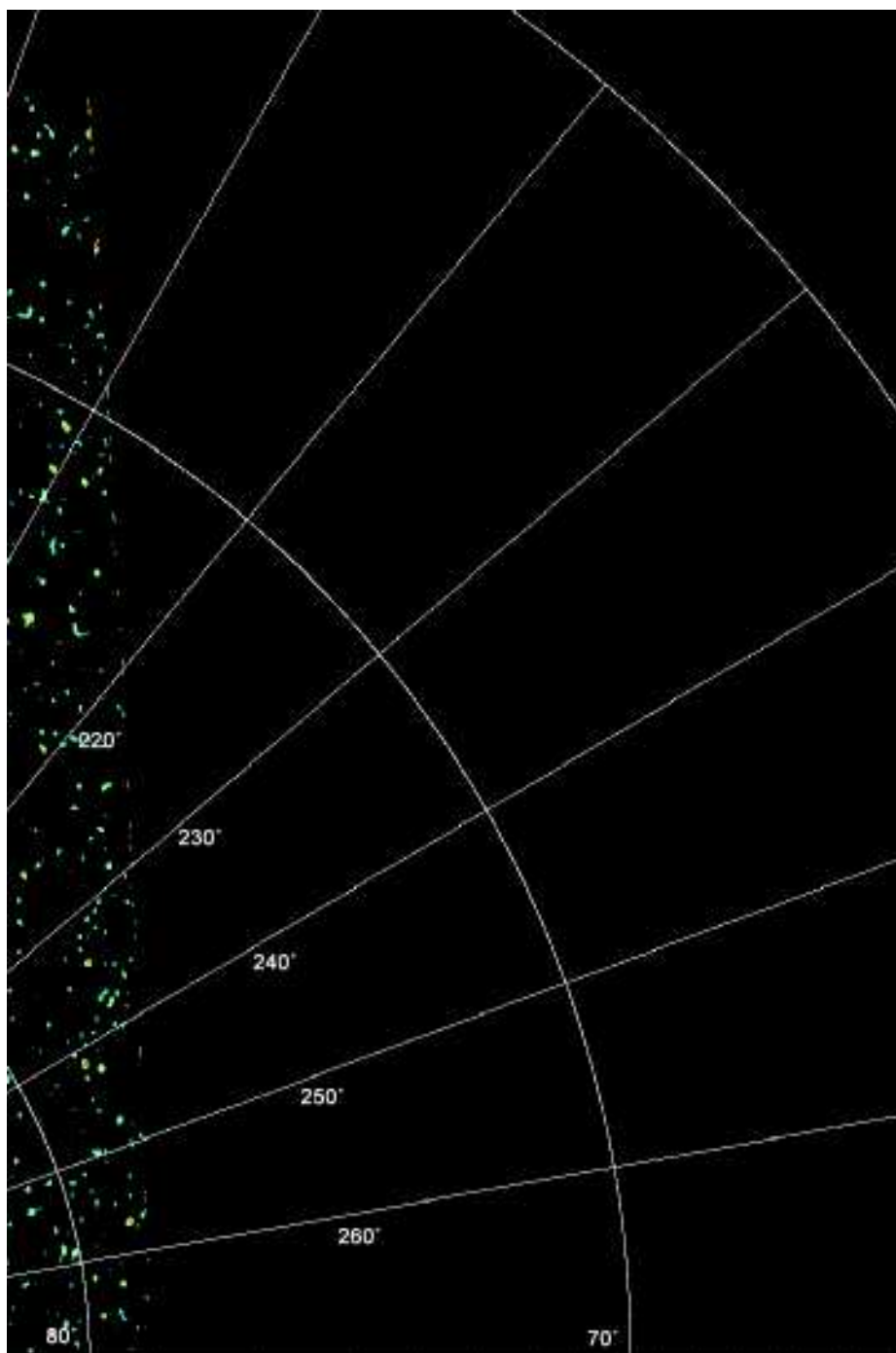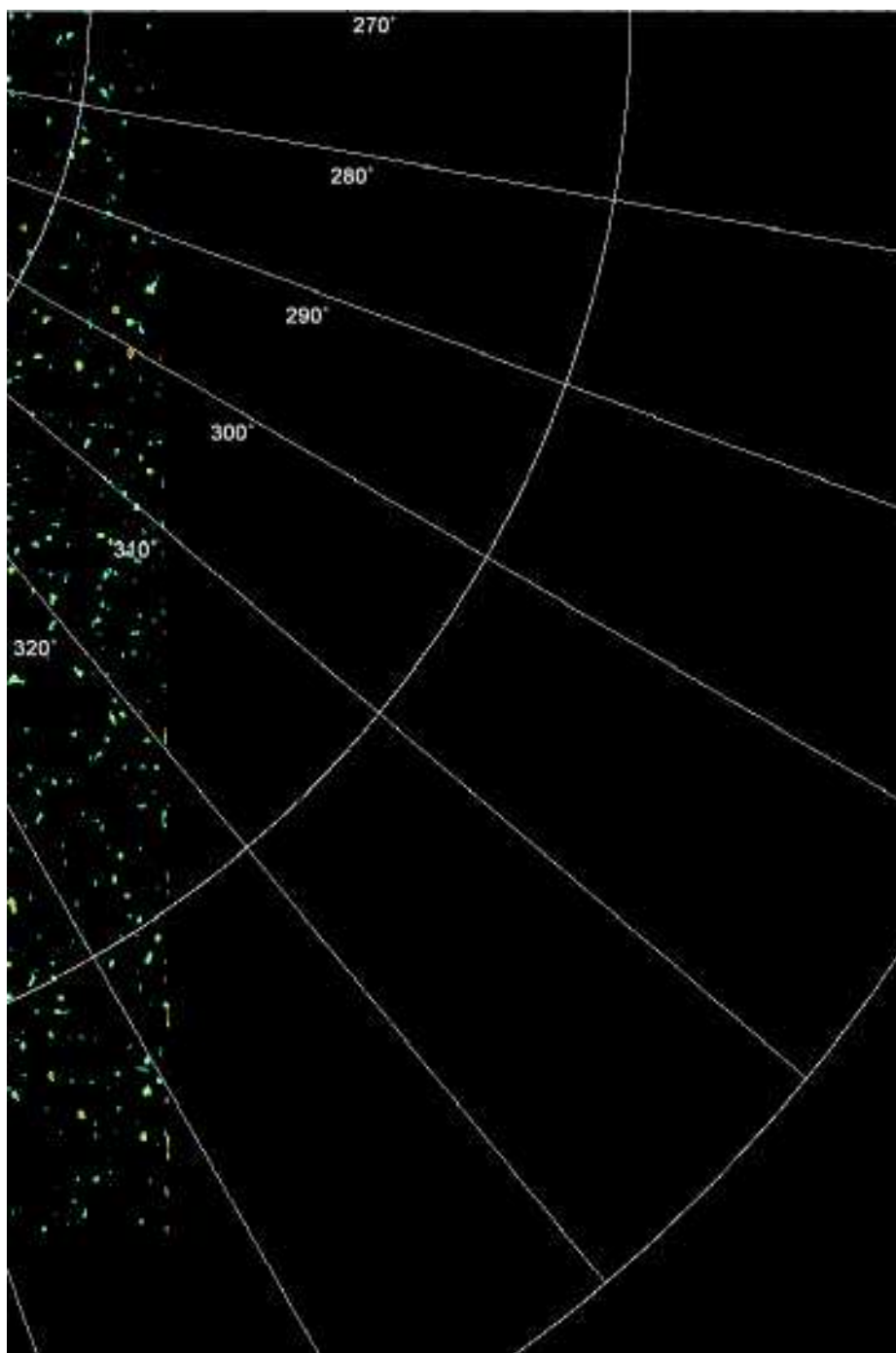
North Pole Plate 1

North Pole Plate 2

North Pole Plate 3

North Pole Plate 4

North Pole Plate 5

North Pole Plate 6

Bibliography

Bay, Z. (1947). Reflection of microwaves from the Moon. *Hungarica Acta Physica*, 1:1–6.

Bibring, J., Langevin, Y., Poulet, F., Gendrin, A., Gondet, B., Berthé, M., Soufflot, A., Drossart, P., Combes, M., Bellucci, G., Moroz, V., Mangold, N., Schmitt, B., and OMEGA team, t. (2004). Perennial water ice identified in the south polar cap of Mars. *Nature*, 428:627–630.

Black, G. J. (1997). *Modeling the radar properties of the icy Galilean satellites as a coherent backscatter effect*. PhD thesis, Cornell University.

Black, G. J., Campbell, D. B., and Harmon, J. K. (2002). New 70-cm wavelength radar images of Mercury's north polar region. In *33rd Annual Lunar and Planetary Science Conference*, number 1946.

Black, G. J., Campbell, D. B., and Ostro, S. J. (2001). Icy Galilean satellites: 70 cm radar results from Arecibo. *Icarus*, 151:160–166.

Booker, H. G. and Clemmow, P. C. (1950). The concept of an angular spectrum of plane waves and its relation to that of polar diagram and aperture distribution. *Proceedings of the Institution of Electrical Engineers*, 97(45):11–17.

Bose, R., Freedman, A., and Steinberg, B. D. (2002). Sequence CLEAN: a modified deconvolution technique for microwave images of contiguous targets. *IEEE Transactions on Aerospace and Electronic Systems*, 38(1):89–97.

Bracewell, R. N. (1956). Strip integration in radio astronomy. *Australian Journal of Physics*, 9(2):198–217.

Bracewell, R. N. (1958). Radio interferometry of discrete sources. *Proceedings of the IRE*, 46(1):97–105.

Bracewell, R. N. (2000). *The Fourier Transform and its Applications*. McGraw Hill, 3rd edition.

Bracewell, R. N. (2003). *Fourier Analysis and Imaging*. Plenum Press.

Bracewell, R. N. and Roberts, J. A. (1954). Aerial smoothing in radio astronomy. *Australian Journal of Physics*, 7(4):615–640.

Bridle, A. H. (1996). A hitch-hiker's guide to VLA observing strategies. Technical report, National Radio Astronomy Observatory.

Butler, B. J. (1994). *3.5 cm Radar Investigations of Mars and Mercury: Planetological Implications*. PhD thesis, California Institute of Technology.

Butler, B. J., Muhleman, D. O., and Slade, M. A. (1993). Mercury: Full-disk radar images and the detection and stability of ice at the north pole. *Journal of Geophysical Research*, 98:15003–15023.

Butrica, A. J. (1996). *To See the Unseen: A History of Planetary Radar Astronomy*. National Aeronautics and Space Administration.

Campbell, B. A., Campbell, D. B., Chandler, J. F., Hine, A. A., Nolan, M. C., and Perillat, P. J. (2003a). Radar imaging of the lunar poles. *Nature*, 426:137–138.

Campbell, D. B., Black, G. J., Carter, L. M., and Ostro, S. J. (2003b). Radar evidence for liquid surfaces on Titan. *Science*, 302(5644):431–434.

Campbell, D. B., Chandler, J. F., Ostro, S. J., Pettengill, G. H., and Shapiro, I. I. (1978). Galilean satellites: 1976 radar results. *Icarus*, 34:254–267.

Campbell, D. B., Chandler, J. F., Pettengill, G. H., and Shapiro, I. I. (1977). Galilean satellites of Jupiter: 12.6 centimeter radar observations. *Science*, 196:650–653.

Campbell, M. J. and Ulrichs, J. (1969). Electrical properties of rocks and their significance for lunar radar observations. *Journal of Geophysical Research*, 74:5867–5881.

Carpenter, R. L. and Goldstein, R. M. (1963). Radar observations of Mercury. *Science*, 142(359):381.

Carr, M. H., Belton, M. J. S., Chapman, C. R., Davies, M. E., Geissler, P., Greenberg, R., McEwen, A. S., Tufts, B. R., Greeley, R., Sullivan, R., Head, J. W., Pappalardo, R. T., Klaasen, K. P., Johnson, T. V., Kaufman, J., Senske, D., Moore, J., Neukum, G., Schubert, G., Burns, J. A., Thomas, P., and Veverka, J. (1998). Evidence for a subsurface ocean on Europa. *Nature*, 391(6665):363–365.

Cassen, P., Reynolds, R. T., and Peale, S. J. (1979). Is there liquid water on Europa? *Geophysical Research Letters*, 6(9):731–734.

Chadwick, R. B. and Cooper, G. R. (1972). Measurement of ocean wave heights with random signal radar. *IEEE Transactions on Geoscience Electronics*, 9(4):216–221.

Clark, B. G. (1980). An efficient implementation of the algorithm CLEAN. *Astronomy and Astrophysics*, 89:377–378.

Clark, P. E., Jurgens, R. F., Thompson, T. W., Robinett, L., Chan, F., Brokl, S., Franck, C., and Stone, E. (1986). Mercury: New results from dual polarization measurements at X-band. In *17th Lunar and Planetary Science Conference*, pages 135–136.

Clark, R. N., Singer, R. B., Owensby, P. D., and Fanale, F. P. (1980). Galilean satellites: High precision near infrared spectrophotometry (0.65–2.5 μm) of the leading and trailing sides. *Bulletin of the American Astronomical Society*, 12:713–714.

Cook, C. E. and Bernfeld, M. (1967). *Radar Signals*. Academic Press.

Cooper, G. R. and Purdy, R. J. (1968). Detection, resolution, and accuracy in random signal radar. Technical Report TR-EE 68-16, Purdue University.

De Vries, C. H. and Harmon, J. K. (1994). The rotation axis of Mercury: A new determination from radar observations. *Bulletin of the American Astronomical Society*, 26:1376.

DeWitt, J. H. and Stodola, E. K. (1949). Detection of radio signals reflected from the Moon. *Proceedings of the IRE*, 37(3):229–242.

Dolph, C. L. (1946). A current distribution for broadside arrays which optimizes the relationship between beam width and side-lobe level. *Proceedings of the IRE*, 34(6):335–348.

Elspas, B. (1955). *A radar system based on statistical estimation and resolution considerations*. PhD thesis, Stanford University.

Eshleman, V. R. (1986). Radar glory from buried craters on icy moons. *Science*, 234:587–590.

Evans, J. V. (1969). Radar studies of planetary surfaces. *Annual Reviews of Astronomy and Astrophysics*, 7:201–248.

Evans, J. V. and Hagfors, T., editors (1968). *Radar Astronomy*. McGraw-Hill.

Feldman, W. C., Maurice, S., Lawrence, D. J., Little, R. C., Lawson, S. L., Gasnault, O., Wiens, R. C., Barraclough, B. L., Elphic, R. C., Prettyman, T. H., Steinberg, J. T., Binder, A. B., and Maurice, S. (2001). Evidence for water ice near the lunar poles. *Journal of Geophysical Research—Planets*, 106(E10):23231–23251.

Gerlach, K. and Kretschmer, F. F. (1992). General forms and properties of zero cross-correlation radar wave-forms. *IEEE Transactions on Aerospace and Electronic Systems*, 28(1):98–104.

Goldstein, R. M. (1964). Venus characteristics by Earth-based radar. *The Astronomical Journal*, 69(1):12–18.

Goldstein, R. M. (1969). A radar view of the surface of Venus. *Proceedings of the American Philosophical Society*, 113:224–228.

Goldstein, R. M. and Green, R. R. (1980). Ganymede: Radar surface characteristics. *Science*, 207:179–180.

Goldstein, R. M. and Morris, G. A. (1973). Radar observations of the rings of Saturn. *Icarus*, 20:260–262.

Goldstein, R. M. and Morris, G. A. (1975). Ganymede—observations by radar. *Science*, 188(4194):1211–1212.

Green, P. E. (1962). Radar astronomy measurement techniques. Technical Report 282, MIT Lincoln Laboratory.

Grolier, M. J. and Boyce, J. M. (1984). *Geologic Map of the Borealis Region of Mercury*. U.S. Geological Survey.

Guey, J.-C. and Bell, M. R. (1998). Diversity waveform sets for delay-Doppler imaging. *IEEE Transactions on Information Theory*, 44(4):1504–1522.

Gurrola, E. M. (1995). *Interpretation of radar data from the icy Galilean satellites*. PhD thesis, Stanford University.

Hagfors, T., Gold, T., and Ierkic, H. M. (1985). Refraction scattering as the origin of the anomolous radar returns of Jupiter's satellites. *Nature*, 315(6021).

Hagfors, T. and Kofman, W. (1991). Mapping of overspread targets in radar astronomy. *Radio Science*, 26(2):403–416.

Hagfors, T., Nanni, B., and Stone, K. (1968). Aperture synthesis in radar astronomy and some applications to lunar and planetary studies. *Radio Science*, 3(5):491.

Haldemann, A. F. C. and Muhleman, D. O. (1999). Circular-polarization radar properties of high-altitude ice: Western Kunlun Shan and central Andes. *Journal of Geophysical Research*, 104(E10).

Hapke, B. (1990). Coherent backscatter and the radar characteristics of outer planet satellites. *Icarus*, 88:407–417.

Harcke, L. J., Zebker, H. A., Jurgens, R. F., and Slade, M. A. (2000). Delay-Doppler imaging of "overspread" planets. In *Proceedings of the IEEE Geoscience and Remote Sensing Symposium*, volume 1, pages 284–286.

Harmon, J. K. (1997). Mercury radar studies and lunar comparisons. *Advances in Space Research*, 19(10):1487–1496.

Harmon, J. K. (2002). Planetary delay-Doppler radar and the long-code method. *IEEE Transactions on Geoscience and Remote Sensing*, 40(9):1904–1916.

Harmon, J. K., Perillat, P. J., and Slade, M. A. (2001). High-resolution radar imaging of Mercury's north pole. *Icarus*, 149:1–15.

Harmon, J. K. and Slade, M. A. (1992). Radar mapping of Mercury: Full-disk images and polar anomolies. *Science*, 258.

Harmon, J. K., Slade, M. A., Velez, R. A., Crespo, A., Dryer, M. J., and Johnson, J. M. (1994). Radar mapping of Mercury's polar anomalies. *Nature*, 369(6477):213–215.

Harmon, J. K., Sulzer, M. P., Perillat, P. J., and Chandler, J. F. (1992). Mars radar mapping: Strong backscatter from the elysium basin and outflow channel. *Icarus*, 95:153–156.

Hogbom, J. A. (1974). Aperture synthesis with a non-regular distribution of interferometer baselines. *Astronomy and Astrophysics Supplement*, 15:417–426.

Horton, B. M. (1959). Noise-modulated distance measuring systems. *Proceedings of the IRE*, 49(5):821–828.

Hudson, R. S. and Ostro, S. J. (1990). Doppler radar imaging of spherical planetary surfaces. *Journal of Geophysical Research*, 95:10,947.

Inan, U. S. and Inan, A. S. (2000). *Electromagnetic Waves*. Prentice Hall.

Ingalls, R. P. and Rainville, L. P. (1972). Radar measurements of Mercury: Topography and scattering characteristics at 3.8 cm. *The Astronomical Journal*, 77(2):185–190.

Jurgens, R. F. (1970). Some preliminary results of the 70 cm radar studies of Venus. *Radio Science*, 5:435–442.

Jurgens, R. F., Goldstein, R. M., Rumsey, H. R., and Green, R. R. (1980). Images of Venus by three-station radar interferometry—1977 results. *Journal of Geophysical Research*, 85:8282–8294.

Khurana, K. K., Kivelson, M. G., Stevenson, D. J., Schubert, G., Russell, C. T., Walker, R. J., and Polanskey, C. (1998). Induced magnetic fields as evidence for subsurface oceans on Europa and Callisto. *Nature*, 395(6704):777–780.

Kotelnikov, V. A., Guskov, G. Y., Dubrovin, V. M., Rzhiga, O. N., Minashin, V. P., Petrov, G. M., Morozov, V. A., Shakhovs, A. M., Kislik, M. d., Podoprig, G. A., Frantsesson, A. M., Nikitski, N. I., and Korenber, E. B. (1962). Radiolocation of Mercury. *Doklady Akademii Nauk SSSR*, 147(6):1320.

Lehtinen, M. S. and Haggstrom, I. (1987). A new modulation principle for incoherent scatter measurements. *Radio Science*, 22:625.

Lerner, R. M. (1960). A matched filter detection system for complicated Doppler-shifted signals. *IRE Transactions on Information Theory*, 6(3):373–386.

Lin, C.-T. (1985). On the ambiguity function of random binary-phase-coded waveforms. *IEEE Transactions on Aerospace and Electronic Systems*, 21(3):432–436.

Liu, G. S., Gu, H., and Su, W. M. (1999). Development of random signal radars. *IEEE Transactions on Aerospace and Electronic Systems*, 35(3):770–777.

Margot, J. L., Campbell, D. B., Jurgens, R. F., and Slade, M. A. (1999). Topography of the lunar poles from radar interferometry: A survey of cold trap locations. *Science*, 284(5420):1658–60.

Margot, J. L., Peale, S. J., Jurgens, R. F., Slade, M. A., and Holin, I. V. (2003). Mercury interior properties from measurements of librations. In *25th Meeting of the International Astronomical Union*, Sydney, Australia.

Margot, J.-L. C. (1999). *Lunar topography from Earth-based radar interferometric mapping*. PhD thesis, Cornell University.

McCauley, J. F., Guest, J. E., Schaber, G. G., Trask, N. J., and Greeley, R. (1981). Stratigraphy of the Caloris Basin, Mercury. *Icarus*, 47(2):184–202.

McCready, L. L., Pawsey, J. L., and Payne-Scott, R. (1947). Solar radiation at radio frequencies and its relation to sunspots. *Proceedings of the Royal Society of London, Series A—Mathematical and Physical Sciences*, 190(1022):357–375.

Mie, G. (1908). Contributions to the optics of turbid media, especially colloidal metal suspensions. *Annalen der Physik—Vierte Folge*, 25(3):377–445.

Mitchell, D. L. and de Pater, I. (1994). Microwave imaging of Mercury's thermal emmission at wavelengths from 0.3 cm to 20.5 cm. *Icarus*, 111(2):489–502.

Morgan, T. H. and Shemansky, D. E. (1991). Limits to the lunar atmosphere. *Journal of Geophysical Research*, 96:1351–1367.

Morrison, D. and Morrison, N. D. (1977). Photometry of the Galilean satellites. In Burns, J. A., editor, *Planetary Satellites*, pages 363–378. University of Arizona Press.

Muhleman, D. O., Butler, B. J., Grossman, A. W., and Slade, M. A. (1991). Radar images of Mars. *Science*, 253:1508–1513.

Muhleman, D. O., Grossman, A. W., and Butler, B. J. (1990). Radar reflectivity of Titan. *Science*, 248:975–980.

Nozette, S., Lichtenberg, C. L., Spudis, P., Bonner, R., Ort, W., Malaret, E., Robinson, M., and Shoemaker, E. M. (1996). The Clementine bistatic radar experiment. *Science*, 274(5292):1495–1498.

Nozette, S., Spudis, P. D., Robinson, M. S., Bussey, D. B. J., Lichtenberg, C., and Bonner, R. (2001). Integration of lunar pole remote-sensing data sets: Evidence for ice at the lunar south pole. *Journal of Geophysical Research—Planets*, 106(E10):23253–23266.

Oppenheim, A. V. and Schafer, R. W. (1989). *Discrete-Time Signal Processing*. Prentice Hall.

Ostro, S., Campbell, D. B., Simpson, R. A., Hudson, R. S., Chandler, J. F., Rosema, K. D., Shapiro, I. I., Standish, E. M., Winkler, R., Yeomans, D. K., Velez, R., and Goldstein, R. M. (1992). Europa, Ganymede, and Callisto: New radar results from Arecibo and Goldstone. *Journal of Geophysical Research*, 97(E11):18,227–18,244.

Ostro, S. J. (1982). Radar properties of Europa, Ganymede, and Callisto. In Morrison, D., editor, *Satellites of Jupiter*. The University of Arizona Press.

Ostro, S. J. (1993). Planetary radar astronomy. *Reviews of Modern Physics*, 65(4):1235–79.

Ostro, S. J. and Pettengill, G. H. (1978). Icy craters on the Galilean satellites? *Icarus*, 34:268–279.

Paige, D. A., Wood, S. E., and Vasavada, A. R. (1992). The thermal stability of water ice at the poles of Mercury. *Science*, 258:643–646.

Pang, K., Hord, C. W., West, R. A., Simmons, K. E., Coffeen, D. L., Bergstralh, J. T., and Lane, A. L. (1979). Voyager 1 photopolarimeter experiment and the phase curve and surface microstructure of Ganymede. *Nature*, 280:804–806.

Pappalardo, R. T., Head, J. W., Collins, G. C., Kirk, R. L., Neukum, G., Oberst, J., Giese, B., Greeley, R., Chapman, C. R., Helfenstein, P., Moore, J. M., McEwen, A., Tufts, B. R., Senske, D. A., Breneman, H. H., and Klaasen, K. (1998). Grooved terrain on Ganymede: First results from Galileo high-resolution imaging. *Icarus*, 135:276–302.

Parks, T. W. and McClellan, J. H. (1972). Chebyshev approximation for nonrecursive digital filters with linear phase. *IEEE Transactions on Circuit Theory*, 19(2):189.

Peters, K. (1992). The coherent backscatter effect: A vector formulation accounting for polarization and absorption effects and small or large scatterers. *Physical Review B*, 46:801–812.

Pettengill, G. H. (1978). Physical properties of planets and satellites from radar observations. *Annual Review of Astronomy and Astrophysics*, 16:265–292.

Pettengill, G. H. and Dyce, R. B. (1965). A radar determination of the rotation of the planet Mercury. *Nature*, 206(4990):1240.

Pettengill, G. H. and Thompson, T. W. (1968). A radar study of the lunar crater Tycho at 3.8 cm and 70 cm wavelength. *Icarus*, 8(3):457–471.

Pike, R. J. (1988). Impact craters on Mercury. In Vilas, F., Chapman, C. R., and Matthews, M. S., editors, *Mercury*. Univ. of Arizona Press.

Price, R. and Green, P. E. (1960). Signal processing in radar astronomy. Technical Report 234, MIT Lincoln Laboratory.

Rees, W. G. (2001). *Physical Principles of Remote Sensing*. Cambridge University Press.

Rignot, E. J., Ostro, S. J., Van Zyl, J. J., and Jezek, K. C. (1993). Unusual radar echoes from the Greenland ice sheet. *Science*, 261(5129):1710–1713.

Rihaczek, A. W. (1969). *Principles of high-resolution radar*. McGraw-Hill.

Robinson, M. S., Davies, M. E., Colvin, T. R., and Edwards, K. (1999). A revised control network for Mercury. *Journal of Geophysical Research*, 104(E12):30847–30852.

Rogers, A. E. E. and Ingalls, R. P. (1970). Radar mapping of Venus with interferometric resolution of the range-Doppler ambiguity. *Radio Science*, 5(2):425–33.

Ruck, G. T., Barrick, D. E., Stuart, W. D., and Krichbaum, C. K. (1970). *Radar Cross Section Handbook*. Plenum Press.

Ryan, T. P. (1997). *Modern Regression Methods*. Wiley.

Schiaparelli, G. V. (1889). Sulla rotazione di Mercurio. *Astronomische Nachrichten*, 123(2944):241.

Seidelmann, P. K., Abalakin, V. K., Bursa, M., Davies, M. E., De Bergh, C., Lieske, J. H., Oberst, J., Simon, J. L., Standish, E. M., Stooke, P., and Thomas, P. C. (2002). Report of the IAU/IAG/COSPAR working group on cartographic coordinates and rotational elements of the planets and satellites: 2000. *Celestial Mechanics and Dynamical Astronomy*, 82(1):83–110.

Shapiro, I. I., Pettengill, G. H., Ash, M., Stone, M. L., Smith, W. B., Ingalls, R. P., and Brockelman, R. A. (1968). Fourth test of general relativity—preliminary results. *Physical Review Letters*, 20(22):1265–1269.

Sherwin, C. W., Ruina, J. P., and Rawcliffe, R. D. (1962). Some early developments in synthetic aperture radar systems. *IRE Transactions on Military Electronics*, 6:111–115.

Siebert, W. M. (1956). A radar detection philosophy. *IRE Transactions on Information Theory*, 2:204–221.

Simpson, R. A. and Tyler, G. L. (1999). Reanalysis of Clementine bistatic radar data from the lunar south pole. *Journal of Geophysical Research—Planets*, 104(E2):3845–3862.

Sivaswamy, R. (1982). Self-clutter cancellation and ambiguity properties of subcomplementary sequences. *IEEE Transactions on Aerospace and Electronic Systems*, 18(2):163–181.

Skolnik, M. I. (2002). *Introduction to Radar Systems*. McGraw-Hill.

Slade, M. A., Butler, B. J., and Muhleman, D. O. (1992). Mercury radar imaging—evidence for polar ice. *Science*, 258(5082):635–640.

Slade, M. A., Harcke, L. J., Jurgens, R. F., Harmon, J. K., Zebker, H. A., and Standish, E. M. (2000). 3.5-cm imaging of the Mercury north polar radar-bright features. In *31st Annual Lunar and Planetary Science Conference*. Abstract no. 1305.

Slade, M. A., Harmon, J. K., Harcke, L. J., and Jurgens, R. F. (2004). 3.5 cm radar observations of polar regions of Mercury using Goldstone to Arecibo configuration. In *35th COSPAR Scientific Assembly*, Paris, France. Abstract no. COSPAR04-A-01154.

Stacy, N. J. S. (1993). *High-resolution synthetic aperture radar observations of the moon*. PhD thesis, Cornell University.

Stacy, N. J. S., Campbell, D. J., and Ford, P. G. (1997). Arecibo radar mapping of the lunar poles: a search for ice deposits. *Science*, 276:1527–1530.

Standish, E. M. (1998). JPL planetary and lunar ephemerides, DE405/LE405. Technical Report IOM 312.F-98-048, Jet Propulsion Laboratory.

Stone, E. C. and Lane, A. L. (1979). Voyager 1 encounter with the Jovian system. *Science*, 204(4396):945–8.

Strom, R. G., Malin, M. C., and Leake, M. A. (1990). *Geologic Map of the Bach Region of Mercury*. U.S. Geological Survey.

Sulzer, M. P. (1986). A radar technique for high-range resolution incoherent scatter auto-correlation function measurements utilizing the full average power of klystron radars. *Radio Science*, 21(6):1033–1040.

Thompson, A. R., Moran, J. M., and Swenson, Jr., G. W. (1986). *Interferometry and Synthesis in Radio Astronomy*. John Wiley & Sons.

Thompson, T. W. and Dyce, R. B. (1966). Mapping of lunar radar reflectivity at 70 centimeters. *Journal of Geophysical Research*, 71(20):4843.

Titus, T. N., Kieffer, H. H., and Christensen, P. R. (2003). Exposed water ice discovered near south pole of Mars. *Science*, 299(5609):1048–1051.

Tsao, J. and Steinberg, B. D. (1988). Reduction of sidelobe and speckle artifacts in microwave imaging: The CLEAN technique. *IEEE Transactions on Antennas and Propagation*, 36(4):543–556.

Urkowitz, H., Geisler, J. D., and Riccardi, N. A. (1973). The effect of weighting upon signal-to-noise ratio in pulse bursts. *IEEE Transactions on Aerospace and Electronic Systems*, 9(4):486–494.

Vasavada, A. R., Paige, D. A., and Wood, S. E. (1999). Near-surface temperatures on Mercury and the Moon and the stability of polar ice deposits. *Icarus*, 141:179–192.

Victor, W. K. and Stevens, R. (1961). Exploration of Venus by radar. *Science*, 134(3741):46–48.

Webb, J. L., Munson, D. C., and Stacy, N. J. S. (1998). High-resolution planetary imaging via spotlight-mode synthetic aperture radar. *IEEE Transactions on Image Processing*, 7(11):1571–1582.

Welch, P. D. (1967). Use of fast Fourier transform for estimation of power spectra—a method based on time averaging over short modified periodograms. *IEEE Transactions on Audio and Electroacoustics*, 15(2):70–73.

Woodward, P. M. (1951). Information theory and the design of radar receivers. *Proceedings of the Institute of Radio Engineers*, 39(12):1521–1524.

Woodward, P. M. (1953). *Probability and information theory, with applications to radar*. Pergamon Press.

Zeoli, G. W. (1982). Comment on "Self-clutter cancellation and ambiguity properties of subcomplementary sequences". *IEEE Transactions on Aerospace and Electronic Systems*, 19(5):780–781.

Zohar, S. and Goldstein, R. M. (1974). Surface featurs on Mercury. *Astronomical Journal*, 79:85–91.

Zuber, M. T., Smith, D. E., Solomon, S. C., Abshire, J. B., Afzal, R. S., Aharonson, O., Fishbaugh, K., Ford, P. G., Frey, H. V., Garvin, J. B., Head, J. W., Ivanov, A. B., Johnson, C. L., Muhleman, D. O., Neumann, G. A., Pettengill, G. H., Phillips, R. J., Sun, X., Zwally, H. J., Banerdt, W. B., and Duxbury, T. C. (1998). Observations of the north polar region of Mars from the Mars orbiter laser altimeter. *Science*, 282:2053–2060.